Mesoscale Numerical Modelling and Failure Prediction of Automated Fibre Placement Composites

Xie Li

A dissertation presented for the degree of

Doctor of Philosophy

March 2022

School of Mechanical and Manufacturing Engineering, Faculty of Engineering,

University of New South Wales, Sydney, NSW 2052, Australia

This page is intentionally left blank.

ORIGINALITY STATEMENT

☑ I hereby declare that this submission is my own work and to the best of my knowledge it contains no materials previously published or written by another person, or substantial proportions of material which have been accepted for the award of any other degree or diploma at UNSW or any other educational institution, except where due acknowledgement is made in the thesis. Any contribution made to the research by others, with whom I have worked at UNSW or elsewhere, is explicitly acknowledged in the thesis. I also declare that the intellectual content of this thesis is the product of my own work, except to the extent that assistance from others in the project's design and conception or in style, presentation and linguistic expression is acknowledged.

COPYRIGHT STATEMENT

AUTHENTICITY STATEMENT

☑ I certify that the Library deposit digital copy is a direct equivalent of the final officially approved version of my thesis.

UNSW is supportive of candidates publishing their research results during their candidature as detailed in the UNSW Thesis Examination Procedure.

Publications can be used in the candidate's thesis in lieu of a Chapter provided:

- The candidate contributed **greater than 50%** of the content in the publication and are the "primary author", i.e. they were responsible primarily for the planning, execution and preparation of the work for publication.
- The candidate has obtained approval to include the publication in their thesis in lieu of a Chapter from their Supervisor and Postgraduate Coordinator.
- The publication is not subject to any obligations or contractual agreements with a third party that would constrain its inclusion in the thesis.

☑ The candidate has declared that **some of the work described in their thesis has been published and has been documented in the relevant Chapters with acknowledgement**.

A short statement on where this work appears in the thesis and how this work is acknowledged within chapter/s:

> My thesis includes several publications and they have been documented in the relevant chapters with acknowledgement in the introduction of each chapter. It should be noted that one publication may be used in two different chapters.
> Chapter 3 include "Tow Wise Modelling of Non-conventional Automated Fibre Placement Composites: Short Beam Shear Study" published in the journal of Composites Part A and "Low-velocity impact and compression-after-impact performance of non-conventional automated fibre placement composites", which has been submitted to the journal of International Journal of Impact Engineering.
> Chapter 4 include "Automation of Tow Wise Modelling for Automated Fibre Placement and Filament Wound Composites" published in the journal of Composites Part A.
> Chapter 5 include "A segment-to-segment cohesive contact network approach for mesoscale composites failure modelling" published in the journal of Composite Structures
> Chapter 6 include "Tow Wise Modelling of Non-conventional Automated Fibre Placement Composites: Short Beam Shear Study" published in the journal of Composites Part A

Candidate's Declaration

I declare that I have complied with the Thesis Examination Procedure.

Abstract

Automated fibre placement (AFP) is an advanced and fully automated composites manufacturing technique and offers a huge design space for lightweight composite structures through flexible fibre distribution and orientation. Advanced placed ply (AP-Ply) and variable stiffness laminate (VSL) are typical examples and are called Advanced AFP Laminates in this thesis. However, due to the machine tolerance and novel fibre path manipulation, a great variety of intrinsic mesoscale geometric features (gaps, overlaps, tow drops, tow crimping, etc.) can be produced, which may have a great impact on the laminate strength depending on specific applications. Despite the increasing awareness of the significance of these features, understanding the corresponding effect on part performance is still challenging due to the huge parameter space, particularly for advanced AFP laminates.

This research has developed a finite element (FE) method to predict the mechanical properties of AFP composites at coupon or part scale while retaining the intrinsic geometric features. The AP-Ply is an example used to validate this technique due to the sophisticated fibre architecture. Several experimental programs including short beam shear, low-velocity impact, combined loading compression and compression-after-impact were conducted at first to facilitate understanding the effect of these geometric features on the structural performance of AP-Ply. The experiments are used as a guideline and database for the model development.

The finite element method provided in this thesis was developed at mesoscale, specifically at a length scale of tows rather than plies or laminates in conventional methods. This method significantly improves the geometric fidelity of the model with the potential of depicting each tow and mesoscale geometric feature individually. To improve the efficiency of model generation, an automated tow-wise modelling (TWM) algorithm was developed, aiming to build the part virtually following the robotic kinematics. The automation significantly reduces the pre-processing effort of finite element model generation, which is also a critical step to bring AFP into industry 4.0 in the future.

The downstream use of TWM in the prediction of different failures is achieved with the implementation of a novel cohesive network approach, which greatly eases the pre-processing effort of explicitly allocating cohesive elements or developing complex fracture criteria. This method allows greater mesh size to be used in the crack front compared to conventional methods. The feasibility and accuracy of TWM in the prediction of mechanical properties of AFP composites, as well as the failure progression, were validated with AP-Ply experiments, specifically the short beam shear and low-velocity impact tests.

Acknowledgements

First and foremost I would like to extend my sincerest gratitude to my primary supervisor, Associate Professor Garth Pearce. I still remember the early days of research when I literally have zero background knowledge on composites, you can be so patient and enthusiastic to teach and guide me until I find the right track. Doing a PhD can be really challenging and painful, but meeting you make me feel it is one of the rightest choices I’ve made in my life. I feel so lucky to have you as my supervisor. Again, thank you!

I would also like to greatly thank my co-supervisor, Dr Sonya Brown, for the detailed guidance and constructive suggestions during the research. Dr Mathew Joosten from Deakin University also provided lots of modelling suggestions.

Many thanks to the AMAC team, Prof Ganga Prusty, Dr Mathew Donough, Dr Md Shamsuddoha, who provided many useful suggestions during the fortnight meettings. I would also like to thank Dr Ebrahim Oromiehie, Dr Phyo Thu Maung, and Seetharam Mahadevan for their help in manufacturing and testing the panels.

Special thanks are given to my friends and colleagues, Nikhil Garg, Congyuan Tao, Nimal Balasubramani, Veldyanto Tanulia, Yiwen Gu, etc., for their help and accompany throughout the journey.

I would like to give my biggest thank you to my family and friends, especially my girlfriend, Yi Wan. Although you are overseas, your mental support is invaluable to the completion of this research.

Finally, I would like to acknowledge the financial support provided by the University of New South Wales. This research is conducted within the ARC Training Centre for Automated Manufacture of Advanced Composites (IC160100040), supported by the Commonwealth of Australia under the Australian Research Council's Industrial Transformation Research Program.

Table of Contents

List of Figures

List of Tables

Nomenclature

The list of symbols is not comprehensive; variations exist between same symbols but are explicitly defined within the text.

Symbol	Description
AP-Ply	Advanced Placed Ply
ASTM	American Society for Testing and Materials
AFP	Automated Fibre Placement
ATL	Automated Tape Laying
CV	Coefficient of Variation
CZM	Cohesive Zone Model
CLC	Combined Loading Compression
CAI	Compression-After-Impact
CT	Computed Tomography
CNC	Computer Numerical Control
CDM	Continuum Damage Mechanics
DCM	Discrete Crack Model
DCB	Double Cantilever Beam
ENF	End Notched Flexure
FPM	Fibre Placement Manager
FRC	Fibre-Reinforced Composites
FW	Filament Winding
FE	Finite Element
FRMM	Fixed Ratio Mixed Mode

LVI	Low-Velocity Impact
N2S	Node-to-Segment
NDI	Non-Destructive Testing
NURBS	Non-uniform rational B-spline
QLT	Quasi-Isotropic Laminate Tensile
S2S	Segment-to-Segment
SSCC	Segment-to-Segment Cohesive Contact
SBS	Short Beam Shear
SBSS	Short Beam Strength
SCM	Smeared Crack Model
SERR	Strain Energy Release Rate
TPP	Tow Path Planning
TWM	Tow-Wise Modelling
UD	Unidirectional
VSL	Variable Stiffness Laminate
VCCT	Virtual Crack Closure Technique

E^i	Penalty factor / contact stiffness
E_{ii}	Young's modulus in ii direction
G_{ic}, G_{iic}	Critical strain energy release rate for mode I and II
G_{ii}	Shear modulus in ii direction
X_{ft}, X_{fc}	Fibre tensile / compressive strength
X_{it}, X_{is}	Interlaminar normal / shear strength
X_{mt}, X_{ms}, X_{mc}	Matrix tensile / shear / compressive strength
k_I, k_{II}	Cohesive stiffness for mode I and II
v_{ii}	Poisson ratio in ii direction
λ_i	Contact stress in i direction

A	Cross-sectional area
b	Specimen width
D	Damage parameter
E	Energy
F	Force
g	Gap function
g	Gravity acceleration
G	Work done (J)
h	Specimen thickness
m	Mass
t	Time
v	Velocity
Γ	Contact area
α	Mix-mode interaction parameter
δ	Displacement
μ	Enhancement factor / friction coefficient
σ	Stress

Chapter 1 Introduction

1.1 Background

Fibre-reinforced composites (FRC) are gaining demand over traditional materials due to their superior performance, enabling weight reduction, higher fatigue resistance and corrosion resistance, etc. With the increased use of composite materials, and maturation of materials technology, the emphasis of industry is placed on cost-efficient manufacturing techniques and design innovation and optimisation. Filament Winding (FW), Automated Tape Laying (ATL), Automated Fibre Placement (AFP), 3D Printing are hence emerging for composite manufacture. Among all the FRC manufacturing methods, AFP is one of the fastest-growing fully automated techniques and has been widely used in various sectors especially in aerospace, transportation, energy, and defence today (2021).

AFP's rapid growth is driven by alignment with industry needs:

- Reduction in labour costs and increased manufacturing up-time.
- Adaptable for manufacturing more complex composite structures which other automated techniques (such as ATL and FW) cannot achieve. The narrow strips of carbon fibre composite tape (tows) allow for the reproduction of highly curved parts.
- Ability to manufacture high-quality parts with high productivity but low material waste.

- The ability of precise fibre positional and directional control, which enables great tailoring flexibilities and uncovers significant potential in laminate multi-objective optimisations [1].

The shortcomings of AFP technique are also substantial:

- AFP systems are expensive and relatively slow.
- Designing for AFP manufacture requires specialised software, training and integrated simulation support.
- The manufacturing-induced defects such as: angle deviation, tow misalignment, waviness, gap/overlap, and twisted tow (to name a few) can pose a threat to the structural performance of the laminates. The existing solution to this is to adopt a higher factor of safety, which, however, substantially offset the weight benefits of composites compared to metallic alloys.
- With the inclusion of various defects in the laminates and many unavoidable consequences of the AFP process, understanding structural performance and failure becomes extremely challenging.

Along with efforts to understand and mitigate the effect of these defects on the structural performance of AFP composites, the industry has also focused on design innovation to reduce overall structural weight. AFP manufacture has two critical features, cut-restart (interrupting a tow mid-part) and fibre steering (independently varying the fibre orientation along a tow), which unlock a vastly expanded design space for composite laminates. These innate features provide AFP with the capability of precise fibre positional and directional control, which can enable huge advances in composite structure design. Variable Stiffness Laminate (VSL) and Advanced Placed Ply (AP-Ply) techniques [2, 3] which are derived from these capabilities, have demonstrated great potential for further optimisation of the in-plane and out-of-plane laminate properties, respectively.

Broadly, these non-conventional AFP laminates are called "Advanced AFP Laminates" in this thesis. Compared to traditional composite laminates, the fibre in advanced AFP laminates can be placed in a very complex way, which substantially increases the difficulties in understanding the structural performance and associated failure mechanisms. Another major limitation of advanced AFP laminates is that it can generate one or two orders of magnitude more local laminates defects than conventional AFP composites, both in terms of the defect size and density. These defects can be regarded as the "key geometric features" of advanced AFP laminates.

Due to these limitations, analytical calculations become challenging or impossible to characterise the material properties for such complex laminate structures. However, to fully exploit the potential of AFP, it is important that the material behaviours are well understood. In turn, a higher demand is placed on simulation tools to predict the material behaviour and properties without onerous and costly experimental tests.

1.2 Challenges in AFP composites modelling

Predicting material properties of composites can be difficult especially for complex structures. To facilitate the understanding of current challenges in AFP composites modelling, a micrograph (Figure 1.1) is used to describe the complex geometries involving gaps, overlaps.

The major challenges of modelling AFP composites are summarized as follows:

(Figure 1.1 is from Figure 4 in [4])

Figure 1.1. Micro-images for gaps, overlaps, and staggered gaps [4]

- The experimental data that can be used for model validation is very limited due to experimental execution complexities, especially in manufacturing panels with a certain size of embedded defects and testing expenses (costs and time).
- The mesoscale geometric features (gaps, overlaps, tow drops, etc), which result in local structural discontinuities that are completely embedded in the laminates can be very tedious and difficult to characterise both experimentally and numerically.
- The full kinetics of the consolidation and cure process can further lead to tow bridging, tow cross-section distortions, as-cured thickness variations, etc. Based on the microscopic images of AFP composites from previous experimental studies [4, 5] (see Figure 1.1), the adjacent tows near the defect area tend to fill the gaps and create fibre waviness for the overlaps during the curing process.

Existing finite element (FE) simulation tools for composites in literature can be simply categorized into three different length scales including micro-, meso-, and macro-scale, as simply described in Figure 1.2. Considering the physical part scales of AFP composites and available computational power, macroscale models (Figure 1.3a) are commonly used, where the structural discontinuities induced

by defects are neglected for simplification. These methods, however, are limited in an approximate global evaluation of elastic behaviours of AFP composites.

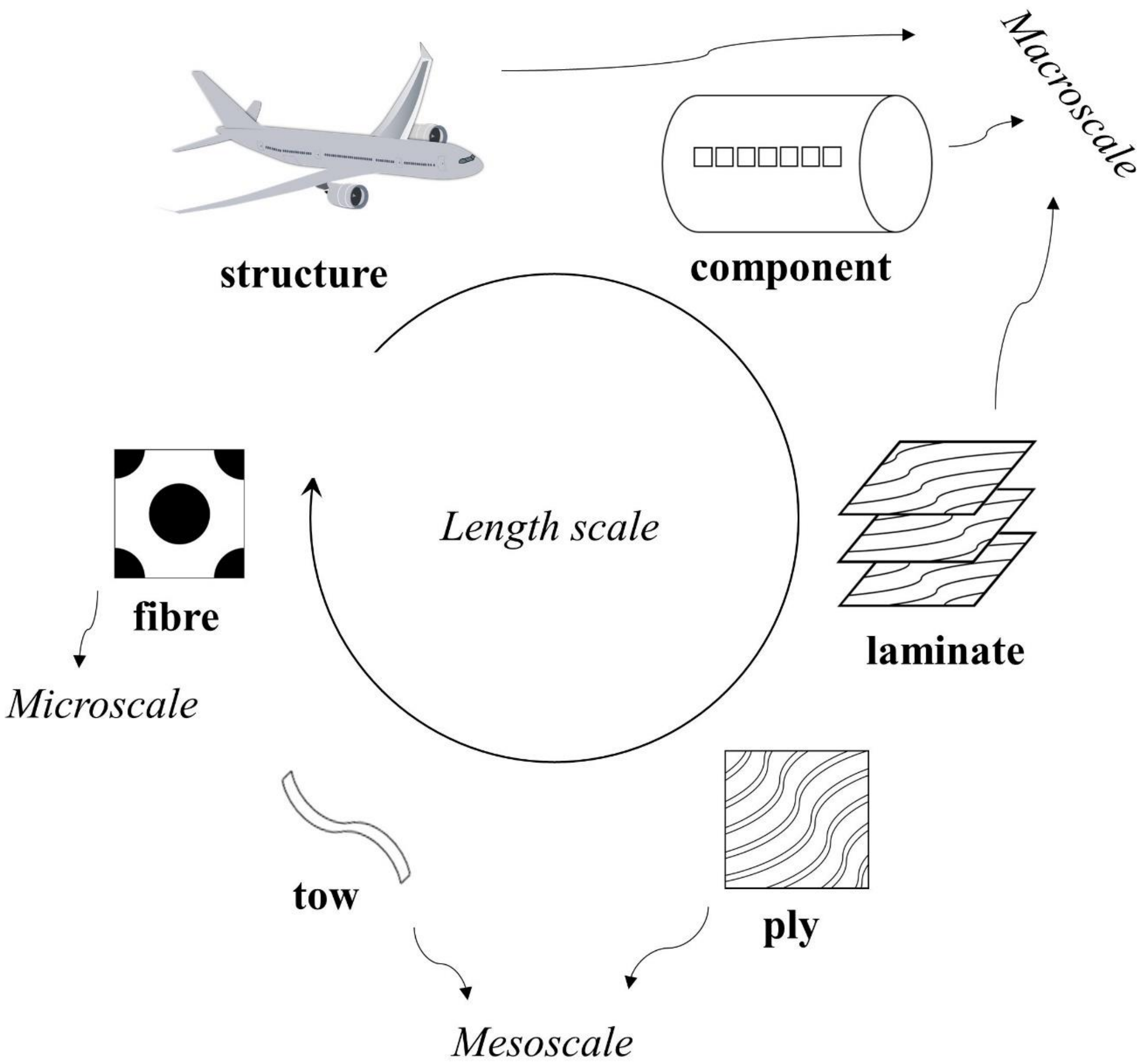

Figure 1.2. The length scales of AFP composites

The strength and damage prediction requires an accurate prediction of local material state, which means the key geometric features are critical to represent in the model. Recent studies [6, 7] have attempted to solve this critical challenge with mesoscale methods (Figure 1.3b), which are established based on a length scale of ply level modelling. In these methods, the geometric discontinuities are introduced between the plies. The defects that result in ply thickness variation can be manually depicted based on micrographs, which although powerful, require significant manual effort and computational resources, and only suit specific cases. In addition to the challenges of defects modelling, it should be noted that the fibre orientations in AFP composites can vary in a very complex way, even without big gaps and overlaps. Modelling this general AFP laminate structure may be possible with exisiting mesoscale methods, but requires plenty of assumptions and simplifications.

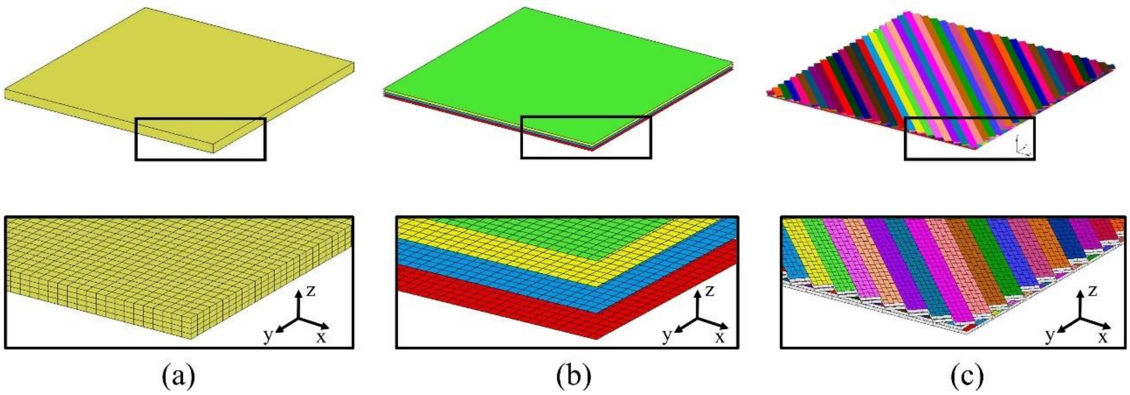

Figure 1.3. AFP modelling methods include (a) macroscale; (b) mesoscale at ply level; (c) mesoscale at tow level. Note: the colour is only used to indicate the structural discontinuities of the model, where (b) represents different plies and (c) represents different tows.

In this thesis, to address these challenges, the length scale of mesoscale modelling is further refined from ply to tow (see Figure 1.2). This refers to a generic modelling approach for representing tows in an AFP laminate (see Figure 1.3c), namely Tow-Wise Modelling (TWM). The major aim of the TWM is to produce a 3D laminate geometry (and associated mesh) that accounts for tow-tow interaction and intrinsically represents the most critical geometric features (gaps, overlaps, and tow drops, etc.). A significant advancement of this approach is to model AFP composites at a length scale of tow rather than ply or laminate, which creates possibilities of depicting each tow individually, hence greatly improves the model fidelity and reduces the required model simplifications.

1.3 Goals of the research

This thesis will address some of the research challenges outlined above. The key objective of this thesis is to develop a robust and computational-efficient mesoscale simulation tool (TWM) that can predict the mechanical properties of AFP composites (stiffness, strength, etc.) with greater accuracy compared to traditional macro- and meso-scale methods. To achieve this, the following critical aims need to be met:

- Experiments used to provide a guideline for model development and a database for model validation need to be designed. To test the model capability in predicting the mechanical properties and failure behaviours of AFP composites with defects, the relevant key failure mechanisms must be understood a priori based on the experiments.
- An automated TWM algorithm that can represent each tow individually following the robotic kinematics needs to be developed to avoid tedious and onerous manual effort of model generation.
- A valid composites failure modelling technique that can be integrated into the TWM to predict critical failure mechanisms involved in AFP composites at mesoscale must be developed.
- The feasibility of TWM in predicting the mechanical properties and associated key failure mechanisms of AFP composites needs to be validated.

1.4 Thesis outline

To facilitate understanding the flow of this thesis, an outline is presented as follows:

1.4.1 Chapter 2 Literature Review

A comprehensive review of the literature is conducted in this chapter. The major aim is to provide a background of the critical importance of the TWM approach. Another emphasis is placed on reviewing the state-of-the-art composites failure modelling methods and identifying the potential approaches that can be used to represent the key failure kinematics of AFP composites at the length scale of tow.

1.4.2 Chapter 3 Experimental Studies of AFP Composites

This chapter provides an experimental database that will be used for model development and validation. One of the representative AFP composites, AP-Ply is studied due to the complex mesostructure, in which tow crimping, tow interweaving, tow drops, and tow undulation are commonly observed and can result in significant challenges with macroscale modelling, and hence can be used to demonstrate the benefits and values of the proposed method.

A variety of experimental programs on AP-Ply are performed including a short beam shear (SBS) test, a low-velocity impact (LVI) test, a combined loading compression (CLC) test and a compression-after-impact (CAI) test. For each test, a comparison is conducted with a traditional AFP benchmark to facilitate the understanding of the associated failure mechanisms with and without defects and thus highlight the benefits and limitations of these key geometric features on the structural performance.

1.4.3 Chapter 4 TWM Method

This chapter presents the development of automated TWM algorithms that can represent each discrete tow and capture the key geometric features of AFP composites. The TWM will be mainly devoted to addressing the geometric modelling challenges of AFP composites with defects. The key inputs, outputs, and assumptions of the TWM method are firstly introduced, followed by a detailed stepwise algorithm description. Case studies are carried out at last to demonstrate the functionalities of TWM in representing these geometric features of AFP composites.

1.4.4 Chapter 5 Cohesive Network Approach

A novel cohesive network method is developed in this chapter to address the failure modelling challenges of AFP composites at the length scale of tow, where each tow is individually modelled and results in non-conformal meshing interfaces. Conventional methods are either too computationally expensive or unable to be used in the case of non-conformal meshing interfaces. Coupon level benchmark testing is carried out to demonstrate the feasibility and efficiency of the proposed method. The numerical results are compared against the literature for validation. It should be noted that this chapter aims to demonstrate the S2S contact algorithms for creating a cohesive network model with contact.

1.4.5 Chapter 6 TWM Demonstration in AFP Composites

This chapter aims to combine these two key capabilities (TWM + Cohesive Network Approach) into a unified TWM modelling framework. The feasibility of the TWM modelling framework in predicting the mechanical properties and failure behaviours of AFP composites will be validated as well. The experimental studies performed in Chapter 3 will be used for comparison, specifically the SBS and LVI tests.

1.4.6 Chapter 7 Conclusion

The final chapter provides a concise summary of the thesis. The remaining areas for development and some potential research trajectories are discussed that provide a foundation for future research.

1.5 Research publication outputs

1.5.1 Conference proceedings

Li X, Prusty BG, and Pearce GM. *Intralaminar and interlaminar progressive failure analysis of AFP composites*, in *the 22nd International Conference on Composites Materials (ICCM22)*. 2019. Melbourne, Australia.

Li X, Brown SA, Joosten M, Pearce GM. *Progressive failure analysis of AP-Ply laminate using tow wise modelling technique*, in *the 5th Australasian Conference on Computational Mechanics (ACCM2021)*. 2021. Sydney, Australia.

1.5.2 Journal papers

Li X, Dufty J, Pearce GM. *Automation of Tow Wise Modelling for Automated Fibre Placement and Filament Wound Composites*. Composites Part A: Applied Science and Manufacturing. 2021:106449.

Li X, Brown SA, Joosten M, Pearce GM. *Tow Wise Modelling of Non-conventional Automated Fibre Placement Composites: Short Beam Shear Study*. Composites Part A: Applied Science and Manufacturing. 2021:106767.

Li X, Brown SA, Joosten M, Pearce GM. *A segment-to-segment cohesive contact network approach for mesoscale composites failure modelling*. Composite Structures. 2022:115205.

Li X, Brown SA, Pearce GM. *Low-velocity impact and compression-after-impact performance of non-conventional automated fibre placement composites*. International Journal of Impact Engineering. **Submitted**.

Chapter 2 Literature Review

2.1 Introduction

Composite materials have been widely used for decades and numerous studies focusing on this area have been presented. The general background of composites, as well as the critical failure modes, have been introduced in a great deal of publications till now, and hence will not be presented here. Instead, this chapter will provide a comprehensive review specifically relevant to the field of AFP composites to highlight the existing research challenges.

Five main topics are presented starting from Section 2.2, which provides an overview of AFP technology. A categorisation of common manufacturing-induced defects underlying this advanced technique is considered in Section 2.3. The state-of-the-art finite element (FE) modelling methods for AFP composites are discussed in Section 2.4. Various failure modelling methods used with composites will be reviewed in Section 2.5. A summary of this chapter regarding the literature findings will be made in Section 2.6.

2.2 AFP technology

This section aims to provide an overview of AFP technology. Section 2.2.1 will firstly introduce the background of AFP. The fundamental manufacturing mechanisms and layup design process are presented in Sections 2.2.2 and 2.2.3, respectively. The concepts of traditional and advanced AFP laminates, as well as their principles of manufacturing, will be introduced in Section 2.2.4.

2.2.1 Background on AFP technology

Automated tape laying (ATL) and filament winding (FW) are the first two automated composite manufacturing techniques to achieve higher productivity compared to hand layup. For FW, the filament which is constrained to move in a near-geodesic path under tension cyclically is mainly used to make revolute parts, such as pressure vessels or tanks. The tension in the filament makes the technique impossible to be used in concave surfaces due to fibre bridging [8]. ATL is essentially an alternative to manual tape placement with a higher deposition rate on larger structures. The geometry of the structure, however, is limited to zero or trivial surface curvature [9].

AFP is another fully automated composite manufacturing technique and was commercially introduced in the 1980s to address the challenges of conforming tapes to a curved surface or a geometry with non-zero gaussian curvature encountered by the ATL system. AFP perfectly inherits the merits of ATL including the compaction and cut-restart capability, which reduces substantial material waste. AFP differs from ATL by using narrower tapes, which sacrifices productivity but gains higher flexibility of laying fibres over more complex geometries. Multiple narrow tapes are generally used in combination to improve manufacturing efficiency. The differential fibre payout capability of FW is also integrated into AFP and this enables each narrow tape to be delivered at different speeds, which is beneficial for fabricating more complex composite geometries such as a fuselage with numerous windows cut-outs, door cut-outs and grid stiffened components. FW can be essentially regarded as a special case of AFP. Any part made with FW could be manufactured with an AFP system by converting the winding geodesics to AFP head coordinates, with a small caveat that the robot head must avoid clashing with the tooling. FW is still preferred for most revolute parts because the entire system is substantially cheaper and simpler due to the reduced complexity of the machinery and design process. AFP avoids many of the limitations of FW (such as geodesic fibre paths) so has the potential to replace FW in high-performance applications.

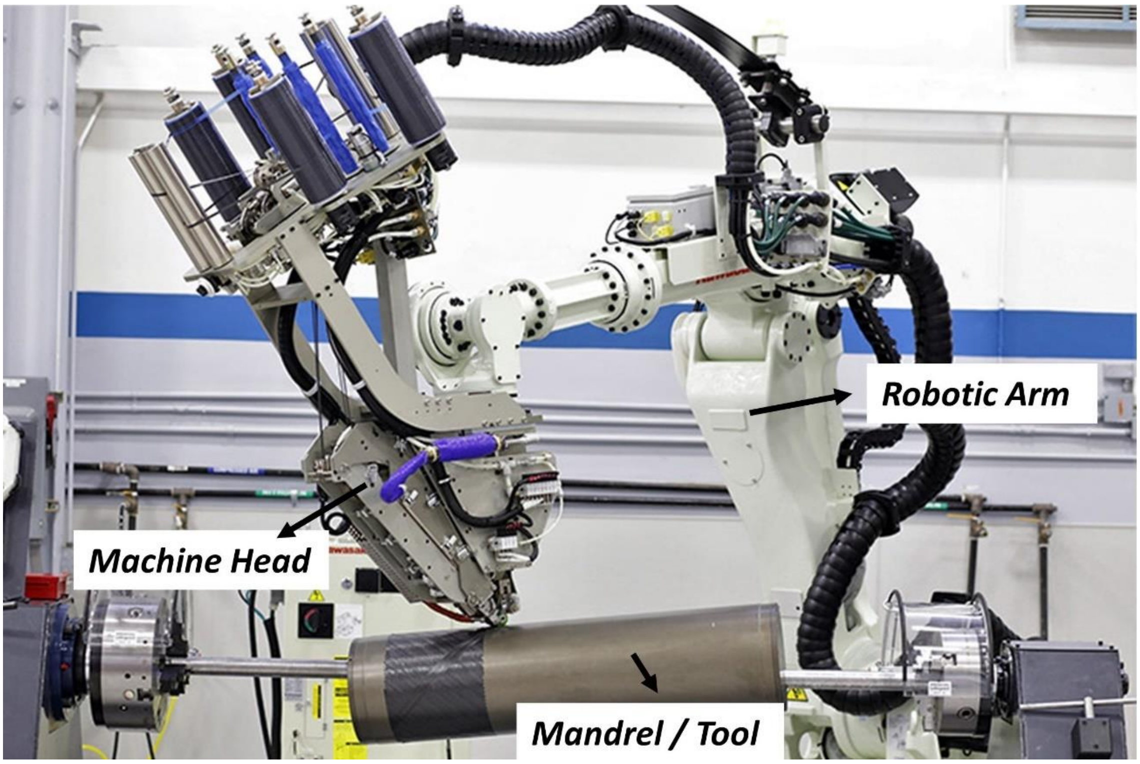

Figure 2.1. The automated fibre placement machine [10]

A typical AFP machine consists of three major parts, a robotic arm, a machine head, and a mandrel, as presented in Figure 2.1. The motion of the AFP machine is governed by the robotic arm, which provides six degrees of freedom including three translational movements and three rotational motions. The machine head is specifically used to handle the fibre placement process and in general, a variety of machine heads exist that can deal with different materials including thermoset prepregs, thermoplastic prepregs and dry fibres. The mandrel is also named the tool, which is essentially a geometry that provides support and guidance for placing multiple consecutive layers to build up the ultimate composite structure. The mandrel provides another self-rotation degree of freedom, which enables the production of complex composite structures in conjunction with the six degrees of freedom provided by the robotic arm.

Automated Dynamics (USA), Accudyne (USA), MAG-Cincinatti (USA), Electroimpact (USA), Foster Miller/ATK (USA), Ingersoll (USA), Coriolis (France), Mikrosam (Macedonia) and MTorres (Spain) are the major suppliers of AFP machine [11].

One of the key advantages of AFP technology, not able to be achieved by alternate lay-up technologies, is fibre steering, which refers to the ability of laying tows in a curved format in-plane. Due to the orthotropic characteristics of fibre reinforced composites, the properties are dominated by fibre orientation. Fibre steering technology uncovers the significant potential of tailoring laminate in-plane properties, thereby creating possibilities for optimisation which further reduces the structural weight.

2.2.2 Description of AFP manufacturing

The idea of AFP technology is to deposit slit prepreg tape on the surface of the preform via the machine head, as schematically illustrated in Figure 2.2. The slit prepreg tape is called a *tow*, which consists of a bundle of unidirectional fibres. Typical AFP machines can have 4 - 32 tows fed simultaneously to improve the manufacturing efficiency with standard tow widths of 3.175mm, 6.35mm and 12.7mm, which is narrower as aforementioned compared to the tape width (75 - 300 mm) used in the ATL system.

The manufacturing processes including material layup, curing/melting and compaction are all assembled into the machine head to improve the manufacturing efficiency. Figure 2.2 depicts a schematic diagram of the AFP manufacturing process, where each tow is coming from an individual material spool and is then placed onto the tool surface along with the internal guide rail. During the placement process, the tow is heated with a hot gas torch system or a laser system to increase the material tackiness and meanwhile, consolidation force is applied via a compaction roller to remove trapped air and ensure the tow adheres to the as-designed trajectories. After each travel is completed, the tow is cut near the designed boundaries through the tape cutter and restarted with a new round, resulting in low material waste.

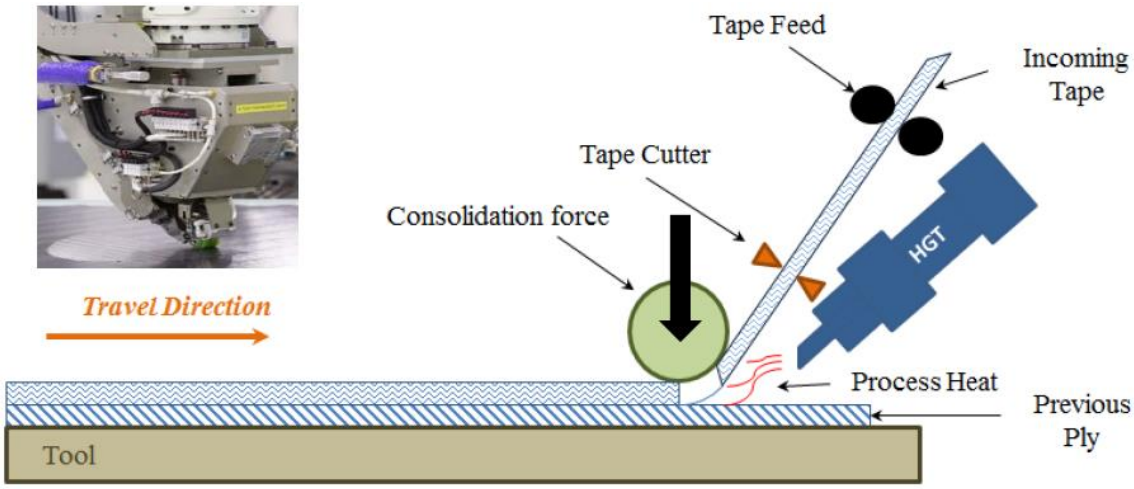

Figure 2.2. The schematic diagram of the AFP manufacturing process [12]

2.2.3 Tow path planning process

Each AFP machine has dedicated in-built software, which controls the material layup and robotic motion. Tow path planning (TPP) software is one of the critical technologies in AFP, as it determines the topology distributions of the fibres to be placed on the tool surface. TPP is critical in the design of AFP composite structures, with a great impact on the geometry precision and manufacturing efficiency [13]. TPP algorithms require inputs such as the tool/mandrel geometry; desired fibre orientation; kinematic constraints of the robot and head; and manufacturing constraints on tow paths, such as allowable radii of curvature, etc. The focus of TPP is to produce optimal 3D tow paths and control instructions for the complex robotics involved in AFP.

TPP involves several steps including:

- designing the CAD geometry of the mandrel and importing it into the in-built TPP software of AFP, such as fibre placement manager (FPM), the standard software for the Automated Dynamics AFP system at the University of New South Wales;
- defining layup boundaries;
- defining layup orientations and selecting a suitable tow path generation algorithm; and
- running a simulation to generate tow paths and checking if it satisfies the robotic requirements (e.g., no collision with the tooling).

The tow path is generally automatically computed by the in-built AFP software with the selected TPP algorithm. The TPP algorithm, however, varies from software to software but generally involves two critical steps. The first step is to define a reference (or guide) curve. Two methods are commonly used, including a triangular mesh-based approach [14, 15] and a parametrical approach [16-18]. The principles of these methods, as well as their respective benefits and limitations, have been discussed in [19]. The second step refers to the generation of the remaining tow paths based on the reference curve. The literature has reported two dominant approaches, the shifted method and the parallel method for the mass production of the other tow paths.

The shifted method (Figure 2.3a) refers to offsetting the reference curve in a specific direction with an equal distance, which was firstly proposed by Olmedo and Gurdal [20] in studies of the bulking response of variable stiffness laminates. This method, however, can easily generate either tow gaps or overlaps as shown in Figure 2.3c.

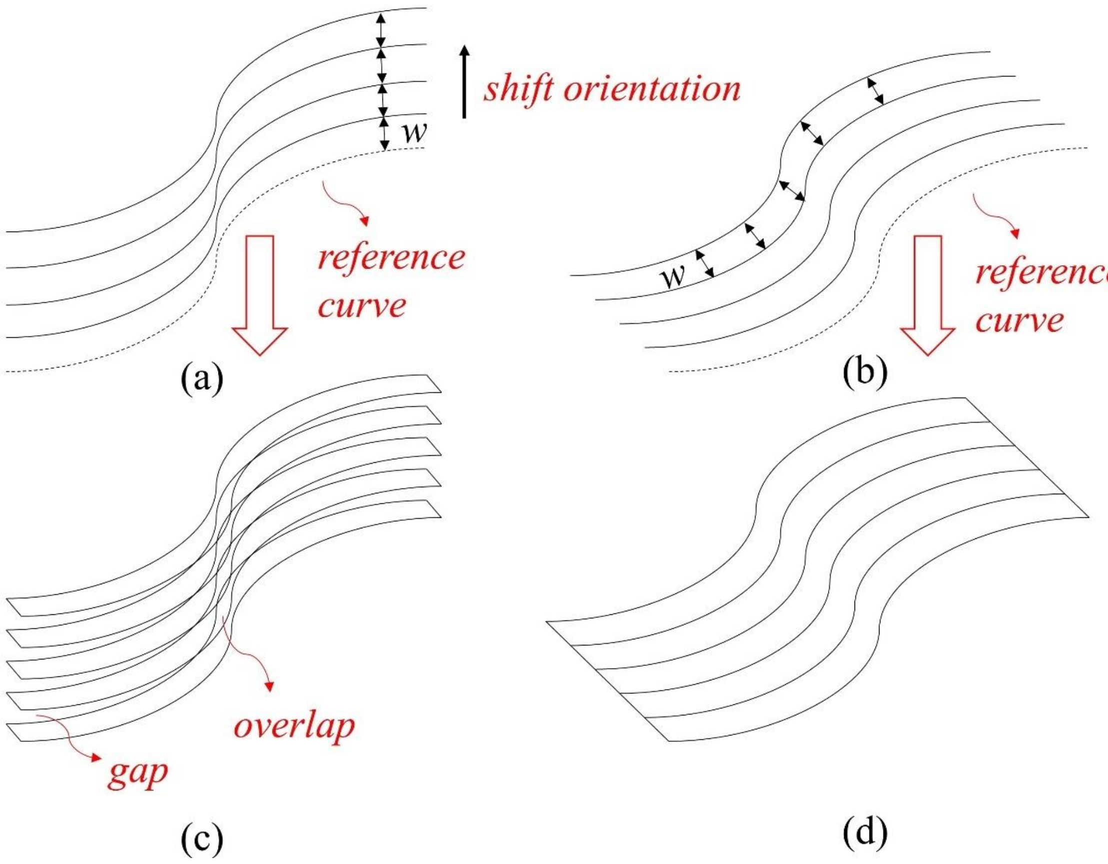

Figure 2.3. Illustration of tow path generation algorithms: (a) shifted method, (b) parallel method. Ultimate laminate configuration generated by (c) shifted method with gaps/overlaps; (d) parallel method with defect-free

In contrast, the parallel method (Figure 2.3b), proposed by Waldhart et al. [8], can be used to generate a defect-free laminate, as indicated in Figure 2.3d. The parallel method refers to offsetting all the points in the reference curve with equal distance, labelled as w in Figure 2.3b. This method, however, may be inapplicable to the generation of variable stiffness laminates because of the smaller turning radius for subsequent tows, as pointed out by Tatting and Gurdal [21]. Thus, the shifted method still gains more favour in many studies [22, 23] with in-plane curved tow placement, despite the intrinsically introduced gaps and overlaps.

It should be noted that TPP software also allows users to manually define every tow path specifically. This function, although tedious, provides huge degrees of freedom for users to customise the fibre architecture and will be mainly used for laminate design in this thesis.

2.2.4 AFP Laminates

In its early stages, AFP was mainly devoted to producing identical laminate structures to manual layup, aiming to obtain higher quality laminates with higher productivity. The conventional fibre reinforced laminates, such as with quasi-isotropic stack sequence, cannot maximise the efficiency of material usage and still suffers from low through-thickness properties. The main feature of fibre reinforce laminates is that the properties are highly sensitive to fibre orientation. Figure 2.4 depicts the relationship between the tensile and compressive strength and fibre orientation for unidirectional laminates. It can be noted that a variation of 10 degrees between the load and fibre orientations can result in an approximate 80% strength drop. Hence, this becomes clear that conventional laminate manufacturing cannot maximise the exploitation of fibres and result in substantial material waste. In another word, fibre path customisation offered by AFP can facilitate the efficient use of materials and open possibilities for designing more lightweight composites structures. This section aims to demonstrate the differences between conventional manufacturing and non-conventional manufacturing of AFP. The advanced laminate concepts achieved via non-conventional manufacturing are also presented in detail.

(Figure 2.4 is from Figure 1 in [24])

Figure 2.4. Relative tensile and compressive strength of unidirectional carbon/epoxy composite with the variation of fibre orientation [24]

(a) Conventional AFP laminates

The most commonly used composite laminates made manually is an assembly of several unidirectional layers, usually with 0°, ±45° and 90°, resulting in a quasi-isotropic characteristic. For conventional AFP applications, each layer is constructed by placing multiple unidirectional tows side-by-side. By manipulating the fibre orientations in each layer, a quasi-isotropic laminate can be manufactured which is identical with the laminate being made manually. The mechanical properties between the conventional AFP laminates and manually fabricated laminates are also nearly identical. This type of laminate is called a constant stiffness laminate and the structural performance optimisation is limited to selecting the best stacking sequence.

(b) Variable stiffness laminates

Variable stiffness laminates (VSL) were the first-born advanced AFP laminates achieved via non-conventional manufacturing of AFP. Instead of laying straight fibres, the tows are steered linearly in-plane to create a laminate with spatially varying properties. Figure 2.5 illustrates the difference of tow paths between conventional laminates and a typical VSL configuration. Allowing fibre steering can potentially benefit from a better stress distribution and higher utilisation of materials.

(Figure 2.5 is from Figure 1 in [25])

Figure 2.5. A comparison between conventional and VSL tow paths [25]

VSL has been shown to have superior structural performance over constant stiffness laminates for a variety of properties, including elastic response [2], buckling response [20, 26, 27], post-buckling performance [28], first-ply failure [29], etc. The flexibility of variable stiffness design also allows for trade-offs between different structural properties. The major issues associated with VSL design are the huge design space and the manufacturing constraints. Compared to conventional laminate design where only a single variable (stacking sequence) is involved, VSL introduces numerous additional variables. Narrowing down the design space is critical in obtaining an optimum VSL configuration. The main optimisation algorithms used for VSL design, as well as their respective benefits and limitations, have been thoroughly discussed by Ghiasi et al. [30] including the gradient-based method, optimality criterion, typology optimisation, direct search methods, multi-level optimisation and hybrid methods.

(Figure 2.6 is from Figure 14 in [11])

Figure 2.6. Tow buckling and pull up due to fibre steering [11]

The design and manufacturing of composite structures are two interdependent factors [31]. To obtain an optimum VSL configuration in different applications, the manufacturing constraints are critical to be considered in the structural design phase. Current studies are limited in demonstrating the theoretical improvements of VSL compared against the conventional laminates due to the practical challenges [31]. The manufacturing constraints primarily refer to the minimum turning radius and the distributions of gaps and overlaps. The fibre steering technique is essentially based on the shearing and bending characteristics of prepreg tow. During the steering process, both sides of the tow will be either under tension (pull up) or compression (buckling) and mismatch in length, as described in Figure 2.6. The shorter side will push the excess material at the compressive side to buckle while the longer side will result in tow pull up or fibre bridging due to the shortage of material. To mitigate this issue, a minimum turning radius needs to be specified and a typical value is 635mm for an AFP machine with 32 tows and 3.175mm tow width [23]. In addition, the distribution of gaps and overlaps during AFP manufacturing (e.g., shifted method) is also a critical factor to be considered in the design of VSLs. These defects can have a significant impact on the structural properties which will be discussed in detail in Section 2.3.

(c) AP-Ply Laminates

One of the major drawbacks of composite laminates is the low through-thickness strength, which makes layered composite parts extremely sensitive to out-of-plane damage, such as that induced by impact. Low-velocity impact (LVI) attracts more attention as the resulting damage can be embedded in the laminate in the form of matrix cracking, fibre breakage and delamination while potentially only leaving a trivial indent on the outer surface, which can easily escape routine inspections. Those internal damages, especially delamination, can reduce the residual compressive strength of the composite structure by more than 50% [32, 33].

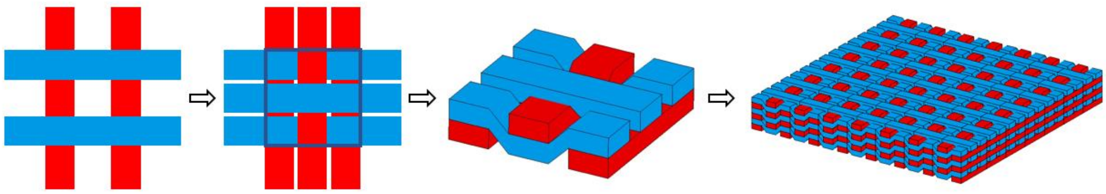

Figure 2.7. The formation process of AP-Ply laminate

Another advanced laminate concept derived from non-conventional AFP manufacturing is named advanced placed ply (AP-Ply), proposed by Nagelsmit et al. [3], aiming to improve the damage tolerance of AFP laminates. The AP-Ply, also named clutch laminate, has shown great potential in damage tolerance improvement and thermal warpage reduction without additional weight penalties [3, 34]. The AP-Ply laminate is manufactured by means of varying the traditional tow placement sequence, forming a semi-woven fabric architecture analogous to textile composites, as shown in Figure 2.7.

As the AP-Ply concept was only proposed during the last decade, the experimental studies are limited in the literature. Nagelsmit et al. [3] have investigated the LVI and compression-after-impact (CAI) performance of AP-Ply structure in terms of numbers of design parameters including tow width, weaving pattern, fibre angle, number of layers to interweave, etc. The results indicated that a slight improvement in the residual compressive strength of 5-10% is achievable with an optimised design. More importantly, from the cross-sectional images of the impacted samples, the AP-Ply indicated more concentrated damage in the form of multiple small delaminations, matrix cracks and fibre failures while the traditional AFP laminates exhibited few major but much wider delaminations. The traditional AFP laminates are also labelled as UD for simplification because each layer consists of unidirectional tapes. Rad et al. [35] studied the high-velocity impact performance of AP-Ply with a hybrid laminate structure, which combines both UD and AP-Ply layers. They found the hybrid laminate can significantly reduce the back surface damage by 45% and deflections by 19.5%. The potential benefits of AP-Ply structure were also investigated analytically and numerically by Zheng et al. [17, 18].

The design space of AP-Ply is huge. Although the potential of this advanced laminate concept has been demonstrated with several specific configurations, the defects including tow crimping, resin pockets, thickness variations, voids, etc., can substantially compromise the structural performance. To obtain an optimum AP-Ply design, a thorough understanding of the effect of these defects, as well as how they interact with the material failures is is still a large area of research interest.

It is worth mentioning a combination of VSL and AP-Ply concepts may be used in the future to achieve a laminate configuration with both optimal in-plane and out-of-plane mechanical properties. However, to fully exploit the potential and benefits brought by this advanced manufacturing approach, understanding various manufacturing-induced defects or geometric features, such as gaps, overlaps, fibre crimping, thickness variation, etc, becomes crucial. Those geometric features, as well as the associated experimental and numerical studies, are categorised and presented in Section 2.3.

2.3 Common defects in AFP laminates

As with other composite manufacturing techniques, various defects can be produced in AFP composites. The defects can be categorised into many types based on their causes and morphology. Thorough reviews regarding manufacturing-induced defects in the AFP process have been conducted by Heinecke and Willberg [1], Sun et al. [36], Harik et al. [37], and Oromiehie et al. [38]. Hence, in this thesis, emphasis is placed on common defects that are split into two major categories based on their sources, being machine-induced and tow path-induced. Other defects induced by external factors such as a foreign object or material flaw, however, are not included in this section. The other focus of this section is reviewing existing experimental and numerical studies regarding the effect of these defects on the mechanical properties of AFP composites and in turn, highlighting the importance of understanding these critical geometric features.

2.3.1 Machine-induced defects

Machine-induced defects essentially refer to imperfections triggered by machine tolerance and manufacturing parameters, specifically layup speed, consolidation force and heating temperature.

(a) Gaps/overlaps

Gaps/overlaps are the most common defects in AFP laminates. The schematic illustration is shown in Figure 2.8. For this case, the tow is not aligned side-by-side exactly with its neighbours due to the machine tolerance, resulting in gaps and overlaps.

(b) Tow drop

One of the limitations of AFP is that the tow can only be cut perpendicular to the fibre orientation. When it meets angled or irregular curved boundaries, a boundary coverage parameter needs to be selected to decide where the tows are terminated (or tow drop occurs). A commonly used coverage strategy is presented in Figure 2.9 ranging from 0% to 100%, where 0% refers to one side of the tow reaching the boundary while 100% refers to both sides of the tow getting to the boundary. The tow drop near the boundary can result in fibre discontinuities for closed structures. This layup strategy can also create either gaps or overlaps or a combination of them.

(c) Twisted tow

A twisted tow (Figure 2.10) may also occur due to several factors including the kinematic constraints of the machine head, the tool geometry, and the feeding rate of material. Good cooperation between these factors is critical to avoid this type of defect.

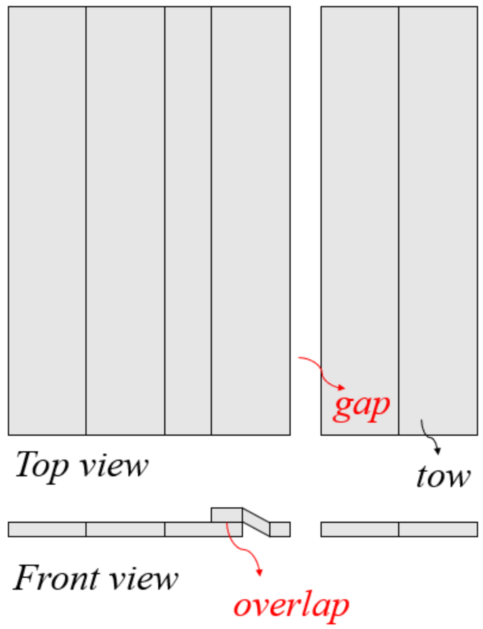

Figure 2.8. Schematic representation of gaps and overlaps

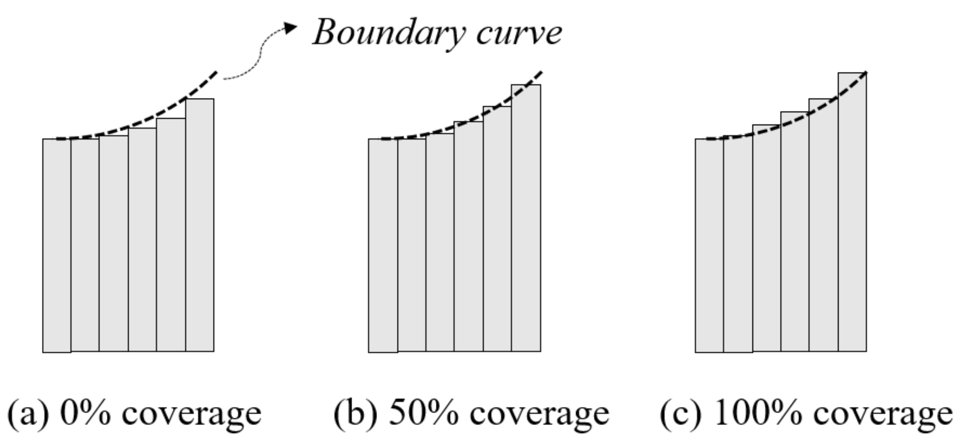

Figure 2.9. Relationship between tow drop defects and boundary coverage parameter

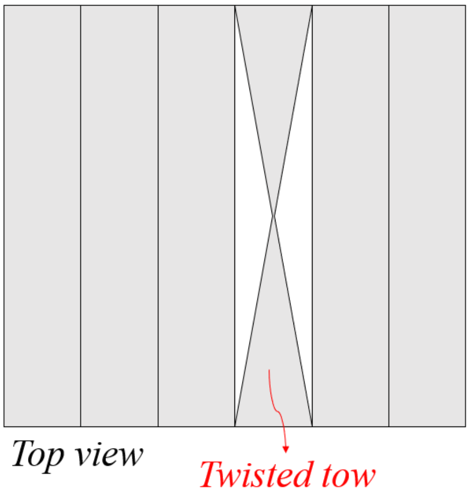

Figure 2.10. Schematic representation of a twisted tow

2.3.2 Tow path-induced defects

The tow path-induced defects also refer to the geometric features in the laminates that resulted from the manufacturing of complex contoured geometries or the non-conventional manufacturing of AFP, such as fibre steering in VSL or tow placement sequence reordering in AP-Ply. The main difference between machine-induced and tow path-induced defects is that the former can be mostly avoided with proper selection of manufacturing parameters while the latter is inevitable. Besides, the latter can introduce many more defects of a larger size.

(a) Gaps/overlaps

For complex geometries such as a conical shell, gaps/overlaps are inevitable due to the different radius of two ends. Figure 2.11a depicts the thickness variations with colour code distinguishing between two, three and four layers of material coverage. Gaps/overlaps are also common features of non-conventional fibre-steered AFP laminates. For instance, due to the limitations of the TPP algorithm (shifted method) as mentioned in Section 2.2.3, gaps/overlaps are commonly seen in VSL as shown in Figure 2.11b-c.

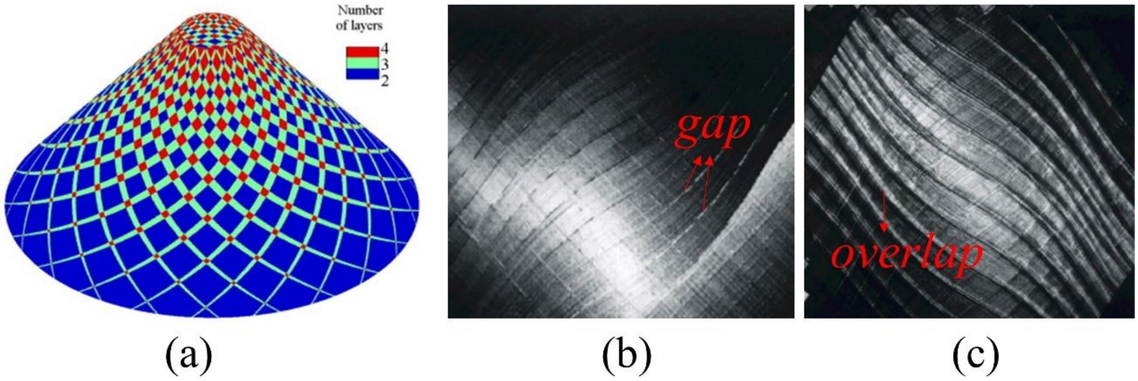

Figure 2.11. Schematic representation of gaps and overlaps due to (a) complex geometry [39] and (b-c) fibre tow path [40]

(b) Tow crimping

Tow crimping here specifically refers to an out-of-plane variation of fibre angle. Tow crimping is commonly seen in the Textile family. While for AP-Ply, tow crimping is designed on purpose to create the interweaving structure which is analogous to textiles. The major aim is to trade improved out-of-plane structural performance with slight reductions in in-plane properties. Typical tow crimping in AP-Ply is illustrated in Figure 2.12.

Figure 2.12. Schematic representation of tow crimping in AP-Ply

(c) Resin pockets and voids

Resin pockets and voids are other terms given to describe gaps. The gaps in some cases can be cured with tow deformations (resin/fibre percolation) during the curing process, resulting in a wider but thinner tow. Some studies [41-43] attempted to study the effect of the consolidation pressure on tow deformations and gap-filling mechanisms during the curing process. However, when the gap size is large, either resin pockets or voids will be produced as shown in Figure 2.13. This image is obtained from a high-resolution optical microscope and demonstrates a cross-sectional morphology of fibre and resin for a typical AP-Ply. The black spots refer to voids, which are air gaps in the laminate.

Figure 2.13. Optical microscopy representation of voids and resin pockets in AP-Ply

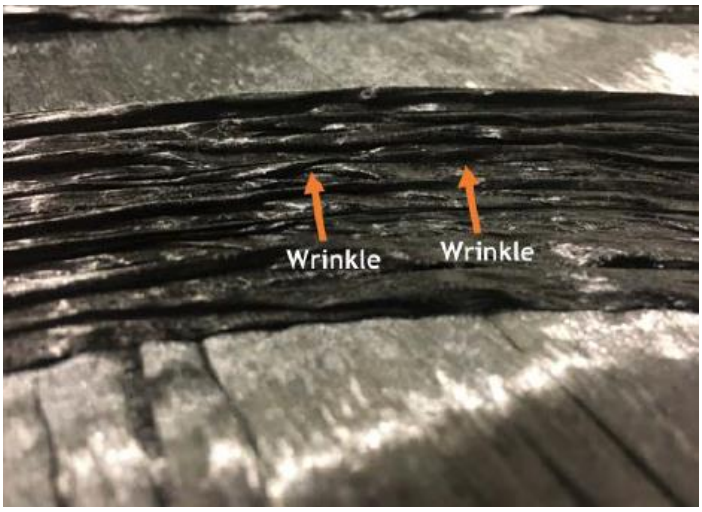

Figure 2.14. Schematic representation of tow wrinkling due to fibre steering [37]

(d) Wrinkling

Wrinkling is commonly associated with the fibre steering technique of AFP. As discussed in Section 2.2.4, a steering radius that breaches the minimum threshold can create buckling and fibre bridging, which further leads to tow wrinkling (see Figure 2.14) after consolidation and curing. This type of defect can also occur in the layup of a contoured surface.

2.3.3 Effect of the defects on structural performance

Understanding potential defects is critical to facilitate the advancement of AFP. Over the years, most of the defect types are barely studied due to the occurrence frequency, and the primary focus lies in the investigation of the effect of gaps/overlaps. Another reason is due to the huge parameter space of defects.

Sawicki and Minguett [44] studied the effect of gaps/overlaps on the compressive strength of unnotched and notched laminates. Defect sizes of 0″, 0.03″ and 0.1″ were tested and it was found that a compressive strength reduction of up to 27% was obtained when the defect size was 0.03″, while further reductions were not observed for larger defects. Unnotched and notched laminates indicated similar reductions and it was concluded that the primary cause of strength reduction was out-of-plane waviness. The results were also shown to be insensitive to the number of defects. Croft et al. [5] have experimentally evaluated the effect of different types of defects (gap, overlap, half gap/overlap and twisted tow) on the ultimate structural strength with a range of tests including tension, compression, in-plane shear, open-hole tension and open-hole compression. For in-plane shear and open-hole compression tests, the defects' effect was investigated with two different triggering mechanisms, being tow length-induced and tow width-induced. It was found the effect of defects has a smaller effect at the lamina level (5%) as opposed to the laminate level (13%). For each specific test, the results were summarised in Figure 2.15.

Lan et al. [45] also examined the effect of gaps/overlaps on shear and compression properties with different defect sizes. A configuration of $[(-45/45)_3/-45]$ was used to assess the in-plane shear performance, while another configuration of $[90_4/0_3/90_4]$ was used to evaluate the compression response. Both configurations were cured under two different conditions, with and without caul plates. A manually made baseline sample without defects was used for comparison. It was found that the effect of overlaps was less critical than gaps on the shear properties, especially when caul plates were used. For the compression test, it was noted that the defects had a trivial effect on the compression response when the gap size was small (0.5mm). However, this difference increased to 55% for the configuration with overlaps when no caul plate was used. Other studies [4, 46, 47] also indicated a significant impact from gaps and overlaps on the mechanical properties of AFP laminates.

(Figure 2.15 is from Table 1 in [5])

Figure 2.15. Experimental results of different defects' effect, subject to various loading conditions [5]

Falcó et al. [48] investigated the effect of tow drops on laminate strength with different boundary coverage strategies as discussed in Section 2.3.1(b). Three different laminate configurations of VSL, 100% coverage, 0% coverage and 0%

coverage with ply staggering, were examined with tensile testing of unnotched and open-hole laminates. Ply staggering refers to shifting each layer, such that the gaps do not overlap. A significant difference was found between 0% coverage and 0% coverage with ply staggering, in which the former showed the most critical strength reduction. This indicated that the ply staggering technique was an effective way to mitigate the effect of defects. In another work also performed by Falcó et al. [49], the effect of tow drops on the damage resistance and tolerance was studied using two VSL configurations, one with and one without ply staggering. The results indicated that the tow drops only had an impact on damage resistance when the impact energy was low. The damage tolerance, however, exhibited a similar response between different laminate configurations, which meant that tow drops did not affect the damage tolerance.

Considering the huge parameter space of defects, studies that focused on developing numerical methods to facilitate the understanding of various defects, as well as their failure mechanisms, are still an ongoing area of research. Among all the numerical methods (boundary element method [50], finite element method [51], finite difference method [52], etc.), the finite element (FE) method is the most promising one, which is capable of handling highly nonlinear systems and adaptable to very complex geometries [53]. Due to the evolution of computational power, FE models that approach reality are emerging. The state-of-the-art FE methods in the AFP field are discussed in Section 2.4.

2.4 Finite element modelling of AFP composites

Based on the review of various defects as well as their effect on the structural response, the significance of representing these geometric features in the model becomes clear. This section aims to review the existing FE modelling strategies for AFP composites in the literature. Due to the geometric complexities of AFP composites, the fidelity of numerical models is highly limited by available computational resources. Figure 2.16 depicts the developing trend of FE modelling strategies for AFP composites against model fidelity over the years in the literature.

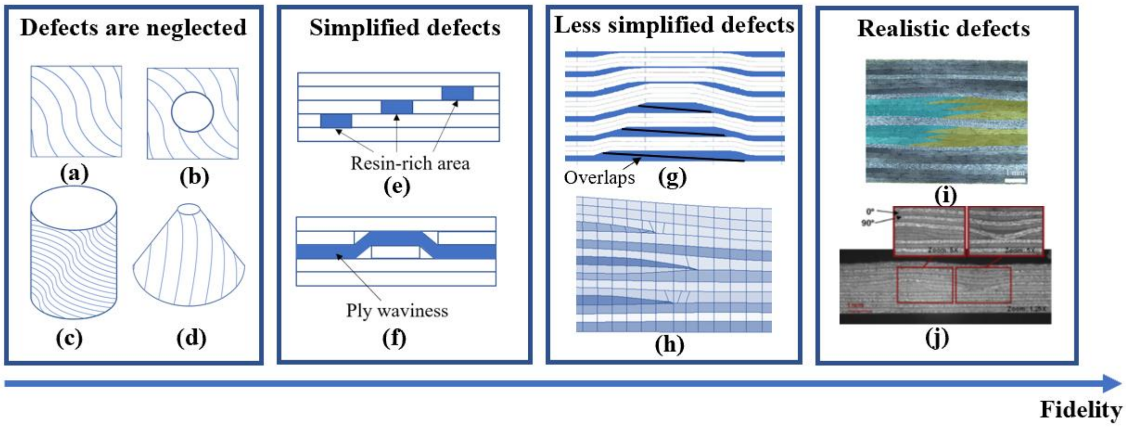

Figure 2.16. The finite element model development of AFP composites, (a~d) neglects the defects in VSL with various structures, (e~h) present recent simplified defects modelling [6, 7], (i~j) realistic defects configuration [4, 5]

2.4.1 Models with defects being neglected

In the early stages, defects were generally neglected in the modelling of AFP composites, which was commonly seen in studies of VSL [54-57]. In these studies, either plate or shell elements were used, and the geometry was modelled as a continuum (Figure 2.16a-d). The material orientation was approximately mapped to the element based on the designed fibre path. These studies were mainly devoted to demonstrating the theoretical improvement of curved fibre paths versus unidirectional configurations in certain applications. A substantial improvement was observed in the stiffness and buckling loads due to the introduction of curved fibre paths, however the defects may compromise the structural strength to a great extent.

2.4.2 Models with simplified defects

After realising the significant role of defects in composite structures, the emphasis of research was focused on understanding the effect of defects. Initially, the defects were greatly simplified due to the constraints of computational power, as shown in Figure 2.16e-f. The geometry was still modelled as a continuum at this stage, but the elements located in the defect region were assigned to pure resin or double homogeneous properties to represent gaps and overlaps. An alternative way to model this was to vary the element thickness (e.g., double thickness to represent an overlap). Sawicki and Minguett [44] studied the effect of gaps/overlaps on the laminate compression strength with this method. In their studies, the material was modelled with plane strain elements and the fibre waviness induced by gaps/overlaps was modelled by varying the local ply thickness. The authors also clarified that gaps were not explicitly modelled as resin pockets.

Blom et al. [58] numerically investigated the effect of tow drops on the stiffness and strength properties of VSLs. In their work, the material was modelled as fully integrated shell elements in ABAQUS. Due to the cut-restart process and the selected boundary coverage parameter (see Section 2.3.1(b)), numerous small triangular gaps were created due to the tow drop of AFP manufacturing, as shown in Figure 2.17. The definition given by the authors was that if the midpoint of the element was identified to be in these small triangular areas, then resin properties would be assigned to these elements to represent the defect of tow drops. The same strategy was also used by Falcó et al. [59] who proposed a mesoscale 3D model to study the effect of tow-drops on the mechanical behaviour of notched and unnotched specimens. An X-ray computed tomography was used in their work to identify the regions of resin pockets.

(Figure 2.17 is from Figure 10a in [58])

Figure 2.17. Representation of small triangular resin pockets due to tow drops [58]

2.4.3 Models with less simplified defects

With the evolution of computational power, recent research is targeting the generation of precise, yet very localised, FE models with embedded defects (Figure 2.16g-h). Li et al. [6] introduced a parameter-based ply-by-ply modelling technique to efficiently capture the gaps and overlaps of AFP composites. The parameters relevant to the defect size were measured experimentally from micrographs and were then implemented in the geometric models algorithmically. The schematic representation of gaps and overlaps modelling used in this study is indicated in Figure 2.18.

Nguyen et al. [7] developed an FE model by interpolating the ply interface using spline points obtained from the cross-section micrographs, as shown in Figure 2.19. Then the cross-section was extruded in the third dimension, which was assumed to be constant because the only defects included were in plies orthogonal to the plane of the micrographs. With this method, the geometric features of AFP composites can be represented with very high fidelity at this cross-section.

(Figure 2.18 is from Figure 4 in [6])

Figure 2.18. The schematic representation of gaps and overlaps modelling in Li et al.'s work [6].

(Figure 2.19 is from Figure 7 in [7])

Figure 2.19. The steps of modelling tow gaps and overlaps in Nguyen et al.'s work [7].

Abdi et al. [60] proposed a layer-wise multi-scale high-fidelity method to assess the impact of gaps. Each layer was modelled as a single shell and the gap areas were explicitly modelled by cohesive or spring elements using resin properties. Although this work does not treat each tow individually, the feasibility and potential of modelling gaps explicitly on the tow level was uncovered.

2.4.4 Existing modelling challenges of AFP composites

These "high fidelity" models discussed above, although powerful, require significant manual effort and computational resources, and only suit specific cases. In reality, defects are stochastically distributed and can be embedded in multidirectional layers. A typical example is AP-Ply.

AP-Ply involves substantial tow interlacing, tow crimping, tow drops, etc. Lack of a robust numerical method that can represent these critical geometric features impedes the deep understanding of the failure mechanisms of AP-Ply, and in turn, significantly hampers the development of this advanced laminate concept. Recent studies of AP-Ply are limited in providing approximate evaluations of the structural response.

Zheng et al. [61] proposed a 2D plane stress finite element model combined with cohesive elements, which were inserted along the interfaces between woven layers, to evaluate the damage onset and progression of AP-Ply. Later an analytical energy-based method was developed by Zheng et al. [62] to study the effect of local stiffness variation originating from woven patterns on the strain energy release rate (SERR). Rad et al. [34] proposed a sub cell approach with 3D shell finite elements to study the thermal and mechanical behaviour of AP-Ply laminate. The authors also pointed out that to predict accurate deformations or failure events of AP-Ply, a geometric model that can capture the tow undulations is necessary. Although the plane stress finite element method proposed by Zheng et al. can model the tow undulations, it is limited in applicable configurations with fibre orientations of 0/90 only. Hence, a high-fidelity model that can represent these critical geometric features is in high demand.

Similar situation also occurred in textile composites field where the tows are interwoven together. In order to resolve this geometrical modelling challenge, several well-known tools were developed such as TexGen [63], WiseTex [64] and Virtual Textile Morphology Suite (VTMS) [65]. Any textile fabric geometry can be automatically generated if the yarn path and cross-section are specified. The yarn / tow path is essentially a series of points with direction vectors representing the centre line of 3D geometry, including cartesian coordinates, normal and transverse vectors. These tools, although are very robust in the applications of modelling weaving technology and 3D fabrics, are not applicable to AFP composites due to few reasons. The first one is that the output AFP tow path is mapped to the mandrel surface, and can roughly represent the projection curves rather than the ultimate 3D spatial locations. This problem also refers to a z-offset issue and will be introduced in detail in Section 4.2. Another reason can be the tow cross-section is not always consistent during the layup such as tow dropping across the width direction. To resolve this and aforementioned challenges of AFP composites, an alternative method is required.

2.5 Review of composite failure modelling methods

To predict the failure mechanisms of AFP composites, as well as understanding the effect of the geometric features on the material failures, the capability of the FE model to represent the proper failure kinematics are critical. Three major composites fracture types are considered in this thesis including matrix cracking, delamination, and fibre breakage. Figure 2.20 depicts the representative failure morphology of each fracture type for composite laminates.

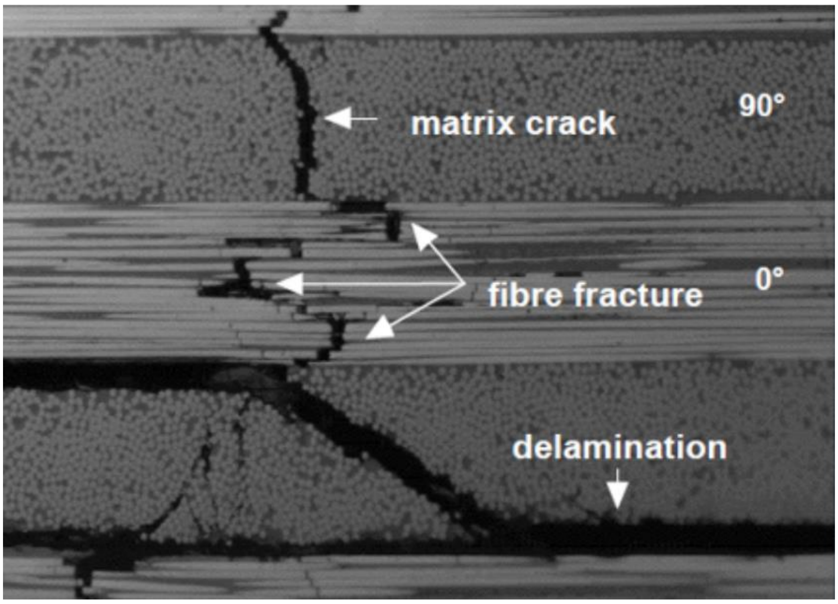

Figure 2.20. The failure morphology of different composite fracture types [66]

This section aims to review the state-of-the-art techniques of modelling material failures in the field of composites. In general, the literature reports two dominant approaches, the smeared crack model (SCM) and the discrete crack model (DCM). The mechanisms of each method and the respective benefits and limitations are discussed and presented.

2.5.1 Smeared crack model

For the SCM, which is developed in the context of continuum damage mechanics (CDM), the failed sections are represented using stiffness degradation of the corresponding elements instead of a crack or displacement discontinuity, as shown in Figure 2.21a. As the crack opens, the load is released, and the stress cannot transfer between the newly generated crack surfaces. The load release can be captured with SCM by reducing the element stiffness. However, spurious stress transfer has been observed across the fully damaged elements, which results in an inaccurate stress redistribution [67]. Aligning the mesh edges with the prescribed crack path can potentially alleviate this issue [68], but this means accurate failure prediction of SCM requires a specific mesh morphology. Another major drawback of SCM is the inability to represent different failure interactions, which sacrifices the accuracy significantly, especially when a strong coupling effect is observed experimentally between transverse matrix cracking and delamination [69].

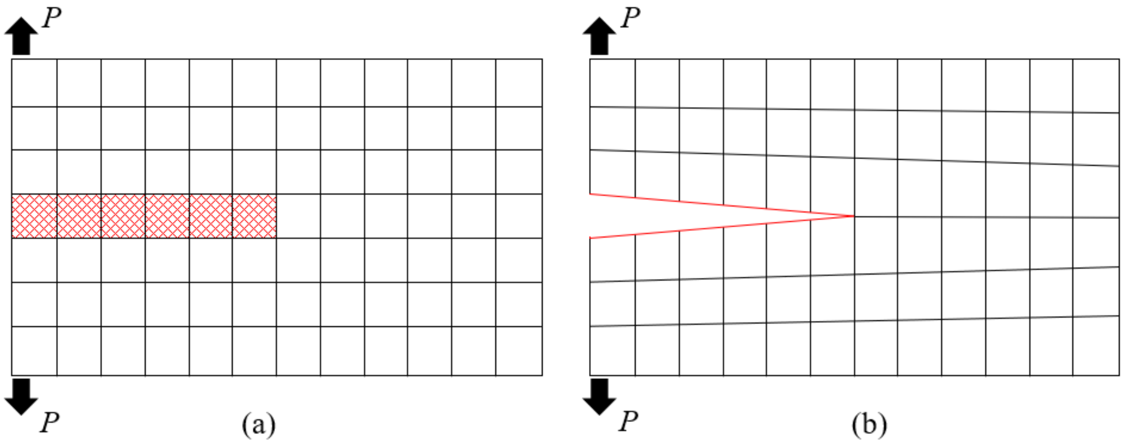

Figure 2.21. The modelling methods of composite failures: (a) smeared crack model; (b) discrete crack model

2.5.2 Discrete crack model

On the other hand, the DCM offers the opportunity to represent the physical discontinuities induced by the cracks, as shown in Figure 2.21b. The most popular methods include the virtual crack closure technique (VCCT) and the cohesive zone model (CZM). The former approach is based on linear elastic fracture mechanics and has been successfully applied in many studies [70-75]. This technique, however, is highly limited in the conditions of small scale yielding and requires the existence of a pre-crack [76]. Hence, the CZM gains more favour, as it can predict both failure onset and growth. More details of the CZM are presented in Section 2.5.2(a).

Other advanced DCM versions include the phantom node method [77-79], the floating node method [80-82], the extended finite element method [83-86], and the augmented finite element method [87, 88]. These methods can provide a high-fidelity representation of cracks while also requiring more computational power, which constrains their application to small-scale coupons.

(a) Cohesive zone model

The CZM is also named the cohesive/interface element method, the behaviour of which is governed by a traction-separation relationship. This method was primarily employed in the prediction of interface failures [89-92]. As CDM is deemed as a less computationally expensive modelling technique than CZM, the integration of CDM and CZM has been widely used for intra- and inter-laminar failure analysis respectively [93-95]. With the evolution of computational power, recent studies [96-98] have gradually started implementing cohesive elements within the ply, forming a cohesive network. The improvements of this approach were shown in accurately capturing the energy absorption and transverse matrix cracks [99]. In these studies, the continuum ply was modelled as an assembly of several strips, joined by cohesive elements.

The major drawback of the cohesive element approach is the strict element size requirements near the crack front, which must be less than 1/3-1/5 of the cohesive zone length to achieve a mesh size-independent solution [100-102]. The cohesive zone length, which is measured over the region ahead of the crack tip that is undergoing irreversible deformation, is generally much smaller than the specimen dimensions. This element size shortcoming limits the application of the cohesive element method to the prediction of just one crack, or a few major cracks, considering the computational effort.

Several improved integration methods proposed by Do [102] aimed to improve the computational efficiency with cohesive elements. In these improved methods, the integration points were increased from 2 to 3, and more importantly, were allowed to move according to the position of the crack tip, enabling the use of a cohesive element size comparable to the cohesive zone length, without compromising the numerical accuracy. Alternative approaches such as an augmented cohesive element method proposed by Mukhopadhyay and Hallett [103] recently also allow a relatively coarse mesh to be used without sacrificing the numerical accuracy significantly.

(b) Cohesive zone model applications

The cohesive element is a representative application of the CZM, in which the traction-separation constitutive relationship is implemented in the element integration points. This method, as schematically represented in Figure 2.22a, is limited to the case where the in-plane mesh size is equally defined for all layers, which is referred to as a conformal mesh. For complex laminate structures such as VSL or AP-Ply, which include numerous interleaving and overlapped fibre tows, achieving a conformal mesh can be extremely challenging or even impossible.

To predict the failures between the layers with a non-conformal mesh, the use of a combined tied contact interaction and cohesive elements was proposed, as used in Sun et al's work [98]. Figure 2.22b illustrates the schematic representations of this method, in which the top and bottom surfaces of the cohesive elements were tied to the material elements. This approach, although feasible, is limited to small-scale samples due to the huge computational cost.

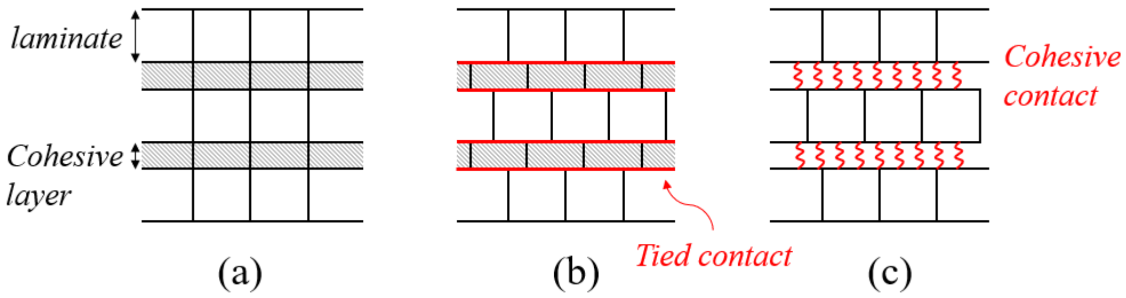

Figure 2.22. Types of CZM in literature: (a) cohesive share nodes with material layers for conformal mesh; (b) tied contact is enforced between cohesive and material layer for non-conformal mesh; (c) cohesive layer is modelled as cohesive contact interaction for non-conformal mesh.

Another potential solution is to use cohesive contacts (Figure 2.22c), in which the cohesive constitutive relationship is implemented in the contact interactions instead of element integration points. Different to the tied contact where the touching surfaces are not allowed to either penetrate to or separate from each other with a stiff connection, the cohesive contact is essentially a soft connection and allows the surfaces to move following the provided kinematic equations.

The cohesive contact is developed based on a node-to-segment (N2S) contact algorithm and has been successfully demonstrated in many studies [104, 105]. However, the major issue associated with N2S contact is the low numerical efficiency due to the master-slave concept. The non-interpenetration contact constraints are only enforced at the slave nodes, which means the master nodes are allowed to penetrate the slave surface. Hence, a strict rule is that the slave surface needs to have a much finer mesh than the master surface, and an inappropriate definition can result in significant penetrations. Another issue that can occur in the slave node is that it can have serious locking problems due to over constraints when it has multiple contact interactions, and hence can provide inaccurate simulation results [106].

2.6 Summary

In this section, the key findings of the literature review are summarised and the research challenges in the field are highlighted based on existing studies.

AFP exhibits great potential in laminate multi-objective optimisations (e.g., stiffness & strength) with the capabilities of fibre steering and tow path customisation. Advanced AFP laminates, VSL and AP-Ply, are hence emerging. Due to the manufacturing constraints of AFP, machine-induced or tow path-induced defects such as gaps, overlaps, tow crimping, tow drops, etc., become the critical geometric features of AFP composites, especially for advanced AFP laminates. These critical geometric features, however, were experimentally identified with minor to significant effects on the material properties.

Despite increasing awareness of the importance of understanding these defects over the last 30 years, research gaps still exist particularly in the field of advanced AFP laminates. The major reason is that experiments cannot thoroughly characterise the effect of these geometric features on the structural properties, as which are highly dependent on their morphology, location, distribution, loading condition, etc. Considering the huge parameter space of defects, a reliable and cost-efficient FE approach is in high demand.

Existing FE methods for AFP composites range from 2D to 3D, from neglecting defects to precise defects characterisation, and are essentially limited in the macroscale length scale. Typical length scales in AFP composites can be categorized as structure, component, laminate, ply, tow, fibre, as shown in Figure 1.2. The reduction of length scale typically refers to an increase in model fidelity and computational resources. With the evolution of computational power, recent studies [6, 7] started to use a smaller length scale (ply) to depict the geometric features of AFP composites. Although these models exhibited good predictive capabilities, their application scope is quite localised as they need a detailed in-situ parameterisation of defects. To further ease the burden of explicitly characterising the geometric features of AFP composites, particularly for advanced AFP laminates, a model with a length scale of tow is required and hence is the primary aim of this research.

Conventional composites failure modelling techniques are either unable to represent the failure interactions between different failure modes or have a strict element size requirement, in which the element size near the crack front must be less than 1/3-1/5 of the cohesive zone length. The reduction of length scale from ply to tow, although increasing the model fidelity and capturing the critical geometric features of AFP composites, requires substantial extra elements to represent these geometric details. Considering the available computational resources, a computational-efficient material failure modelling approach that is applicable to the numerical model at tow scale is required.

Chapter 3 Experimental Studies of AFP Composites

3.1 Introduction

Various types of defects of AFP composites, as well as their impact on the mechanical properties have been thoroughly discussed in Chapter 2. Advanced AFP laminates can potentially introduce more than one order of magnitude greater defects than traditional AFP manufacturing, where the defects are merely produced by the machine tolerance. The potential of advanced AFP laminates has been demonstrated, however the benefits can be significantly offset by the defects. To obtain an optimum configuration, understanding the failure mechanisms of these advanced laminate concept are critical.

Based on the literature, we have developed a basic understanding of the effect of these defects on the mechanical performance of the AFP laminate with strict control of defect size and distribution. They can have either trivial or significant knock-down effect on some properties subjected to different loading conditions. Despite the increasing awareness of the significance of the defects, a huge research gap still exists in understanding them due to the huge parameter space, particularly for advanced AFP laminates. This chapter, although is not attempting to thoroughly resolve this critical challenge, aims to facilitate our understanding of the defects' impact on the structural performance of advanced AFP laminates with several specific laminate configurations.

AP-Ply laminates are relatively easy to be manufactured, simply by altering the tow placement sequence. The variable stiffness laminates, however, require the fibre steering technique which has a minimum turning radius to achieve a wrinkle-free laminate. This limitation substantially constrains the panel size achievable for experimental studies. Hence, in this chapter, AP-Ply laminates are used to study the failure mechanisms of AFP composites with defects. As aforementioned in Chapter 2, the AP-Ply concept was developed to optimize the out-of-plane mechanical properties of AFP composites as traditional laminates all suffer from low through-thickness strength which leads to a low delamination threshold. To demonstrate the effect of the defects, several experimental studies were conducted in this Chapter.

AP-Ply laminates have already exhibited excellent out-of-plane mechanical performance in toughness-based tests such as DCB and ENF, demonstrated by Nagelsmit et al. [3]. It hasn't yet been determined if the AP-Ply laminates affect the inter-laminar shear strength (ILSS) and failure initiation mechanisms. Hence, the short beam shear (SBS) test was selected to measure the ILSS. In addition, the fibre waviness introduced by the AP-Ply is likely to have an effect on the tensile and compressive in-plane properties. Literature on textile composites indicates that compressive properties are more strongly affected than tensile, hence the combined load compression (CLC) was selected in preference to a standard tensile test for the main study. Low-velocity impact (LVI) and compression-after-impact (CAI) tests were also performed to evaluate the core improvement of AP-Ply in terms of the damage resistance and tolerance. These experimental results will serve as a database for the development and validation of the numerical model.

Some of the results presented in this chapter are included in the following publications:

Li X, Brown SA, Joosten M, Pearce GM. *Tow Wise Modelling of Non-conventional Automated Fibre Placement Composites: Short Beam Shear Study*. Composites Part A: Applied Science and Manufacturing. 2021:106767.

Li X, Brown SA, Pearce GM. *Low-velocity impact and compression-after-impact performance of non-conventional automated fibre placement composites*. International Journal of Impact Engineering. **Submitted**.

3.1.1 AP-Ply notation

The AP-Ply laminate is formed by using the tow-wise additive manufacturing characteristic of AFP, specifically the tow skip and refill manipulation process. Because the AP-Ply geometry includes many more design parameters than conventional laminates, a clear notation is necessary to define and communicate the extra geometric laminate information. The notation also describes the degree of interweaving and the manufacturability of the AP-Ply configuration [3]. Different to the conventional laminate notation, where each ply is simply defined as θ (ply angle), the notation in AP-Ply is defined as $\theta_{\frac{m}{n}}$. These two extra indices indicate the total number of ply divisions (n) and the specific division number (m). This notation simply covers most of the AP-Ply laminates. A simple example that consists of 0° and 90° tows shown in Figure 3.1, is employed to further illustrate the notation.

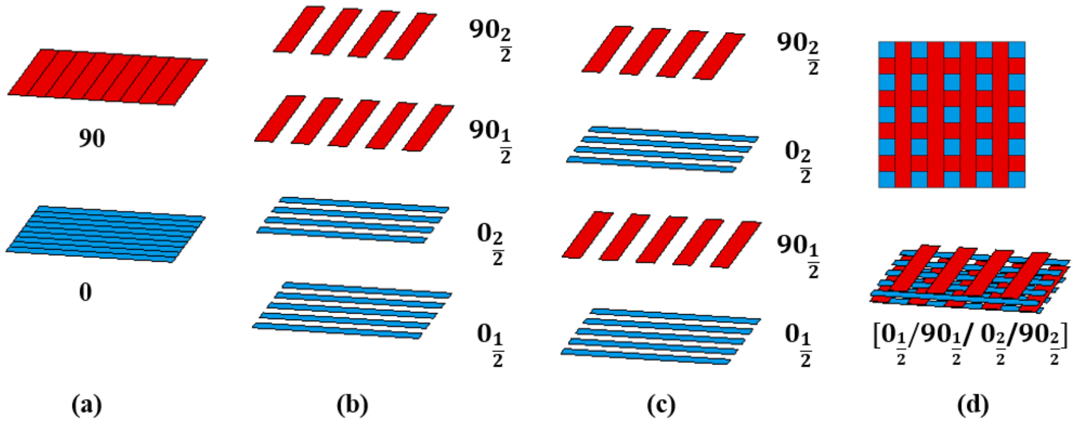

Figure 3.1. The illustration of AP-Ply notation in the AFP manufacturing process: (a) designing a two-ply laminate example consists of 0° (blue) and 90° (red), (b) dividing each ply into 2 divisions, (c) reordering the tow placement sequence, (d) placing the tows with the new sequence.

3.1.2 Introduction of different weaving concept

The customisation of the tow placement sequence provides a huge design space for AFP manufacturing. Based on the notations introduced in Section 3.1.1, the parameters can be the ply angle, ply division number and the sequence of tow placement. To achieve an optimum design in practice, these parameters require a thorough understanding and investigation, which is out of the scope of this thesis. Instead, some typical AP-Ply laminate structures will be used for the investigation of the defects' effect on the structural performance. Specifically in this chapter, two typical fibre architecture of AP-Ply laminates including 2D weaving and 3D weaving are introduced.

(a) 2D weaving

The 2D weaving concept originates from the plain weave of textile composites, where every layer consists of two unidirectional interlacing tows, as shown in

Figure 3.2. However, due to the additive manufacturing characteristic of AFP, the tow cannot be placed underneath preceding tows. Hence, for every layer, a semi-woven architecture can be achieved instead of fully woven structure, as schematically illustrated in Figure 3.3. Other differences include the tow dimension (3.2, 6.4 or 12.7mm for AP-Ply), and the shape of the tow cross-section (roughly rectangular for AP-Ply), etc.

(Figure 3.2 is from Figure 1b in [107])

Figure 3.2. Schematic diagram of the 2D plain woven in the through-thickness direction [107]

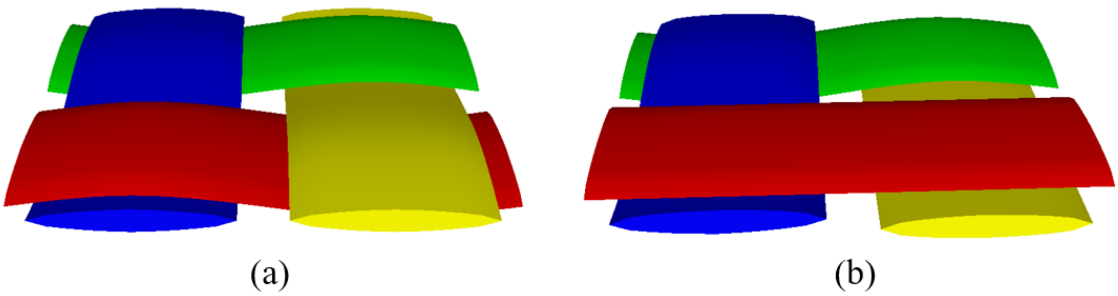

Figure 3.3. Schematic illustration of (a) fully woven and (b) semi-woven structure

(b) 3D weaving

The primary issue associated with 2D weaving is between every two woven plies, there is a clean and flat interface where the crack can propagate without any resistance. Hence, a 3D weaving concept is introduced, which is derived from the

3D interlocked architectures in textile composites (see Figure 3.4), where the tow can pass through the through-thickness direction, resulting a fully interlocked laminate. While for AP-Ply laminates, the interlocked structure is created by tailoring the tow placement sequence. This concept was firstly proposed by Nagelsmit et al. [3]. The specific tow placement sequence to achieve a fully interlocked structure is presented in Figure 3.5. Using this approach, each layer can be designed to be interlocked with adjacent layers.

(Figure 3.2 is from Figure 1a in [107])

Figure 3.4. Schematic diagram of the 3D interlock in the through-thickness direction [107]

3.1.3 Non-destructive testing methods

In this chapter, two non-destructive testing (NDT) methods will be used to facilitate the visualisation and evaluation of the cracks inside the specimen without secondary damage including a high-resolution optical microscope and a X-ray computerized tomography (CT) scan.

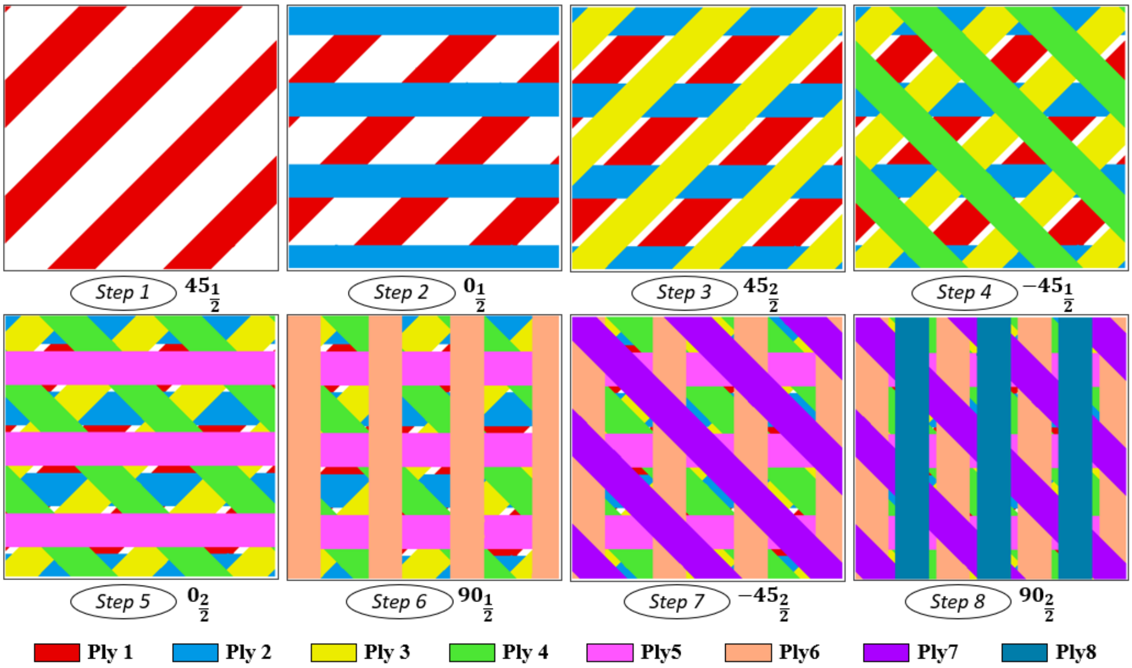

Figure 3.5. The tow placement order to achieve a fully interlocked laminate structure.

3.1.4 Chapter scope

- Section 3.2 presents the specimen preparation procedures including the manufacturing, panel curing and cutting.
- Section 3.3 aims to investigate the defects' effect on the SBS strength of AP-Ply.
- Section 3.4 will evaluate the impact resistance of AP-Ply versus traditional AFP laminates using a LVI test.
- Section 3.5 will assess the pristine and residual compressive strength of AP-Ply versus traditional AFP laminates via CLC and CAI tests, respectively.
- Section 3.6 will summarize and highlight the key findings based on these experimental studies.

3.2 Specimen preparation

The HST45E23/E-752-LT prepreg (145gsm and resin content of 35%) was used in the Automated Dynamics AFP machine at the University of New South Wales (see Figure 3.6) for the manufacturing of AP-Ply and unidirectional laminates in this chapter. This section aims to illustrate the specimen manufacturing procedures including the tow path design, the panel curing and the panel cutting.

It should be noted that the additional design parameters of AP-Ply also creates multiple manufacturing challenges including requiring more manufacturing time as also mentioned in Nagelsmit et al's work [3], more preprocessing efforts in tow path design as no dedicated algorithm has been implemented so far, and more material defects during the manufacturing due to the variation of laminate thickness and robotic kinetics.

3.2.1 Tow path design

The tow path is designed in the Fibre Placement Manager [108], which is the standard tow path planning software for the Automated Dynamics equipment. Due to the concept of AP-Ply being relatively new, the associated tow path generation algorithm and the tow skip command for the robot have not been developed yet. The in-built tow path generation algorithms at this stage are mostly used for conventional manufacturing. Hence, the only potential option is to define each tow path manually, which is used for the tow path generation of the AP-Ply in this thesis.

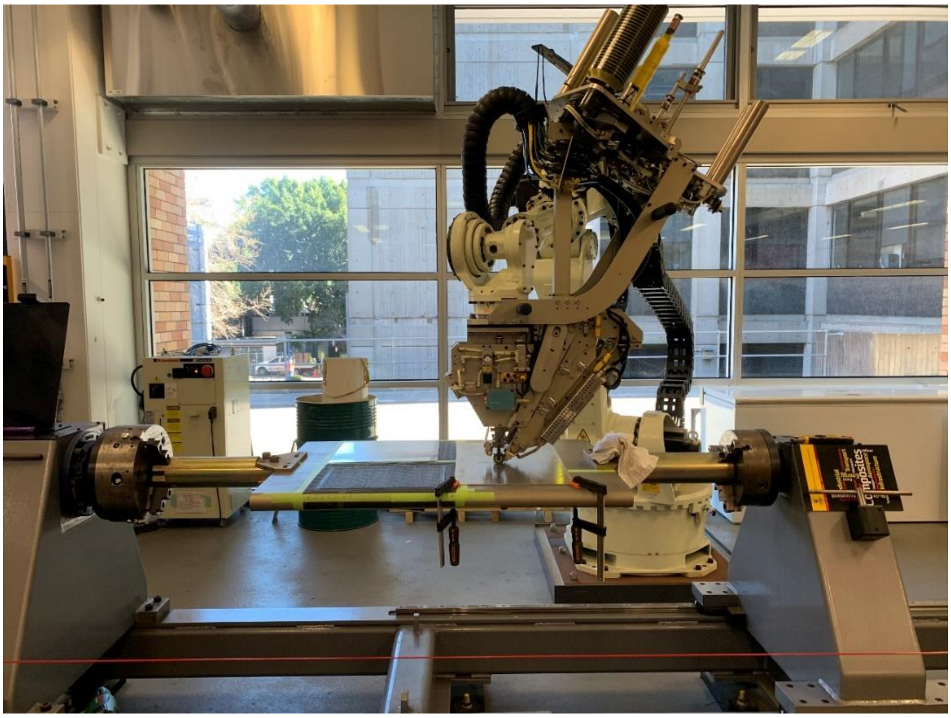

Figure 3.6. The AFP robot at the University of New South Wales.

3.2.2 Panel curing

The panels are cured in the autoclave (see Figure 3.7) following the curing recipe provided by the material data sheet, which includes several steps:

- Apply full vacuum and a pressure of 2 bar.
- Increase the temperature to 177 ± 2.8°C with a rate of $0.6 - 2.2$°C / min.
- Vent the vacuum to atmosphere and increase the pressure to 6.2 ± 0.35 bar when the leading thermocouple reaches 107°C.
- Dwell for 120 ± 10 mins at 177°C once the lagging thermocouple reaches 171°C.
- Reduce the temperature at 2.2°C / min.
- Release the pressure when the temperature is lower than 66°C.
- Remove the panels when the temperature is lower than 49°C.

Figure 3.7. The autoclave facility at the University of New South Wales.

Considering the panel thickness designed in this thesis is thicker than that was used for demonstration in the material datasheet, the dwell time was extended to 150 mins to ensure the panels were fully cured. Caul plates were placed on top of each panel to achieve a uniform thickness and consistent surface finish.

3.2.3 Panel cutting

The cured panels were allowed to settle at room temperature (around 20℃) for at least 24hrs before cutting specimens via a Multicam Computer Numerical Control (CNC) Routing system, as shown in Figure 3.8.

Figure 3.8. The Multicam CNC Routing system at the University of New South Wales

3.3 Short beam shear

For the SBS test, two different AP-Ply configurations with different weaving morphology were studied and a comparison with a unidirectional ply counterpart was conducted. It should be noted that this experiment was limited to a coupon level analysis with 0/90 cross-ply configurations to obtain a preliminary understanding of the failure mechanisms of the AP-Ply laminates, while the following sections in this chapter investigate more complex laminates.

In this section, the specimen design is firstly described. Then the SBS experimental setup and testing procedure are introduced. The results in terms of the crack path, the short beam strength and the global response between different laminate configurations are compared and discussed at last.

3.3.1 Specimen design

(a) Design of weaving morphology of AP-Ply laminates

As aforementioned in Section 3.1.2, a fully interlocked AP-Ply laminate structure was designed for this study to avoid a clean and flat interface in which the failure is likely to initiate and propagate without any resistance. For this purpose, a special tow placement sequence was used, as shown in Figure 3.9. Using this approach, each layer can be designed to be interlocked with adjacent layers. The 3D visualisation of the AP-Ply configuration and associated layups are presented in Section 3.3.1(b).

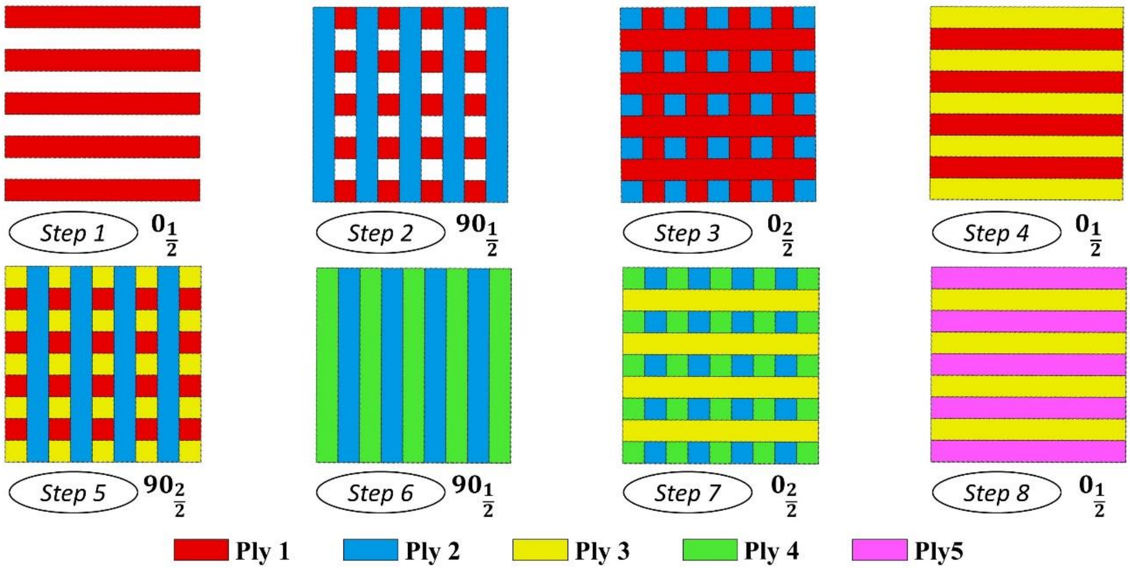

Figure 3.9. Illustration of a fully interwoven AP-Ply laminate sequence. Note: This image only presents 8 steps to indicate how a fully woven laminate is achieved. Steps 2 to 5 can be repeated multiple times until reaching the required laminate thickness.

(b) Design of specimen dimensions and layup

The specimen dimensions were determined following the American Society for Testing and Materials (ASTM) D2344 short beam shear test standard [109]. This standard does not have a specific requirement for the specimen dimensions but recommends a length/thickness ratio of 6 and a width/thickness ratio of 2. However, the AFP tow width used in the present study was limited to 6.35mm. To incorporate the in-plane weavings along with the width direction, the specimen width was designed as 14mm, which resulted in a requirement of a 7mm thick laminate. Considering the tow thickness variation before (0.15mm) and after cure, a ply number of 53 was chosen to achieve global symmetry relative to the centre of the mid-layer for the unidirectional configuration and meet the required laminate thickness. It should be noted that AP-Ply laminates are never precisely symmetric in the same way as traditional laminates, while the corresponding layup has been chosen to mirror the symmetric unidirectional configuration as much as possible.

The in-plane specimen dimensions were then finalized as 52 x 14mm, with a loading span length of 40mm. In Xie et al's work [110], the result indicated that the through-thickness interlaminar shear stress distribution varied from trapezoidal to parabolic with an increasing span-to-thickness ratio. Hence, the span-to-thickness ratio was chosen to be around 6, low enough to avoid bending failure while high enough to avoid complex stress field interaction between the loading nose and the support rollers [110, 111].

As the fibre crimp angles had a significant effect on the mechanical performance of AP-Ply laminates [61, 112], two configurations with different fibre crimp angles were designed in this study to investigate the failure mechanisms with a unidirectional baseline which was labelled as the Benchmark. The fibre crimp angle, however, is related to the tow thickness, temperature, consolidation pressure, material properties, etc. The most straightforward way to tailor the fibre crimp angle is to increase the tow thickness, which can be achieved by overlapping multiple tows in the same position. In this study, the AP-Ply configurations were designed as single-tow weaving and double-tow weaving (Figure 3.10), namely AP-Ply1 and AP-Ply2 separately for differentiation.

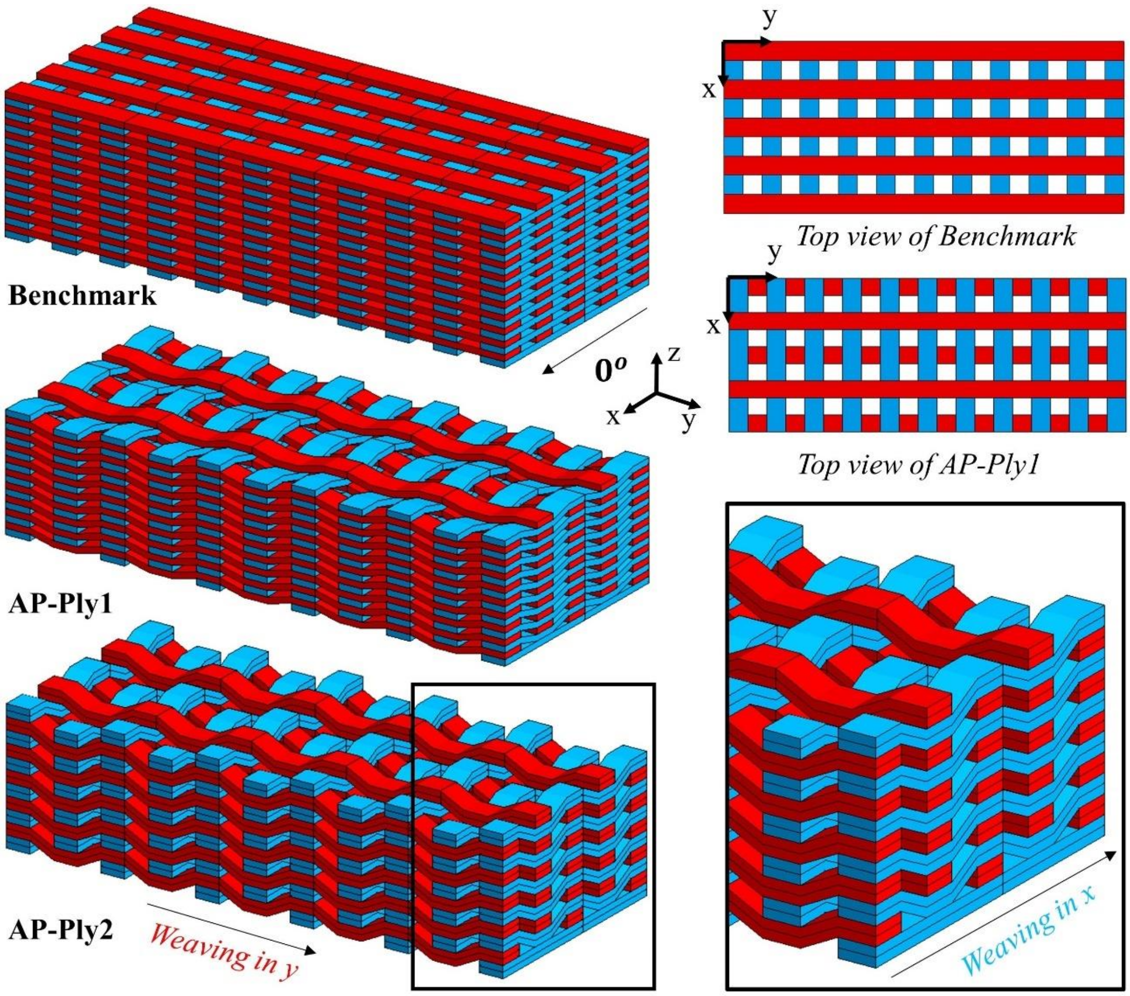

Figure 3.10. The schematic representation of each laminate configuration. Note: this image is only used to indicate the 3D woven architecture of the AP-Ply laminates used in this study which does not correlate to any dimension of the actual laminate, such as the gaps between tows here are shown only for visualisation purposes.

Based on the discussions above, the notations of the three laminate configurations can be represented as below, where the repetitive tow placement sequence for AP-Ply1 and AP-Ply2 is highlighted within the round brackets.

- Benchmark: $[(0/90)_{13}/\bar{0}]_s$

- AP-Ply1: $[0_{\frac{1}{2}}/(90_{\frac{1}{2}}/0_{\frac{2}{2}}/0_{\frac{1}{2}}/90_{\frac{2}{2}})_{26}/0_{\frac{2}{2}}]$

- AP-Ply2: $[0_{\frac{1}{2}}/(90_{\frac{1}{2}}/90_{\frac{1}{2}}/0_{\frac{2}{2}}/0_{\frac{2}{2}}/0_{\frac{1}{2}}/0_{\frac{1}{2}}/90_{\frac{2}{2}}/90_{\frac{2}{2}})_{13}/0_{\frac{2}{2}}]$

To demonstrate the difference in the fibre architecture between these laminate configurations, a 3D view of each case is presented in Figure 3.10. It should be noted that this figure does not correlate with any physical dimensions of the manufactured laminates. In the amplified view of AP-Ply2, it can be observed clearly that the tows are weaving in both x and y axes, resulting in an integrated woven architecture.

(c) Design of "artificial" tow-to-tow gaps

A major problem with AP-Ply laminates can be the undulation of thickness around the weaving corner, leading to many ribbed areas, as described in Figure 3.11a. The thickness undulation in this area becomes more severe with the increase in total laminate thickness. The sharp ribs can also trigger manufacturing issues for the upcoming tows, leading to the generation of many additional defects in the laminate. Hence, to mitigate this issue but not create many extra resin pockets, a 1.3mm tow-to-tow gap (around 1/5 of the tow width) was designed in this study, as schematically shown in Figure 3.11b.

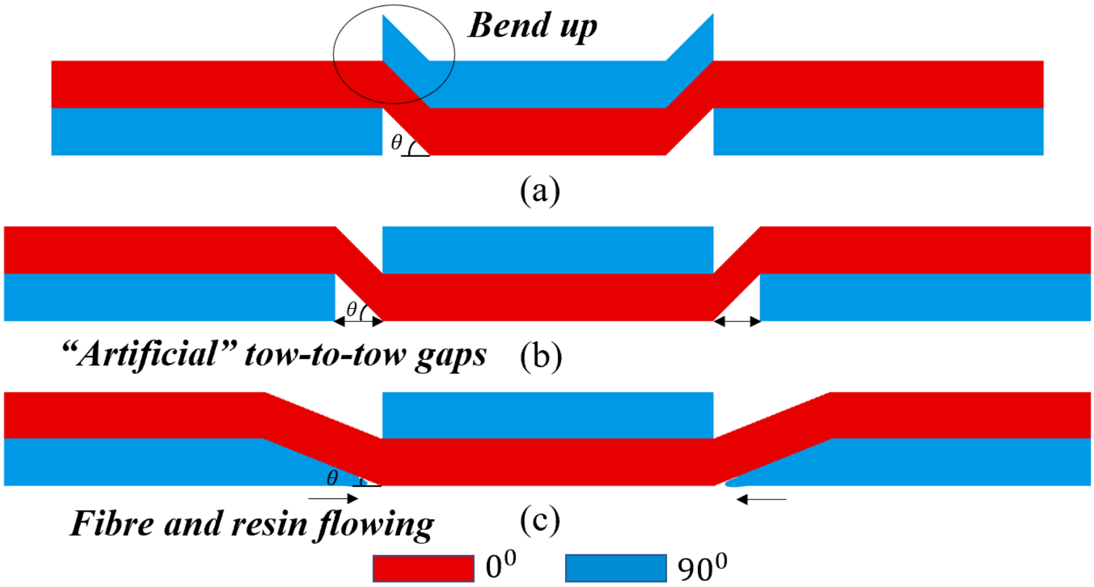

Figure 3.11. (a) Thickness undulation issue representation in AP-Ply laminate, (b) Theoretical fibre crimp angle, (c) Actual fibre crimp angle after consolidation

The two AP-Ply configurations that use single-tow and double-tow weaving separately can theoretically result in fibre crimp angles (θ as shown in Figure 3.11) of 5.3° and 10.5°, computed based on the tow thickness and tow-to-tow gap. Theoretically, these artificial gaps can generate many resin-rich pockets or voids. However, the majority of the tow-to-tow gaps are filled with both fibres and resins after cure, generating a relatively uniform laminate. This is mainly because, during the curing process, the tows tend to deform and squeeze out the resins and fibres simultaneously to flow into the gaps, as illustrated in Figure 3.11c. This phenomenon is observed in the cross-sectional micrographs of the cured laminates, as presented in Figure 3.12, where the designed gaps near the weaving area have disappeared except for some small resin pockets as highlighted with red circles.

The consolidation process which leads to the deformation of adjacent tows reduces the crimp angles considerably, as indicated in Figure 3.11c. As mentioned in Zheng and Kassapoglou's work [61], the crimp angle had a significant impact on the delamination initiation and propagation. Hence in this study, the crimp angles of AP-Ply laminates were taken with special care via measuring multiple times under the optical microscopes, and the results are presented in Section 3.3.2.

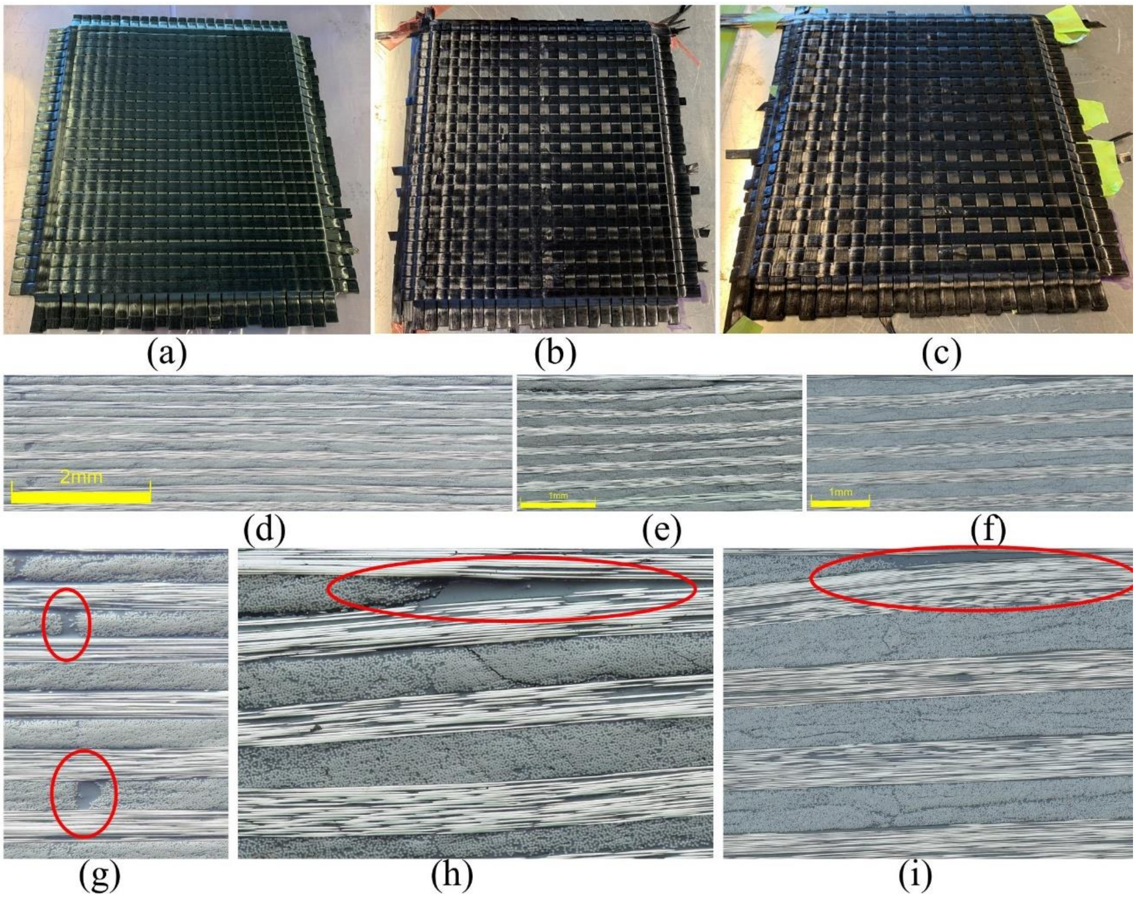

Figure 3.12. The AFP manufactured panels before curing (a~c), the micrographs of cured specimens (d~f), and the amplified view of tow-tow-tow gaps (g~i). Note: (a,d,g) corresponds to the Benchmark, (b,e,h) refers to AP-Ply1, and (c,f,i) denotes AP-Ply2.

3.3.2 As-cured tow dimensions

The final as-cured specimen thickness, width, and crimp angle before and after cure are summarized in Table 3.1. The as-cured tow thickness was computed by dividing the specimen thickness by the total number of layers (53). The mean value and coefficient of variation (CV) were determined from 16 specimens for each configuration. A slight thickness discrepancy between different laminate configurations was observed and this might be because the weaving geometry constrained the resin and fibre flow to some extent. It should be noted that the

Table 3.1. Measurement of the specimen thickness, width and crimp angle before and after cure.

	Thickness (mm) Mean (CV %)		**Width (mm) Mean (CV %)**		**Crimp angle (deg) Mean (CV %)**
Config	Before-cure	After-cure	Before-cure	After-cure	After-cure
Benchmark	7.98 (1.4)	6.36 (1.47)	6.35	7.63 (0.26)	-
AP-Ply1	8.09 (1.3)	6.46 (0.89)	6.35	7.69	3.01 (21.33)
AP-Ply2	8.30 (0.16)	6.54 (1.11)	6.35	7.75	4.63 (20.12)

average as-cured ply thickness was approximated as 0.121mm which is smaller than the value (0.14mm) specified in the manufacturer's datasheet [113]. This was attributed to the tows spreading and reducing in thickness as the samples were cured.

The as-cured tow width and tow crimp angle were measured via the micrograph under the optical microscope. The as-cured tow width can be estimated as the summation of the pristine tow width (6.35mm) and one gap size (1.3mm) as no resin-rich pockets were identified between contacting tows. This approximation was roughly identical with the measurements obtained from the micrograph. The tow crimp angles, however, showed a significant variation across the thickness.

3.3.3 Experimental setup

An Instron 3369 50kN machine (Figure 3.13) was used to perform the short beam shear test in accordance with ASTM D2344, with a span-to-thickness ratio of 6, at room temperature. Displacement control at a rate of 1mm/min was applied to the loading roller via the crosshead. The dimensions of each specimen were set as 52mm x 14mm x 6.41mm (LxWxt) with a span length of 40mm. The typical configuration of the AP-Ply specimen is shown in Figure 3.13. The diameters of the loading nose and support rollers used in this test were 6mm and 3mm respectively. The reaction force, time and crosshead displacement were recorded for each test. As delamination is a very unstable fracture mode, eight samples were used for each configuration to obtain a reliable result. A digital camera was set in front of the specimen to amplify the cracks during the test for monitoring safely.

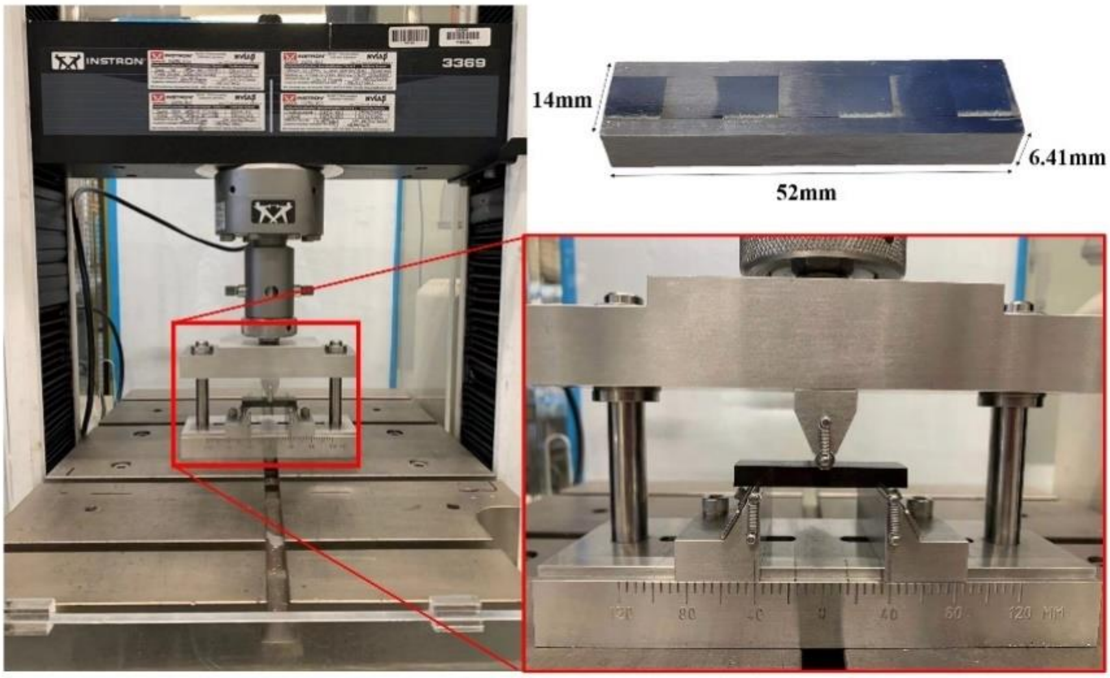

Figure 3.13. The Instron 3369 50kN machine

3.3.4 Results

The global responses and failure mechanisms are presented and compared between the different laminate configurations in this section. The pristine and fractured samples are described in Figure 3.14. Similar failure mechanisms can be observed among the three laminate configurations including (i) non-catastrophic damage initiated under the loading roller; (ii) the damage propagated in the through-thickness direction at a small angle; (iii) catastrophic failure occurred and the delamination suddenly went across the entire laminate in the length direction. A comparable global load-displacement trend, presented in Figure 3.15, can also be observed.

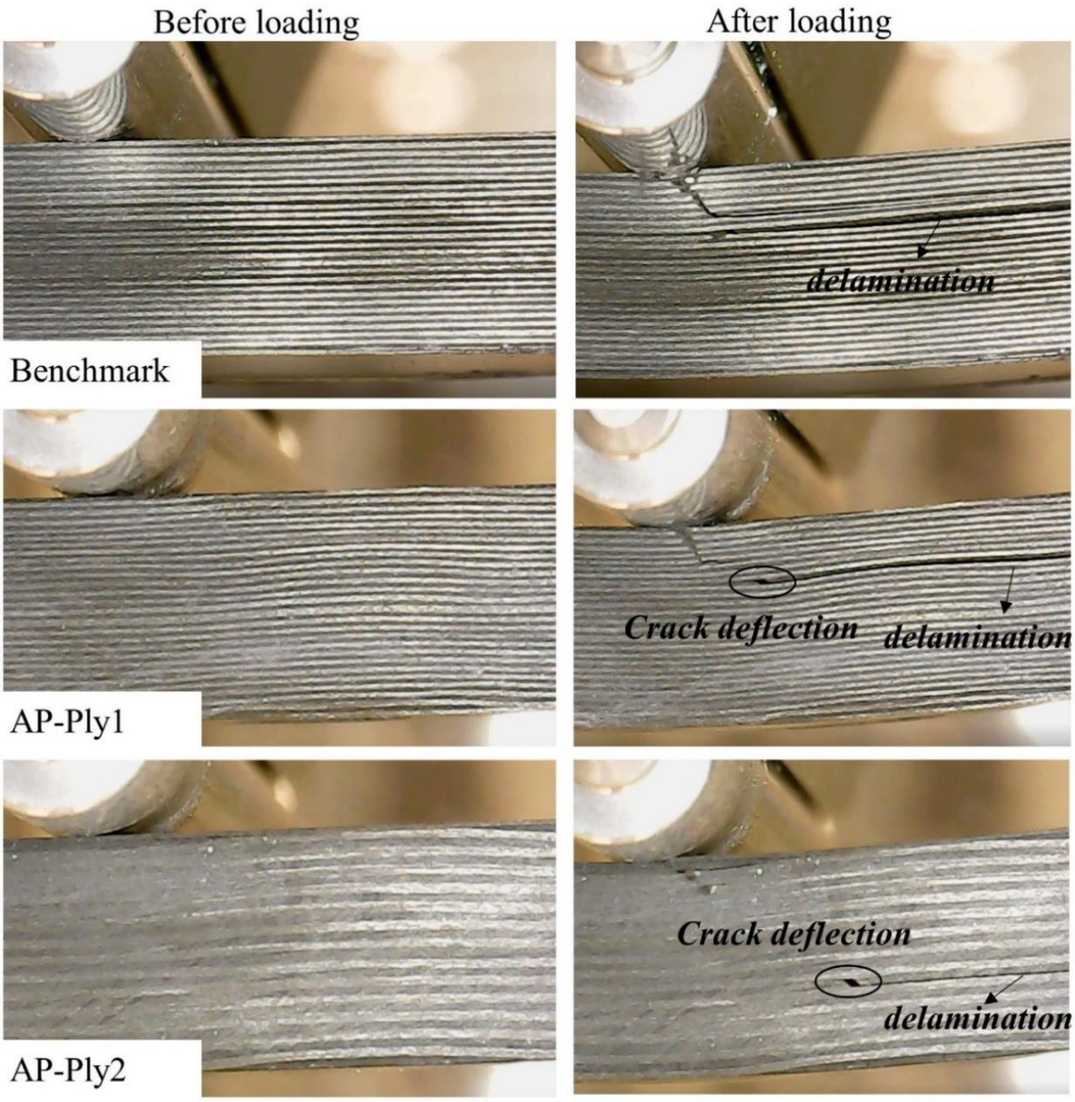

Figure 3.14. The comparison of different laminate configurations before and after loading.

The representative global load-displacement response for each case was plotted in Figure 3.15 for clarity. A linear elastic response was firstly noted, and a small stiffness drop was then found when the damage initiated under the loading nose, which was primarily due to high-stress localisation. The crack was propagating near the specimen edges in the through-thickness direction, with a slight angle to the vertical axis. The transverse shear stress tended to keep growing at this stage. When it reached the critical shear strength, the accumulated strain energy in the system was suddenly released via delamination, which was accompanied by a sharp load drop.

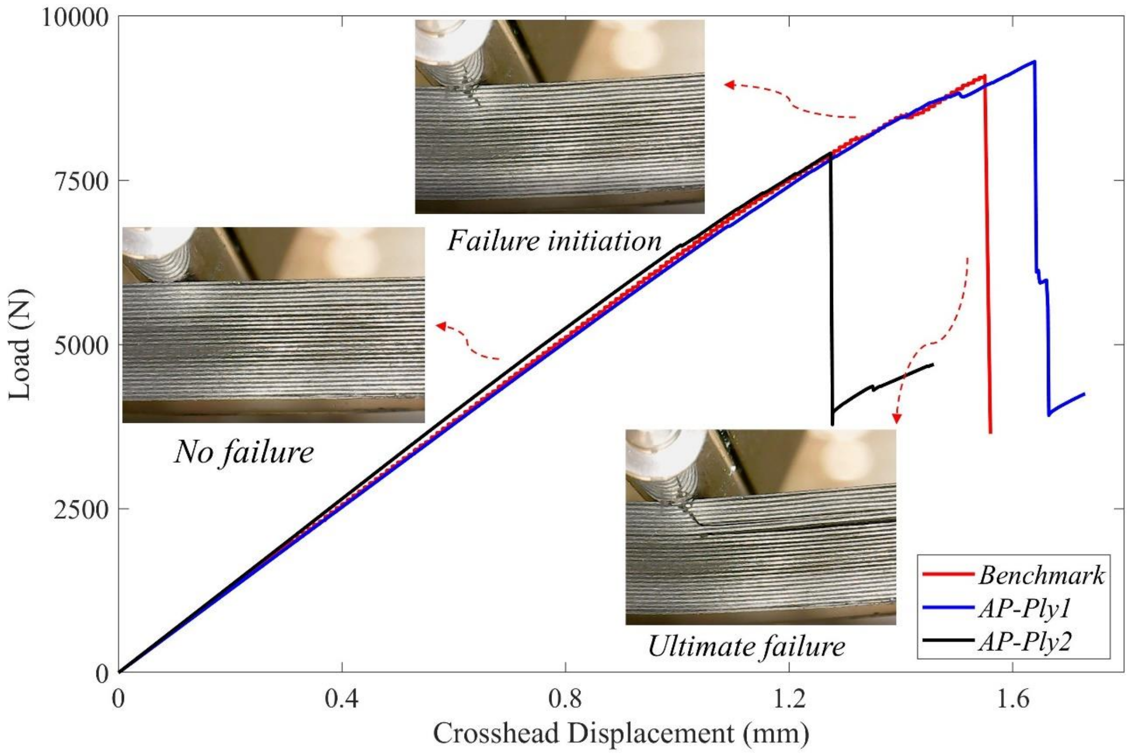

Figure 3.15. The comparison of global responses of different laminate configurations

In Figure 3.14, the differences in the crack path between the Benchmark and AP-Ply laminates are clearly identified. In the Benchmark case, a flat crack path was observed. While in both AP-Ply1 and AP-Ply2, a crack deflection in the through-thickness direction was found, which was mainly attributed to the effect of the

3D woven architecture. Most of the cracks, however, were either closed due to the unloading or hidden by uncleaned debris, which increased the complexities in identifying the specific crack spot. Hence, to facilitate understanding of the failure mechanisms between different laminate configurations, a non-destructive inspection (NDI) was carried out after the testing with a high-resolution optical microscope, OLYMPUS DSX 510. It should be noted that the specimens were ground and polished in advance of the testing for a better visualisation under the optical microscope. The results of another three samples were scanned and presented in Figure 3.16, where the crack deflection was highlighted with black rectangles.

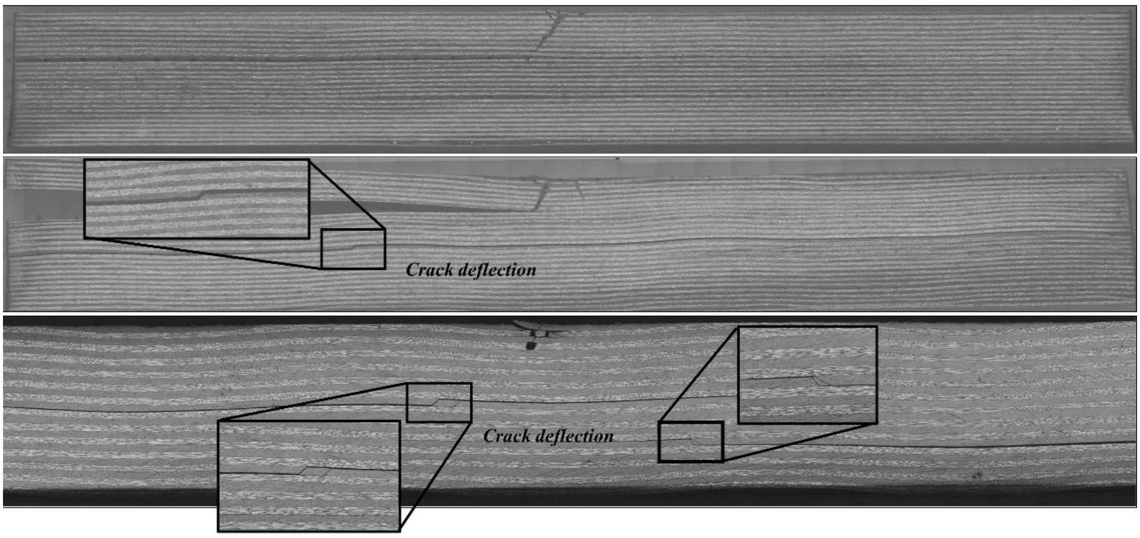

Figure 3.16. The cross-sectional micrographs of the tested samples (from top to bottom: benchmark, AP-Ply1, AP-Ply2)

Instead of a curve plot, a scatter plot was used to compare the differences between the different laminate configurations regarding the global load-displacement responses. The scatter plot is presented in Figure 3.17, in which each point corresponds to the peak load and associated displacement. A box plot is also provided to indicate the variations and distributions of the peak load. The configuration with single-tow weaving (AP-Ply1) showed a similar global response to the Benchmark, while the configuration with double-tow weaving (AP-Ply2) exhibited a 14% lower critical load.

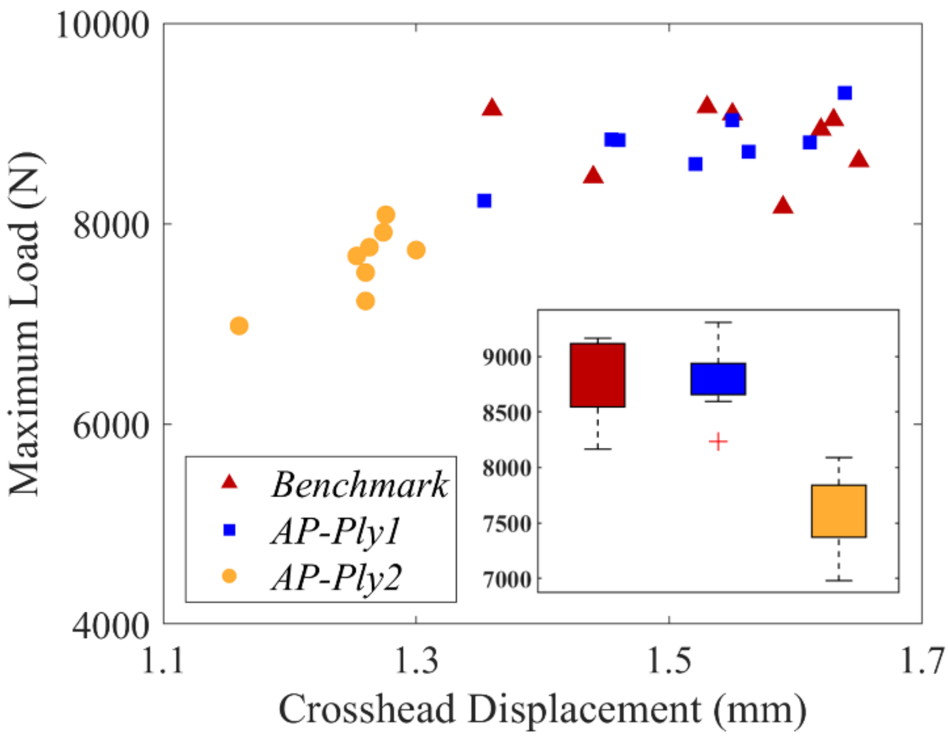

Figure 3.17. The summation of the peak load and the corresponding crosshead displacements of the short beam shear experiments

To account for the geometric discrepancies between different laminate configurations, the short beam shear strength (SBSS) was computed following the formula provided in ASTM D2344: $\sigma^{sbss} = 0.75 \times \frac{F_m}{b \times h}$, where σ^{sbss}, F_m, b, h refer to the SBSS, maximum load, specimen width and thickness, respectively. The final results were compared and recorded in Table 3.2. A nearly identical SBSS was observed between AP-Ply1 and the Benchmark while AP-Ply2 indicated a -11% difference. This was because the interweaving structure also introduced fibre crimping, which tended to accelerate the failure initiation and subsequent propagations. It can be found that the effect of fibre crimping was significantly reduced when the crimp angle was smaller as in AP-Ply1.

Table 3.2. The comparison of the SBSS between different configurations

Configuration	SBSS (MPa) Mean (CV %)	Difference
Benchmark	73.42 (3.54)	-
AP-Ply1	72.78 (2.97)	-0.87%
AP-Ply2	65.08 (3.15)	-11.36%

3.4 Low-velocity impact

This section aims to investigate the LVI performance of AP-Ply laminates while the residual strength after impact will be studied with a CAI test in Section 3.5. In this section, the panel design will be introduced, following by the experimental setup. Finally, the results will be presented and discussed.

3.4.1 Specimen design

In this test, two typical fibre architectures of AP-Ply laminates were manufactured and tested including 2D weaving and 3D weaving, which are analogous to the concept of plain-woven and 3D angle-interlock woven in textile composites. These two different AP-Ply architectures were labelled as AP2D and AP3D for simplification throughout the present study. A traditional AFP laminate was also used as a benchmark for comparison (analogous to a UD tape laminate). To differentiate with the terminologies used in the SBS test, the traditional AFP configuration was labelled as UD while the AP-Ply laminates were designated as AP2D and AP3D depending on the specific weaving architecture. It is worth noting that UD refers to multiple unidirectional layers with different fibre angles stacked here rather than unidirectional laminates. Figure 3.18 depicts the difference in fibre architectures between these laminates. It also should be noted that the visualisation is only used here to illustrate the weaving morphology and does not correlate with any physical specimen dimensions.

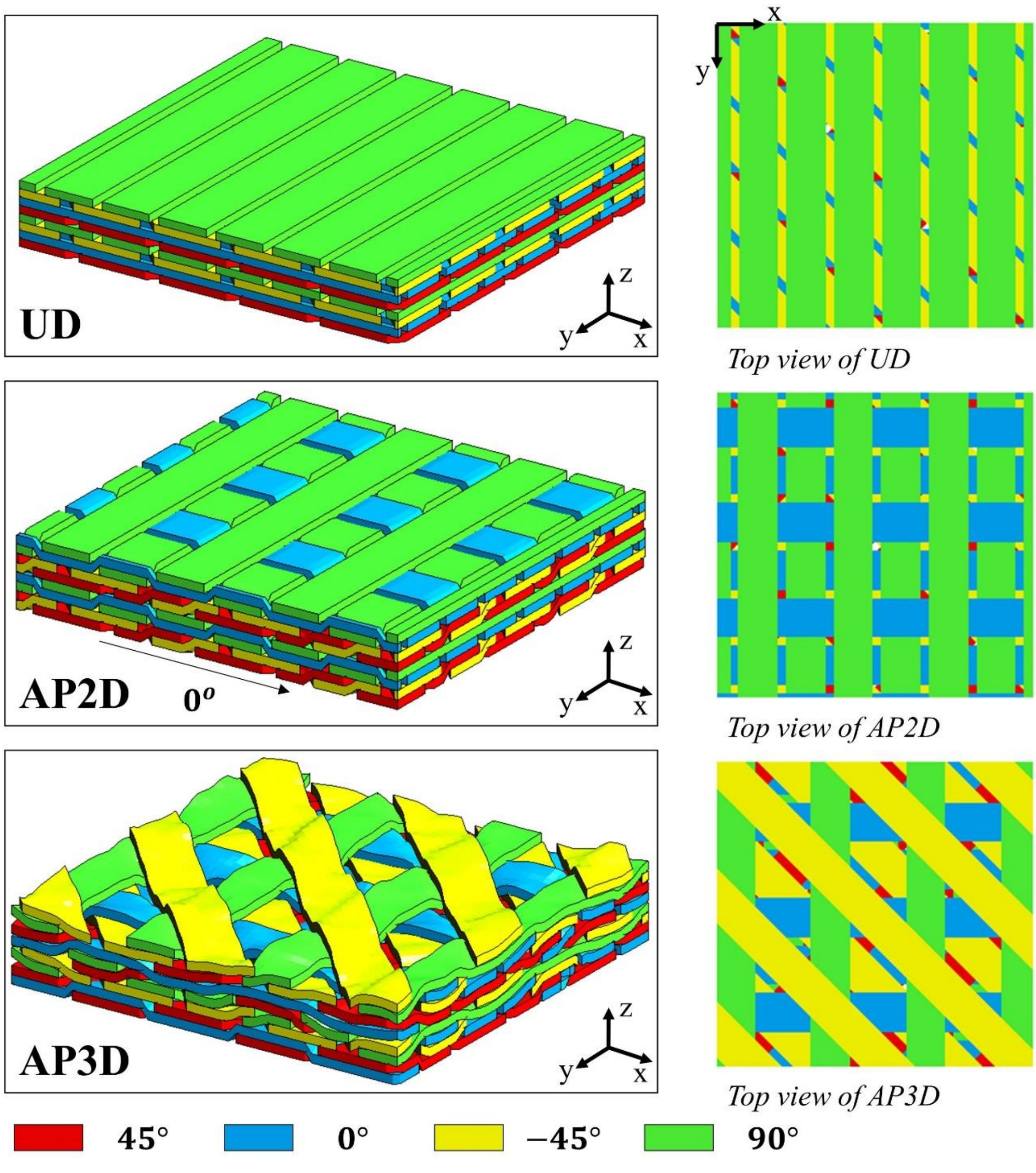

Figure 3.18. 3D visualisation of fibre architectures between different laminate configurations

Every two orthogonal layers were designed to be semi-woven for AP2D. While for AP3D, an interlocked structure in the through-thickness direction was achieved with a special tow placement sequence, as presented in Figure 3.5. This technique is called fully interwoven, which was proposed by Nagelsmit et al. [3]. Using this approach, each layer can be designed to be interlocked with adjacent touching layers, resulting in an integrated woven structure.

The specimen dimensions of this test were designed following ASTM D7136 [114], which requires an in-plane specimen size of 150 x 100mm and a thickness of 4 to 6mm. A recommended layup $[(45/0/-45/90)]_{4s}$ from the standard was used for the UD configuration. The AP-Ply laminate layups were designed based on the same stack sequence with a goal of achieving comparable layups with the UD. This is to mitigate the effect brought by the differences induced by the stack sequence. A total layer number of 32 was designed for each configuration to achieve an approximately 4mm thick laminate. To illustrate the tow placement sequence, the notation for each configuration is presented below:

- UD: $[(45/0/-45/90)]_{4s}$
- AP2D: $[45_{\underline{1}\atop 2}/-45_{\underline{1}\atop 2}/45_{\underline{2}\atop 2}/-45_{\underline{2}\atop 2}/0_{\underline{1}\atop 2}/90_{\underline{1}\atop 2}/0_{\underline{2}\atop 2}/90_{\underline{2}\atop 2})]_{4s}$
- AP3D:

$$[45_{\underline{1}\atop 2}/(0_{\underline{1}\atop 2}/45_{\underline{2}\atop 2}/-45_{\underline{1}\atop 2}/0_{\underline{2}\atop 2}/90_{\underline{1}\atop 2}/-45_{\underline{2}\atop 2}/45_{\underline{1}\atop 2}/90_{\underline{2}\atop 2})_7/0_{\underline{1}\atop 2}/45_{\underline{2}\atop 2}/-45_{\underline{1}\atop 2}/0_{\underline{2}\atop 2}/90_{\underline{1}\atop 2}/-45_{\underline{2}\atop 2}/90_{\underline{2}\atop 2}]$$

All the laminates were manufactured in the Automated Dynamics AFP machine at the University of New South Wales with the HST45E23/E-752-LT prepreg (145gsm and resin content of 35%). The materials were cured with a pressure of 6.2 bar at 177°C for 150 mins. Caul plates were placed on top of each panel to achieve a uniform thickness and consistent surface finish. The specimen cutting was accomplished with a Multicam Computer Numerical Control (CNC) Routing system. More details have been included in Section 3.2.

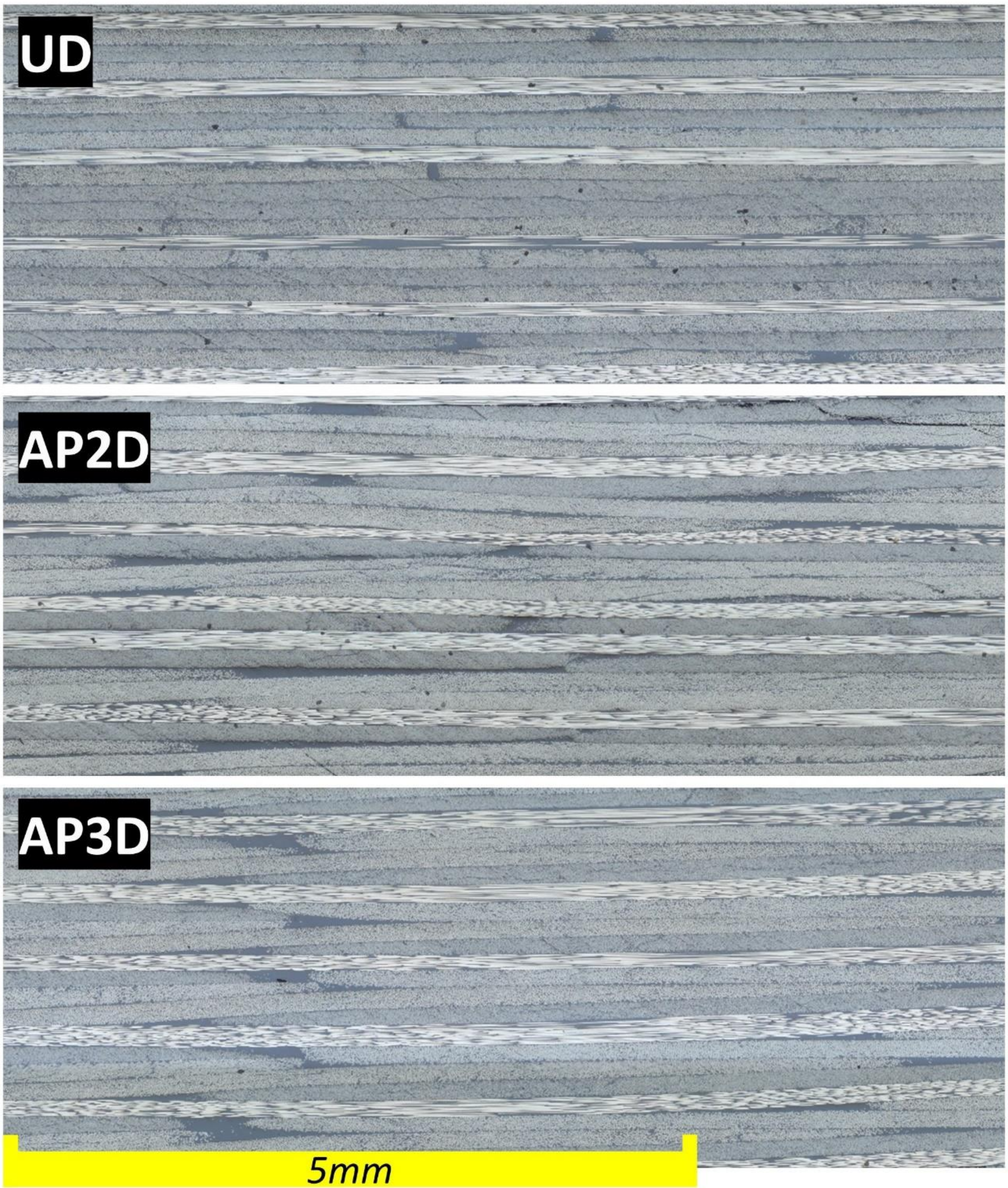

Figure 3.19. The detailed cross-sectional view of different laminates

To mitigate the thickness undulations near the tow overlap areas, an artificial tow-to-tow gap size of 1.3mm was intentionally added to all plies (see UD in Figure 3.18). This does not lead to large resin-rich regions in most laminates as the tows easily spread under consolidation pressure. Figure 3.19 presents the cross-sectional tow distributions and resin pockets of the cured laminate configurations. It can be observed that the tow-to-tow gaps have nearly disappeared in the UD case, while for AP-Ply laminates the resin pockets were concentrated on the weaving corner, which might be because the weaving structure constrained the flows of fibre with different orientations. The resin gaps observed in the semi-woven configurations are comparable to, or smaller than, those found in fully-woven textile composites.

3.4.2 LVI experimental setup

The LVI experiment was carried out with an Instron CEAST 9350 Drop Tower system, as per the ASTM D7136 [114]. A schematic diagram of the LVI experimental setup is presented in Figure 3.20. A hemispheric indenter with a diameter of 16mm and a mass of 4.392kg was used as the drop weight impactor. The specimens were placed in the centre of the impact support fixture base including a 125 x 75mm cut-out and secured with four clamps with rubber tips. Guiding pins were used to ensure the specimen was centrally aligned over the cut-out. An anti-rebound system was activated after impact to prevent secondary damage to the samples. The force-time response during the LVI event was captured by the data acquisition system. All the laminate configurations were tested with two different impact energies, 25J and 40J, which were controlled by adjusting the drop height of the impactor. Three samples were tested for each laminate configuration and energy level.

To quantify and understand the damage mechanisms occurring between different laminate structures, a Non-Destructive Inspection (NDI) method, X-ray CT scanning, was carried out on the impacted specimens.

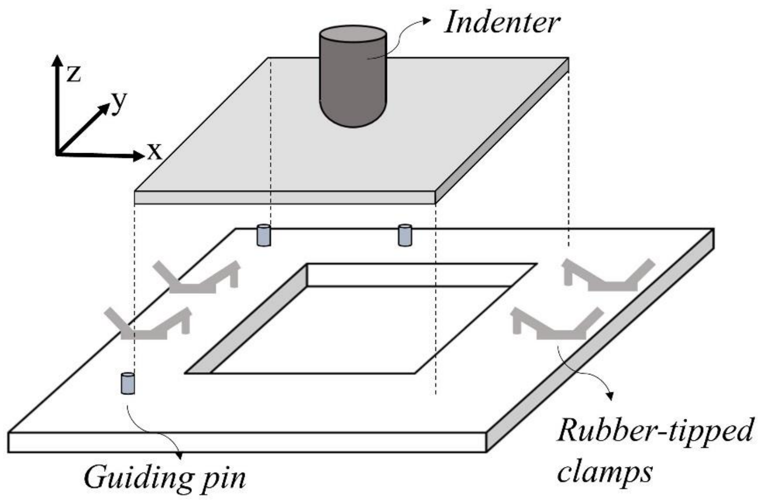

Figure 3.20. The schematic setup of low-velocity impact test

The displacement ($\delta(t)$) and absorbed damage ($E(a)$) can be computed based on the force-time response following the formulations provided by ASTM D7136 [20], as expressed by

$$\delta(t) = \delta_i + v_i t + \frac{gt^2}{2} - \int_0^t \left(\int_0^t \frac{F(t)}{m} dt\right) dt \tag{3-1}$$

$$E(a) = \frac{m(v_i^2 - v(t)^2)}{2} + mg\delta(t) \tag{3-2}$$

Where δ_i refers to the initial impactor displacement from the reference point, v_i denotes the initial impact velocity, g represents the gravity acceleration, and m refers to the impactor mass. The indenter velocity ($v(t)$) during the impact can be computed by

$$v(t) = v_i + gt - \int_0^t \frac{F(t)}{m} dt \tag{3-3}$$

3.4.3 Results

(a) Global response

The global responses of different laminate configurations subjected to various impact energy levels are presented in Figure 3.21. The representative force-time, force-displacement, and energy-time responses were compared between the different laminates. The global trend of the LVI response in this work shows a similar pattern with previous studies [115, 116], in which 3-phases of damage mechanisms were identified including: (i) in phase-1, an approximate linear elastic behaviour was observed, matrix failure can occur in this stage; (ii) in phase-2, a clear load drop and structural stiffness variation occurred when the load reached the delamination threshold, multiple interfaces failure and matrix cracking initiated and propagated; (iii) in phase-3, fibres started to break and eventually, catastrophic failure occurred due to multi-layer fibre failures, which was accompanied by a significant load drop.

The delamination threshold (F_{dt}), peak load (F_p) and absorbed energy (E_{absorb}) were used as the primary metrics of comparison. Specifically in this study, these parameters for UD at an impact energy of 25J are highlighted with dashed lines in Figure 3.21 and they refer to the load before the first major drop, the maximum load before catastrophic failure, and the kinetic energy of the impactor after impact, respectively. The results for each laminate configuration at the tested impact energies are recorded in Table 3.3.

Table 3.3. The results comparison between different laminate configurations in terms of delamination threshold (F_{dt}), peak load (F_p) and absorbed energy (E_{absorb}). For each configuration, the mean value is used, and the bracketed value refers to the coefficient of variation.

	Impact energy: 25J			**Impact energy: 40J**		
	UD	***AP2D***	***AP3D***	***UD***	***AP2D***	***AP3D***
F_{dt} *(N)*	4.88 (5.17)	5.52 (2.10)	4.89 (7.06)	4.53 (0.93)	5.50 (2.69)	4.98 (2.21)
F_p *(N)*	9.32 (0.12)	9.25 (1.84)	8.4 (6.96)	10.15 (2.32)	10.04 (4.77)	8.35 (6.83)
E_{absorb} *(J)*	12.64 (1.44)	13.17 (3.27)	16.3 (12.32)	34.05 (3.39)	33.93 (2.00)	36.16 (0.00)

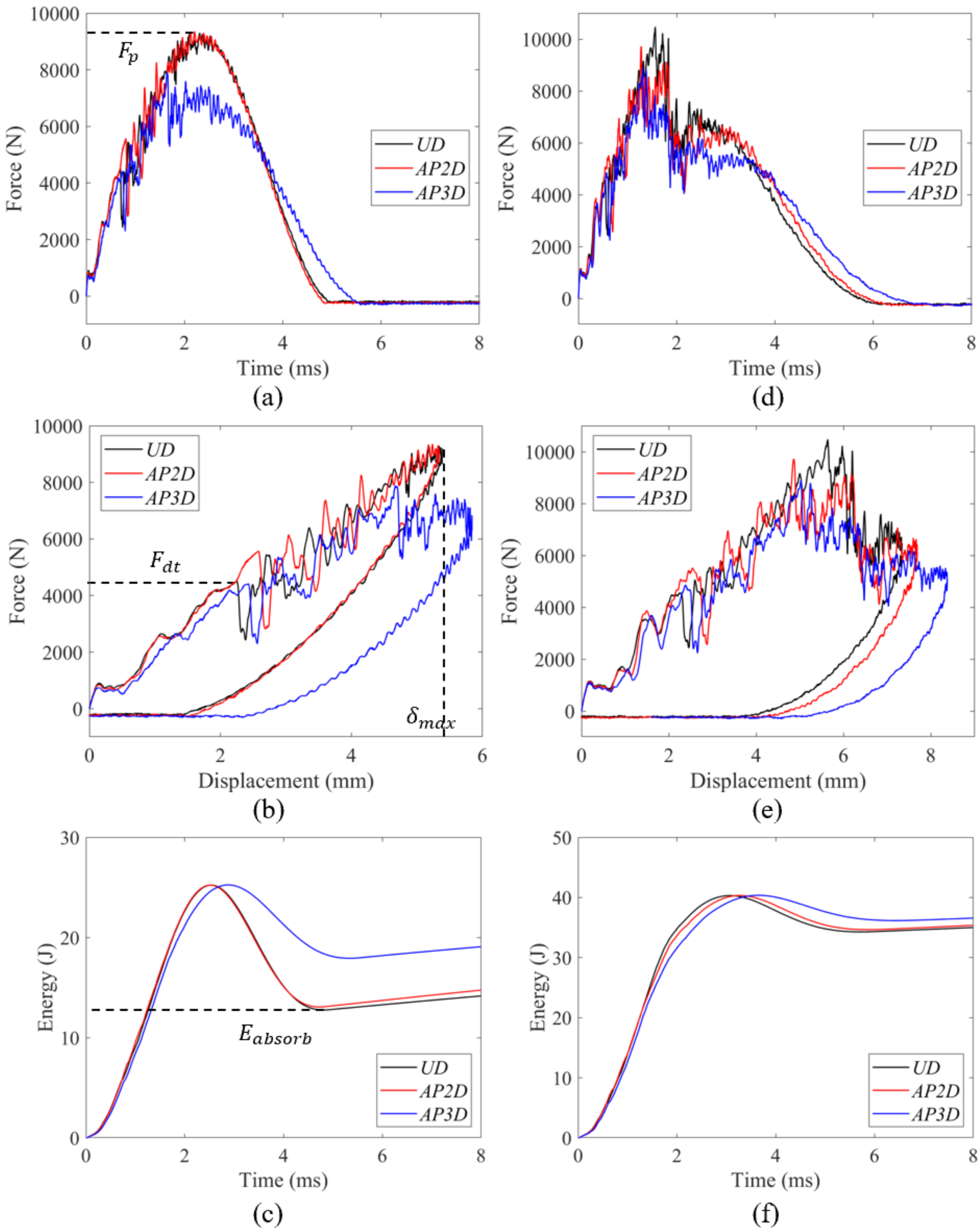

Figure 3.21. Representative global responses of LVI tests for different laminate configurations, where (a-c) refer to the impact energy of 25 J, and (d-f) refer to the impact energy of 40 J.

When the impact energy was 25J, the phase-3 damage mechanism was not observed, and nearly identical loading and unloading global responses were obtained in both UD and AP2D configurations. Small indentations and limited splitting were observed on the impacted and back surfaces of the laminate, as shown in Figure 3.22. While for AP3D, a substantial difference regarding the global response can be observed and notably more back face damage was observed. This means that for AP3D, the impact energy of 25J reached the load level where the phase-3 damage mechanism started to occur. This can also be confirmed with the absorbed energy, which showed that AP-3D absorbed 15% more impact energy than the other two configurations. However, it should be noted that this trend occurred in two of the three AP3D samples while the other one showed similar behaviour to the UD and AP2D samples. The AP-Ply laminates have spatial variation in their properties due to the weave pattern, so the impact event may have been affected by impact location to some extent.

All the laminates indicated a substantial failure in the form of a greater indentation size and increased back face damage at an impact energy of 40J, as shown in Figure 3.23. The global responses also experienced a sharp load drop for every configuration. Instead of an instant significant load drop, both AP2D and AP3D exhibited a degree of plasticity, as illustrated in the force-displacement plot shown in Figure 3.21e. In exchange for that, the catastrophic failure initiated slightly earlier, which can be noted from both the force-time and force-displacement plots (Figure 3.21d-e). A comparable amount of impact energy was absorbed by UD and AP2D whereas AP3D recorded a slight increase of 5%. Moreover, Figure 3.23 depicts similar size of indent at the front face but a completely different back face damage pattern, where UD showed an elongated hump, while AP2D presented very concentrated but relatively smaller damage and AP3D exhibited twisted and concentrated damage with extensive fibre failures. To understand the differences in damage mechanisms between these laminates, a non-destructive internal damage evaluation needs to be performed and the results are presented in Section 3.4.3(b).

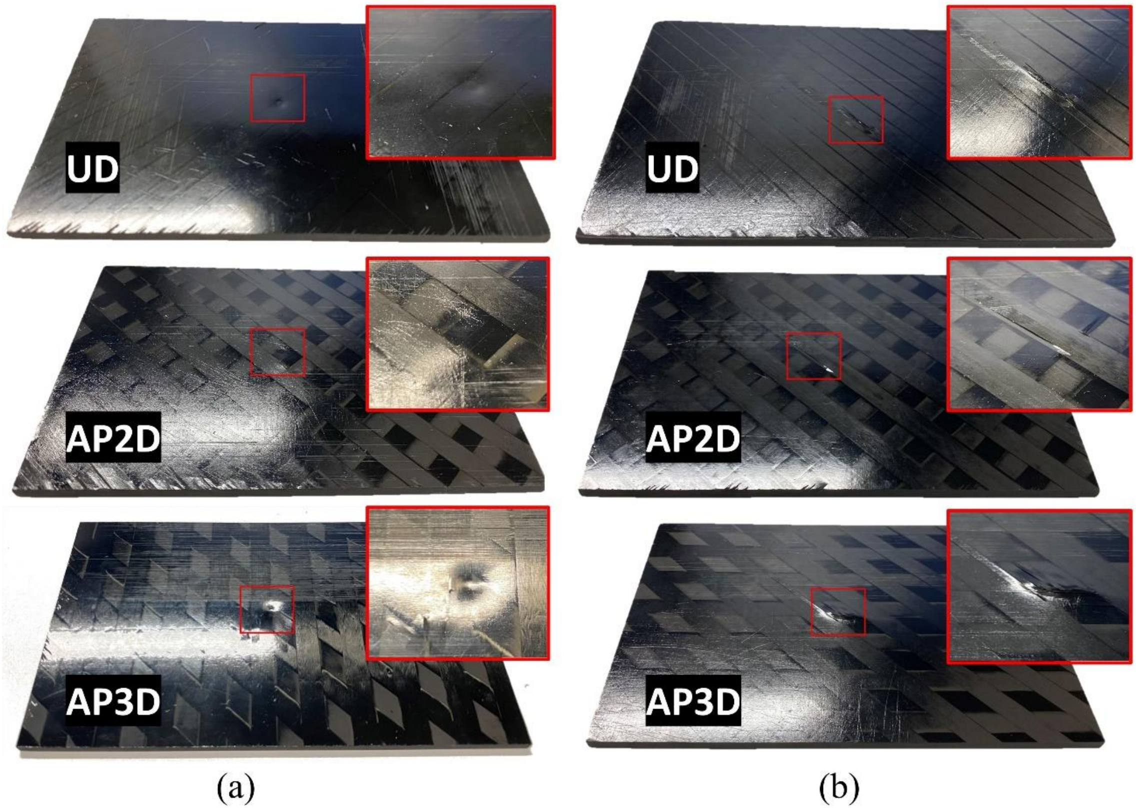

Figure 3.22. The visualisation of impact damage (a) front and (b) back surface for UD, AP2D and AP3D at the impact energy of 25J.

It can be found from Table 3.3 that for each laminate configuration, the delamination threshold showed a consistent result between impact energy 25J and 40J. AP2D exhibited an approximate 10-20% higher delamination threshold than UD and AP3D. The high delamination strength of AP2D can be induced by the difference in fibre architecture. A lower peak load was noticed at an impact energy of 25J than 40J for both UD and AP2D, whereas the difference was trivial for AP3D. AP3D recorded up to 17.7% lower peak load than the other two configurations for both impact energies. However, AP3D exhibited a higher energy absorption for both impact energies by 5-10%. As a result, this suggested that the AP-3D had the highest degree of plasticity among these configurations.

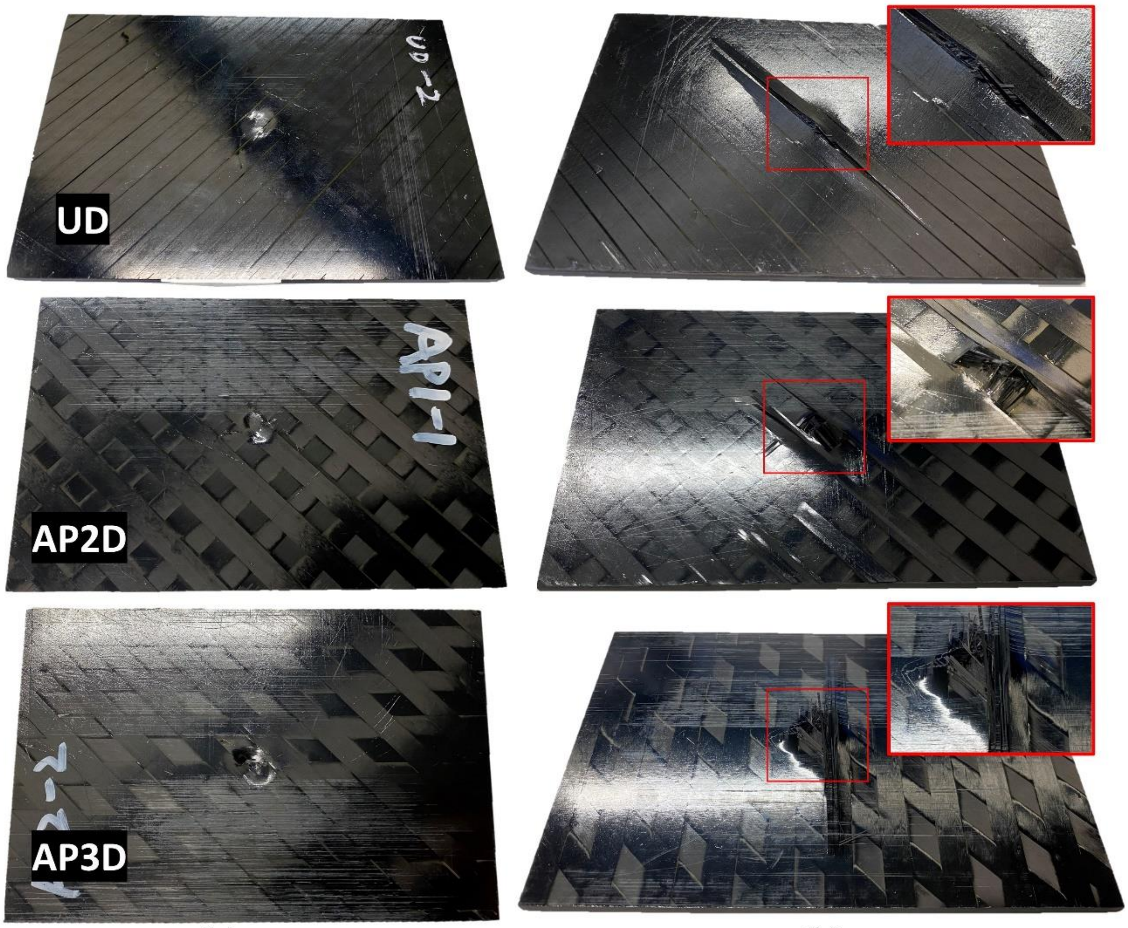

Figure 3.23. The visualisation of impact damage, (a) front and (b) back surface for UD, AP2D and AP3D at the impact energy of 40J.

(b) Damage area

The majority of the damage is in the form of matrix cracking, delamination and fibre fracture that occurs inside the laminate, hence a non-destructive inspection technique, μCT scanning, was carried out to assess the failure mechanisms and damage size. Specimens tested at both impact energies of 25J and 40J were scanned, the 25J specimens indicated trivial failure damage which was localised near the impact area. The group with 40J included more significant damage and hence are presented and compared across different laminate configurations in this section.

Considering the size of the panel (150 x 100mm) and image resolution, only the region of interest near the impact location was scanned as shown in Figure 3.24a. The crack morphology in the through-thickness direction near the impact centre (section A-A), in which the maximum deflection and damage occurred, was visualised in Figure 3.24b. The black areas attached to the specimen surface both above and below refer to air. In addition to this, several differences can be observed in the impacted regions (i) the after-impact indentation depth: AP3D > AP2D > UD; (ii) UD exhibited many wide through-thickness delaminations, while AP-Ply indicated a more concentrated fracture mode with smaller delaminations but extensive matrix and fibre failures, particularly for AP3D.

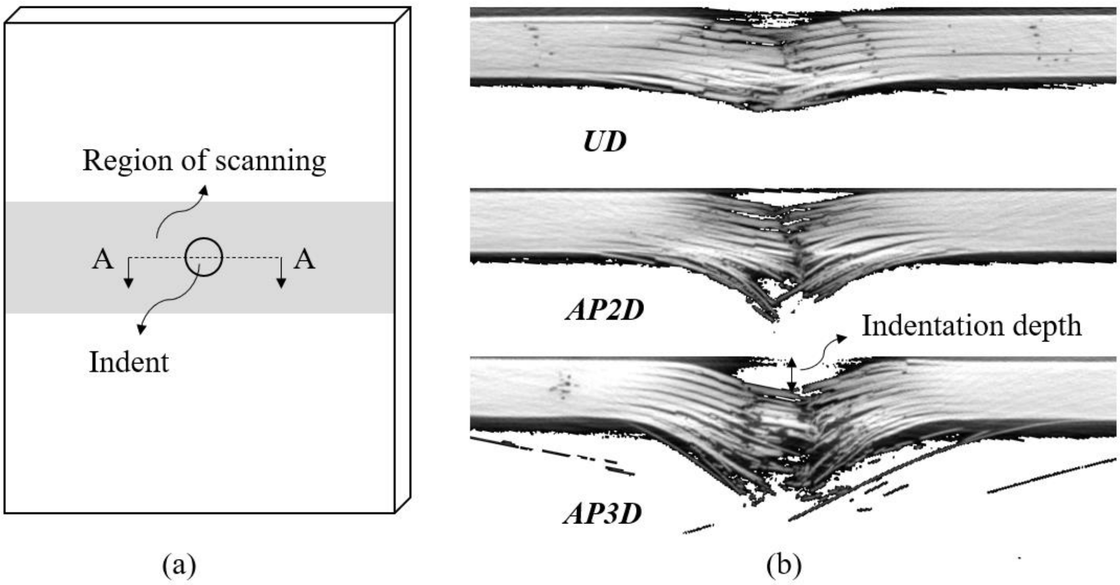

Figure 3.24. (a) The schematic representation of the CT scanning sample. (b) The cross-sectional views (A-A) of different laminate configurations at the impact region.

To further analyse the damage, a 3D damage visualisation of the impacted specimen was obtained via Avizo 2020. The segmentation technique can be used to partition the cracks based on different material grayscale. Figure 3.25 depicts the approximate size of the in-plane damage of different laminate configurations. As the voxel size is around the same magnitude as the ply thickness, identifying the

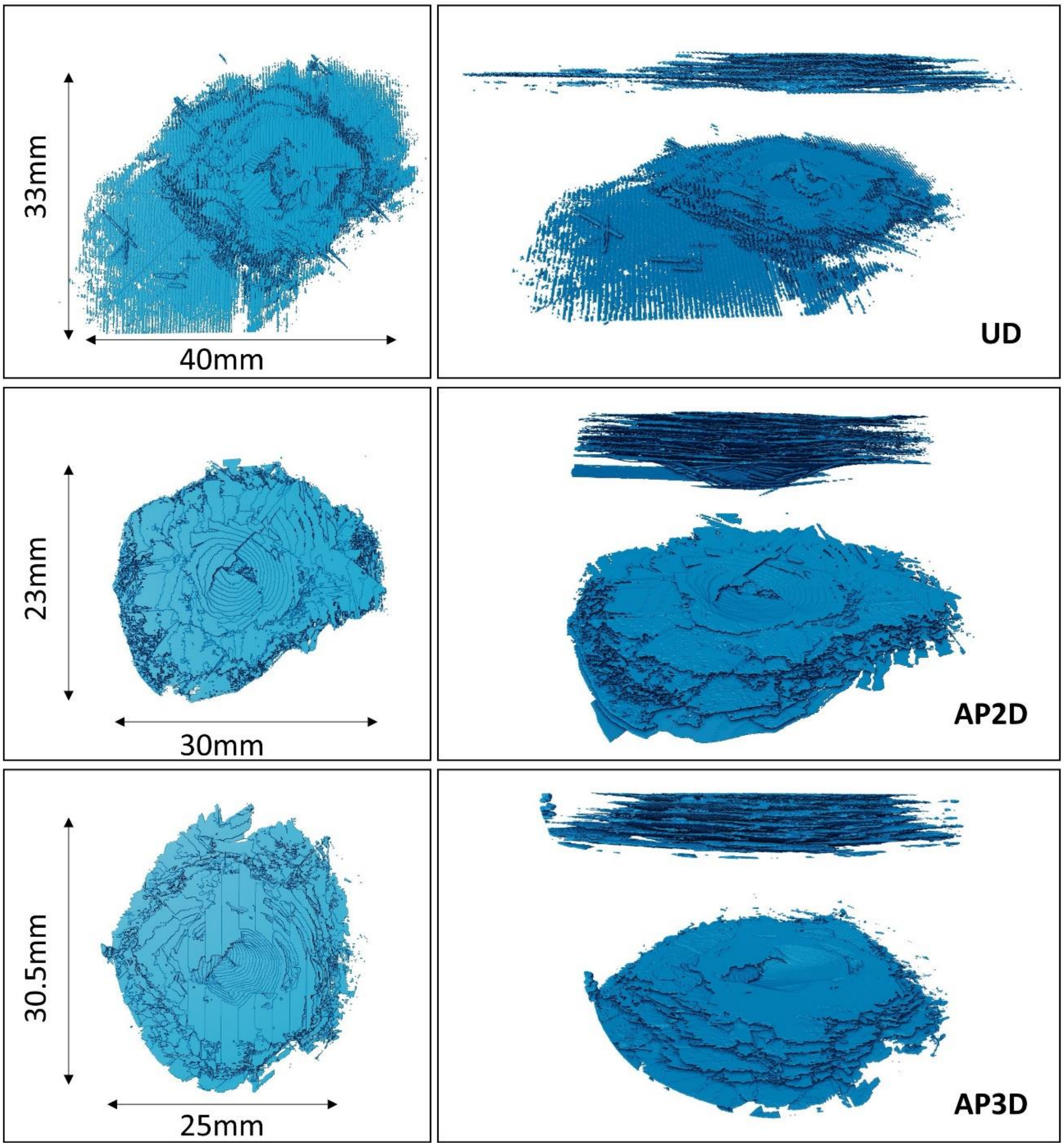

Figure 3.25. The results of CT-Scan with different laminate configurations, including a top view, a front view and an isometric view.

specific interface damage is challenging. Hence, the damage is not separated by interface angle in this visualisation. An isometric view and a front view are provided for the visualisation of the 3D damage morphology. To quantitatively assess the impact resistance, the damaged area was computed based on the maximum in-plane dimensions. Two of the three samples were scanned and computed to ensure the results were representative. The results are presented in Table 3.4. It can be concluded that the impact resistance of both AP2D and AP3D were much greater than UD.

Table 3.4. Damage resistance of different laminate configurations at an impact energy of 40J. Note: the measurements refer to mean values.

	Max length (mm)	***Max width (mm)***	***Impact resistance (J/mm²)***
UD	42.3	33.38	0.028
AP2D	25.6	22.87	0.068
AP3D	28.8	29.5	0.047

3.5 Compression after impact

3.5.1 CAI and CLC experimental setup

The CAI and CLC (baseline) tests were both conducted with a servo-hydraulic testing machine, Instron 8804 with a load cell of 500kN. The schematic setup of CAI test is displayed in Figure 3.26. For the CAI test, the impacted samples were placed in a multi-piece support fixture to prevent buckling during the compression loading. Instead of being fully clamped at all the specimen edges, the side supports are four steel plates with knife edges which do not provide constraints against local rotations. The compression was applied via two flat platens with a displacement rate of 1.25mm/min in accordance with the ASTM D7137 [117]. All the impacted samples for each laminate configuration were tested.

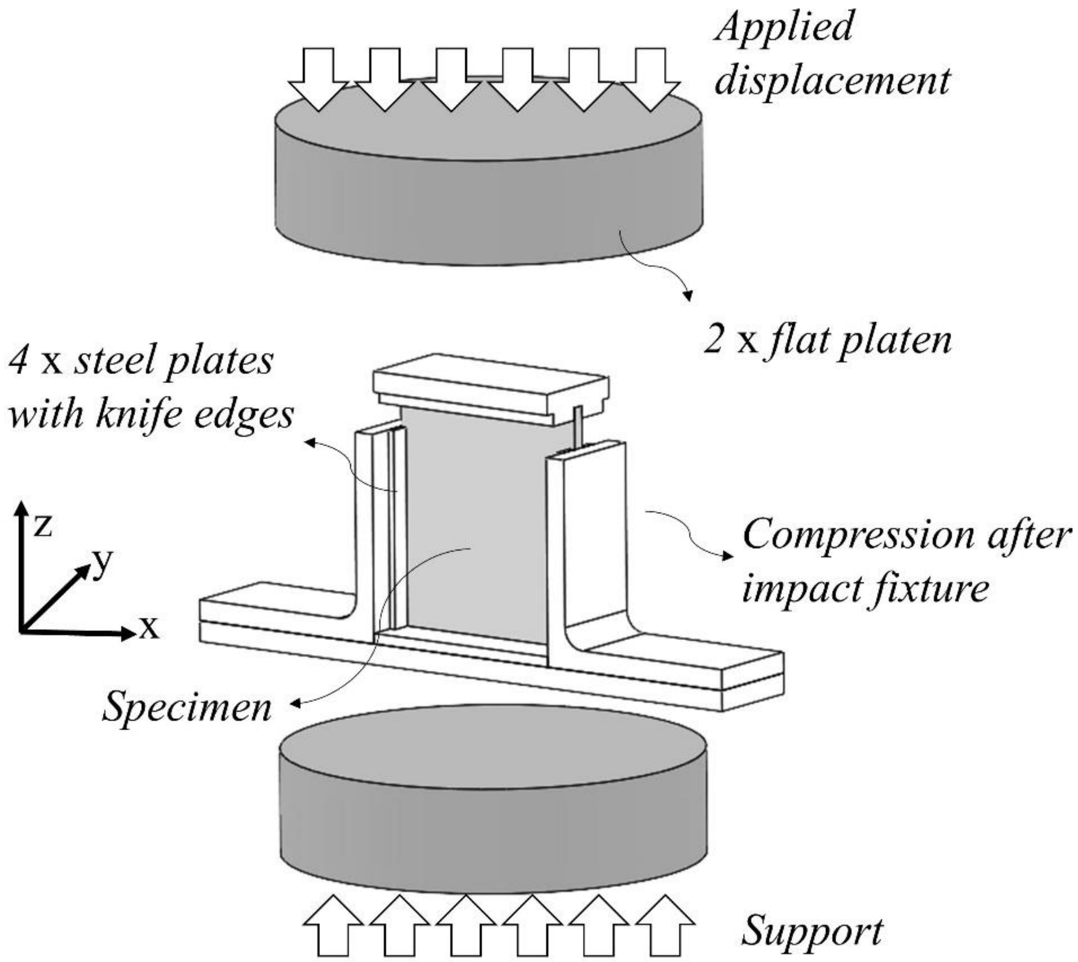

Figure 3.26. The schematic setup of compression-after-impact

For the CLC test, the in-plane dimensions of the specimen were designed as 140 x 30mm with a gauge length of 13mm, as per the ASTM D6641 [118]. The maximum suggested specimen width was used in this test to incorporate a representative weaving material volume. Similar to the CAI test, the compression was applied via two flat platens but with a displacement rate of 1.3mm/min. Five samples for each laminate configuration were tested. The pristine and residual strength can be computed by $\sigma = F/A$, where F and A refer to the maximum force prior to failure and the cross-sectional area, respectively.

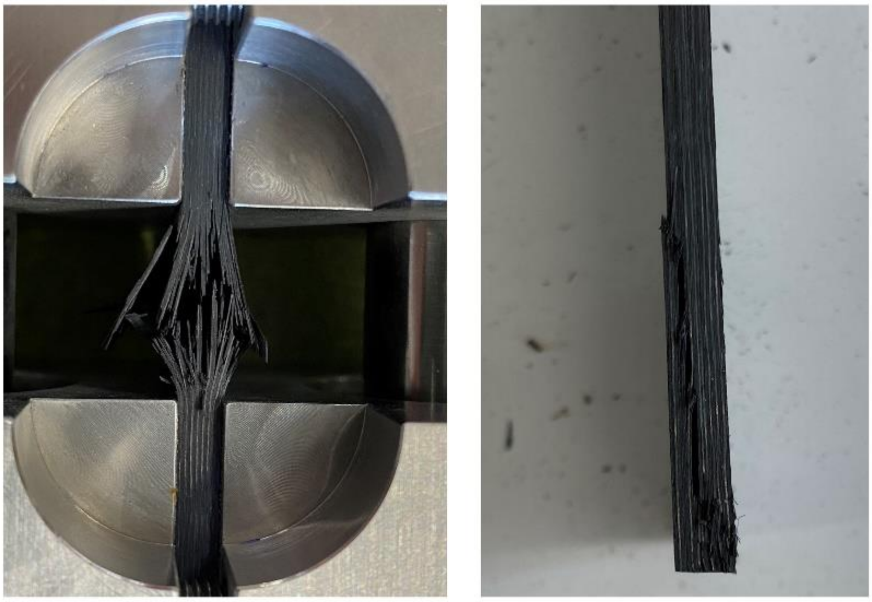

(a) (b)

Figure 3.27. The CLC test with (a) acceptable fracture mode; (b) unacceptable fracture mode with end-crushing

3.5.2 Results

Figure 3.27 depicts two different fracture modes that were observed in the CLC test. Figure 3.27a shows an acceptable fracture mode per ASTM D6641, where the failure occurred in the gauge section. Instead, an unacceptable fracture mode refers to failure that appeared elsewhere within the gripped area, such as end-crushing. In this test, the unacceptable fracture was more commonly observed in AP-Ply laminates rather than UD. This suggests that the spatial variation of the semi-woven structure had a significant impact on the load introduction at the specimen boundaries. The global load-displacement responses of all the specimens excluding the samples with unacceptable failures are plotted in Figure 3.28. A comparable ultimate fracture load was observed between the different laminate configurations while AP3D indicated a slight stiffness drop, which was induced by the larger fibre crimping. The pristine compressive strength, as recorded in Table 3.5, can be computed based on the ultimate fracture load and specimen dimensions.

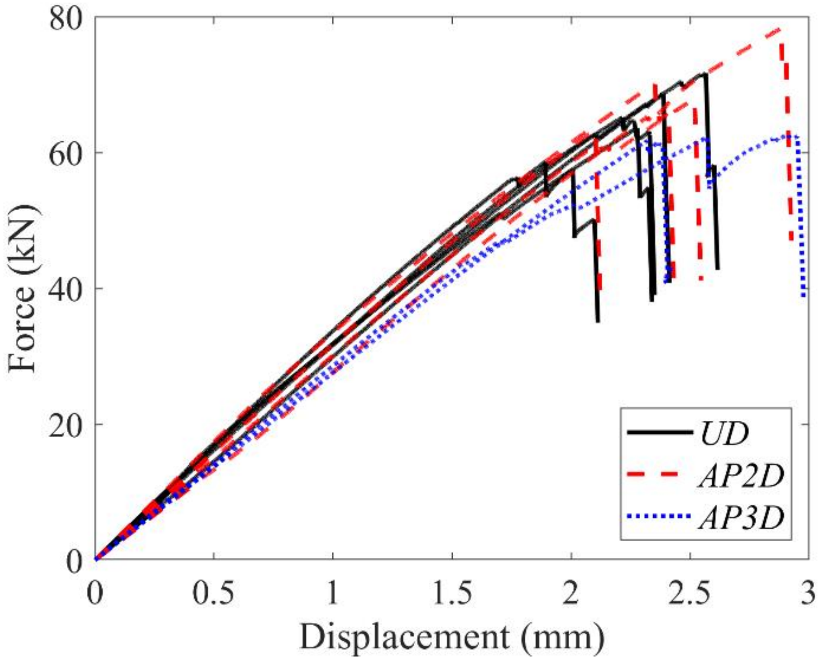

Figure 3.28. The global responses of CLC tests

Table 3.5. The comparison of pristine and residual strength between UD, AP2D and AP3D.

Configuration	Pristine (MPa)	Impact energy: 25J (MPa)	Impact energy: 40J (MPa)
UD	551.24	192.84	140.32
AP2D	581.52	225.56	181.31
AP3D	524.92	215.98	180.96

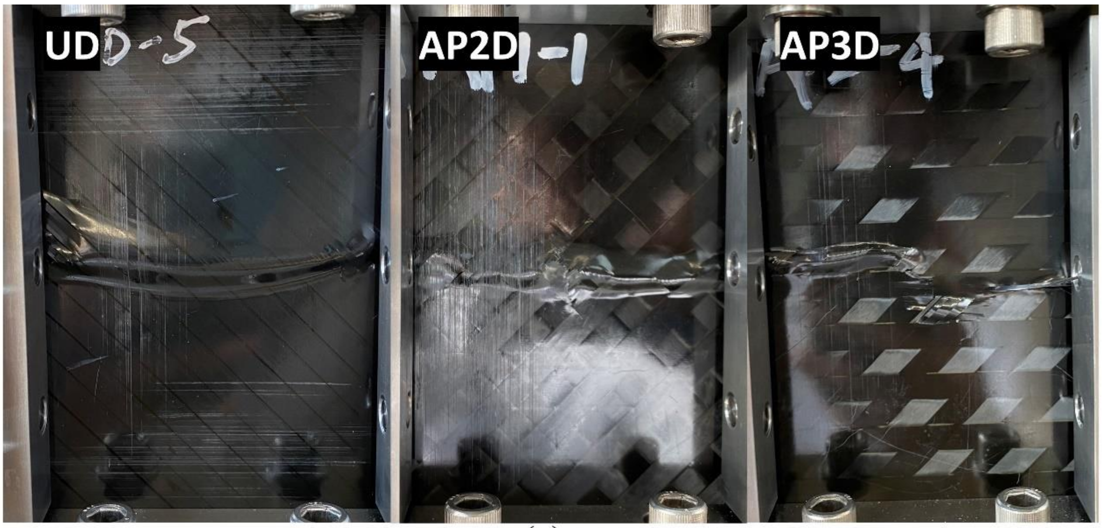

(a)

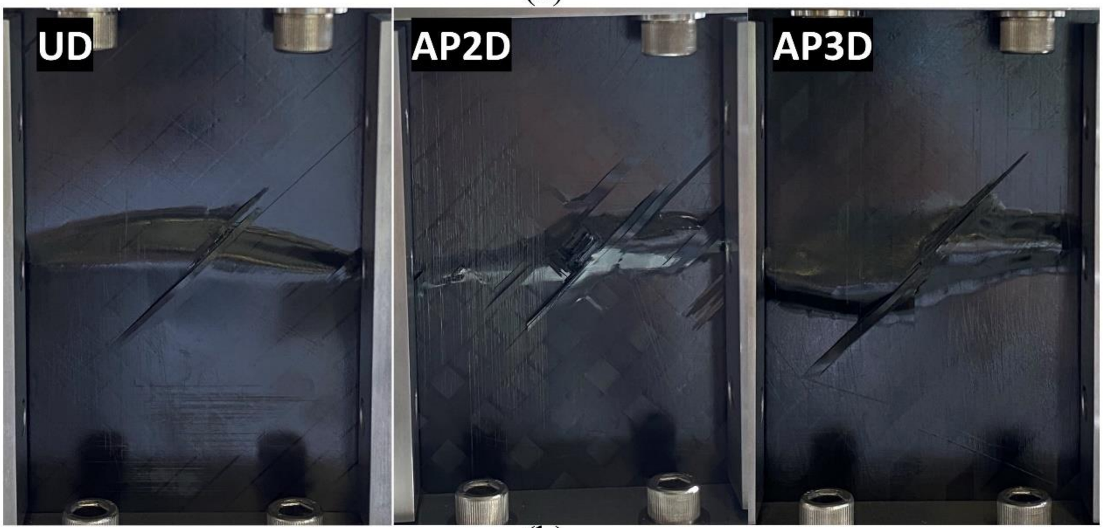

(b)

Figure 3.29. The (a) front, and (b) back face damage of CAI test result for different laminates at impact energy level of 40J.

For each laminate configuration of CAI test, the outer ultimate fracture pattern is similar between different impact energy levels. Hence, one typical fractured sample of each configuration was used to show the ultimate CAI failure in Figure 3.29. It was observed that the ultimate damage consisted of explosive matrix cracking, delamination and fibre failures, which initiated near the pre-impact damage area and propagated transversely. The typical global responses of UD, AP2D and AP3D at both impact energies are compared and shown in Figure 3.30.

A similar trend was observed with the ultimate fracture load at both impact energies: AP2D > AP3D > UD. It should be noted that the difference of fracture load between AP-Ply and UD was amplified substantially at the impact energy of 40J. The residual strengths of different laminate configurations were determined based on the fracture load and respective specimen dimensions. The results are recorded in Table 3.5. At an impact energy of 25J, AP2D and AP3D indicated 17% and 12% higher residual strength, respectively over UD. The improvement of the residual strength at an impact energy of 40J is further increased by 29% for both AP-Ply configurations. This indicates that the AP-Ply is more advantageous than the UD at larger impact energies. This is potentially induced by the different failure mechanisms between UD and AP-Ply, where UD tends to have a few wider and dominant cracks in the form of delaminations while AP-Ply is inclined to have a more concentrated but extensive matrix and fibre failures.

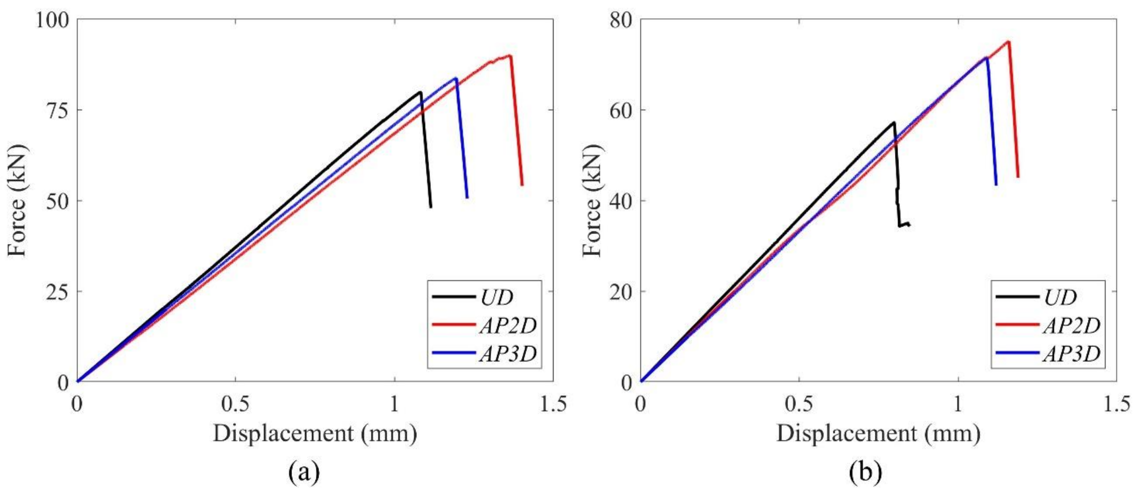

Figure 3.30. The global responses of CAI tests, (a) at an impact energy of 25J, and (b) at an impact energy of 40J

3.6 Summary

AFP composites contain numerous geometric features such as gaps, overlaps and tow drops that may have a significant impact on the material properties and the failure mechanisms. AP-Ply is used as a representative example of AFP composites in this chapter to study the effect of these complex geometric features on the structural response. Due to their weave-like meso-structure, it has been proposed that AP-Ply laminates can reduce interlaminar damage propagation under certain loading conditions [3]. The geometric features, on the other hand, also have been demonstrated with significant impact on failure initiation and progression [6, 61, 62]

The behaviour of AP-Ply laminates was further experimentally investigated in this chapter with a variety of tests including the SBS, LVI, CLC, and CAI. For each test, a traditional AFP laminate configuration was used for comparison to facilitate the understanding of the effect of these geometric features. Based on these experimental tests, the key findings include:

- It has been demonstrated that a small degree of inter-ply tow weaving has little impact on SBSS. Conversely, increasing the tow weaving depth resulted in an SBSS drop of 11.36%. The differences can be attributed to the effect of different tow crimp angles and weaving morphology. The experimental results indicated that an optimum AP-Ply configuration can be achieved which improves impact resistance without reducing static laminate strength.
- The 3-phase damage mechanisms under LVI were similar between UD and AP-Ply. However instead of an instant load drop in phase 3, both AP2D and AP3D exhibited a degree of plasticity. The semi-woven

structure has also been shown to have a great impact on the delamination threshold, peak load and energy absorption.

- The failure mechanisms between UD and AP-Ply are different under LVI, in which UD tends to have a few major delaminations while AP-Ply tends to have many more concentrated matrix cracks, delaminations and fibre failures. By definition, the impact resistance of both AP-Ply configurations was higher than the UD laminate.
- A comparable pristine compressive strength was observed between AP-Ply and UD. This means that a small degree of inter-ply tow weaving can substantially increase the damage resistance and damage tolerance without affecting the laminate in-plane compressive strength.
- AP2D and AP3D have improved the CAI residual strength by 12% and 17%, respectively at an impact energy of 25J. The improvement is more advantageous with 29% achieved for both AP-Ply configurations at a larger impact energy of 40J.

Chapter 4 TWM Method

4.1 Introduction

A very complicated failure phenomenon, which is highly dependent on the spatial arrangement of tows, was noted via the experimental testing of AP-Ply laminates in the previous chapter. To precisely predict the failure events and better understand the associated failure mechanisms, a high-fidelity numerical model that can represents these geometric features is thus becoming critical. This chapter aims to develop a high-fidelity geometric modelling approach named the Tow Wise Modelling (TWM). The basic concept of this method is to model every discrete element (tow for AFP) at mesoscale, which hence, provides a chance to model the tow undulations and structural discontinuities introduced during the AFP manufacturing process.

As aforementioned, the TWM aims to model each discrete element of AFP composites, in which the minimum structural unit is a discrete narrow tow, instead of a distributed ply. Unfortunately, the manual creation of laminate geometry from these discrete tows, and the associated laminate defects, is costly and tedious, especially for large and complex components. Hence, a python-based script is developed, which attempts to build the model using automation by simulating the tow placement process. This tool will serve as the foundation of finite element analysis for a more accurate prediction of local and global structural performance of AFP composites. The main feature of this tool is the capability of modelling each tow individually to offer an opportunity of depicting the gaps /overlaps, tow drops, and out-of-plane waviness explicitly. The specific steps involved in this tool will be presented in detail in this chapter.

Most of the results presented in this chapter are included in the following publication:

Li X, Dufty J, Pearce GM. *Automation of Tow Wise Modelling for Automated Fibre Placement and Filament Wound Composites*. Composites Part A: Applied Science and Manufacturing. 2021:106449.

4.2 Inputs, outputs, and assumptions of the TWM

The design and manufacture of AFP composite structures are critically dependent on CAD software and extensions for Tow Path Planning (TPP) [19]. As discussed in Chapter 2, TPP algorithms require inputs such as the tool/mandrel geometry; desired fibre orientation; kinematic constraints of the robot and head; and manufacturing constraints on tow paths, such as radius of curvature, etc. The focus of TPP is to produce optimal 3D tow paths and control instructions for the complex robotics involved in AFP.

On the other hand, TPP algorithms are not designed or intended to produce a precise map of the tow locations in an AFP laminate. Crucially, tow paths output from TPP software are mapped to the mandrel surface, or some fixed stand-off distance, and do not account for the small “z-offset” which develops as tows overlap or fill existing gaps, as shown in Figure 4.1. These small discrepancies do not affect the manufacturing process but are critical to consider when modelling defects in the laminate.

In conventional AFP applications, a laminate is sequentially formed by placing roughly parallel 1D tows into an approximation of a 2D ply. The process is repeated for each "ply" of the laminate stack. In this way, the tows in each ply follow roughly the same orientation as the adjacent tow in a 2D plane. Thus, all tows for a given ply can be reasonably approximated to have a constant z-offset from the mandrel surface (Figure 4.1a). For the non-conventional AFP applications, however, such as AP-Ply or fibre steering, the z-offset is a function of path length (Figure 4.1b). Besides, if two tows overlap obliquely, the z-offset is also a function of position across the tow width. TPP algorithms do not need to consider this effect, as AFP processing heads always have some form of physical offset compensation, such as a pneumatic piston.

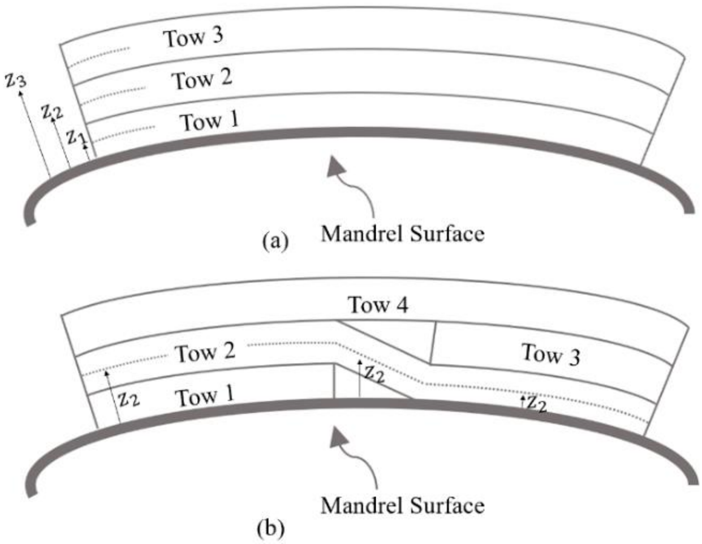

Figure 4.1. Comparison of z-offset in (a) conventional / (b) non-conventional AFP manufacturing

The TWM algorithm, therefore, fills the gap between the TPP outputs and a 3D description of the tow locations in the final laminate. Explicitly, the TWM algorithm requires the following inputs, which are readily available as exports from TPP software:

1. Geometric properties of the AFP tows (i.e. width, thickness)
2. Mandrel/tool 2D surface geometry as CAD export or surface mesh

3. A list of 1D *tow paths* in the order that they are added to the tool. Each tow path is defined in a piecewise fashion as a spline across a list of *tow points*. Each tow point contains the following information:
   - Location vector: The position of the point in space
   - Orientation vector (optional): The local orientation of the tow projected onto the mandrel.
   - Normal vector (optional): The local surface normal direction of the tow (and tool).

The TWM algorithm converts each 1D tow path to a discretely defined 2D surface mesh and nests the mesh against the tool and previously laid tows. The resulting non-continuous 2D surface mesh approximates the as-manufactured mesostructure of a general AFP laminate. The implementation described in this chapter also retains crucial FE pre-processing information, such as fibre orientation. The algorithm is described in detail in the next section, and output case studies are discussed in Section 4.4.

4.3 TWM algorithm description

As described, the TWM algorithm converts AFP manufacturing data to a geometric model with the cooperation of an FE pre-processor. In this study, the input data was generated by Fibre Placement Manager (FPM) [108], the standard software for the Automated Dynamics AFP system at the University of New South Wales. The algorithm was implemented in Python 3.7 coupled to an FE pre-processor MSC Marc-Mentat with its powerful built-in scripting tools. A schematic overview of the automatic geometric model generation is shown in Figure 4.2 and the according flowchart is presented in Figure 4.3. Each step is described in detail in the following sections.

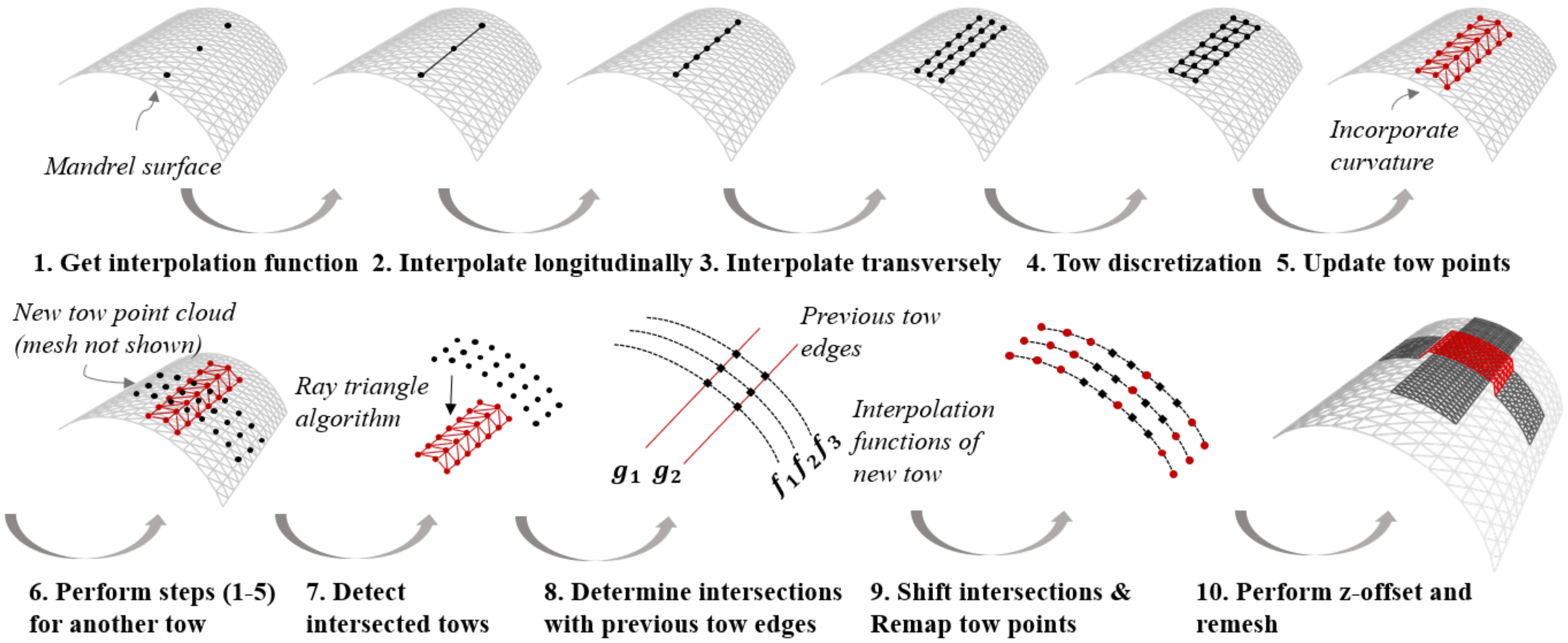

Figure 4.2. The key procedures to realize FE model generation from AFP manufacturing data

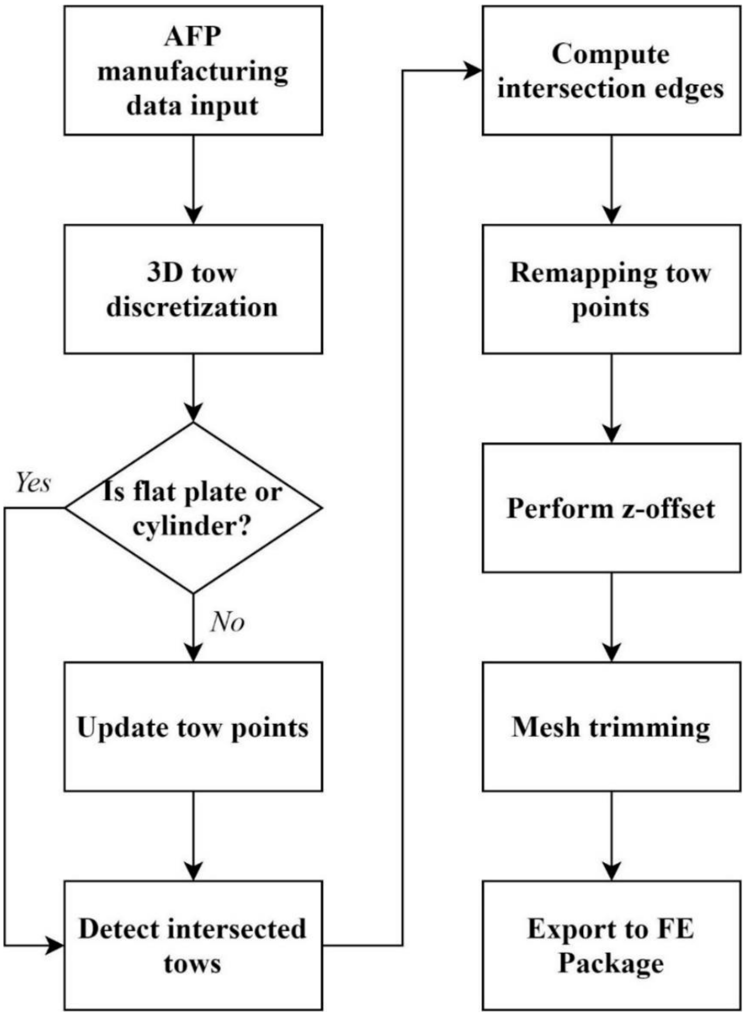

Figure 4.3. A flowchart representation of the key procedures used in automatic geometric model generation

4.3.1 Input processing

As discussed previously, the TWM algorithm requires three input datasets. The first set is trivial and consists of tow geometric properties, such as thickness, width, etc. Mandrel/tool surface geometry is required by the algorithm as a scaffold for tow placement. The surface description can be provided as a triangular mesh (e.g., Figure 4.2) or in a portable CAD format. Internally, the algorithm uses a meshed representation of the tool surface. In the present work, the mesh file of the mandrel is generated in MSC Marc-Mentat and exported as an STL file.

The specific tow path data structure is dependent on the TPP software used. An example of the data structure generated by FPM is presented in Figure 4.4. Tows (or Strips) are defined as a spline over a list of points. For each point, Coordinate, Orientation, and Normal vectors are provided as scalar triples. FPM also provides an Angle column, but this is only an indicative angle for design purposes. In FPM, tows usually extend beyond the manufacturing volume and the Boundary value is used to filter invalid points located outside the margins.

```
begin
#    PlyNo    PlyAngle
ply 3    0
strip    1
#    idx    X       Y      Z      I  J  K   SDist  Angle  InBounds    Dir X  Dir Y  Dir Z
pt   1      346     -97    25.4   0  0  1   0      0      30000000H   1      0      0
pt   2      582     -97    25.4   0  0  1   236    0      20000000H   1      0      0
pt   3      591     -97    25.4   0  0  1   245    0      20000000H   1      0      0
pt   4      600     -97    25.4   0  0  1   254    0      20000001H   1      0      0
pt   5      800     -97    25.4   0  0  1   454    0      20000001H   1      0      0
pt   6      818     -97    25.4   0  0  1   472    0      20000000H   1      0      0
pt   7      1054    -97    25.4   0  0  1   708    0      20000000H   1      0      0
end 1
end
```

Tow ID **Coordinates** **Normal vector** **Boundary** **Orientation vector**

Figure 4.4. The tow path structure of FPM output

4.3.2 Tow point definition (Steps 1-4)

In FPM, the number of provided definition points along the length increases with increasing curvature, especially in transition regions from low curvature to high curvature. Conversely, for straight tows, only two valid points, located at either end, are included. The TWM algorithm first interpolates the tow points with a high-order interpolation spline and then inserts additional (interpolated) tow points to define the path to the desired point density (see Figure 4.5). The python library SciPy was used for interpolation purposes in the present work.

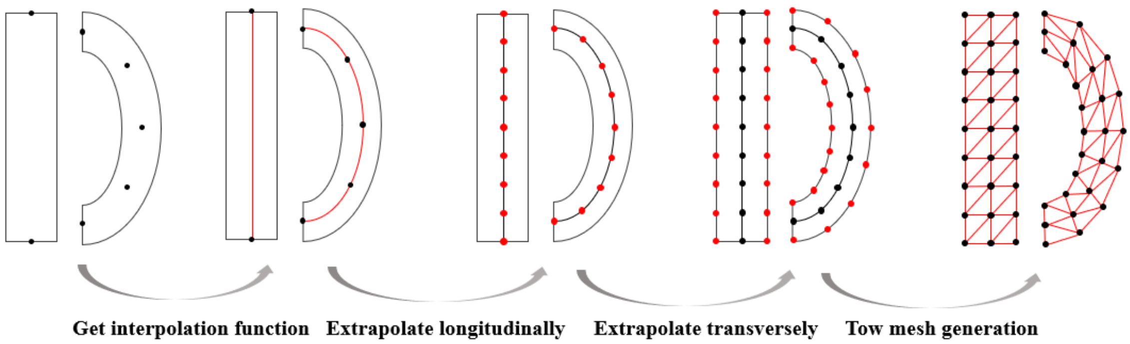

Figure 4.5. Tow discretisation procedures for straight and curved paths (red colour shows step changes)

The transverse extent (width) of the tow is then defined by projecting each tow point to the edge of the tow (Figure 4.5). The projection direction is normal to both the tow orientation and the surface normal (i.e. cross-product) and the distance is half the physical tow width. Finally, the tow surface is defined using a regular triangular mesh over the grid of points. It should be noted that the tow points can be further interpolated in the width direction to achieve a finer mesh. This allows for a better resolution of the distorted tow geometry in later steps, at the expense of computational effort. In the current work presented in Section 4.4, seven points were used across the width of each tow. All triangular mesh processing, for the tows and mandrel, was completed in python library trimesh [119], including STL file import of the mandrel CAD surfaces.

4.3.3 Transverse tow points update (Step 5)

As stated previously, the tow points not on the tow centreline are extrapolated transversely using the local tow orientation and normal vectors. Hence, each tow is approximated as locally flat and not conforming to the curvature of the mandrel surface (Figure 4.6). This effect is negligible for narrow tows and mandrels with limited curvature. In some cases, though, to ensure geometric compatibility and avoid excessive tow distortions, the tow points need to be corrected using the mandrel surface curvature.

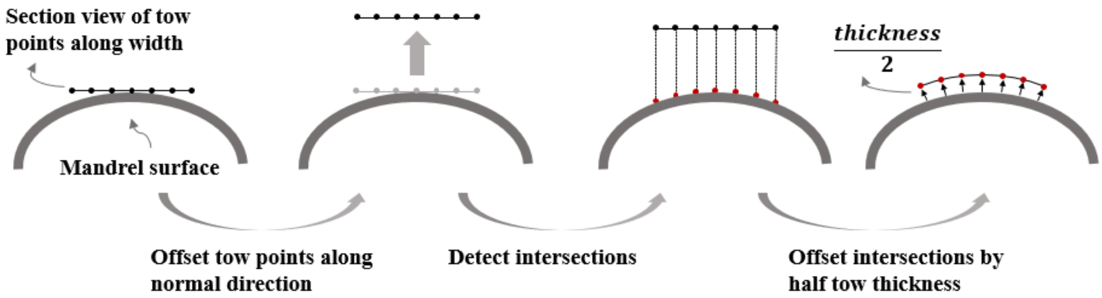

Figure 4.6. The procedures of updating tow points to incorporate the curvature of mandrel surface

In the TWM algorithm, the projections of the tow points on the mandrel surface are calculated. The projections are used to remap the tow points and the detailed procedures are described in Figure 4.6. Seven interpolation points are used in the transverse direction here to define the curvature of the mandrel surface. The projections can be efficiently determined through a ray-tracing algorithm embedded as a submodule of trimesh. If the ray origin and direction are specified, the intersected mesh and the specific intersection position can be calculated. The intermediate step of offsetting the tow points slightly upwards (in Figure 4.6) is to ensure a robust ray-triangle intersection.

Finally, the tow points will be updated by shifting the intersections along the normal direction of the mandrel surface by half tow thickness to account for the thickness effect. The updated tow points are used to represent the mid surface of the tow geometry. The resultant tow width/length will differ slightly from the nominal dimension due to the curved surface projection, but this is a second-order error and is negligible for the majority of real problems. This step can be skipped for simple geometries such as flat plate or cylinders. The cylinder with single curvature can be included by using the cylindrical nodal transformation to improve computational efficiency.

4.3.4 Tow-tow intersections (Steps 6-8)

In the TWM algorithm, the tow-tow intersections in the region of tow drops and overlaps are assumed based on geometric/kinematic constraints alone. Heuristics may be included, in future versions of the TWM algorithm, to account for distortions resulting from the consolidation process, but this is still an active area of experimental work and outside the scope of the current algorithm.

The tow-tow intersection edges can be computed by determining the intersections between the interpolation functions of current tow and preceding intersected tows. The interpolation functions are obtained based on the latest tow points. The intersected tows are computed by determining whether it contains the intersected mesh, obtained by projecting down current tow points on the mesh assembly of preceding tows using a ray-tracing algorithm. The ray-tracing algorithm which determines tow intersections, however, will detect edge-edge intersection along the entire length of parallel tows. To avoid these spurious intersections and ignore very small tow interpenetrations, a small tolerance (1/6 tow width) was set by using inner tow points only (red dots shown in Figure 4.7) to detect tow intersection. The tolerance is essentially computed by the distance between the outermost inner points and edge points, which can be further optimized by using bias or increasing the number of transverse tow points.

The general process of determining the tow-tow intersection edges is presented in Figure 4.7. For every identified intersected tow, only the interpolation functions at edges are used to compute the intersections with current tow (7 interpolation curves). The intersection edge is represented by a series of determined intersections, calculated by a 'fsolve' function in the SciPy library.

This function is used to approximately determine the intersections between high order interpolation curves and works for both linear and nonlinear cases. A small numerical tolerance $1x10^{-6}$ is used in the current study. It should be noted that the number of points along each intersection edge depends on the number of interpolation curves of current tow, seven in this work.

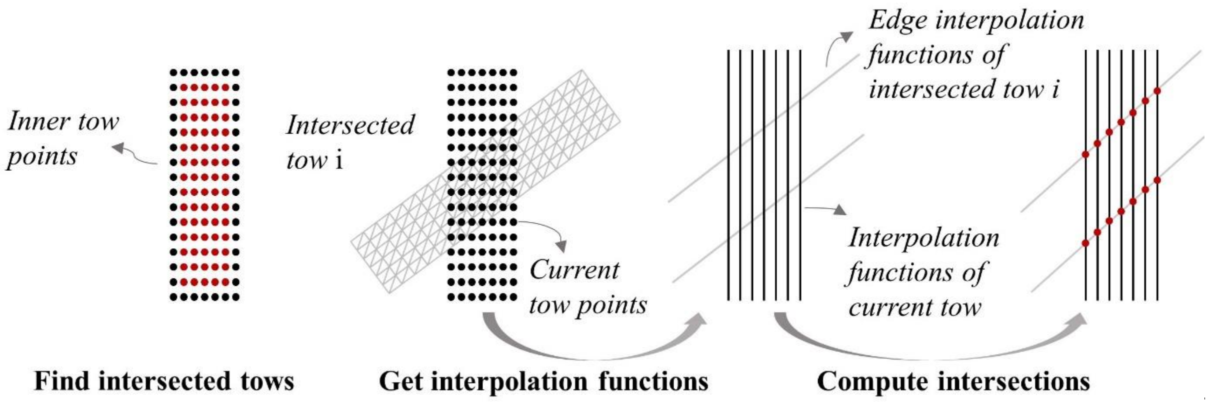

Figure 4.7. Process of determining tow-tow intersections

4.3.5 Tow points remapping (Step 9)

The tow-tow intersections can be a very simple case (see Figure 4.8a), where only two tows are intersected in the middle portion without any geometric interference of other tows, creating small prismatic zones called "resin-rich area". The pre-determined intersection edges are used to remap the tow points, which are utilized to precisely depict the prismatic zones for simple tow drop and overlap cases with the combination of a robust z-offset algorithm. While for other uncommon complex cases, precise geometric description of tow drops becomes extremely challenging, such as parallel or shallow angle tow intersections (Figure 4.8b), multiple tows intersections (Figure 4.8c), and partial intersections (Figure 4.8d) near tow drops or part boundaries, etc. It should be noted that the three complex intersection cases primarily aim to demonstrate the difference and challenges of tow drop modelling with the comparison of the regular and well-intersected case (Figure 4.8a). Any irregular intersection condition not categorised as regular will be handled by the general z-offset algorithm. These and other complex intersection cases are treated separately and require a more general z-offset algorithm with a slight drop in geometric fidelity of overlap features. A compromise method, presented in detail in Section 4.3.6, is employed to describe the defect zone.

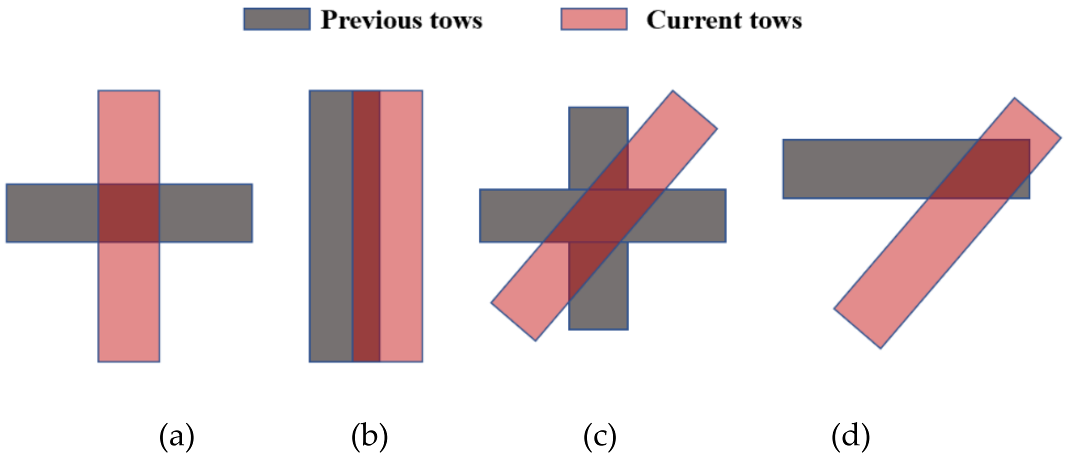

Figure 4.8. Tow-tow intersections for simple case (a) regular cross intersection and complex cases: (b) transverse intersections; (c) multiple tows intersections; (d) partial intersections

The simple and complex intersection cases can be distinguished by checking the constituents and characteristics of intersection edges. For the simple intersection case (Figure 4.8a), two intersection edges can be defined for each intersected tow, and each edge will have a computable number of interpolated intersection points (see Figure 4.7). If these intersection edges cross they are removed as per Figure 4.9.

Other cases where the intersection edge is not computable, for example, there can be 0 (Figure 4.8b) or less than 7 internal intersections (Figure 4.8d) along an edge, are also removed. For the remaining simple tow intersection edges, the intersection points are duplicated to create a prismatic and regular tow-drop around the overlapped region, according to the procedure shown in Figure 4.9. The point duplication parameters are determined based on a desired tow-drop angle and the tow thickness. The remaining tow points are re-mapped to avoid high mesh distortion, especially for oblique tow intersection angles.

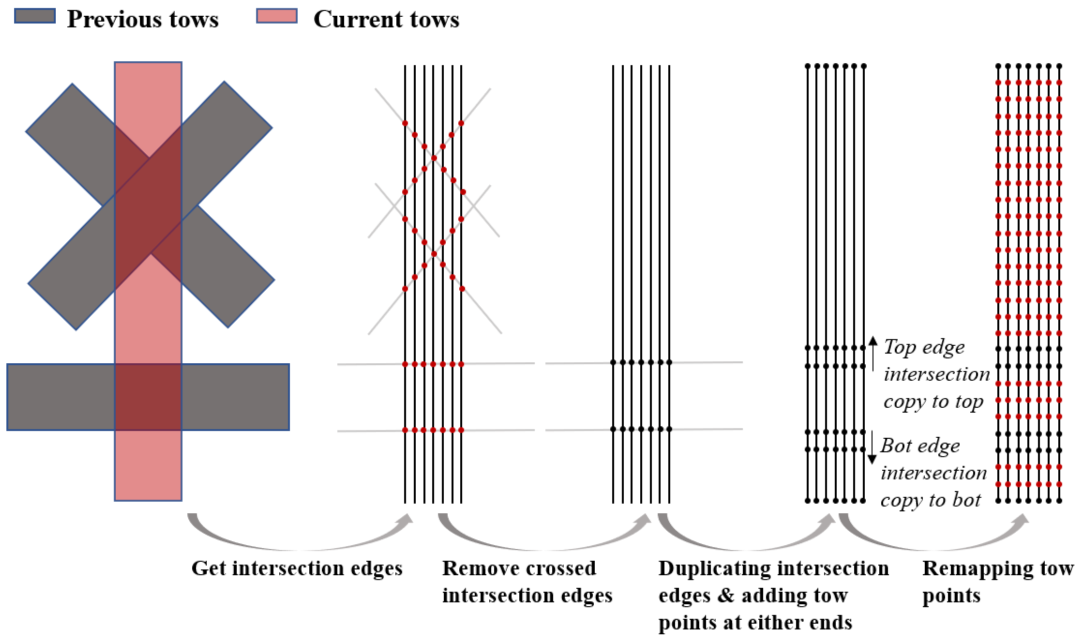

Figure 4.9. The procedures of tow points remapping

Another special case in the simple tow-tow intersection is if the intersection angle of the tows is very shallow, such as 5 degrees. Although intersection edges can be easily computed in this case, the remapped tow points based on these edges can generate a very distorted mesh. A minimum angle criterion is set before the tow points remapping procedure. The criterion states that if the intersection angle between the intersection edge and current tow is less than the minimum angle, the intersection edge is ignored, and this case is treated the same as the complex tow-tow intersection category. The minimum angle criterion can be defined by the user.

4.3.6 Z-offset algorithm (Step 10)

After all, simple tow intersections have been identified, and in-plane tow point remapping has occurred, a general algorithm is used to adjust the z-offset of the tows to capture the overlaps. For each tow point, a ray-tracing algorithm (Section 4.3.3) is used to compute the z-offset of the tows to be overlapped at that location. For the special case of simply overlapping tows, the remapped tow points conform to the underlying tow geometry, and a simple z-offset of one tow thickness can be applied to each tow point in the overlap region, along the normal direction of corresponding intersected triangles. The prismatic resin-rich regions at the edges of the overlap are well captured in this case; the tow points are preconfigured to conform to the geometry of both intersecting tows. The outcome of the simple z-offset manipulation is presented in Figure 4.10.

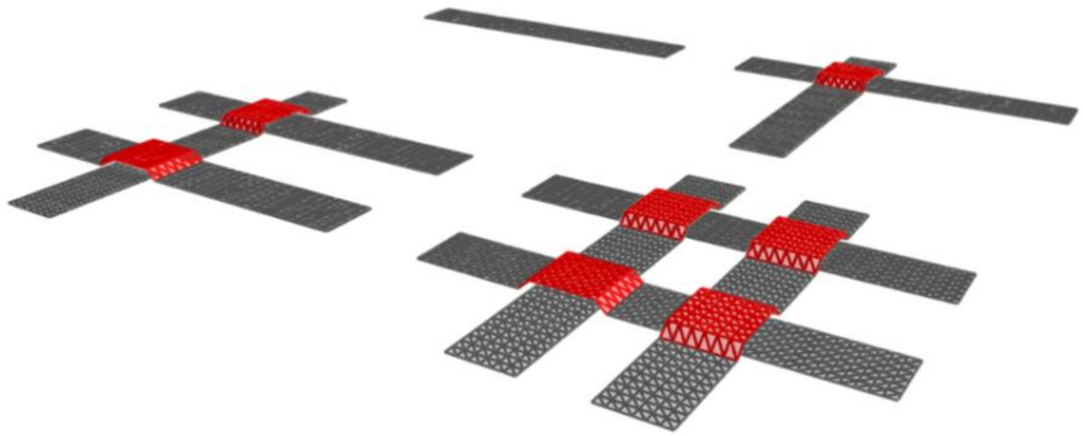

Figure 4.10. The outcome of z-offset manipulation for simple tow-tow intersection case

For complex tow drops, the straightforward z-offset algorithm can lead to tow penetrations, as shown in Figure 4.11b at the expense of larger and wider gaps. This is easily corrected, at the expense of wider tow-drops, by raising the height of every point to the z-position of its highest neighbour. This is named neighbour rule which is used to check the z-positions of each tow point after offsetting half tow thickness from the corresponding intersections. If the adjacent point (top, bottom, left or right) has a higher z-position, then raise the current point to the same height, as shown in Figure 4.11c. This can break the ideal triangular tow drop (Figure 4.11a) for the regular and well-intersected case so a small correction is added to each point lying directly above a tow edge to preserve the computed tow drop. A complex tow-tow intersection example using the z-offset rule is presented in Figure 4.12. In this case, there are three height levels including one, two, and three tow thickness, represented by different colours. The outcome of the z-offset manipulation (including the neighbour rule) for this complex tow drop and overlap is presented in Figure 4.13.

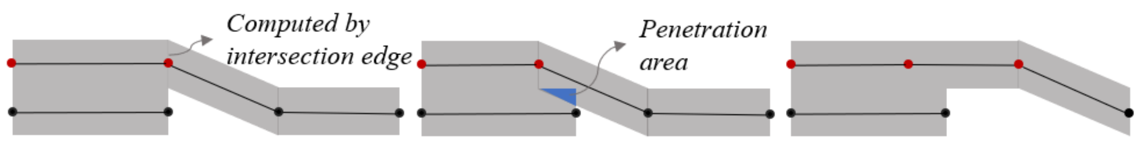

(a) (b) (c)

Figure 4.11. (a) Ideal triangular tow drop, (b) Offset causing physical penetration, (c) Penetration removed at the expense of larger and wider gaps

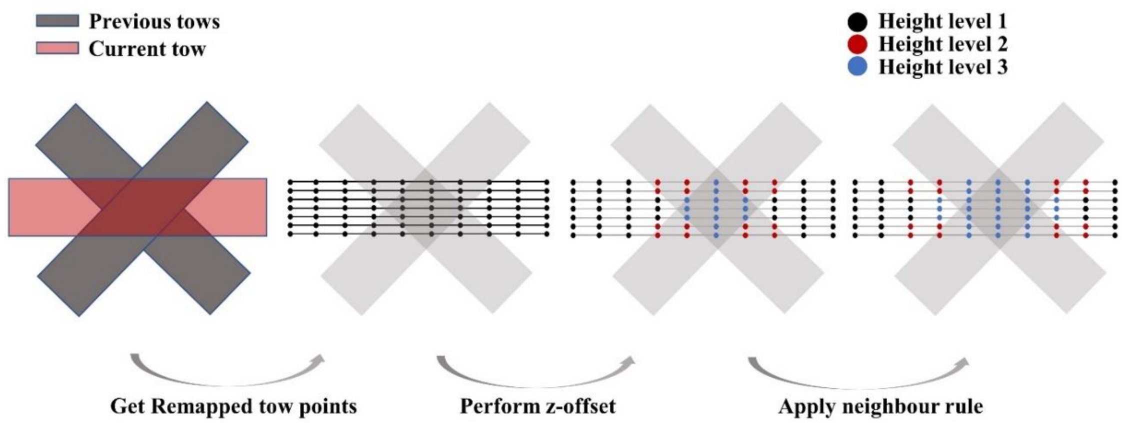

Figure 4.12. Application of z-offset rule in complex tow-tow intersection case

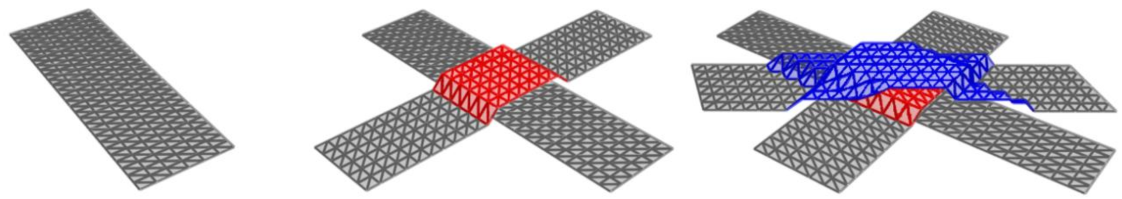

Figure 4.13. The outcome of z-offset manipulation for complex tow-tow intersection case

As the defects have a significant knockdown effect on the mechanical properties as shown in various studies [4, 5, 45, 47], precise defects representation is critical in predicting the local and global material behaviours. However, the 3D shape of the resin-rich pocket is generally irregular and hard to define a priori, such as for the case with multiple tows intersections as mentioned in Section 4.3.5. This issue is greatly simplified with a wider gap representation, leading to a conservative simulation result. The gaps can be minimized by geometry and mesh refinement approaches, such as refinement of the tow point grid. A more targeted solution, not yet implemented, maybe the implementation of a quadtree mesh refinement in the region of overlapping tows [120].

One final special consideration must be made for revolute mandrels (common to all filament wound and many AFP structures). Ray tracing algorithms for tow point intersections can detect spurious intersections with tows on the opposite side of the revolute tool. This can easily be negated by including a maximum distance threshold in the intersection algorithm.

4.3.7 NURBS interpolation

By this step in the algorithm, each tow is defined by a triangular surface mesh over a distorted but regularly connected, grid of points. The points and mesh lie at the midplane of their respective tows and the laminate is nested such that no two tows intersect, i.e. in the surface normal direction, tows are at least one tow thickness apart. At this stage, the surface mesh can be directly exported to a FE package as a triangular mesh or quadrilateral mesh (although the quad elements may be slightly warped). In this case, the tow geometry can be regarded as a linear interpolated surface.

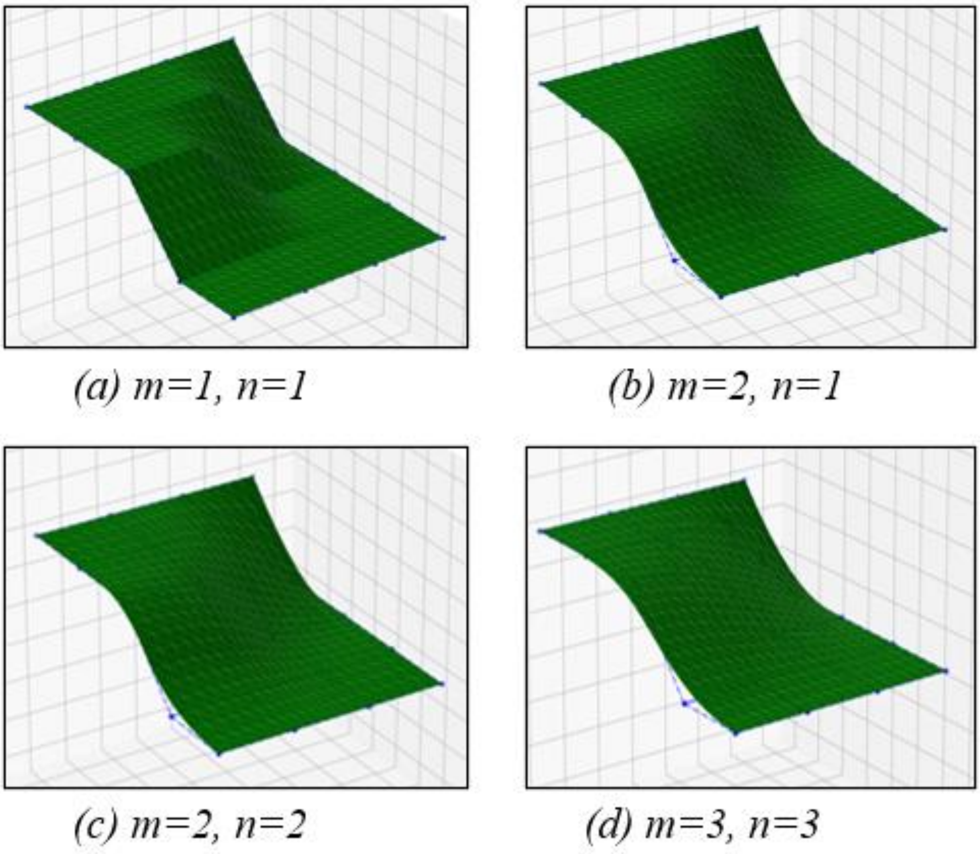

Figure 4.14. Different order of surface interpolations, where m and n refers to x- and y-axis interpolation order, respectively

To obtain the tow geometry with greater fidelity, a higher-order surface can be used such as Bezier or NURBS (Non-uniform rational B-spline). The grid of points is used as control points to determine the shape of the NURBS surface. Figure 4.14 illustrates the difference between linear and high-order surface interpolations, where m and n refer to the interpolation orders along the X and Y axes respectively. It can be noted that instead of a zigzag shape, the high-order surface has more precise approximations of tow geometry. This step is achieved with a pure python library "geomdl". Another example using Bezier surface interpolation is provided in Section 4.3.9.

4.3.8 Mesh trimming

For most AFP laminates, the FE mesh generated by Section 4.3.7 cannot be directly used due to the zigzag boundaries (refer to Section 4.4.1) or some specific requirements, such as a cutout. For FE analysis, the TWM needs to be trimmed as required. A plane and hole cut is used in this section to demonstrate the trimming procedure of TWM.

The planar cutting is achieved through a submodule in the trimesh library named "intersections". This module can detect the intersections between the cutting plane and the FE mesh, and automatically generate new mesh based on these intersections. To clearly illustrate this procedure, a 90° and −45° ply cut is presented in Figure 4.15. Four plane cuts were performed in sequence to obtain perfect straight edges, which allows the specific boundary conditions to be applied in FE analysis.

The hole cut, however, requires a mesh boolean process. This can be done in the FE package or 3D computer graphics software, such as Blender or OpenSCAD, which is used for backends mesh boolean computation. The mesh file of a cylinder was used as a hole cutter to trim the geometries. The open-hole geometry of 90^{o} and -45^{o} are used for demonstration purpose as shown in Figure 4.16. It can be noted the mesh near the cutting boundary can be very distorted. This issue can be tackled by refining the boundaries or combining the distorted elements into adjacent elements such as the in-built function in Abaqus, "collapse edge (tri/quad)". The main advantage of the mesh trimming approach is to preserve the structured tow mesh within the part (at the expense of distorted mesh at the boundaries).

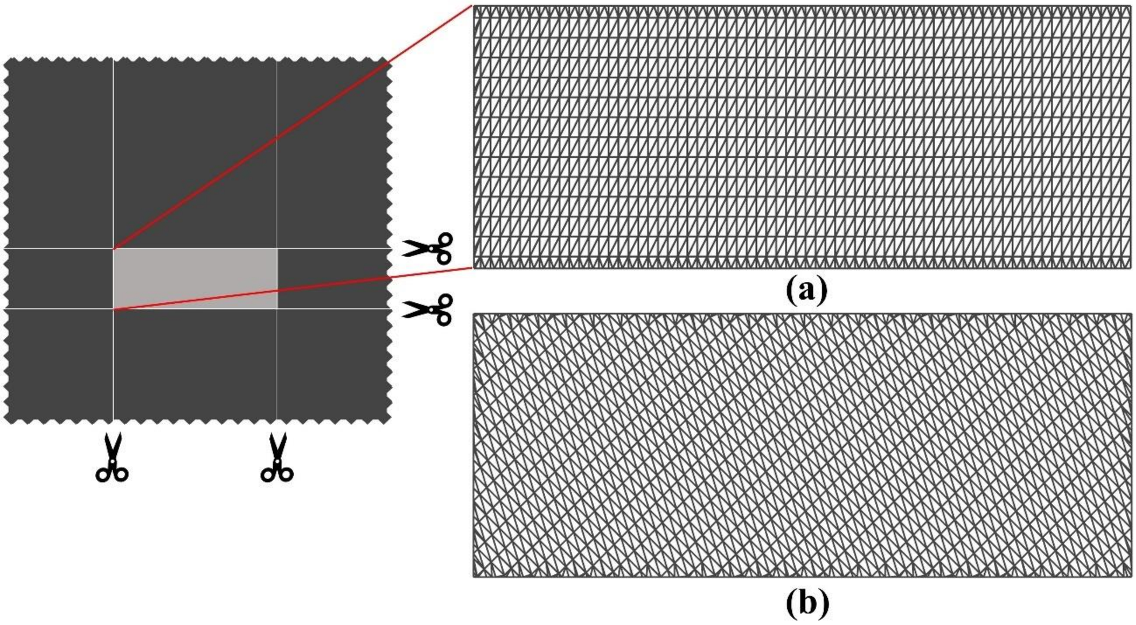

Figure 4.15. The illustration of the plane cut of FE mesh (a)$90°$*, (b)* $-45°$

An alternative to FE mesh trimming way is to cut the geometry prior to using an unstructured meshing algorithm on the irregular trimmed tow shapes. This approach better preserves mesh quality near the boundaries but can create poor mesh in the interior of tows. Optimising and balancing these two approaches is still an ongoing area of investigation.

4.3.9 Final tow geometry and finite element mesh

In this step, the tow geometry and finite element mesh can be exported to a FE package directly as a compatible file format (.stl). Generally, quad elements are recommended over triangles as far fewer are required to achieve the same converged result. A major benefit of the TWM is the generation of a structured aligned, quadrilateral mesh pattern as used in Falcó et al's work [121, 122]. It is also worth mentioning that a structured quad mesh can significantly improve the numerical accuracy by reducing the effect of mesh dependency and alleviating the pre-processing efforts defining local material orientations, as the fibre axis can be simply defined as parallel to specific element edges. Hence, the quad mesh has been selected based on the given benefits instead of the pristine triangular elements.

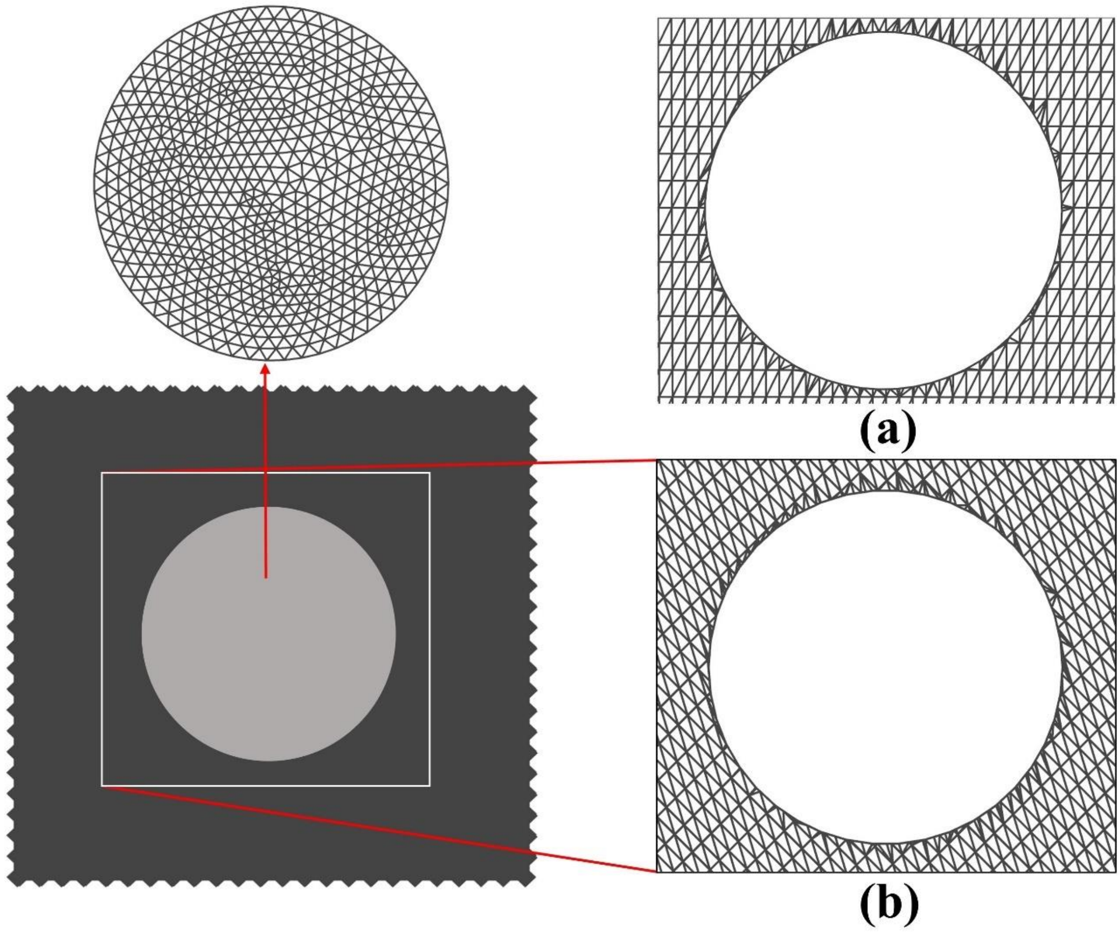

Figure 4.16. The illustration of a hole cut of FE mesh (a) 90^o, (b) -45^o

Several different methods can be used to generate the quad tow mesh, as indicated in Figure 4.17. On the one side, the tow geometry can be exported as a faceted surface geometry file (i.e. STL) into the FE package. The faceted surface can then be converted to quad elements by the built-in Mesher with a specified element size. Alternatively, an intermediate procedure can be performed to convert the triangular mesh to quad mesh with a 3rd party software such as Salome. A simple case study consisting of several intersecting tows is carried out to demonstrate the mesh conversion process, as shown in Figure 4.18. When the tow numbers reach up to hundreds or thousands, Salome may crash due to the huge amount of data which needs to be processed at once. As Salome is also a python-based user interface, an automatic mesh conversion process can be done before the final export to the FE package as an I-DEAS file (.unv) which is supported by Marc Mentat. Other file formats may also be used such as .dat.

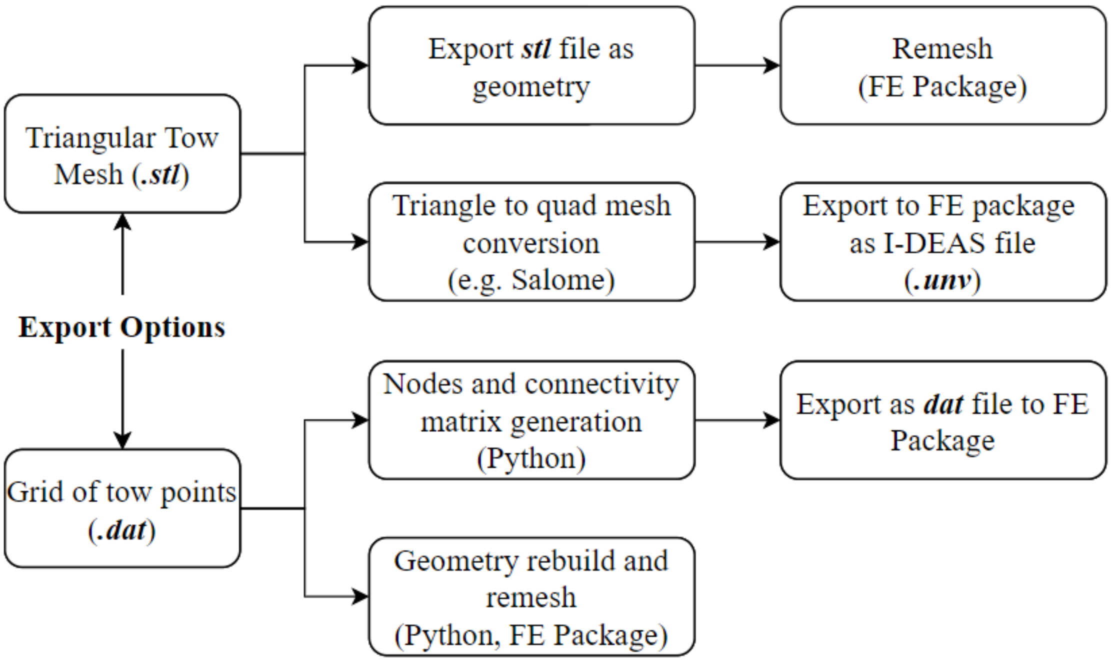

Figure 4.17. Different methods of final tow geometry and mesh generation

Another way is to use the grid of tow points, which can be translated into an FE package through a scripting interface. These points can be equally regarded as nodes, in which the mesh can be generated based on a predefined nodal connectivity matrix. In this case, however, the mesh size is fixed which might not satisfy some specific conditions such as a mesh sensitivity test. To address this, the curves or surfaces can be defined based on the grid of points prior to the generation of the mesh. Then a re-meshing procedure can be performed with the in-built Mesher of the FE package. Exporting geometry (as opposed to directly exporting the mesh) has the advantage of utilising the powerful internal meshing algorithms available in commercial FE codes.

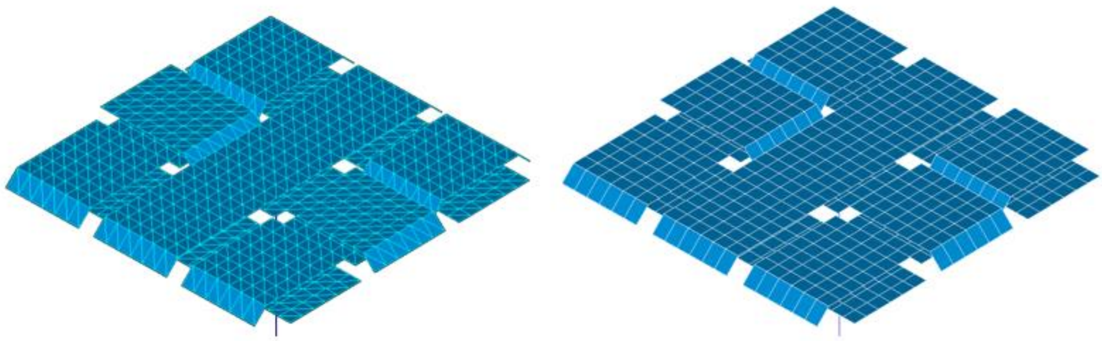

Figure 4.18. Mesh conversion from triangle to quad in Salome

In this work, the tow points were directly converted to geometry in MSC Marc Mentat using the available PyMentat module. Surface interpolation and meshing were conducted automatically within the Mentat GUI using PyMentat commands. Shell or solid mesh of the tow domain can be created depending on the desired modelling strategy. An example of the solid element and shell element representation is presented in Figure 4.19, which uses the same geometric information as Figure 4.13. In this case, a high order surface definition near the tow drop area, Bezier, is generated by regarding the tow points as a set of control points to smooth out the sharp edges due to the tow drop. The flat areas are modelled with linear surfaces. The ultimate mesh is generated by the surface to mesh convert function. For the solid element, it can be noted that slight penetration occurs due to the high order interpolation functions. The penetration can be removed before applying any mechanical loading in the FE package without introducing extra initial stress, such as the function "adjust to remove overclosure" in Abaqus [123]. Importantly, if solid elements are desired, it is relatively trivial to translate and extrude the surface definition along the tow normal vector to create a solid mesh.

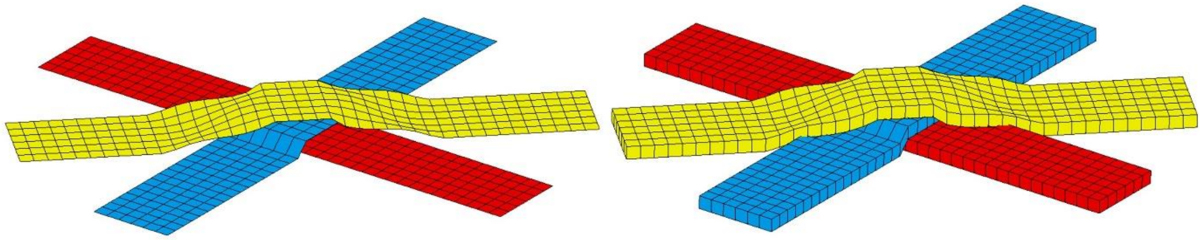

(a) (b)

Figure 4.19. Representation of the gaps, overlaps, and tow drops using (a) shell element, (b) solid element (discrete tows are represented as different colours)

FE pre-processing and modelling of the TWM geometry is the subject of future work and beyond the scope of this thesis. Nonetheless, several powerful FE techniques are available to make use of the geometry, depending on the desired simulation results. Stacked-shell modelling, originally proposed by Johnson [124] is an ideal approach, as are closely related methods using stacked solid or solid-shell elements [125, 126]. These approaches have already been used successfully to model gap networks in AFP laminates [60] and can intrinsically capture delamination growth. Embedded element and semi-conformal embedded element approaches can also be used to embed the discrete tow elements in a distributed matrix domain [127, 128].

4.4 Case studies

This section primarily aims to demonstrate the functionality of the TWM with several case studies ranging from laminate level to part level. The intrinsic representation of laminate defects including gaps, overlaps, and tow waviness is demonstrated within these studies. Both shell and solid elements can be used in this section. While considering the computational effort, the tows are modelled as shell element and a virtual thickness can be applied by the Mentat GUI for visualisation purposes. It should be noted that solid element can also be generated easily by expanding the shell element in the surface normal direction.

4.4.1 Case 1: Quasi-isotropic laminate

The first case study involves a quasi-isotropic laminate of $[0/90/45/-45]_s$ which highlights the difference between ply-level and tow-level geometric model for standard laminates. The lower half of the laminate is shown in Figure 4.20, using different colours for each tow. This is a trivial case for AFP manufacture, as the laminate has zero net curvature and tows are straight and perfectly nested.

It should be noted that the TWM algorithm produces a zig-zag edge wherever a tow crosses the laminate boundary obliquely. The laminate edges can be made conformal with additional preprocessing steps, but this is left for a future discussion.

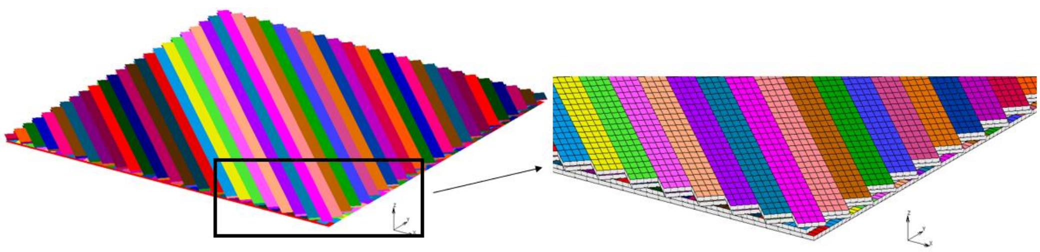

Figure 4.20. Tow-level FE model representation of a quasi-isotropic laminate

The TWM algorithm does offer some benefits for this problem, although the benefits must be weighed against the additional preprocessing and simulation cost. Individually modelling each tow, when coupled with cohesive contact interactions, allows discrete inter- and intra-ply cracking to be modelled efficiently and accurately without the need for complex fracture laws and re-meshing techniques. Cohesive contact has been successfully applied in various studies in modelling interlaminar failures [104, 105, 129]. The traditional cohesive zone model, however, has a strict requirement in terms of the element size near the crack front which must be smaller than 1/3-1/5 of the cohesive zone length to obtain an accurate representation of crack propagation [100-102]. A more efficient technique, such as improved integration methods [102] or augmented cohesive element method [103] which allows using comparable or relatively coarser mesh size needs to be integrated into the TWM to predict the failure events. It is worth mentioning that the developed algorithm can record the sets of tow-tow contact pairs which greatly ease the implementation difficulties for subsequent interlaminar failure modelling.

4.4.2 Case 2: AP-Ply laminate

The AP-Ply laminate is chosen as the second case study due to the interweaving architecture which generates a network of distributed defects in the laminate. The AP-Ply laminate offers many other benefits and is the focus of considerable studies such as [3, 34, 61].

AP-Ply laminates are manufactured by adjusting the tow placement order of a regular AFP laminate. AP-Ply skips certain tows and space is temporarily left. A similar strategy is used for the next ply which is oriented in another direction. The tows nest into the space left in the first pass which creates a wavy pattern. Then the gaps left in the first pass are filled by the following passes, as shown in Figure 4.21. A uniform thickness can be achieved through proper skip-and-fill manipulations. The resulting laminate can be designed with a fully interlocking structure, where a nominal layer of each orientation is “woven” into the layer above and below.

To numerically predict the mechanical performance of the AP-Ply, the TWM approach that able to capture the local geometric features is critical. In this case study, a layup configuration of $[0/90]_{13s}$ was manufactured and used for

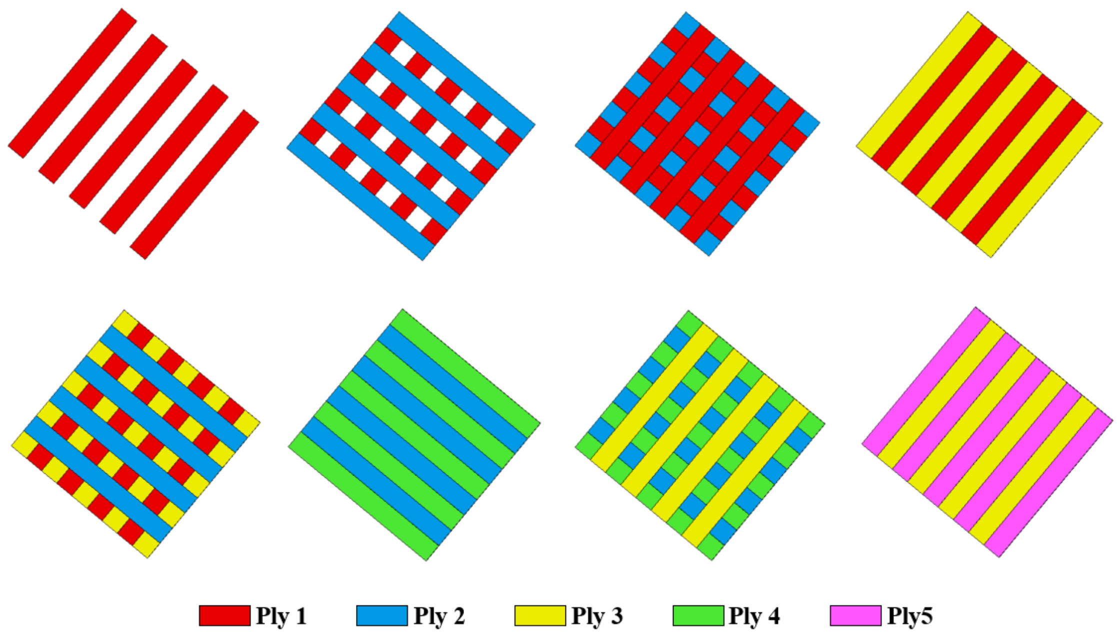

Figure 4.21. The layup procedures of AP-Ply laminate

demonstration purposes, as shown in Figure 4.22a. A small sample was cut through the CNC Router and the cross-section was scanned under an optical microscope. The corresponding tow waviness and resin-rich pocket resulted from the wavy pattern are shown in Figure 4.22c.

The as-cured tow thickness was obtained by averaging the total laminate thickness. The crimp angle was measured from the micrographs (~5^0). These parameters were applied to the TWM algorithm for the generation of the FE model, as indicated in Figure 4.23. The triangular resin-rich pockets and tow waviness with a user-defined crimp angle are explicitly captured.

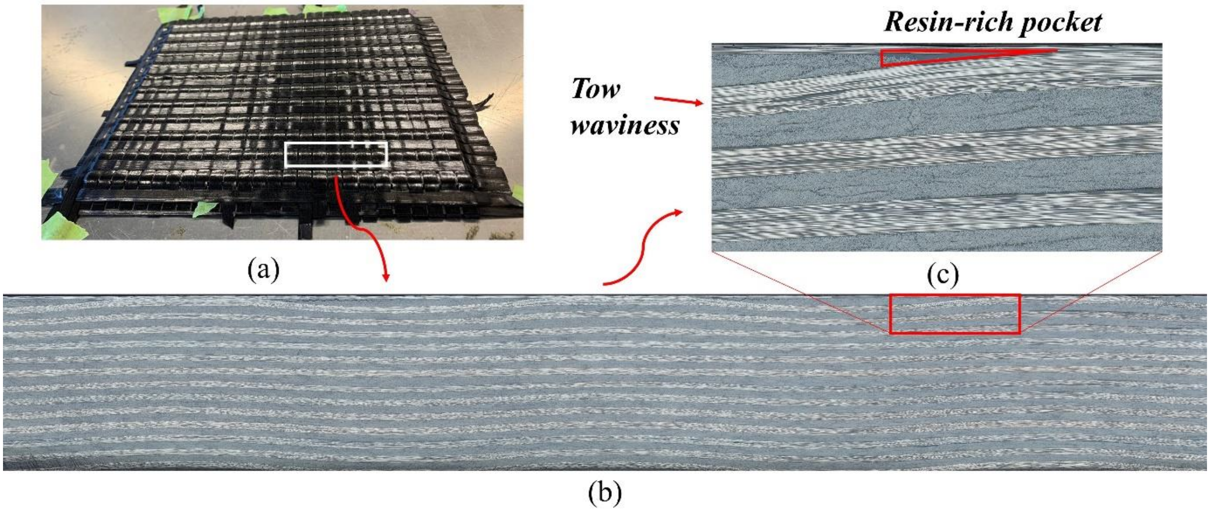

Figure 4.22. (a) Final configuration of the AP-Ply laminate, (b) Cross-section scan of the cut sample, (c) Magnified cross-sectional view of the cut sample

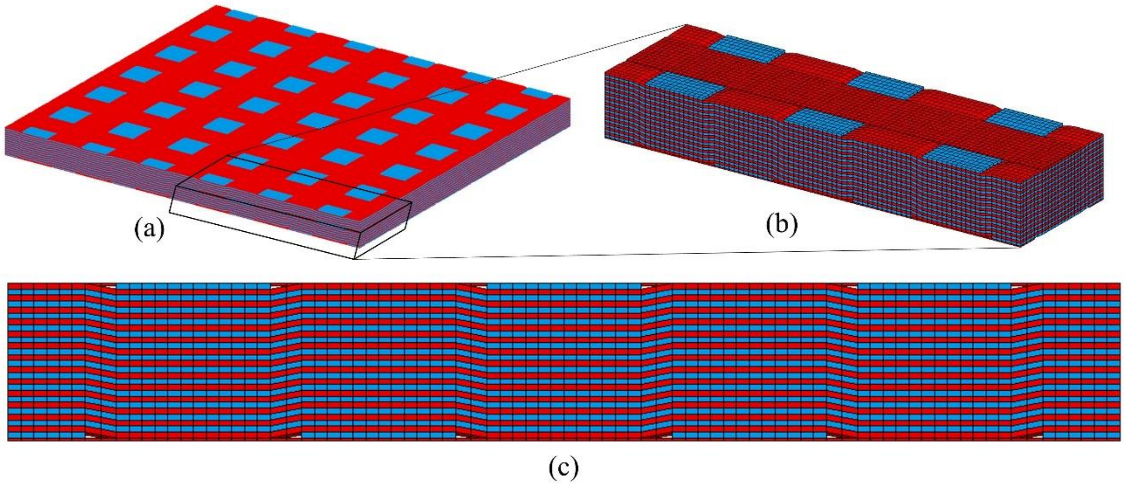

Figure 4.23. (a) The FE model of AP-Ply laminate (mesh not shown for clarification), (b) The FE model of magnified sample view cut from AP-Ply, (c) Cross-sectional view of the FE model

4.4.3 Case 3: Pressure vessel

The third case study demonstrates the application of TWM in a part level of AFP composites, which includes a layup of a filament-wound pressure vessel. A 45-

degree helical and a hoop wind layer were modelled using the TWM algorithm (Figure 4.24a, b) to capture the semi-woven nature of the vessel wall. Although the vessel is manufactured from a single continuous tape, the tow path has been pre-processed to segment the tape at each polar approach. The pre-processing step is facilitated to avoid computational limitations of placing one very long tow, improve the robustness of the z-offset and help with visualisation. The separate tows are reconnected at their adjoining ends before any FE modelling is conducted.

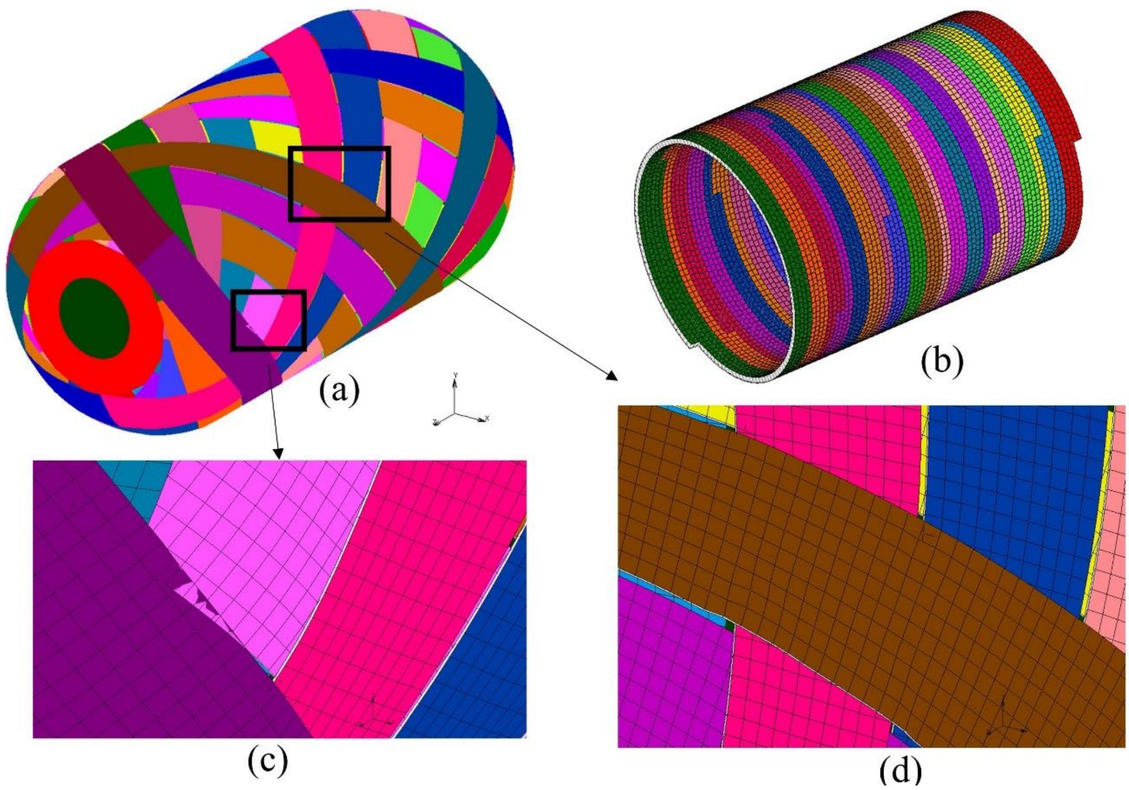

Figure 4.24. Tow-level FE model representation of a pressure vessel, (a) helix wind, (b) hoop wind, (c) indication of slight penetration issue, (d) magnified view of helix wind. Note: the artificial gaps introduced in the helix wind are only used for clarification purpose and the actual tow width needs to be adjusted based on the as-cured width.

Several slight penetrations are unavoidable due to the limitations of intersection detection using inner tow points, as shown in Figure 4.24c. The penetration can be mitigated by reducing the detection tolerance but comes at a computational cost. As the contact area between the penetrated tows is very small, it can be accounted for during the contact-detection phase of any subsequent simulation. Alternatively in most FE codes such as Abaqus, the penetration issue can be tackled by invoking the option "adjust to remove overclosure" before applying any mechanical loads.

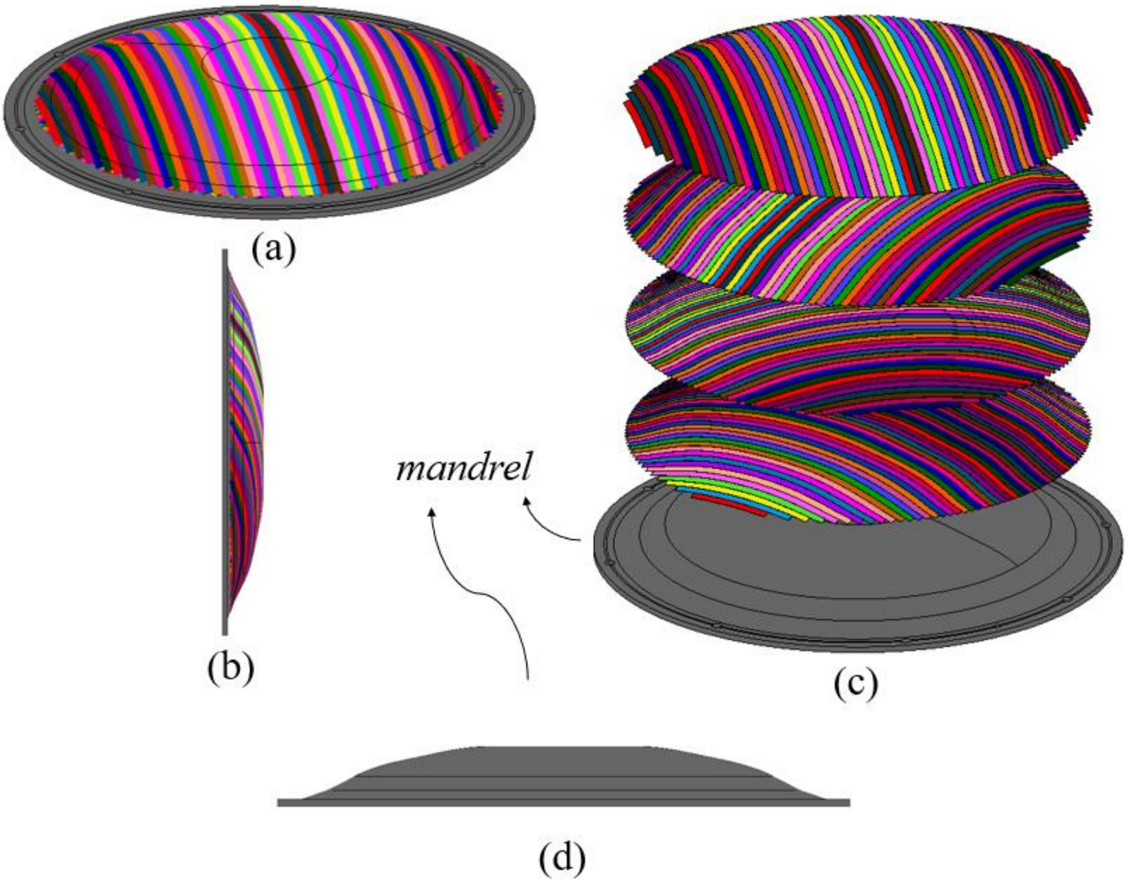

Figure 4.25. Tow-level FE model representation of a wheel disk: (a)assembled view, (b) left view, (c) exploded view, (d) front view of the mandrel

4.4.4 Case 4: Wheel disk

The fourth case study is another part level application of the TWM, which involves a wheel disk. A layup of four layers with [0/45/90/-45] was modelled, as presented in Figure 4.26. This application is like Case 1 but with a more complex tool surface. To fully cover the entire tool surface without introducing large gaps and overlaps, the tows were steered with a small angle, resulting in a variation of fibre angle along the tow path. The TWM offers an opportunity for users to define the material orientations locally along the trajectories of each tow. The fibre steering feature of AFP can also be represented precisely with the TWM method.

4.5 Sensitivity analysis of the TWM

To demonstrate the efficiency of the TWM, a sensitivity test was performed in terms of the effect of the tow number, element size and geometric complexity on the computational cost. In this study, two different geometries were studied including a flat panel with dimension 200x200 mm and a pressure vessel with dimension 500x250mm (length x diameter). To include the double curvature of the pressure vessel, the extra step indicated in Section 4.3.3 needed to be performed to update the transverse tow points. Hence, it is expected that the flat panel case would be more computationally efficient.

For the flat panel, varying tow numbers from 250 to 1000 with element size 1~4 mm were studied. For the pressure vessel, the tow numbers from 20 to 80 were investigated as the tow length is much longer than that in the flat panel. The results for different cases are presented in Figure 4.26. For each case, a similar trend is observed, where the computational time is significantly increased with reducing element size. While only trivial differences are observed between different tow numbers. It should be noted that when the tow number doubled, the element number is essentially doubled as well. Hence to isolate the effect of the tow count, the total element needs to be the same, such as the 500 tows with an element size of 1mm was compared with the 1000 tows with an element size of 2mm.

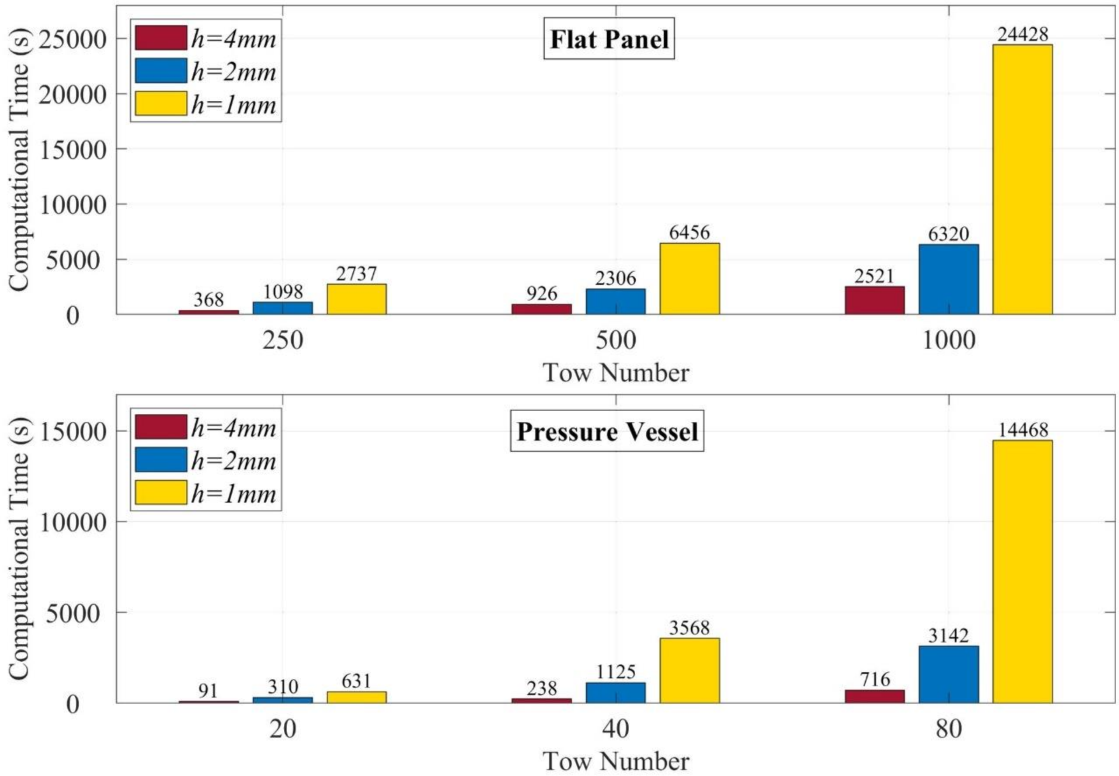

Figure 4.26. The result of the sensitivity analysis of the TWM for flat panel and pressure vessel. Note: the computational time here only includes the time for mesh generation and does not include any FE analysis.

The reason why the TWM is element size (number) sensitive is due to the checks of tow-tow intersections. When the element number is getting larger, the file of preceding tows is getting bigger. As the present tow needs to be checked if it is intersected with the previous large mesh assembly, the loading speed requires much more computational effort. It should be noted that the total element number for the case with 1000 tows in the flat panel is around 1.2e06, which costs around 6.7hrs. At present, this is the worst scenario as no optimisation technique is applied. Several potential ways can be implemented in the future to improve the computational efficiency when the element number is getting larger. For instance, it can be designed such that the current tow only checks intersections with the last ten layers as it is nearly impossible for ply 100 to intersect with ply 1 in reality.

4.6 Summary

The automatic geometric modelling tool (TWM) is illustrated in detail in this chapter. The functionalities of this tool to capture the 3D architectures of AFP composites are demonstrated through a range of case studies. The algorithm presented is the basis for a general geometric modelling algorithm for tow-by-tow manufactured composite laminates. The geometry can be efficiently created based on the manufacturing data and the defects induced by the tow path can be captured to a useful degree of precision. The pre-process of FE simulation by creating geometry and mesh is also shown within this study.

Several potential approaches can be considered for modelling the defects included in the TWM. For the regular and well-intersected cases, in which the shape of the resin-rich area is easy to define, it is recommended to model the resin as bulk material. While for other complex cases, where the 3D shape of the resin-rich area can be irregular and extremely hard to define, such as for the case with multiple tows intersections as mentioned in Section 4.3.5, the resin can be modelled in two potential ways. The first way is to model the resin with cohesive contact interactions between adjacent tows surfaces by increasing the contact tolerance in this area. The same or different cohesive parameters with the interlaminar fracture can be defined depends on the resin properties. The second way is to add an extra strain energy release rate to the area close to the boundaries of the resin pocket to model the strain energies absorbed by the resin. This phenomenon is demonstrated in Zheng's work [62], where the strain energy release rate tends to increase/decrease dramatically when the crack is crossing stiffer/softer materials. The downstream use of the TWM generated geometry for Finite Element Modelling will be demonstrated in the following chapters, include robust cohesive contact models that enable the tows to be modelled as a continuous laminate.

Several limitations of this algorithm, however, need to be pointed out that will form the basis for future work. The algorithm occasionally produces small tow-tow intersections (or penetrations). These intersections can always be resolved with mesh and geometry refinement, at the expense of computation cost. The user may decide on an acceptable level of geometric fidelity for the problem at hand.

Besides, there will be no sharp edges near the area of the defect in reality. To tackle this issue, a higher-order surface definition, Bezier or NURBS, is used to smooth out the sharp edges (from C0 to C1 continuity). The point cloud near the area of the defect (tow drop) is regarded as a set of control points, which are used to generate the Bezier / NURBS surface. The Bezier / NURBS surface can be converted to FE mesh in the FE package later. For the flat regions, a linear surface definition can be applied directly. A typical example comparing the geometry before and after smoothing is shown in Figure 4.13 and Figure 4.19. Although there will be slight penetrations induced by the higher-order interpolation, it can be removed entirely in the FE package without introducing extra initial stress before applying any mechanical loading, such as the function "adjust to remove overclosure" in Abaqus.

One major benefit of the TWM is the generation of a structured or material aligned, quadrilateral mesh pattern as used by Falcó et al [121]. However, the triangular mesh is inevitable to be used near the trimming boundaries and the areas closed to the defects to avoid element warping or distortion. A limitation of the TWM algorithm is that it is entirely geometrical and kinematic. The full kinetics of the consolidation and cure process can lead to tow bridging, cross-section distortions, as-cured thickness variation, etc to be included in the cured part. The TWM algorithm does not attempt to model the kinetics of consolidation and cure, so will always incur a small accuracy penalty in regions of complex mesostructure. To predict the 3D tow deformations, a robust consolidation model that can accurately predict the fibre/resin flow is required, which, however, is still an active area of research. Other induced defects such as tow wrinkling, tow misalignment or tow twisting, etc., although challenging, can still be potentially included in the TWM with the assistance of the inline monitoring and feedback system and proper geometric descriptions.

Chapter 5 Cohesive Network Approach

5.1 Introduction

Strength and damage prediction for fibre composite laminates and structures is a continued area of research interest. The fibre customisation capability provided by AFP, creates new design and optimisation possibilities while also generating process-induced defects. These defects can potentially induce premature failure and reduce the strength of the structure, which has been demonstrated in many studies [5, 44]. Chapter 4 has presented a new numerical modelling method for AFP composites at a length scale of tow, which results in many non-conformal meshing interfaces between discrete tows.

The smeared crack models are computational expensive and cannot be used to represent the failure kinematics of the interactions between different fracture modes. The discrete crack models, on the other hand, shows the promise to capture the different failure interactions. To deal with the failure modelling in the TWM, the conventional methods are either too computationally expensive or unable to be used in the case of non-conformal meshing interfaces. Hence, this chapter aims to present a novel and more computationally efficient cohesive network approach, which can be used to predict the failure mechanisms of AFP composites at the length scale of tow.

Most of the results presented in this chapter are included in the following publication:

Li X, Brown SA, Joosten M, Pearce GM. *A segment-to-segment cohesive contact network approach for mesoscale composites failure modelling*. Composite Structures. 2022:115205.

5.1.1 Cohesive network approach

The cohesive network approach originates from the "brick and mortar" concept [130] (Figure 5.1), where the reinforcement is regarded as "brick" and the contact interfaces between those bricks are regarded as "mortar". Specifically, in AFP composites, each tow can be regarded as a brick and the tow-by-tow interfaces can be considered as mortar. The bricks will govern the global structural compliance while the mortar will control the local failure initiation and evolution. In previous studies [96-98], the mortar was commonly modelled as cohesive elements with a traction-separation constitutive relationship, which was implemented in the element integration points. A significant challenge, however, arises due to the limitation of cohesive elements which require conformal meshing interfaces. This refers to the in-plane mesh size which must be equally defined for all layers. This can be extremely challenging or impossible to achieve in the TWM as each tow is meshed independently. Hence, the cohesive contact interaction is used for modelling the mortar instead.

The cohesive network approach is essentially to allocate the cohesive interaction along with the potential failure paths, forming an interconnected network to capture the intra- and inter-laminar failures. This method avoids using complex fracture criteria as in CDM, and removes the tedious geometric partitioning process for allocating interface elements especially for large and complex composite structures, which substantially reduces the pre-processing effort of modelling.

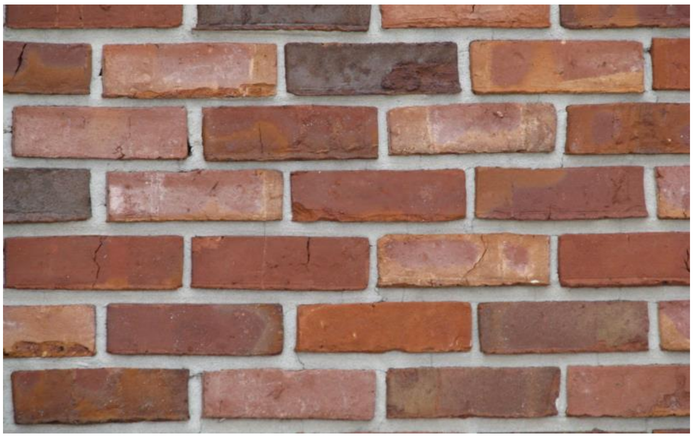

Figure 5.1. Brick and Mortar Model [130]

Three major failure modes of AFP composites at mesoscale can be considered including matrix cracking, delamination, and fibre breakage. These different failure modes can be predicted explicitly with the input of various cohesive parameters, which can be obtained from standard or non-standard experimental characterisation. To further illustrate the cohesive network approach, a laminate consists of [90/0/-45/45] schematic diagram is used, as presented in Figure 5.2, where the discrete tows and cohesive contact interactions are plotted in different colours for visualisation purposes. The intralaminar fibre and matrix failure, which were assumed to be orthogonal and parallel to the fibre direction, respectively. In Figure 5.2, the fibre failure is represented as yellow, and the matrix failure is indicated as blue. The interlaminar failure, which was assumed to occur between adjacent plies, is plotted in green.

A constraint of this method is that the in-plane crack plane is always assumed to be either parallel or perpendicular to the fibre direction, corresponding to matrix and fibre failure, respectively. In reality, this assumption only holds when the crack occurs due to tension. For matrix and fibre compression, it is found that the failure is due to shear which leads to a 53° inclined fracture plane and a kink band separately [131]. For a general quasi-isotropic laminate or other laminate structures where the adjacent layers have different fibre orientations, this assumption seems reasonable when the ply thickness is small enough compared to the global thickness [97].

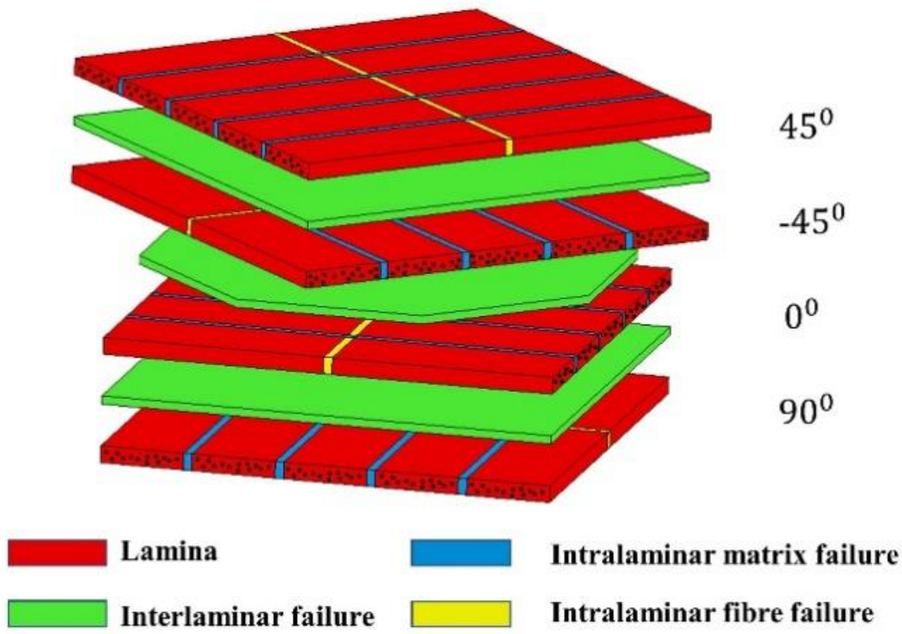

Figure 5.2. Schematic diagram of the SSCC Model

5.1.2 A new cohesive contact interaction

The traditional cohesive contact interaction is developed based on a node-to-segment (N2S) contact algorithm and has been successfully demonstrated in many studies [104, 105]. However, the major issue associated with N2S contact is the low numerical efficiency due to the master-slave concept. The non-interpenetration contact constraints are only enforced at the slave nodes, which means the master nodes are allowed to penetrate the slave surface. Hence, a strict rule is that the slave surface needs to have a much finer mesh than the master surface, and an inappropriate definition can result in significant penetrations.

Another issue that can occur in the slave node is that it can have serious locking problems due to over constraints when it has multiple contact interactions, and hence can provide inaccurate simulation results [106].

Hence, in this chapter, a more advanced contact formulation, segment-to-segment (S2S), is used to improve the computational efficiency and mitigate the effect brought about by the selection of master and slave bodies. The S2S contact formulation applies contact constraints along the entire boundary in a weak integral sense instead of at a particular node as for N2S contact, thus greatly improving the numerical convergence and weakening the dependence on the master-slave definition [132].

The key differences of S2S contact interaction between Marc-Mentat and other commercial FE package (such as Abaqus) is the way how contact points (called "proximity points" in ABAQUS) are generated. In many FE packages, the contact points are generated based on the nodal position or Gauss points of the element, and the number of contact points are generally roughly equal to the number of nodes. While in Marc-Mentat, the contact points are generated with a different mapping algorithm, where the number are much higher than many available FE packages. Another major difference is the contact interaction in Marc-Mentat is enforced at these contact points in a weak integral sense, hence significantly improves the convergence challenges in implicit finite element framework and also allows greater mesh size tolerance. The user-developed subroutine allows the kinematics of the contact behaviour of each contact point to be controlled precisely. The damage status of each contact point can also be tracked and visualized via the subroutine.

In this study, the new cohesive interaction is established by integrating the cohesive traction-separation law into the S2S contact formulation by modifying the default kinematics of contact via a user-developed subroutine (called ugluestif_sts) in MSC Marc-Mentat.

5.1.3 Chapter scope

For a better understanding of the structure presented in this chapter, the scope is summarized into several points below:

- In Section 5.2, the theories and mechanisms behind the new cohesive interaction including the S2S contact theory, the cohesive traction-separation constitutive relationship and the fracture criteria of different failure modes will be presented. A modified cohesive law, which is integrated into the new cohesive interaction will then be proposed to improve the numerical convergence challenges in implicit finite element (FE) framework.
- Section 5.3 aims to validate the new cohesive interaction in predicting interface failures against the traditional cohesive element method. Three commonly used delamination geometries will be compared including double cantilever beam, end notched flexure, and fixed ratio mixed mode.
- In Section 5.4, the computational efficiency of this new cohesive interaction will be firstly demonstrated. The numerical results with various element sizes will be compared to the outcomes of the cohesive element approach. A sensitivity study is also performed regarding the non-physical numerical parameters including the load increment size, the contact stiffness and mesh conformality to further explore the limits of this approach.
- Section 5.5 will validate the cohesive network method with the implementation of the new cohesive interaction in the prediction of both intra- and inter-laminar failures considering a 2D application.

- Section 5.6 will further demonstrate the feasibility of the cohesive network method in predicting both intra- and inter-laminar failures with a more complex 3D application.

5.2 Segment-to-segment cohesive contact (SSCC) theory

5.2.1 Segment to segment contact

The Augmented Lagrange method is used in MSC Marc by default to enforce the boundary constraints for the S2S contact algorithm. Multiple contact points are generated to ensure a robust contact interaction and smooth load transfer. The difference between N2S and S2S is presented in Figure 5.3.

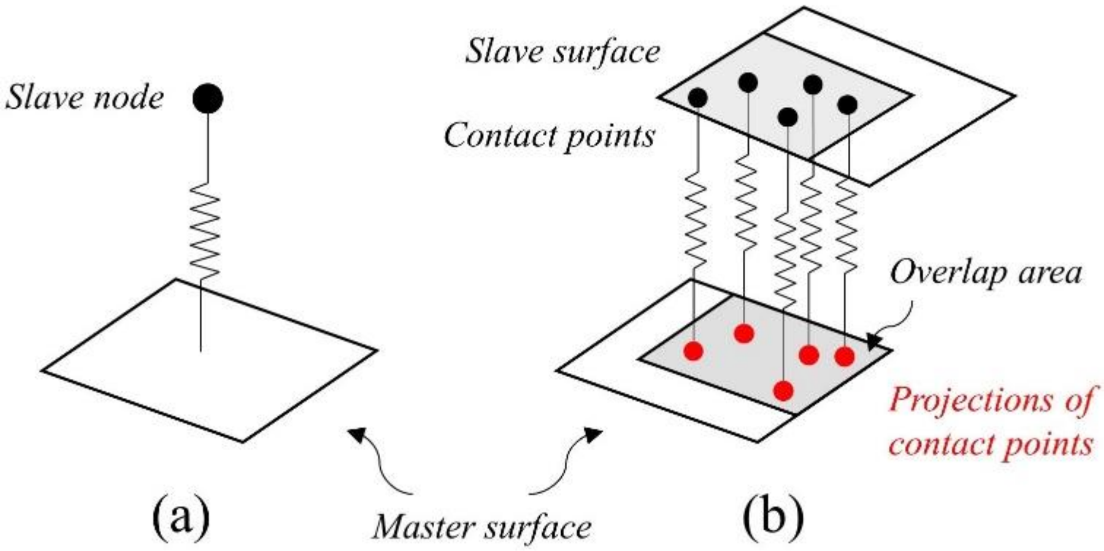

Figure 5.3. The schematic diagrams of contact principles (a) Node-to-segment, (b) Segment-to-segment. Note: five contact points are shown here only for visualisation purposes. The number and distribution of the contact points depend on the geometry of the contact patches.

As the contact constraints are enforced at these contact points instead of the nodes at the slave body, the effect of the slave-master definition sequence is significantly alleviated. The contact is essentially a constraint minimisation problem, where the virtual work of a set of contact bodies can be expressed as

$$\delta G^{int}(\delta u, u) - \delta G^{ext}(\delta u, u) - \delta G^{c}(\delta u, u) = 0 \qquad \text{5-1}$$

Where G^{int}, G^{ext} and G^{c} refer to the work done by internal, external and contact forces respectively, u denotes the displacement field. The Lagrange multiplier λ is introduced to enforce the gap to be zero. Hence, the virtual work done by the contact can be expressed by

$$\delta G^{c}(\delta u, u) = \int_{\Gamma} \lambda_n \delta g_n d\Gamma + \int_{\Gamma} \lambda_t \delta g_t d\Gamma \qquad \text{5-2}$$

Where:

$$g_n = \left(u^{(1)} - u^{(2)}\right) \cdot n^1 \qquad \text{5-3}$$

$$g_t = \left(u^{(1)} - u^{(2)}\right) \cdot s^1 \qquad \text{5-4}$$

with g denotes the gap function, Γ represents the contact area, n and t represent the normal and tangential directions separately. It should be noted that positive and negative g_n represent gap and overlap respectively. The Lagrange multiplier is a function of the gap function, and it is determined in an iterative fashion using the Newton Raphson method, which is expressed as

$$\lambda^i = P^{i-1} + E^i g^i \qquad \text{5-5}$$

The augmentation P is used to minimize the overlaps when large penetration occurs. In this study, augmentation is not used which means the equation becomes a pure penalty method, and the Lagrange multiplier is a linear function of the gaps when the penalty factor E is constant. This formula is further modified by a bilinear cohesive law, where the penalty factor and Lagrange multiplier can be referred to as contact stiffness and contact stress, respectively. More details are presented in Section 5.2.2.

5.2.2 Constitutive relationship of the cohesive interaction

The cohesive behaviour of the cohesive contact model is achieved by degrading (and eventually failing) the penalty contact interactions shown in Figure 5.3. Hence the failure behaviour is controlled by three orthogonal stress states in the fracture plane. The constitutive relationship of the interface is described in Eq. 5-6

$$\begin{bmatrix} \lambda_n \\ \lambda_t \\ \lambda_s \end{bmatrix} = \begin{bmatrix} E_n & 0 & 0 \\ 0 & E_t & 0 \\ 0 & 0 & E_s \end{bmatrix} \begin{bmatrix} g_n \\ g_t \\ g_s \end{bmatrix} \tag{5-6}$$

Where the three orthogonal stresses (λ) represent the traction in the normal (n), 1st tangential (t) and 2nd tangential (s) directions, respectively. The interface failures can be categorised based on the different loading cases, including mode I (the opening mode) induced by normal loads, mode II caused by in-plane shear loads, and mode III triggered by out-of-plane shear loads. These failure modes are considered by introducing a universal damage parameter D in the contact interaction.

$$\lambda = Eg(1 - D) \tag{5-7}$$

The fracture energy is dissipated by softening the contact response with the damage variable which ranges between zero and unity. Zero means no damage has occurred, while unity represents a fully damaged state.

5.2.3 Failure modes and associate failure criteria

Many complex fracture criteria have been proposed over the last few decades and have shown great correlation with the specific experimental studies [131, 133, 134]. In this chapter, however, the major aim is to demonstrate the novel cohesive network framework instead of demonstrating the accuracy of any specific fracture criteria. Due to a strength-based criterion combined with a mixed-mode power-law being commonly used in the cohesive element method to model the interface failure initiation and evolution, the same criteria were also implemented into the cohesive network method for comparison.

(a) Failure initiation criteria

Quadratic stress-based failure initiation criteria were used, which are common for composite CZM implementations [89]. The criteria are expressed in Eq. 5-8, Eq. 5-9, Eq. 5-10, Eq. 5-11, Eq. 5-12 below.

- Fibre tension failure

$$\left(\frac{\lambda_n}{X_{ft}}\right)^2 = 1 \tag{5-8}$$

- Fibre compression failure

$$\left(\frac{\lambda_n}{X_{fc}}\right)^2 = 1 \tag{5-9}$$

- Matrix tension failure

$$\left(\frac{\lambda_n}{X_{mt}}\right)^2 + \left(\frac{\lambda_t^2 + \lambda_s^2}{{Y_{ms}}^2}\right) = 1 \tag{5-10}$$

- Matrix compression failure

$$\left(\frac{\lambda_n}{X_{mc}}\right)^2 + \left(\frac{\lambda_t^2 + \lambda_s^2}{{Y_{ms}}^2}\right) = 1 \tag{5-11}$$

- Delamination

$$\left(\frac{<\lambda_n>}{X_{it}}\right)^2 + \left(\frac{\lambda_t^2 + \lambda_s^2}{{Y_{is}}^2}\right)^2 = 1 \tag{5-12}$$

Where X_{ft}, X_{fc} are the tensile and compressive fibre strength, respectively; X_{mt}, X_{mc} are the tensile and compressive matrix strength, respectively; Y_{ms} is the matrix shear strength, X_{it} is the interlaminar tensile strength, and Y_{is} is the interlaminar shear strength. Although the interface failure due to tension loads is the major consideration, the compression failure can potentially be modelled by allowing slight interpenetrations between the contact interfaces when the corresponding failure criterion is met. As mentioned earlier, a critical assumption of this method is that the fracture plane was assumed to be normal or parallel to the fibre direction which, however, is invalid for local matrix/fibre compressive failure. Hence, the cohesive network approach can only give an approximate prediction of matrix and fibre compressive failures. For the laminate structures where the adjacent plies have different fibre orientations, such as quasi-isotropic laminate, the error resulting from this assumption was likely small.

(b) Failure evolution criteria

The interface failure due to tension loads are used for demonstration in this section. Once the damage initiates, the contact interaction is softened and the crack starts to propagate when the mixed-mode power-law criterion is met, as expressed in 5-13. It should be noted that for fibre failure, only mode I was considered in this chapter. The mixed-mode interaction fracture criterion for fibre failure can also be used which depends on specific applications.

$$\left(\frac{G_I}{G_{IC}}\right)^{\alpha} + \left(\frac{G_{II}}{G_{IIC}}\right)^{\alpha} = 1 \qquad \text{5-13}$$

Where $G_I = \int_0^{g_n} \lambda_n d g_n$ and $G_{II} = \int_0^{g_t} \lambda_t d g_t$ represent the real-time strain energy release rates in the normal and tangential directions; and G_{IC} and G_{IIC} indicate the critical strain energy release rates for the normal and shear modes respectively. The corresponding damage variable d is computed as in Eq. 5-14 which is a function of mixed-mode displacement u. The power α is an empirical parameter and is generally in the range between 1 and 2. The critical and ultimate mixed-mode displacement u_c and u_f are determined by Eq. 5-15 and Eq. 5-16.

$$d = \frac{u_f(u - u_c)}{u(u_f - u_c)} \qquad \text{5-14}$$

$$u_c = \begin{cases} g_n^c g_t^c \sqrt{\dfrac{1+v^2}{{g_t^c}^2 + v^2 {g_n^c}^2}} & if\ g_n > 0 \\ g_t^c & if\ g_n \leq 0 \end{cases} \quad \text{5-15}$$

$$u_f = \frac{2(1+v^2)}{u_c}\left(\frac{E_n}{G_{IC}} + \frac{v^2 E_t}{G_{IIC}}\right)^{-1} \quad \text{5-16}$$

Where g_n^c and g_t^c represent the critical displacement of pure mode I and combined mode II separately; v represents the loading ratio which is calculated by $v = \frac{g_n}{g_t}$; and u is computed by $u = \sqrt{{g_n}^2 + {g_t}^2}$. The softened traction separation response is thus defined according to Eq. 5-17 and Eq. 5-18. A schematic diagram of the bilinear cohesive law and corresponding damage plot is presented in Figure 5.4.

$$\lambda_n = \begin{cases} E_n g_n & if\ g_n \leq 0 \\ (1-d)E_n g_n & if\ g_n > 0 \end{cases} \quad \text{5-17}$$

$$\begin{bmatrix} \lambda_t \\ \lambda_s \end{bmatrix} = \begin{bmatrix} (1-d)E_t & 0 \\ 0 & (1-d)E_s \end{bmatrix} \begin{bmatrix} g_t \\ g_s \end{bmatrix} \quad \text{5-18}$$

5.2.4 A modified cohesive law

Convergence can be extremely challenging for the implicit time integration finite element (FE) analysis once the failure initiates, resulting in a highly nonlinear problem. By default, the contact stiffness, which is a function of damage, needs to be updated for every iteration within one increment using the Newton-Raphson method, and this can result in a severe non-convergence issue. To resolve this, MSC Marc-Mentat tends to reduce the load increment size by half several times until the numerical result is converged or terminated after the maximum specified times (10 by default). The increment reduction process due to non-convergence resulting from interface failures, however, provides no benefits and increases the computational effort.

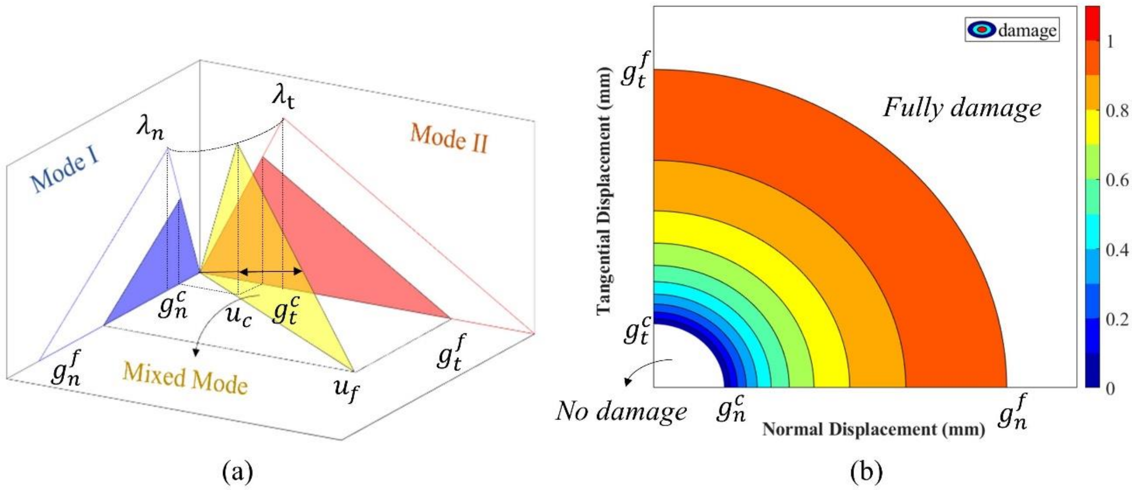

Figure 5.4. (a) 3D representation of the bilinear cohesive law, (b) corresponding damage plot

The zigzag cohesive law, initially proposed by Rots et al. [135], has been shown to mitigate the convergence issue. In this method, the stiffness was degraded in a stepwise manner instead of linearly, as shown in Figure **5.5**a. The negative stiffness in the softening region was replaced by a piecewise positive linear stiffness with the total strain energy release rate being equivalent. Instead of updating the contact stiffness in every load increment when damage initiates, the local response within the model can behave almost linearly with slight strain variations, substantially improving the numerical convergence. The feasibility of this technique has been validated in many applications [96, 136, 137].

In this chapter, a modified cohesive law was developed to simplify the implementation effort, while also addressing the convergence issue. The modified law refers to keeping the contact stiffness constant within every individual increment, instead of updating it for every iteration. Hence, the cohesive contact interaction can be regarded as linear within every increment. The damage variable is updated only at the end of the increment and the corresponding initial contact stiffness/stress are updated at the beginning of the next increment with incorporating the updated damage variable, as schematically shown in Figure **5.5**b. This approach, however, also leads to the generation of additional artificial strain energies. The total additional strain energies generated through the model depends on the load increment size, specifically the area of the triangle. It has been shown in Section 5.4 that the additional strain energy created does not have a significant impact on the results of the analysis when the load increment size is small enough.

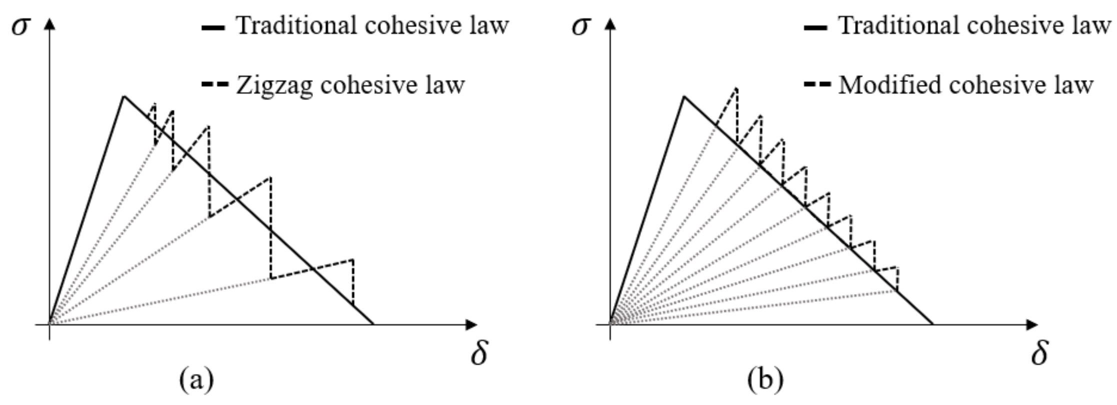

Figure 5.5. (a) Representation of zigzag cohesive law, (b) Representation of modified zigzag cohesive law

5.3 Benchmark validation of SSCC interaction

This section aims to demonstrate the feasibility and accuracy of the SSCC in modelling interface failures with the comparison of the cohesive element approach. Three commonly used tests, double cantilever beam (DCB), end notched flexure (ENF), and fixed ratio mixed mode (FRMM), were utilized. These tests are corresponding to mode I, mode II, and mixed-mode failure, respectively. As there are already numerous experimental and numerical data been published regarding these tests, the numerical results from Harper et al. [89] were used for comparison here to avoid experimental artifacts such as fibre bridging. The same material properties, as recorded in Table 5.1, were applied to the SSCC model to keep consistent.

Table 5.1. Material properties and cohesive properties for HTA6376/C **[89]**

Material Properties		**Cohesive Properties**	
E_{11} (MPa)	120000	G_{IC} (N/mm)	0.26
$E_{22} = E_{33}$ (MPa)	10500	G_{IIC} (N/mm)	1.002
$G_{12} = G_{13}$ (MPa)	5250	σ_{max} (MPa)	30
G_{23} (MPa)	3480	τ_{max} (MPa)	60
$v_{12} = v_{13}$	0.3	k_I (MPa/mm)	1e+05
v_{23}	0.51	k_{II} (MPa/mm)	1e+05

This study was performed with an implicit time integration FE framework in MSC Marc-Mentat 2019, a nonlinear FE package which provides a powerful S2S contact algorithm and efficient contact pair definitions within large assemblies. To further improve the computational efficiency, the stacked shell approach proposed by Johnson et al. [124] was employed in the present study. Instead of modelling the laminate as a continuum body, the laminate was modelled as multiple discrete shells to provide an opportunity to capture interface failures (Figure 5.6). This method has been successfully used in many applications [93-95].

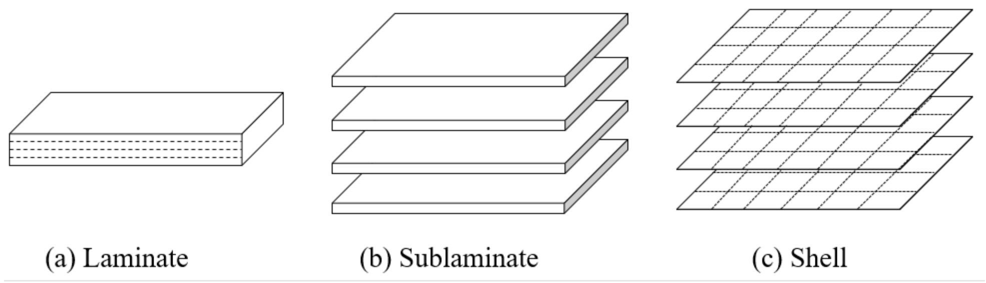

Figure 5.6. Schematic diagram of the Stacked Shell Model

5.3.1 Double cantilever beam

In this test, each arm of DCB was modelled as one stacked shell to improve computational efficiency. A fully integrated shell element, with the implementation of Mindlin–Reissner plate theory [138, 139] (element type 75), was used, as it takes the transverse shear deformation into account. This type of element has a better prediction than the Kirchhoff-Love theory-based shell element [140, 141] especially when large bending deformation is involved.

The test configuration and finite element model of the DCB are shown in Figure 5.7. The pre-cracked region is identified as the area (dark grey) without any contact defined, while the region of interest is assigned a SSCC interaction. A comparable mesh size of 0.5mm with Harper et al's work was used for this test. The ultimate numerical result is presented in Figure 5.7, where the current result is labelled as "SSCC" while the numerical data from [89] were designated as "Benchmark". These labels are also used for the following tests in this chapter.

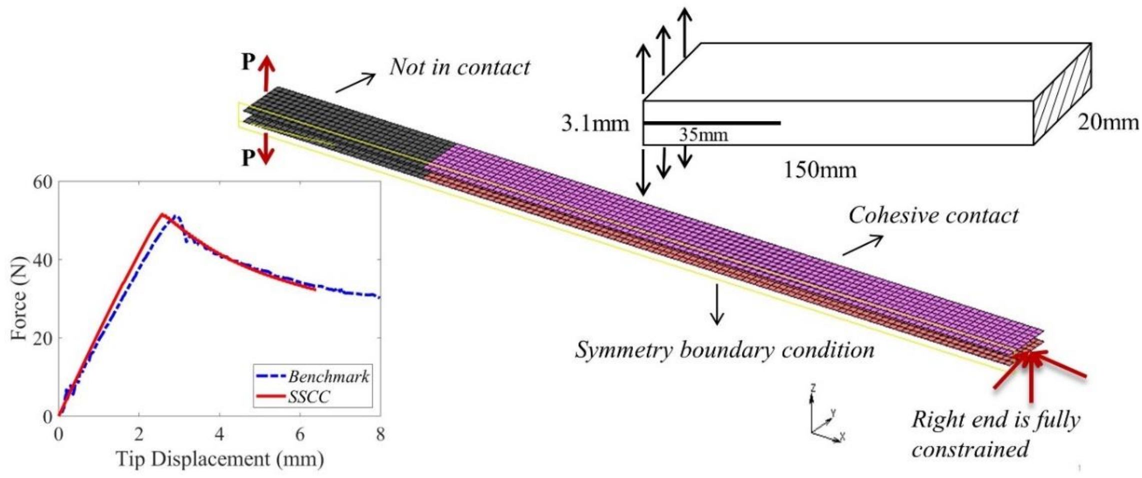

Figure 5.7. DCB test configuration, finite element model setup and the numerical result

A great agreement can be noted in terms of the global reaction force against the tip displacement, except for a slight difference shown in the linear stiffness. The discrepancy is induced by the shell element type, which is stiffer than the solid elements used in [89]. Although the Mindlin–Reissner shell is used in this study, it still cannot fully capture the transverse shear deformation. A higher-order plate theory with the introduction of some additional degree of freedoms in the displacement field will provide better prediction, but this requires extra computational effort.

5.3.2 End notched flexure

ENF is a mode II dominate delamination test which has been selected to evaluate the capabilities of the SSCC method in modelling the delamination progression induced by shear loading. The specimen dimensions and finite element model geometry is shown in Figure 5.8. Instead of assigning no contact in the pre-cracked region for the DCB test, a normal touching contact algorithm was applied to this area to avoid potential penetration due to the bending effect. A converged mesh size of 0.5mm is assigned to both the top and bottom arms. The global load-displacement response of the SSCC model displays very good correlation with the benchmark case, as presented in Figure 5.8.

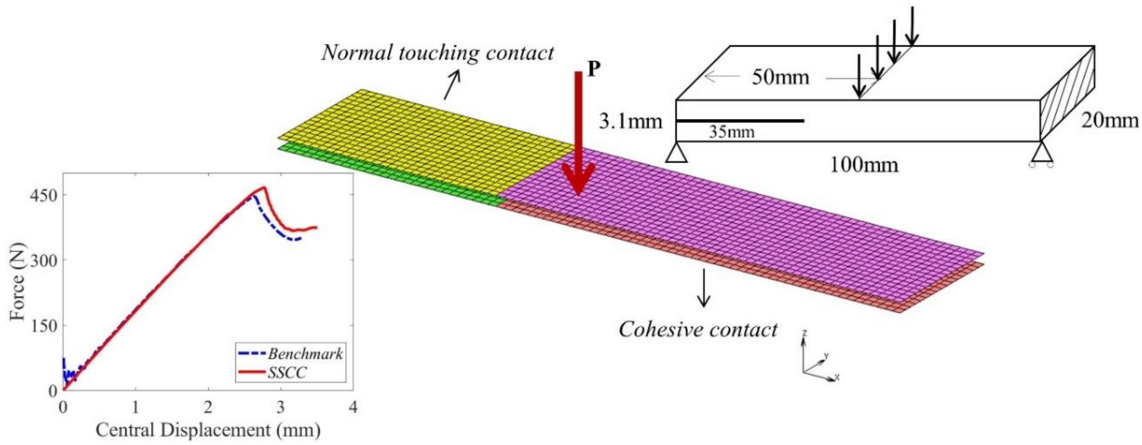

Figure 5.8. ENF specimen information, finite element model geometry and simulation results

5.3.3 Fixed ratio mixed mode

The capability of SSCC in modelling the mixed-mode interactive failure is validated with a fixed ratio mixed-mode (FRMM) bending test. The specimen geometry and finite element model of this test are presented in Figure 5.9. Similar to the ENF test, a penalty-based touching contact algorithm was applied to the pre-crack region to avoid potential penetration. A converged mesh size of 0.5mm was used for both arms. The ultimate simulation result is also presented in Figure 5.9. A good agreement regarding the global-load displacement response is observed between the SSCC and Benchmark. Similar to the DCB test, a slight difference is also noted in terms of the linear stiffness, which is due to the difference of element type.

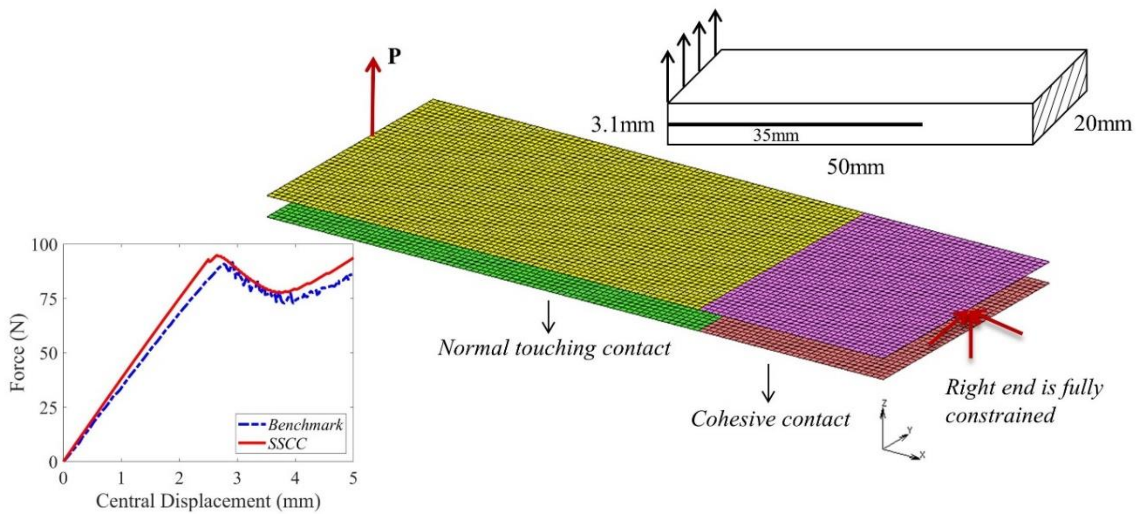

Figure 5.9. FRMM specimen information, finite element model geometry and simulation results

5.4 Parametric studies of SSCC

Section 5.3 has demonstrated that the segment-to-segment cohesive contact (SSCC) method can achieve comparable accuracy with the cohesive element approach in the prediction of interface failures. As the cohesive element method has a strict requirement for the mesh size, which must be less than 1/3-1/5 of the cohesive zone length near the crack front, using this approach for predicting multiple cracks is too computationally heavy in the TWM. Hence, this section aims to demonstrate the efficiency of the SSCC method in predicting the interface failures with a sensitivity test of various mesh sizes. Other non-physical numerical parameters that can potentially affect the efficiency and accuracy of the simulation results were also tested, including the load increment size, the S2S penalty factor, and the mesh conformality.

The DCB test was used here to study the effect of these numerical parameters, as it is a mode I dominate delamination test, and the associated strain energy release rates are much smaller than those in mode II. This relates to a smaller cohesive zone length in mode I, and hence leads to a stricter requirement for these numerical parameters. The validated numerical result of SSCC as presented in Section 5.3.1 and Figure 5.7 was used as the benchmark, where the mesh size is 0.5mm, the load increment size is 0.0025mm, and the penalty factor (or contact stiffness) is 10^5.

5.4.1 Effect of mesh size

Different mesh sizes ranging from 2 to 0.25mm were tested while keeping all other parameters constant to investigate the mesh sensitivity of the SSCC model. The final mesh sizing results are plotted in Figure 5.10. It was observed that when the mesh size was around or less than 1.25mm, rapid convergence was achieved. The converged mesh size of the SSCC model was comparable to the cohesive zone length, which was 1.2mm as stated in [89]. Compared to the traditional CZM which requires at least 2-3 elements positioned in the cohesive zone to obtain reliable results, the SSCC model only needs 1 element, which substantially eases the restrictions relating to the mesh size near the crack tip. It can also be observed that mesh refinement can also improve the stability of the crack propagation.

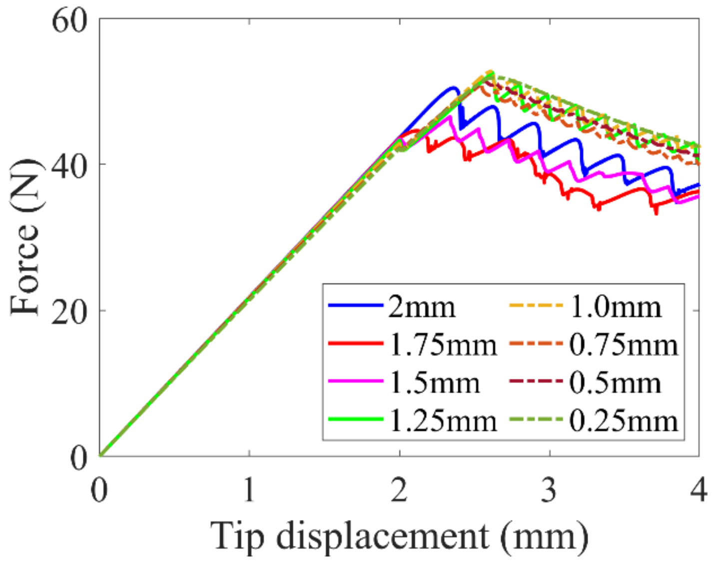

Figure 5.10. The global response of DCB test with various mesh sizes

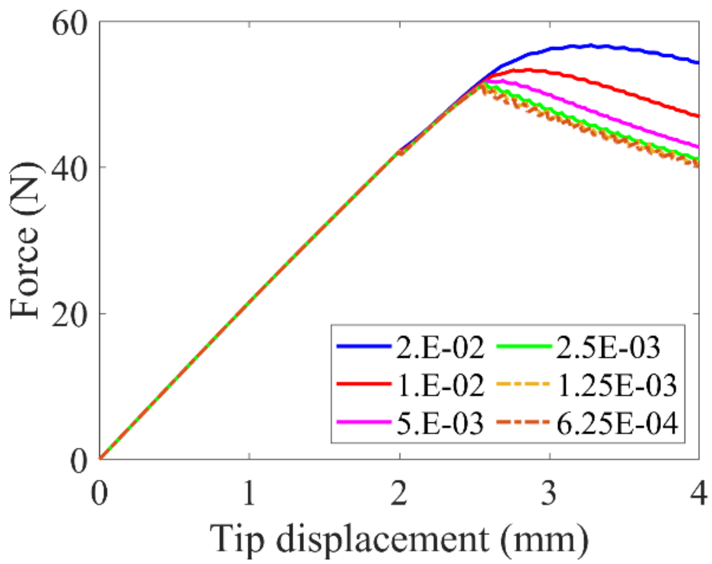

Figure 5.11. The global response of DCB test with various load increment sizes (mm)

5.4.2 Effect of load increment size

The load increment size is a critical parameter for nonlinear finite element analysis. To account for the system nonlinearity resulting from the contact and aforementioned additional strain energy generated by the modified cohesive law, a range of load increment size between 0.02 and 0.000625mm were examined while keeping the contact stiffness of 10^5 MPa/mm and mesh size of 0.5mm constant. The simulation results are compared and indicated in Figure 5.11. It can be noted that the global response converges when the load increment size is around 0.0025mm, and no obvious benefits can be gained from lower load increment values. It is recommended to apply a large load increment size to the linear elastic region, while using a lower load increment size once the failure initiates to further improve the computational efficiency.

5.4.3 Effect of contact stiffness

The extra contact interfaces introduced in the SSCC model can greatly soften the original laminate if an inappropriate stiffness is used. Lower contact stiffness can affect structural compliance, while an extremely high value can cause severe convergence issues and reduce the computational speed. Although values between 10^5 and 10^7 were commonly used as the initial stiffness in the literature for cohesive elements, there is no definitive selection of this parameter. It was reported by Lu et al. [142] that the only potential way to obtain the optimum value of the penalty stiffness was a trial-and-error process.

It should be noted that the contact stiffness is not a physical quantity and hence to obtain a optimum value without affecting the numerical accuracy, a parametric study was performed in this section. As the ideal value was commonly identified in the range between 10^5 and 10^7 in balancing the numerical accuracy and model compliance in the area of composites area, which have been thoroughly reviewed in Lu et al.'s work [142]. Hence, values ranging from 10^2 to 10^8 MPa/mm were tested to incorporate the ideal range in the present study. For clarity purpose, only the simulation results in the range from 10^3 to 10^6 MPa/mm was presented in Figure 5.12 as a fast convergence was observed during the testing.

The results (Figure 5.12) indicated that when the contact stiffness was a similar magnitude to, or higher than, the adjacent continuum material properties (10^4), a stable global response can be achieved. Higher stiffness can result in increased oscillations or iterations to converge. Hence, to balance the numerical accuracy and convergence difficulties, the contact stiffness of 10^5 MPa/mm was used in the present study. It should be noted when the normalized stiffness was 10^3, the structural compliance was increased, and the failure was delayed significantly. A similar phenomenon was discovered in Lu et al.'s work [142], the delamination progression was not observed, as the peak stress cannot reach the cohesive strength with such low penalty stiffness.

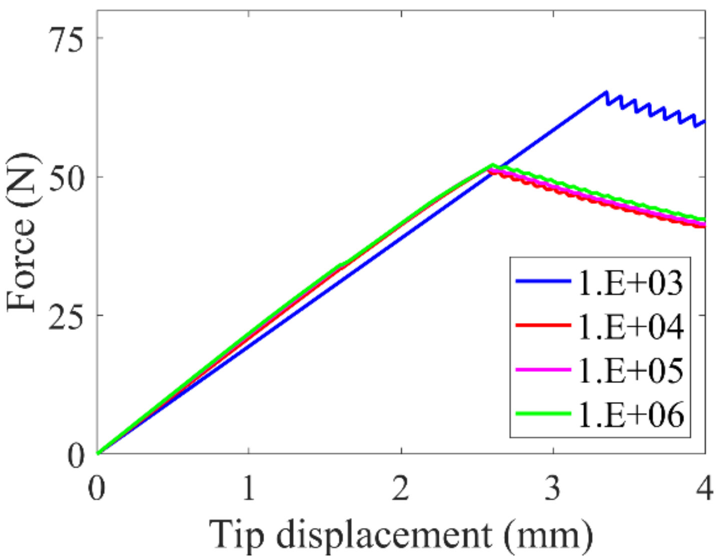

Figure 5.12. The global response of DCB test with different normalized contact stiffness

5.4.4 Effect of mesh conformality

One of the major benefits of contact-based over element-based CZM is the capability of simulating interface failures with non-conformal meshing, saving numerous pre-processing efforts and opening up the possibility for modelling irregular structures, in which generating a conformal mesh is extremely challenging. To test this capability of the SSCC approach, two different non-conformal mesh patterns were introduced (Figure 5.13). In the first case, the non-conformal mesh is induced by different mesh sizes (1mm for the top arm and 1.25mm for the bottom arm). While in the second case, elements with different orientations and certain distorted elements are introduced in the top arm where the mesh size is approximately 0.3mm; the mesh size and regularity of the bottom arm is maintained the same as the first case. It should be noted that the material orientation in this test is defined by the axes of the global coordinate which is not affected by each elements' orientation. The converged simulation result of the conformal mesh pattern (1.25mm), shown in Section 5.4.1, was used as the benchmark for comparison. For these two cases, a very good correlation was achieved between the conformal and non-conformal meshing configurations, as presented in Figure 5.14.

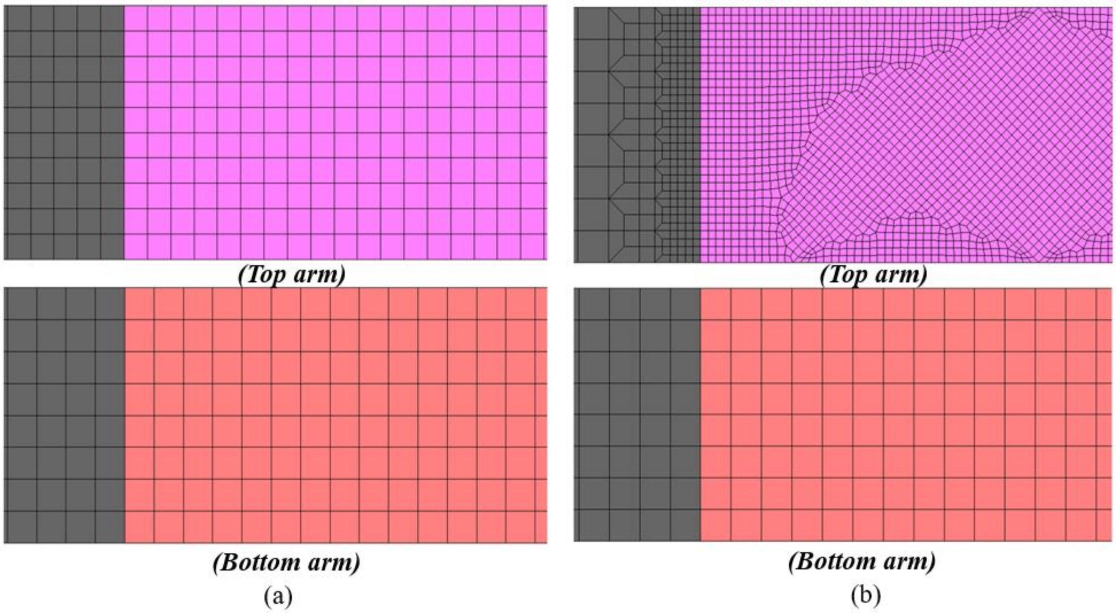

Figure 5.13. Representation of two different unaligned meshing paradigms

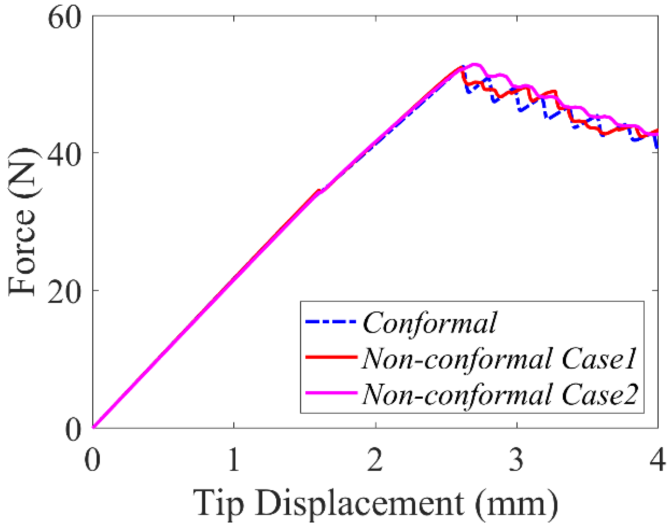

Figure 5.14. The DCB test results for conformal and non-conformal meshes

5.5 2D application of cohesive network method

After the validation of the new cohesive interaction, SSCC, and the sensitivity study on the input parameters, the cohesive network method can be built by allocating the SSCC interaction along with both intra- and interlaminar paths. To demonstrate the capability of the cohesive network method in modelling both intra- and inter-laminar failures, a 2D application is used in this section before complex 3D demonstrations, which would be presented in Section 5.6. A L-beam bend test with stacking sequence $[0/90_3/0_2/90_3/0]_s$, conducted by Cao et al. [143], was used in this study. A 2D plane strain element model, in conjunction with cohesive elements was proposed in their work for the prediction of kinking failures. The model was validated with good agreement between numerical and experimental results. This work is repeated using the SSCC method instead of cohesive elements in the present study. To isolate the effect of SSCC, all model settings remain the same.

The FE setup is illustrated in Figure 5.15, where the bottom-left end is fully constrained in both x and y, and the right-top corner is fixed at x but moves vertically with a displacement control. The region of interest is modelled with a number of small discontinuous sections and connected with SSCC interactions. The density of radial cohesive interaction with $1/15^{o}$ is adopted in this test considering the computational effort. The material model is recorded in Table 5.2.

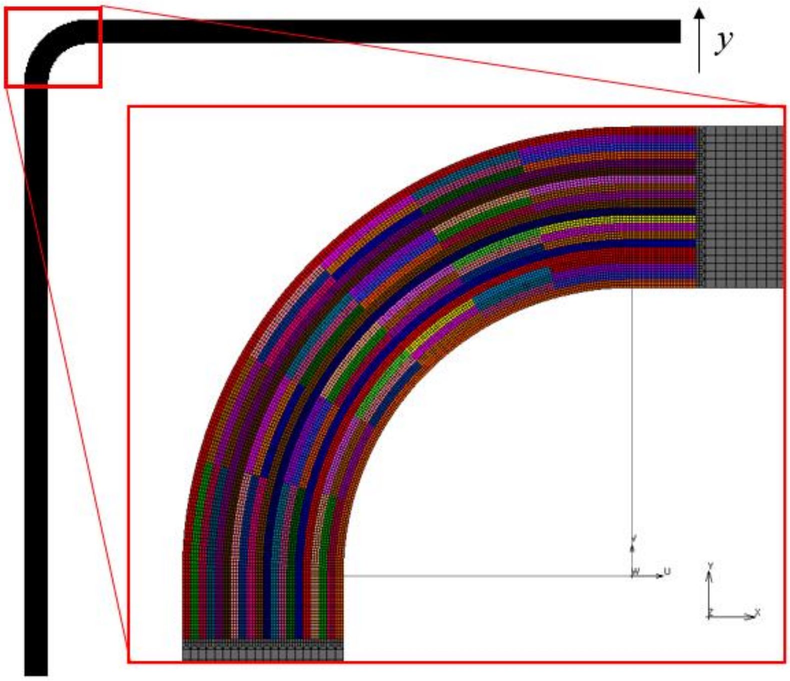

Figure 5.15. Finite element model setup of L beam bend test

The ultimate numerical results of SSCC were compared with [143] regarding the kinking failure mode, the radial stress and hoop stress distribution. The results are presented in Figure 5.16-Figure 5.18. In general, a great correlation is achieved except for a slight difference in the crack location. This is mainly due to the kinematic differences between cohesive elements and the SSCC. This validates the predictive capability of the SSCC method for both the intra- and inter-laminar failures as well as their interactions in 2D applications.

Table 5.2. Material properties and cohesive properties for Hercules AS4/3501-6 [143]

Material Properties		**Cohesive Properties**	
E_{11} (MPa)	126000	G_{IC} (N/mm)	0.128
$E_{22} = E_{33}$ (MPa)	11000	G_{IIC} (N/mm)	0.653
$G_{12} = G_{13}$ (MPa)	6600	σ_{max} (MPa)	48

G_{23} (MPa)	3900	τ_{max} (MPa)	79
$v_{12} = v_{13}$	0.29	k_I (MPa/mm)	1e+07
v_{23}	0.40	k_{II} (MPa/mm)	1e+06

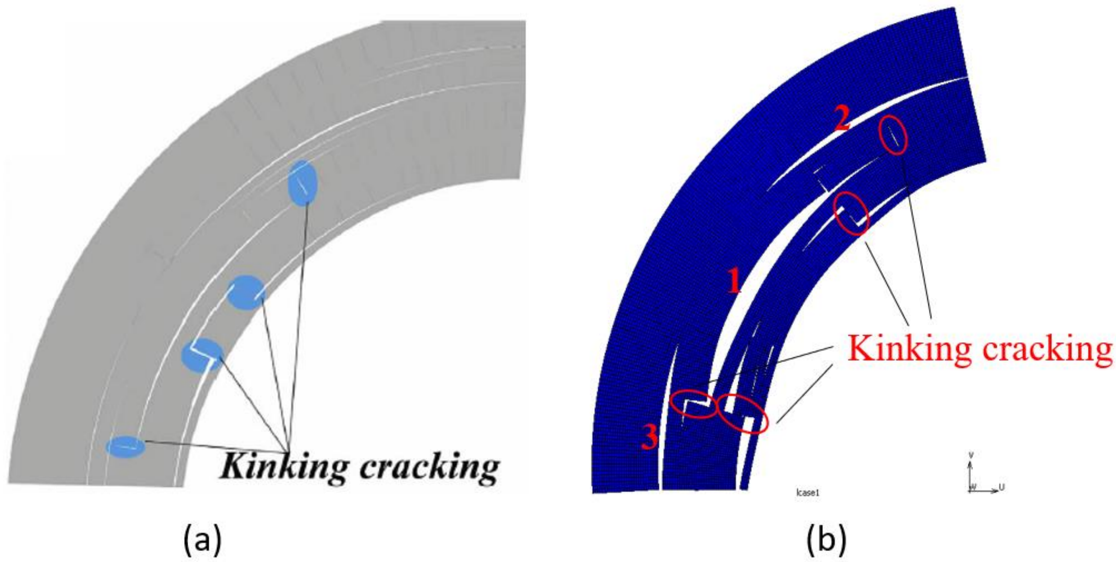

Figure 5.16. Failure mode comparison between (a) Cao et al.'s [143] work (b) SSCC method

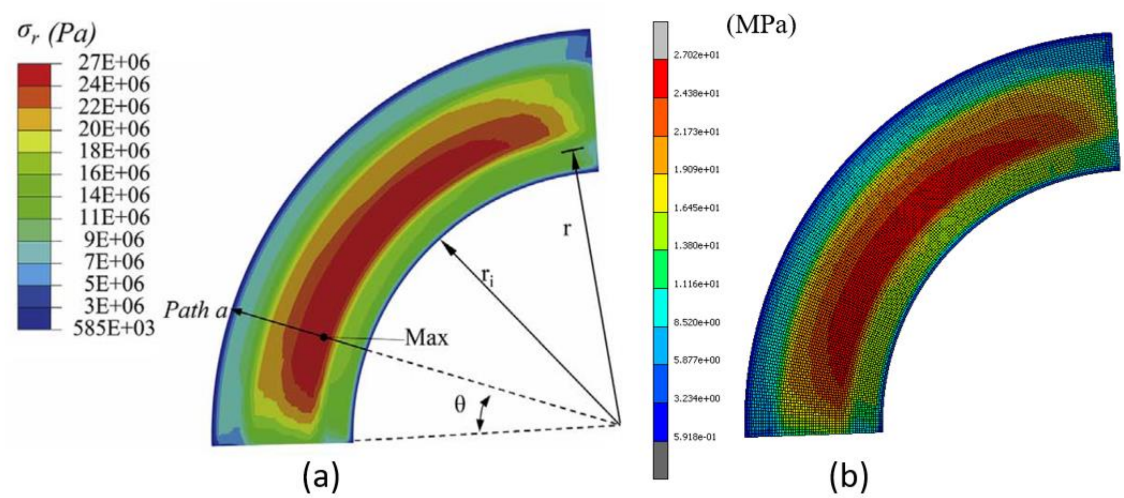

Figure 5.17. Radial stress contour comparison between (a) Cao et al.'s work [143] (b) SSCC method

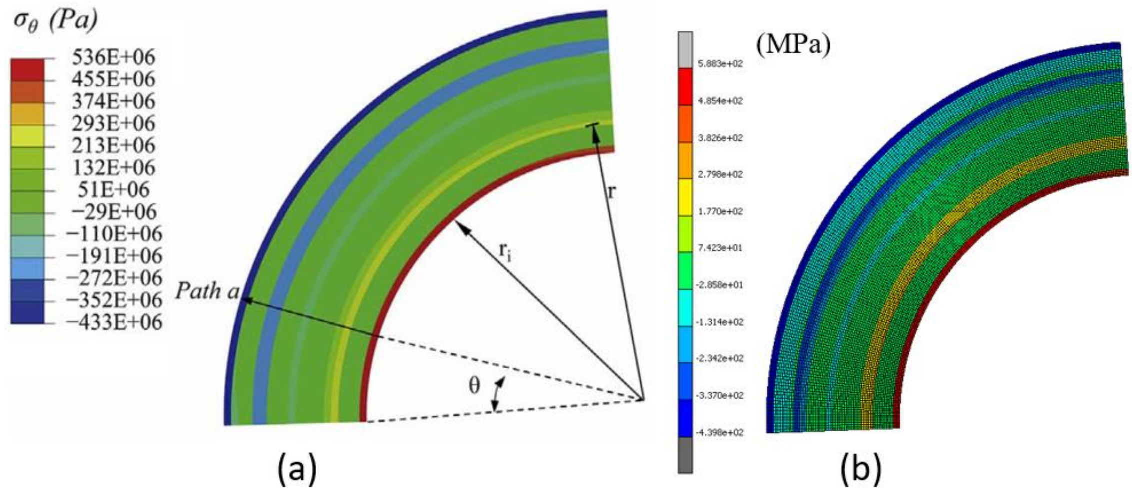

Figure 5.18. Hoop stress contour comparison between (a) Cao et al.'s work [143] (b) SSCC method

5.6 3D application of cohesive network method

This section aims to further explore the capability of the cohesive network method in modelling both inter- and intra-ply failures with a 3D application. A quasi-isotropic laminate tensile (QLT) test, which was performed by Hallett et al. [144], was used in this study as this test involves very complex failure interactions. Based on the experiment, it was found that the failure was triggered by matrix cracking, which then induced delamination and ultimately resulted in fibre rupture. 1D cohesive elements between coincide nodes were used in [144] to predict the delamination failure.

Although a range of different scales of quasi-isotropic samples was tested by Hallett et al., the set with $[45_4/90_4/\text{-}45_4/0_4]_s$ was used in this study for demonstration purpose due to the relatively complete experimental data presented than other sets. The Hexcel IM7/8552 used in the experiment and the material properties are recorded in Table 5.3.

Table 5.3. Material properties and cohesive properties for Hexcel IM7/8552 [144]

Material Properties		**Cohesive Properties**	
E_{11} (MPa)	161000	G_{IC} (N/mm)	0.2
$E_{22} = E_{33}$ (MPa)	11380	G_{IIC} (N/mm)	1.0
$G_{12} = G_{13}$ (MPa)	5170	σ_{max} (MPa)	60
G_{23} (MPa)	3980	τ_{max} (MPa)	90
$v_{12} = v_{13}$	0.32	k_I (MPa/mm)	1e+06
v_{23}	0.436	k_{II} (MPa/mm)	1e+06

In reference [144], a matrix crack was input into the numerical model as an initial condition, since the matrix failure strain is much lower than the delamination failure strain which was observed from the experiments. Hence, this test was conducted twice in this study. The first test was a benchmark, which used the same assumptions with Hallett et al.'s work, where a matrix crack was pre-assumed and fibre failure was neglected. This test was used to validate the input parameters by comparing the cohesive network method against the published finite element result. The second test utilized the same input parameters while the matrix pre-crack assumption was removed, and fibre failure was also considered.

5.6.1 Baseline test

For the baseline test, the geometrical discontinuities result from pre-assumed matrix crack along the fibre direction in each ply, leads to significant challenges in generating conformal mesh between the adjacent layers. Thus, the non-conformal mesh is generated for the present study (see Figure 5.19). As no delamination was observed between the layers with the same fibre orientation based on the experiments from Hallett et al. [144], these layers were modelled as one stacked shell to reduce computational effort. The laminate can be turned into [45_{4t}/90_{4t}/-45_{4t}/0_{8t}/-45_{4t}/90_{4t}/45_{4t}] where the subscript refers to the total thickness of each stacked shell. Meanwhile, a fine mesh was used in the critical regions and a coarse mesh is applied to the other areas to further reduce the computational effort. The geometric representation, finite element model and simulation result of SSCC are presented in Figure 5.19. The residual stress trapped in the laminate during the manufacturing process was considered by applying a thermal load of -160^0C before any mechanical loading. Same thermal expansion coefficients with reference [144] were used here where $\alpha_1 = 0, \alpha_2 = \alpha_3 = 3.0\ \times 10^{-5}\ {}^0C$.

Since only the crosshead movement was available for the experiment which introduced extra compliance to the test, the numerical result was scaled to match the initial linear stiffness. The same strategy was used in the present study as well. The stress of two turning points and the second linear stiffness were compared against the published simulation and experimental data. An excellent correlation was achieved except for a slight difference between the simulation results which potentially induced by the displacement scaling ratio, element types and implicit/explicit analysis. The ultimate damage pattern of each interface was plotted and also compared against the published simulation result as shown in Figure 5.20. Nearly identical failure patterns were observed within each interface.

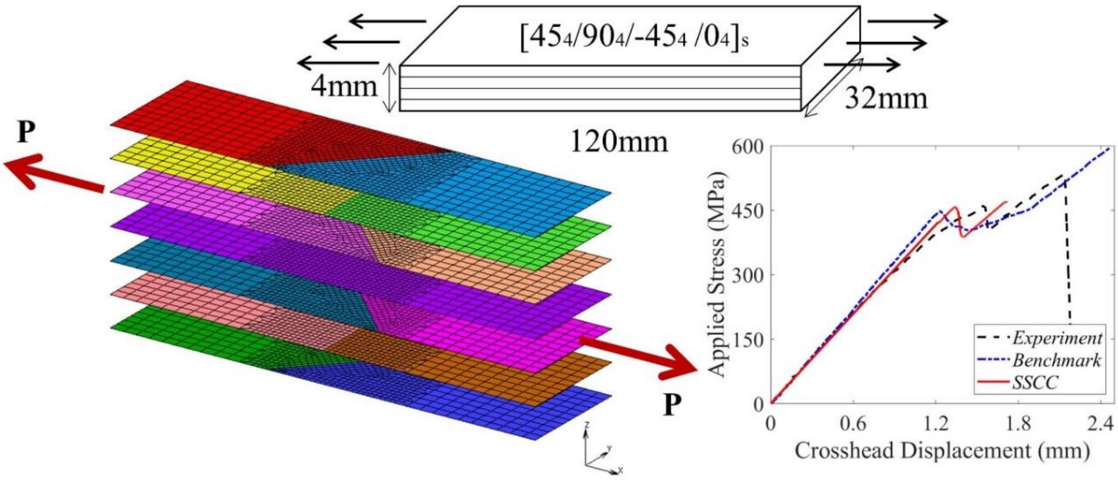

Figure 5.19. The QLT test configuration, finite element model and simulation result. Note: the thickness of the finite element model is artificially made to visualise the mesh pattern of each stacked shell. Note: the colour scheme refers to different contact bodies.

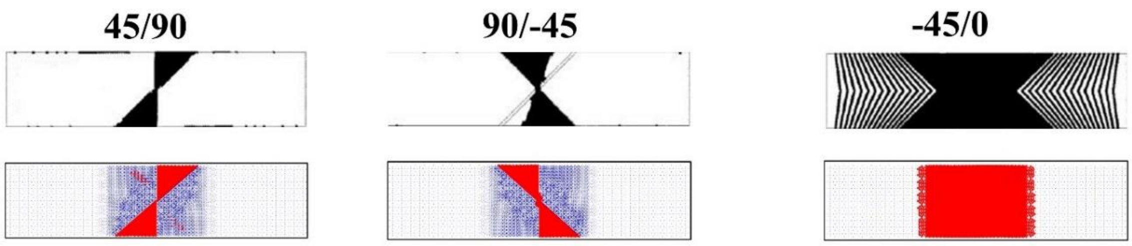

Figure 5.20. Final damage pattern comparison for each interface, where the top three are adapted from [144] and the bottom 3 are from the SSCC model. The failure was visualized by exporting the damage status of the contact points, where blue represents no damage and red denotes fully damage. A finer mesh is applied to the region of interest, which also generates dense contact points.

5.6.2 Multiple failures test

The second test is to explore the capabilities of the cohesive network method in modelling multiple failures including matrix cracking, delamination, and fibre failures. The potential intralaminar matrix cracking path was assumed in all the sublaminates along with fibre orientation except 0^0 layers as the loading direction align with the 0^0 fibre direction. While the ultimate fibre failure is assumed in 0^0 sublaminate perpendicular to the fibre axis in the central region, as plotted in Figure 5.21. The cohesive properties of intralaminar matrix cracking were assumed to be identical with interface properties. It was stated in reference [144] that the fibre failure tended to occur due to localized stress concentration raised by the delamination of the outer plies. In this study, the potential fibre failure path was assumed based on the empirical method which can only give an approximate location, the central area perpendicular to 0^0 axis here.

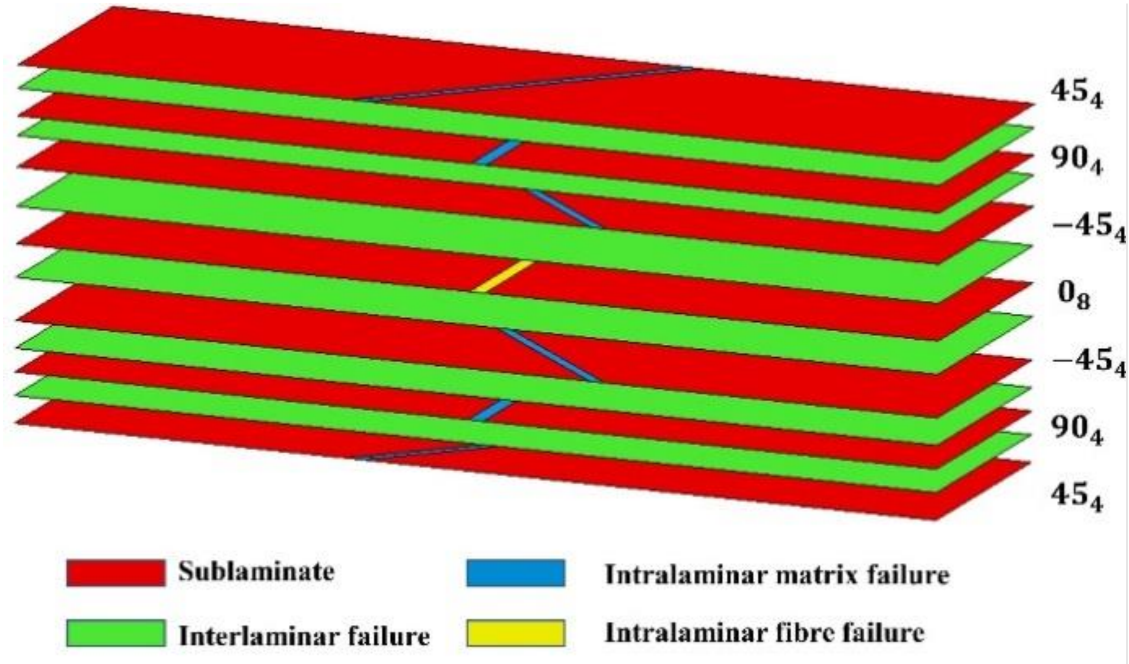

Figure 5.21. The potential failure paths assumed in the SSCC model

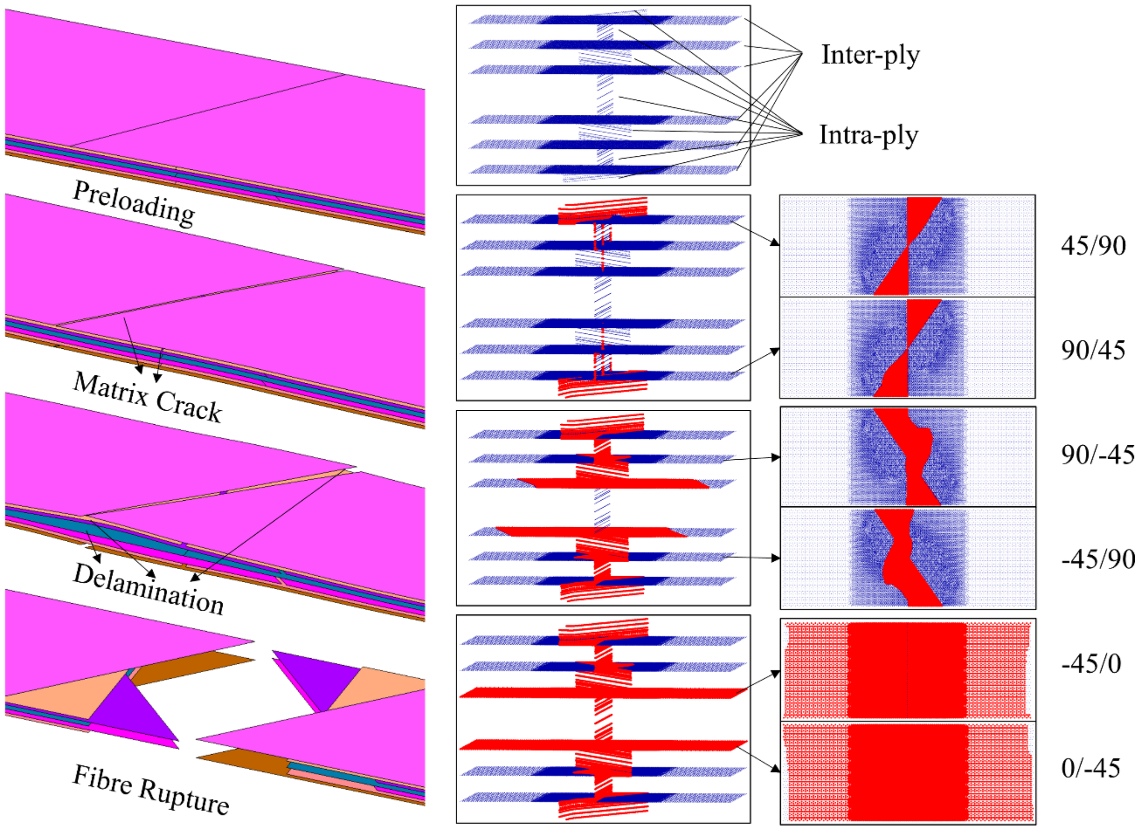

Figure 5.22. The progressive failures of the QLT test. Note: The simulation would be terminated before fibre completely fails due to non-convergence. Hence, the fibre rupture is magnified via separation for better visualisation purpose.

The effect of the thermal load was studied by comparing the simulation results with and without the thermal load being applied. For the baseline case where the matrix cracks were pre-assumed, trivial effect was observed for the introduction of thermal load. While for the case without pre-assuming matrix cracks, thermal loads does play a role in the global response, in which the one without thermal load leads to a slight delay of the first turning point. This is potentially because the thermal loads can lead to a premature failure of matrix which aligns with the results of the baseline case. The fibre failure strength of 2300 MPa was assumed in the present study. Different strain energy release rates have been attempted and it was found the magnitude has a trivial effect on the global response. This is because once the fibre failure initiated, all the loads were immediately transferred to the weak interface which can only carry a small amount of load, resulting in an instantaneous load drop. The progressive failure patterns and the corresponding interface failure plots are presented in Figure 5.22. The final global response of the SSCC model with the comparison of the published numerical and experimental results are indicated in Figure 5.23. It can be observed that the fibre strength was slightly overpredicted than the experiment. This is because fibre failure in reality rarely occurs in a well-defined path. Instead, it is mostly arising together with explosive matrix cracks which separate the 0^0 layer into multiple strips [81]. The stress concentrations raised due to surrounding matrix cracking and delamination ultimately led to the breakage of these strips and resulted in a load drop. The stochastic nature of the fibre failure path is an extremely complex failure phenomenon, which, is still an ongoing area of interest.

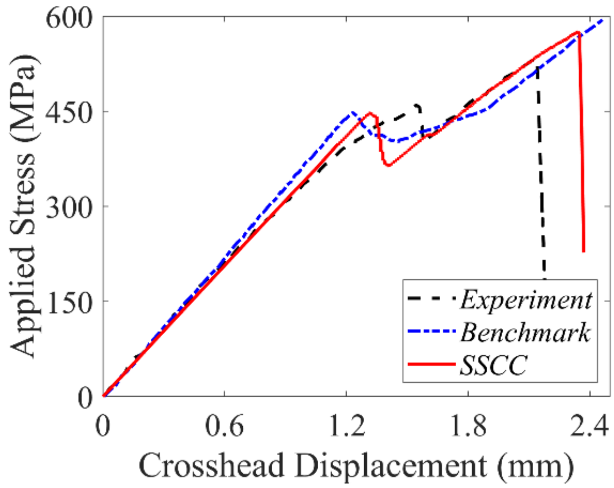

Figure 5.23. The global response of the SSCC model with the inclusion of matrix and fibre failures

5.7 Summary

This chapter presents a robust and efficient cohesive network approach, aiming to address the failure modelling challenges of AFP composites. This method is developed based on a new cohesive interaction, SSCC, which is established based on an advanced S2S formulation and a user written subroutine “uglue_stif_sts”. The subroutine provides a great capability for users to control the kinematics of each contact point. A modified cohesive law is also proposed and implemented in the SSCC to substantially improve the numerical convergence difficulties in the implicit FE framework.

The feasibility and accuracy of the SSCC in modelling interface failures have been demonstrated via DCB, ENF and FRMM load cases. A comparable accuracy between the SSCC approach and the cohesive element method was shown. The efficiency of the SSCC is demonstrated using a DCB test with various mesh size. It can be found that compared to the CZM, which requires at least two or three cohesive elements in the cohesive zone near the crack tip to achieve numerical stability and accuracy [14], the SSCC model allows using a comparable mesh size with the cohesive zone length, which greatly eases the element size restrictions near the crack tip. This outstanding outcome creates the possibility of predicting multiple failure events in AFP composites at mesoscale.

Several critical non-physical numerical parameters including load increment size, contact stiffness, and mesh conformality that might affect the behaviour of the SSCC model were also thoroughly studied using a DCB test. It has been shown that the selection of an appropriate load increment size is critical once the failure initiates. Small load increment sizes can ensure stable crack propagation without generating a significant amount of extra energy, due to the effect of the modified cohesive law. Hence, it is recommended to use a large increment size in the initial linear elastic response and a smaller value in the nonlinear area to improve the computational efficiency. The definition of contact stiffness would require a trial-and-error process before the testing to ensure a balance between numerical accuracy and convergence difficulties. For the mesh conformality, it is shown that non-conformal mesh exhibits comparable performance with conformal mesh. This creates the potential of using cohesive network method in conjunction with the TWM to simulate failures of AFP composites.

After the demonstration of benefits and limitations of the SSCC method, the cohesive network method is further demonstrated with 2D and 3D applications via allocating SSCC along with potential failure paths for both intra- and inter-ply. The 2D application is with a L-beam bend test. The kinking failures from intra- to inter-ply has been well predicted with the cohesive network method. For the 3D application, a QLT test was utilised to demonstrate the capabilities of the cohesive network method in predicting multiple failure modes including matrix cracking, delamination, and fibre ruptures. This test was divided into two sections. The first section validated the SSCC approach by keeping the assumptions consistent with the published numerical benchmark model, where the matrix cracking was pre-assumed and the fibre failure was neglected. An excellent agreement was achieved between the simulation result of the SSCC model and the published numerical result. The second section implements the potential matrix and fibre failure capabilities of the SSCC model, by removing the pre-assumed matrix crack and inserting the fibre failure path in the 0° layers. The initial matrix cracking, interactions between the matrix cracking and delamination, and ultimately the induced fibre rupture were fully captured. A good correlation has been achieved between the simulation result and the experimental data. It also should be noted that the fibre rupture due to the stress concentrations caused by the explosive matrix cracks and adjacent delaminations can result in an extremely stochastic failure path. This phenomenon is simplified with a well-defined failure path placed in the central region, which leads to a slightly overpredicted fibre strength.

Chapter 6 TWM Demonstration in AFP Composites

6.1 Introduction

Defects can either have a trivial or significant impact on the structural performance of AFP composites. Accurately understanding these geometric features require extensive material tests as they are highly dependent on the defects' morphology and distributions. Existing numerical models, however, are either too localised or too simplified to represent these geometric features. The developed TWM technique is a high-fidelity geometric modelling tool that aims to retain the localised details that pertain to tow gaps, overlaps, thickness variations, tow drops, etc.

After the comprehensive description of the TWM algorithm (Chapter 4) and the cohesive network approach (Chapter 5), this chapter aims to demonstrate the applications of TWM with the integration of the cohesive network method in predicting the mechanical properties (stiffness/strength) of AFP composites, as well as simulating the associated failure progress. The advanced AFP laminate, AP-Ply, is used as an example due to the complex geometric features. Among those experimental studies presented in Chapter 3, the SBS and the LVI tests will be simulated and compared against the experimental results for validating the feasibility of the model in this chapter. These simulations are performed in an implicit FE package, MSC Marc-Mentat 2019.

Some of the results presented in this chapter are included in the following publication:

Li X, Brown SA, Joosten M, Pearce GM. *Tow Wise Modelling of Non-conventional Automated Fibre Placement Composites: Short Beam Shear Study*. Composites Part A: Applied Science and Manufacturing. 2021:106767.

6.2 Model description

The critical inputs for the TWM generation include the programmed tow path, mandrel/tool surface and tow placement orders, which were exported from the in-built software of the AFP equipment, the Fibre Placement Manager. Based on these critical inputs, the TWM can be generated by virtually simulating the manufacturing process. The TWM algorithm is described in detail in Chapter 4, and hence will not be repeated here. Instead, several key steps of the 3D tow mesh generation are presented in Figure 6.1. It should be noted that this image is only used for illustrative purposes.

After the generation of the finite element model, another critical step is to define the material orientations. For structured mesh, the material orientation can be directly assigned to each individual element following the element axis, as shown in Figure 6.2a. In this case, for example, the fibre angle of 45^{o} is assigned with reference to the element edge 1-2. For some irregular tows where the boundaries are trimmed and a structured mesh is hard to achieve, Marc-Mentat allows user to define the material orientation with reference to the global axis system, where the material orientation of 45^{o} is assigned with reference to the x-axis (Figure 6.2b). This method, however, is not applicable to some complex geometries such as a curved tow. For this case, a reference curve can be used as shown in Figure 6.2c. In AFP applications, the reference curve can simply be the tow trajectory.

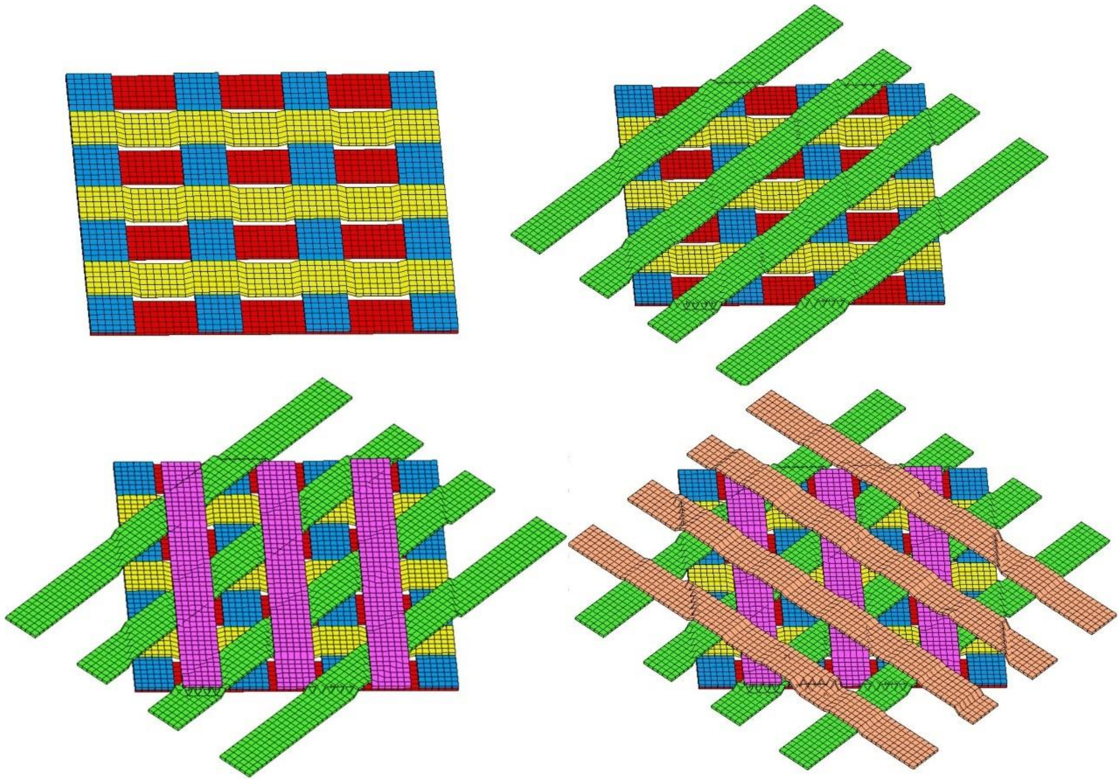

Figure 6.1. The demonstration of the TWM algorithm. Note: the colour code refers to the ply number.

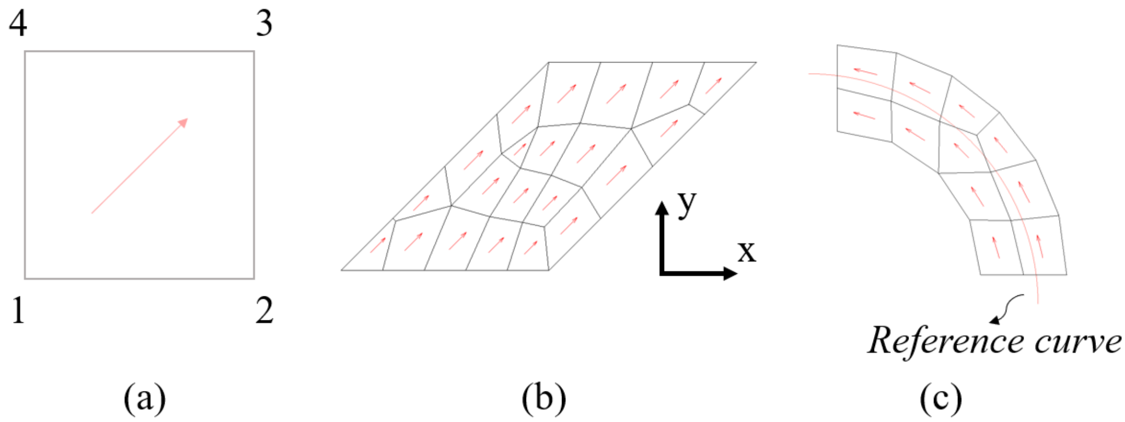

Figure 6.2. Potential ways of material orientation mapping: (a)local axis system; (b) global axis system; (c) reference curve method.

6.2.1 Interlaminar and intralaminar failure modelling

The material behaviour cannot be accurately captured if the required kinematics are not provided in the numerical model [121]. However, considering the computational efficiency, a good balance between model simplification and numerical accuracy is required.

This chapter aims to model the failure events of AP-Ply with a more generalised cohesive network approach, while it is also impractical to allocate cohesive interactions everywhere within the model. To balance the computational effort and accuracy, the cohesive contact interactions were implemented along with the tow-by-tow interfaces both in-plane and out-of-plane, forming an interconnected network that also allows the interactions between in-plane and out-of-plane failures to be captured. This assumption seems reasonable as the resin-rich areas tend to arise at the tow-by-tow contact interfaces, hence having a greater possibility of failure.

Figure 6.3 illustrates the implementation of the cohesive network approach within the TWM. The interlaminar failure refers to delamination (blue) between tows in the through-thickness direction. The intralaminar failure refers to matrix cracking (yellow) between tows with edge-to-edge contact and fibre failure (green) within the tows. The TWM method can intrinsically represent the delamination and matrix fracture interface. The fibre failure interface, however, requires an extra process, that is, cutting the tows orthogonally. This is achieved via the mesh trimming procedure in the TWM algorithm. The distributions of the fibre failure interfaces can be user defined.

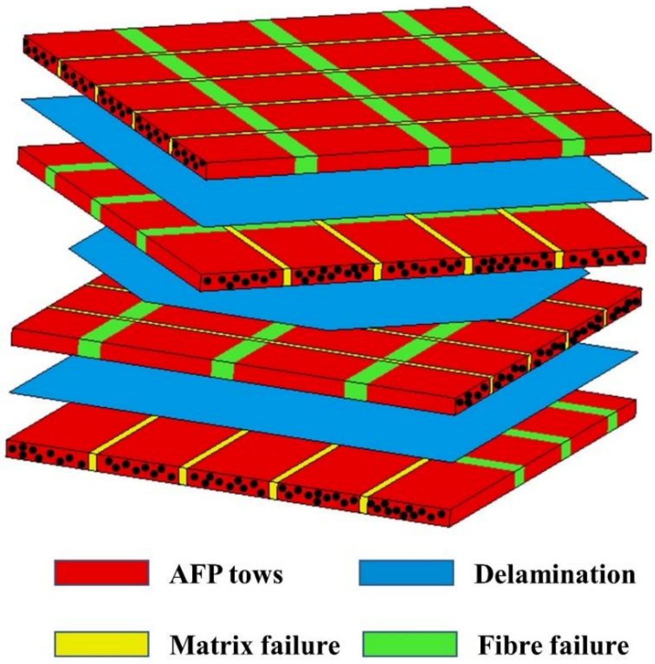

Figure 6.3. The schematic diagram of the tow-wise finite element model.

6.2.2 Failure criteria

The failure theories have been described in detail in Chapter 5 and hence only the key equations are presented here. A mixed-mode quadratic stress-based failure criterion and a fracture energy-based power law as described in Eq. (1) and Eq. (2), was used to model the interface damage onset and growth, where λ_n^* and λ_t^* denote the Mode I and Mode II strength, respectively. G_{IC} and G_{IIC} refer to the critical strain energy release rate of modes 1 and 2, in which $G_I = \int_0^{g_n} \lambda_n dg_n$, $G_{II} = \int_0^{g_t} \lambda_t dg_t$. α is an empirical parameter, which was generally in the range between 1 and 2. A sensitivity study was performed to investigate the effect of α and the result is presented in Section 6.3.2. Different failure modes were modelled with different cohesive inputs ($\lambda_n^*, \lambda_t^*, G_I, G_{II}$). It should be noted that only mode I is considered to include potential fibre failure.

$$\left(\frac{<\lambda_n>}{{\lambda_n^*}^2}\right)^2 + \left(\frac{\lambda_t^2 + \lambda_s^2}{{\lambda_t^*}^2}\right) = 1 \qquad 6\text{-}1$$

$$\left(\frac{G_I}{G_{IC}}\right)^{\alpha} + \left(\frac{G_{II}}{G_{IIC}}\right)^{\alpha} = 1 \qquad 6\text{-}2$$

In addition, the effect of through-thickness compression on mode II fracture is generally ignored, which has been shown to have a considerable impact on suppressing the delamination as reported in many studies [129, 145-150]. Hence in this work, the modified failure initiation and progression criterion proposed by Li et al. [147], as presented in Eq. (3-4) and Figure 6.4, where the shear strength and mode II fracture energy were enhanced by a common factor μ, can be used to accurately predict the failure events of AP-Ply laminates. It should be noted that this enhanced parameter is only valid when the through-thickness stress is compressive. This parameter was suggested to be in the range between 0.6 and 0.9 by Zhang et al. [129] and 0.74 by Li et al. [147] and May et al. [148]. This parameter was further investigated with the current material system in Section 6.3.2.

$$\lambda_t^{*\prime} = \lambda_t^* - \mu\lambda_n \qquad 6\text{-}3$$

$$G_{IIC}{}' = G_{IIC}\left(\frac{\lambda_t^{*\prime}}{\lambda_t^*}\right)^2 \qquad 6\text{-}4$$

6.2.3 Material inputs

A set of reliable material properties are critical in demonstrating the predictive capabilities of a numerical model. In this chapter, the material inputs can be divided into two main parts, the tow and the interface, which govern the global elastic behaviour and local material failures, respectively. To characterise those material properties, a comprehensive experimental program following the respective ASTM standard is required. In practice, some variations or uncertainties can be observed during the experiment testing. To minimise the effect of these variations, a mean value is generally taken from several samples (~5) and used for numerical investigation.

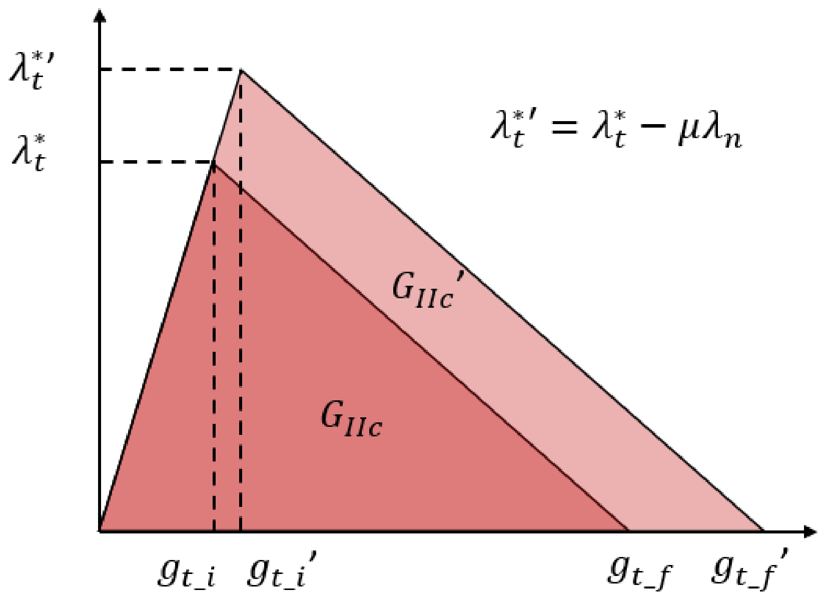

Figure 6.4. A modified cohesive law considering the through-thickness compression effect.

The material properties of HST45E23/E-752-LT prepreg, which has been characterised by Park Aerospace Corp [113], are recorded in Table 6.1. It should be noted that the material properties were measured with a normalised cured ply thickness of 0.14mm. Due to the artificially introduced tow-to-tow gaps in the experiments (Chapter 3), the tow became thinner and wider after cure. The resin and fibre were squeezed into the gaps, leading to a variation in the volume fractions of the fibre and resin. Hence, the homogeneous elastic properties were calibrated analytically based on the final cured tow thickness and width, assuming the total fibre amount remained constant before and after cure.

The interface properties used for representing the failure kinematics of various failure modes are different, specifically for matrix failure, delamination, and fibre fracture. These interface properties may be defined separately in the TWM approach. This, however, requires a comprehensive material characterisation process. It should be noted that the material model used for cohesive failure modelling in this chapter is provided as a means to demonstrate this scaffold modelling framework for AFP laminates and is not being put forward as a novel approach in isolation. Hence, for the purpose of convenience, the failure criteria

Table 6.1. Material and interfacial properties for HST45E23/E-752-LT prepreg

Tow property	**Mean (CV %)**	**Source**
E_{11} (MPa)	125000	Park
$E_{22} = E_{33}$ (MPa)	8600	Park
$G_{12} = G_{13}$ (MPa)	4300	Park
$v_{12} = v_{13}$	0.3	Assumed
v_{23}	0.487	Assumed
Interface property		
G_{IC} (N/mm)	0.20 (2.7)	In-house test
G_{IIC} (N/mm)	0.89 (10.06)	In-house test
λ_n^* (MPa)	30 - 90	Assumed
λ_t^* (MPa)	73.42 (3.54)	In-house test
k_I (MPa/mm)	1e+05	Assumed
k_{II} (MPa/mm)	1e+05	Assumed
X_{ft} (MPa)	2243	Park

and material properties used for matrix cracking and delamination were assumed to be the same. These include the critical strain energy release rate for modes I and II (G_{IC}, G_{IIC}), the interlaminar normal and shear strength (λ_n^*, λ_t^*), and the cohesive stiffness for mode I and II (k_I, k_{II}). In this chapter, the critical strain energy release rates for $0° / 0°$ interfaces were characterised via double cantilever beam (DCB) and end notched flexure (ENF) tests following the respective standards (ASTM D5528 [151] and ASTM D7905 [152]), with the results listed in Table 6.1. For interfaces with mismatched ply angles (0° / θ°), previous studies [153-155] disagree on interface properties and behaviour when θ increases. In this study, 0° / 90° ply interfaces were assumed to be identical to 0° / 0° for simplification, but in general, these properties can be varied for each interface pair if these interfaces have been well characterised.

The cohesive strengths were generally assumed since these properties are challenging to measure experimentally. In this study, the interlaminar normal strength (λ_n^*) was assumed to be in the range between 30 and 90 MPa, which is a frequently assumed value. A sensitivity study, described in Section 6.3.2, was performed on the interlaminar normal strength (λ_n^*) and it was shown that the model was insensitive to this value within this range. The interlaminar shear strength (λ_t^*) was measured using the benchmark configuration per ASTM D2344 [109], per the results presented in Section 3.3.4. The cohesive stiffness (k_I, k_{II}) between 10^5 to 10^7 was commonly used in the literature [89, 100] while there is no definitive selection process for this parameter. A trial-and-error process is the only way to screen out the optimum value considering a good balance between numerical accuracy and convergence difficulty, as reported in Lu et al's work [142]. Values in the range of 10^3-10^7 were used in modelling with the benchmark configuration. The optimum value of 10^5 was selected for this analysis by checking the convergence of the model compliance.

For the fracture properties for fibre failure, the cohesive strength was essentially the tensile strength of 0° (X_{ft}), which is recorded in Table 6.1. For an accurate analysis, a thermal loading of -160℃ was applied to the model before any mechanical loading to account for the residual thermal stress results from the cooling process after cure. The corresponding thermal expansion coefficients were assigned as $\alpha_1 = 0.0$, $\alpha_2 = \alpha_3 = 3e - 5^o C^{-1}$.

6.2.4 Mesh size

The major advantage of the segment-to-segment cohesive contact interaction is that it allows a comparable mesh size with the cohesive zone length to be used. The cohesive zone length (l_{CZ}), or the length of the process zone, can be estimated via the Rice method [156], as expressed in Eq. (5). $G_c(\theta), \lambda^*(\theta)$ refer to the fracture toughness and maximum strength for a specific mixed-mode loading ratio (θ). E_m denotes the Young's Modulus of the matrix.

$$l_{CZ} = \frac{9\pi}{32} E_m (\frac{G_c(\theta)}{\lambda^*(\theta)^2}) \quad \text{6-5}$$

6.2.5 Strategies of modelling resin pockets, interpenetrations, and clearances

In the TWM method, although it can intrinsically capture the tow gaps and overlaps, small tow interpenetrations are inevitable due to the z-offset algorithm as discussed in Chapter 4. Another limitation of the algorithm is that the NURBS surface interpolation algorithm is essentially an approximation of the tow geometry, which also can cause some unexpected interpenetrations and clearances for complex structures. "Interpenetrations" and "clearances" are terms used to describe the geometric modelling errors resulting from the TWM algorithm and are used to distinguish from pristine tow gaps and overlaps.

Figure 6.5 depicts the interpenetrations and clearances for a typical AP-Ply configuration. This is an amplified view of tow thickness to highlight these geometric imperfections. Most FE packages, such as ABAQUS, have in-built functions to remove these small interpenetrations and clearances at the beginning of the simulation. Marc-Mentat also provides two options to deal with these small geometric errors, these are "Gaps/Overlaps Removed" and "Gaps/Overlaps Retained". The main issue with the former option is that the pristine tow gaps can be modified as well if this function is invoked. Hence, the latter approach was considered preferable and used in this work. The effect of the interpenetrations and clearances can be greatly mitigated by increasing the contact tolerance, which enables the neighbour tows to be still in contact without introducing any artificial initial stress. To verify this method, two single elements with and without geometric errors were tested and compared across tension, compression, and shear loading. Identical responses were recorded between these two cases.

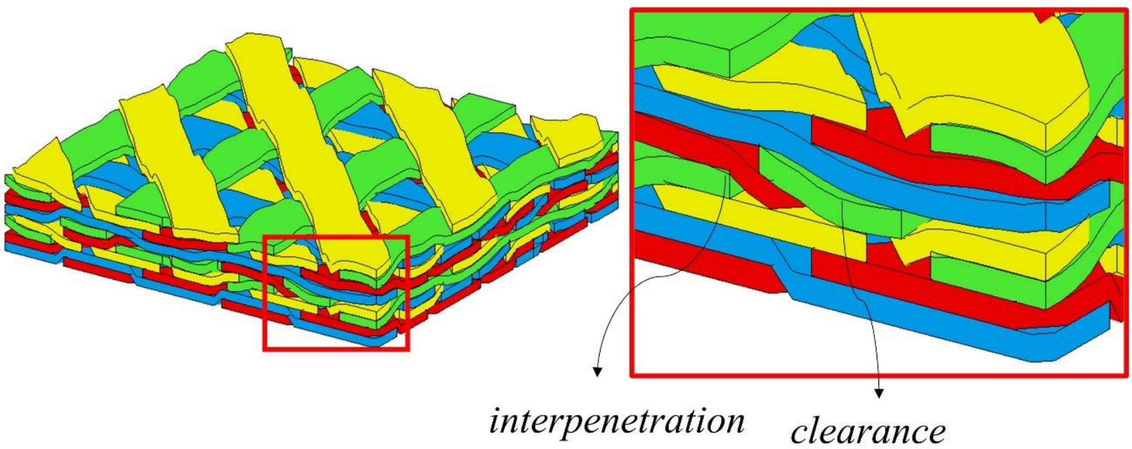

Figure 6.5. A schematic illustration of interpenetration and clearance issue.

The resin pockets induced by the pristine tow gaps during the curing process can be explicitly modelled as resin properties for simple applications, where the resin geometry can be defined using a triangular or rectangular shape (see Figure 6.6a). For complex resin geometries, explicitly modelling them is impractical. Hence, the resin pockets were often considered as voids (see Figure 6.6b). This assumption was used in Gan et al.'s work [157] and was supported by their experimental studies [158], which found resin pockets were often porous and failed at very low loading, and hence can be neglected for the prediction of a conservative strength property. An alternative way to model the resin pockets is to use cohesive contact interactions, as illustrated in Figure 6.6c. The initial distance of each contact interaction can be computed automatically by the in-built contact algorithm of FE packages. The cohesive stiffness of each interaction can be defined individually via dividing the resin elastic modulus by the respective initial contact distance.

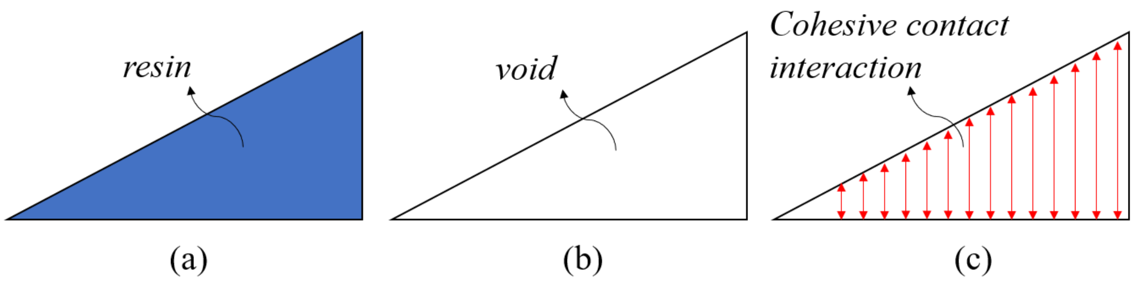

Figure 6.6. Potential ways of modelling resin pockets.

6.3 Short beam shear modelling

This section aims to demonstrate the application of the TWM method in the SBS test of AP-Ply. The finite element model setup is firstly introduced. Parametric sensitivity studies are performed next to mitigate the effect brought by the assumptions made in the material parameters. The numerical results are presented at last and a comparison with the experimental results is conducted.

6.3.1 Finite element model setup

For the SBS test, each tow was modelled with a layer of solid elements (type 7 in Marc-Mentat). Simplifications can be applied to AP-Ply2 by modelling two overlapped tows as one continuum body because delamination tended to arise at the interface with different fibre orientations. For clarity, the finite element (FE) model setup of AP-Ply2 is presented in Figure 6.7. The loading nose and support rollers were modelled as analytical rigid surfaces. Penalty-based touching contact interactions were assigned between the rigid bodies and the material model with a friction coefficient of 0.1 to avoid rigid body motion. Displacement control was applied to the loading nose via a control node with three rotational and two translational (X and Y) degrees of freedom being suppressed. A coarse displacement incremental size was applied when the model was linear elastic, and a finer incremental size was used near the region of failure initiation to further improve the computational efficiency.

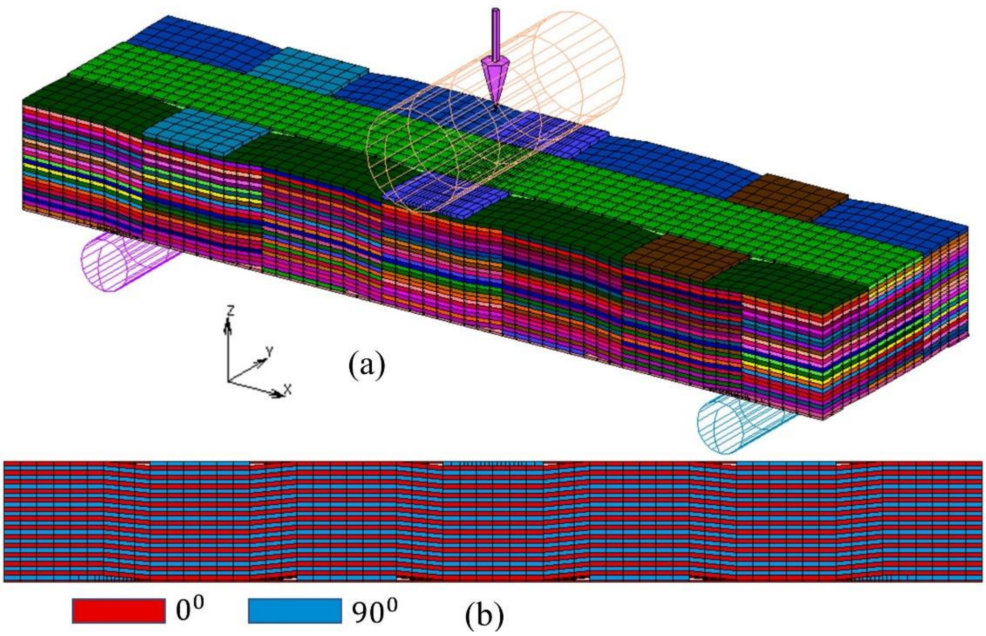

Figure 6.7. The finite element model setup of the short beam shear test, (a) The contact bodies assignment of AP-Ply2. Note: each 0 or 90 is assigned as an individual contact body (shown in different colours) while the same colour of different contact bodies can be observed as well, which is due to the colour scheme in Marc-Mentat (the colour will repeat after certain numbers), (b) The cross-sectional FE representation of crimping tows.

A global mesh size of 0.9mm was used with a mesh refinement of 0.2mm near the loading nose to improve the local contact interaction. Fibre failure, however, was not included as it is a rare occurrence in the short beam shear test. Although a small fibre crack near the specimen edge was observed in the present experiments, this was primarily induced by the loading nose with a small diameter (6mm), which led to a localised high-stress concentration under the contacting area. The replacement of a loading roller with a larger diameter or adding a rubber pad can significantly alleviate this issue as shown in Abali et al.'s work [159]. Close inspection of the global load-displacement curve and failure initiation and propagation in Figure 6.8 shows that the failure under the loading nose leads to a slight global stiffness variation without affecting the ultimate short beam shear failure response. Additional failure modes introduce extra model complexity and numerical parameters that dilute the main aims of this work and hence were left out of the scope in this study.

As observed from the SBS experiments, each tow was thinner but wider due to the artificially designed tow-to-tow gaps. Hence, the as-cured tow dimensions were used as the input parameters for the TWM. The differences in ultimate specimen thickness between AP-Ply configurations and the Benchmark were in the range of 0.2mm, which leads to a variation of as-cured ply thickness of 0.0037mm. This difference is minimal and can be neglected, and thus the tow cross-section was modelled as 7.65 x 0.121 mm in this study. For AP-Ply laminates, the mean crimp angle was used as the first trial and the variation effect were further studied in Section 6.3.3. The resin pockets were primarily observed in the top and bottom layers across the thickness of the AP-Ply laminates, which are beyond the region of interest. The size of this small triangular area was computed based on the as-cured tow thickness and crimp angle.

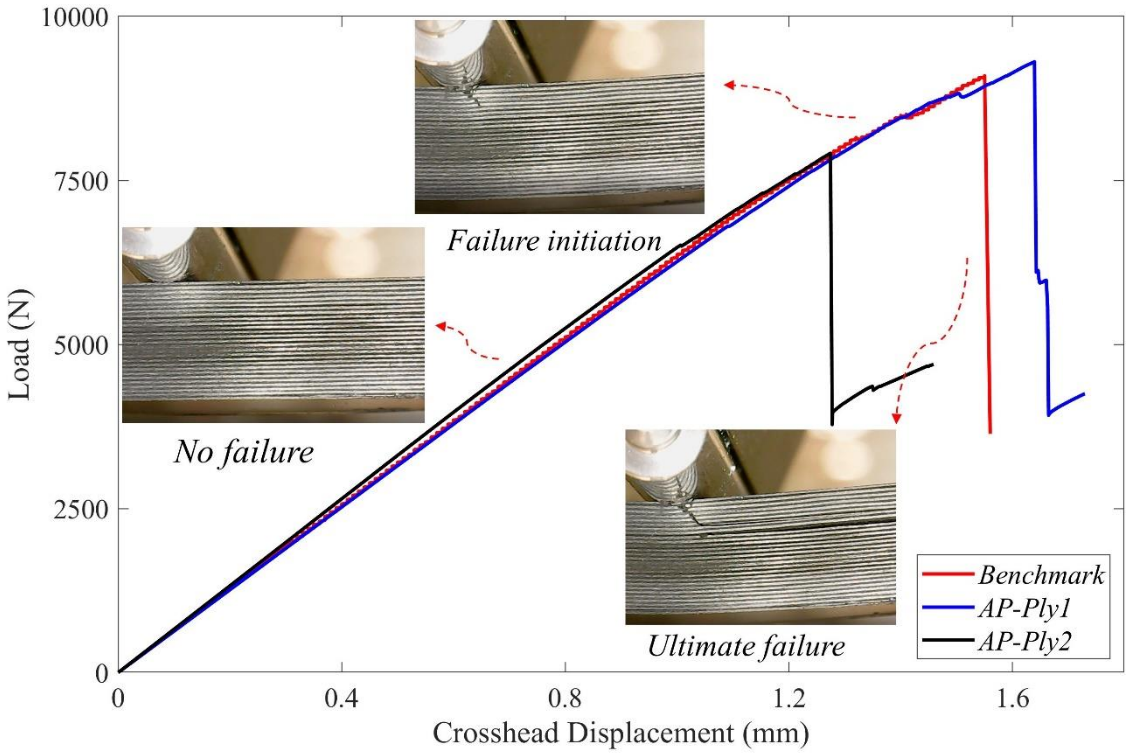

Figure 6.8. The comparison of global SBS responses of different laminate configurations.

6.3.2 Parametric sensitivity study

In this section, a sensitivity study is conducted to mitigate the effect brought by the assumptions made in the material parameters, including the enhancement factor μ, the mixed-mode interaction parameter α, and the interlaminar normal strength λ_n^*. For simplification purposes, a 2D plane strain finite element model was used to perform the parametric sensitivity study with the Benchmark configuration. The initial estimation of these values was obtained from the literature, which indicated $\mu = 0.7$, $\alpha = 1$, and $\lambda_n^* = 30$ MPa. To isolate the effect of the tested parameter, other parameters were kept constant with the initial assumption.

As suggested by Li et al. [147], the enhancement factor was related to the material strength which could be dependent on the material type. It is thus worth investigating the effect of different values on the failure response. In this study, the value of μ ranging from 0.1 to 0.8 was analysed. It was found that the numerical results tended to converge when the enhancement factor μ was greater than 0.5. The representative failure responses and global load-displacement curve are indicated in Figure 6.9 and Figure 6.10 respectively. When μ was smaller than 0.5, some of the sub-cracks were observed to occur near the loading roller, leading to a small percent of load drop as shown in the global load-displacement response. While when μ was increased, these sub-cracks can be suppressed completely, and a converged global-load displacement response can be obtained. This confirmed a similar result shown in Zhang et al.'s work [129], where a converged result can be achieved when the friction coefficient included in their model was greater than 0.6. Hence in this study, the enhancement factor 0.7 was applied throughout the 3D modelling of the Benchmark and AP-Ply configurations.

The mixed-mode interaction parameter is an empirical parameter, which is in the range from 1 to 2. Although the value of 1 was commonly used in many studies [98], the effect of the parametric variation on the numerical result needs to be investigated. In this section, the parametric values of 1, 1.2, 1.4, 1.6, 1.8, 2 were analysed, and all other model parameters remained constant. The global response and the crack morphology, however, were identical. The same trend was also observed when a parametric study was performed using the interlaminar normal strength. The strength was varied between 30 and 90 MPa, which is a commonly used range in the literature with cohesive interface failure modelling [89, 144]. This is because the short beam shear test in this study is a mode II-dominated failure test, which is independent of the mixed-mode interactions and Mode I parameters.

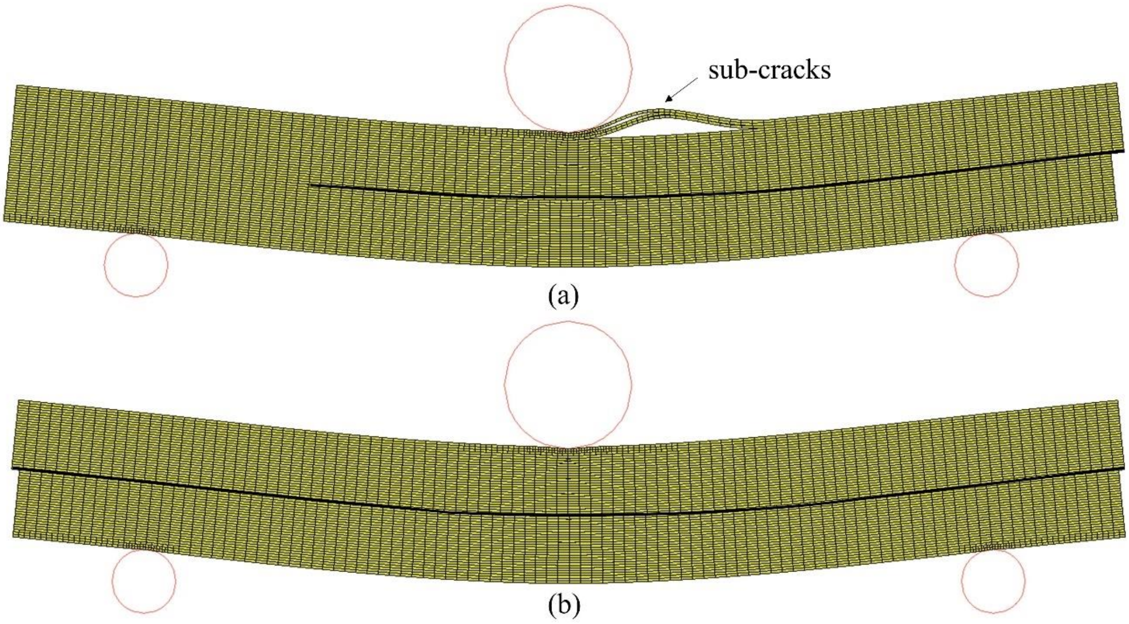

Figure 6.9. Representative failure responses of the numerical model with different enhancement factors (a) 0.1 to 0.4, (b) 0.5 to 0.8.

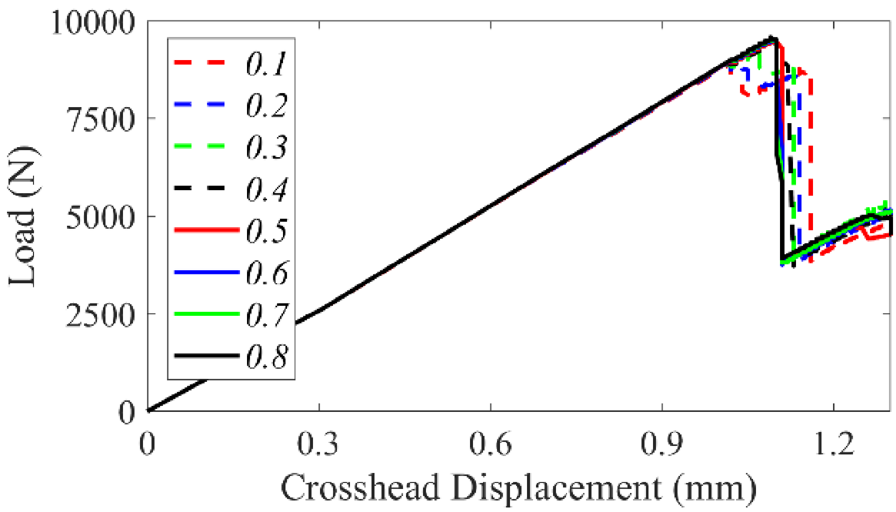

Figure 6.10. The global responses of the numerical model with different enhancement factors.

6.3.3 Results

With the aforementioned FE settings in Section 6.3.1, the SBS model in total have approximately 82k nodes and 33k elements. The simulation was performed with a Intel Xeon 8-core computing node. The total run time is around 6hrs.

For the SBS test, the crack path and global response were the primary metrics of comparison. It was observed from the experiments that for two different AP-Ply configurations, the main crack propagated along with the weaving interface and deflected in the through-thickness direction at a certain spot. This was a critical phenomenon to predict in understanding the failure mechanisms of the AP-Ply laminate. The numerical predictions of the three laminate configurations using the TWM and the comparisons with the experiments are presented in Figure 6.11. It can be noted that instead of a clean and flat crack as observed in the Benchmark, the through-thickness deflections of the crack were identified in both of the AP-Ply configurations.

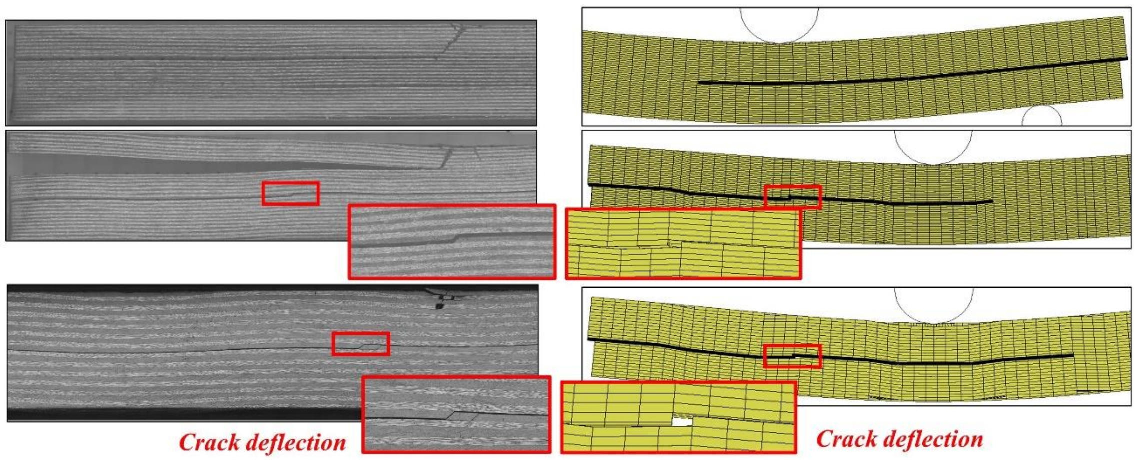

Figure 6.11. The short beam shear failure predictions of three laminate configurations (from top to bottom: Benchmark, AP-Ply1, AP-Ply2).

For the AP-Ply laminates, the simulation results indicated that the crack initiated near the woven area and subsequently propagated in both directions. This can be induced by the stress concentration resulting from fibre crimping, which in turn, explained the critical effect of fibre crimp angles on the short beam strength. AP-Ply1, with a smaller crimp angle, showed comparable short beam strength, as both shown in the experimental and numerical results. It should be noted that the major crack location in the through-thickness direction, however, showed some differences between the experiment and simulation. This was mainly due to the stochastic nature of the composite material properties and geometric variations, which induced slight differences in maximum interlaminar shear stress across the thickness.

To account for the variation in the measurement of the tow crimp angle in the AP-Ply laminates, 3 different values with 20% variation of the mean value were modelled for AP-Ply1 (2.4°, 3°, 3.6°) and AP-Ply2 (3.7°, 4.6°, 5.5°) and the results were represented as the coefficient of variation (CV) in Table 6.2. It can also be noted that the tow crimp angular variations applied caused minor discrepancies in the SBS results. For each laminate configuration, an identical ultimate fracture mode and location were found despite the variations of tow crimp angle. The significant SBS difference between AP-Ply1 and AP-Ply2, as noticed from both the experiment and simulation, suggested that a single-tow weaving can provide better performance in this specific loading condition. This could be related to the effect of crimp angle and weaving morphology which, however, is out of scope in the present study.

Table 6.2. The comparison of the SBS between numerical and experiment. Note: the CV of AP-Ply laminates in simulation refers to the results of different tow crimp angles.

Configuration	**Experiment Mean (CV %)**	**Simulation Mean (CV %)**	**Difference**
Benchmark	73.42 (3.54)	78.99	7.59%

AP-Ply1	72.78 (2.97)	76.09 (0.91)	4.55%
AP-Ply2	65.08 (3.15)	64.22 (2.52)	-1.32%

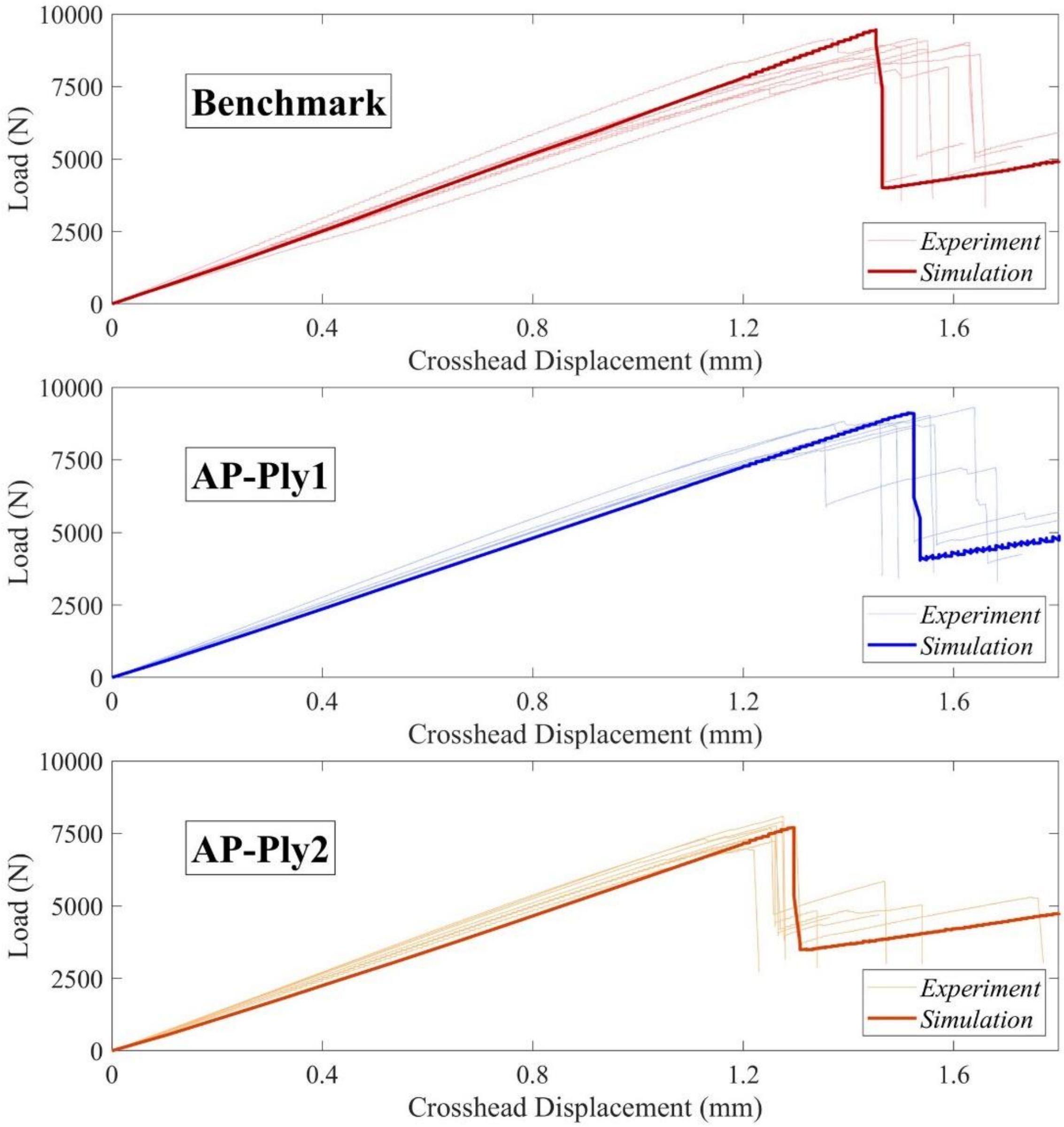

Figure 6.12. The comparison of global responses of different laminate configurations between simulation and experiment for SBS test.

Besides the cracks, the numerical global load-displacement responses were also compared against the experiment, as shown in Figure 6.12. As the displacement was recorded in terms of the crosshead movement, the simulation results were all scaled with a common factor of 1.2 to match the initial elastic stiffness. The same strategy was also used by Hallett et al. [144] to account for the compliance of the testing fixture. An excellent agreement was achieved for both the global load-displacement response and the SBS between the simulation and experimental results, which hence, validated the feasibility of the TWM in the applications of AP-Ply laminates with SBS test.

6.4 Low-velocity impact modelling

This section demonstrates the application of the TWM method in the LVI test of AP-Ply. The finite element model setup, as well as the modelling strategies, are firstly introduced. Identical material inputs to the SBS test were also used in the LVI test to maintain consistency. The comparison between the numerical and experimental results is presented.

The LVI test was assumed to be quasi-static which means the kinetic inertia was neglected. This assumption has been confirmed by many studies [160-163], which identify a high degree of equivalence between the LVI and the quasi-static indentation tests. Due to the LVI event occurring within a short period, only the ultimate fracture pattern is captured. Understanding the failure initiation and propagation mechanisms during the LVI can facilitate the development of more efficient structural designs. Hence, some studies [98, 115] adopted quasi-static indentation tests to facilitate the understanding of the failure mechanisms during the LVI event.

6.4.1 Finite element model setup

(a) Modelling strategies

Considering the physical size of the LVI specimen (150x100mm) compared to the SBS sample (52x14mm), the total required elements are substantially increased. Due to the limitations of available computational power, several strategies were used in this test to improve the computational efficiency which include:

- The TWM was only applied to the region of interest while the other areas were modelled as continuum.
- The effective area of the specimen is 125x75mm which is identical to the cut-out size. Hence, the specimen was modelled as 130x80mm instead of 150x100mm.

To illustrate these strategies, the finite element model setup of the LVI test is presented in Figure 6.13. The impactor was modelled as a hemisphere with brick elements (~0.4mm). An isotropic material property with modulus of $2x10^7$ was used to ensure a negligible deformation occurred in the impactor without having numerical convergence difficulties. The load was applied to the impactor via a control node. The support platform and clamps were modelled as analytical rigid surfaces, which were contacting the laminates with a friction coefficient of 0.1.

Based on the experimental observations of internal damage size, the maximum value of 42.3x33.38mm was noted at the UD configurations. Hence, the size of the region of interest was identified to be 50x50mm as shown in Figure 6.13c. This region was modelled at a length scale of tow (TWM) while the outer areas were modelled as continuum. A full glue (tied) interaction was used to connect these two parts. To achieve this, the TWM was firstly applied to generate the full scale of the laminates, this was followed by a global mesh trimming procedure to obtain the FE model of the region of interest. The FE representations of each laminate configuration at this region is shown in Figure 6.14.

The mesh density of the FE model can be observed via Figure 6.13a-b, in which a coarse mesh size of 4mm was used in the outer region while a fine mesh size of 1mm was applied to the region of interest. For the outer region, a composite element type of 149 in Marc-Mentat was used. While for the TWM, each tow was modelled with a layer of solid elements (type 7 in Marc-Mentat).

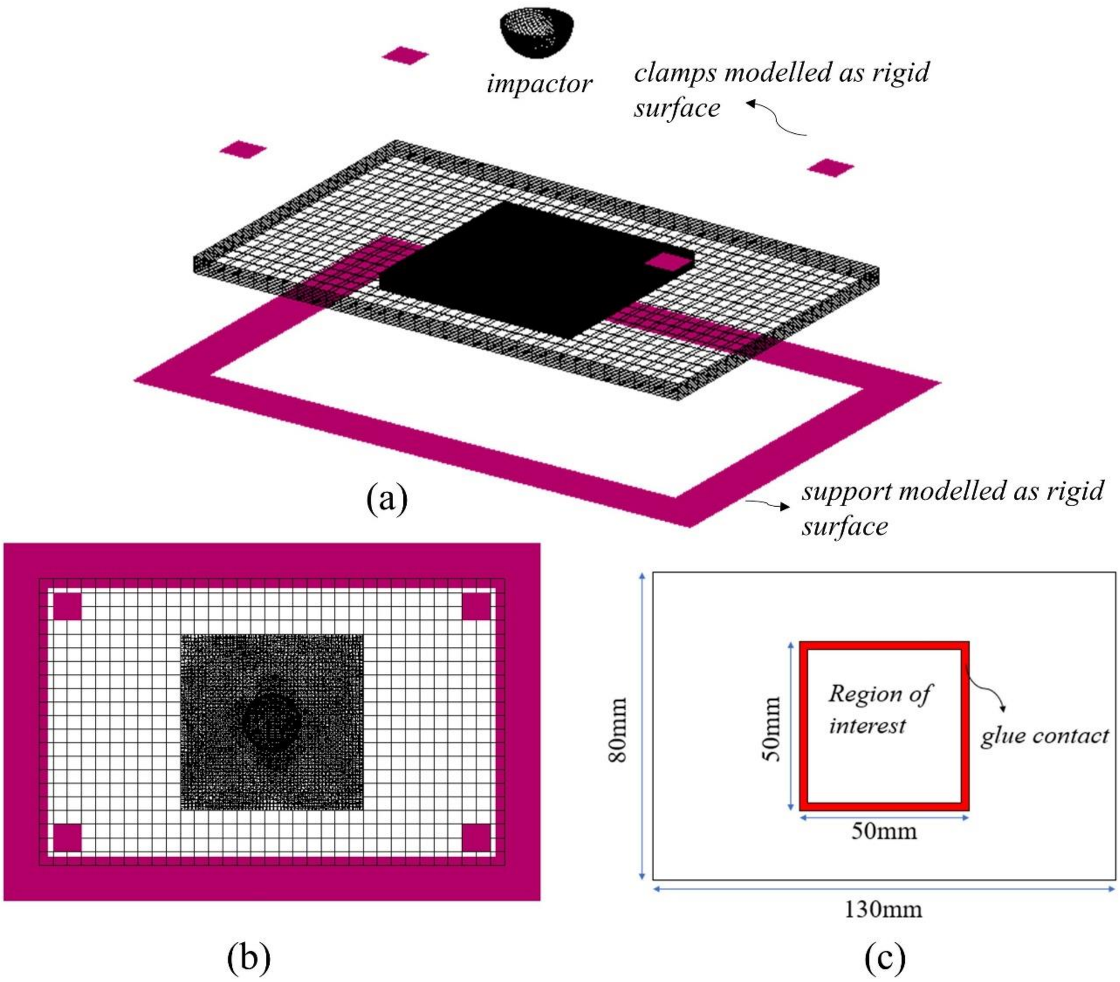

Figure 6.13. The FE setup of LVI test.

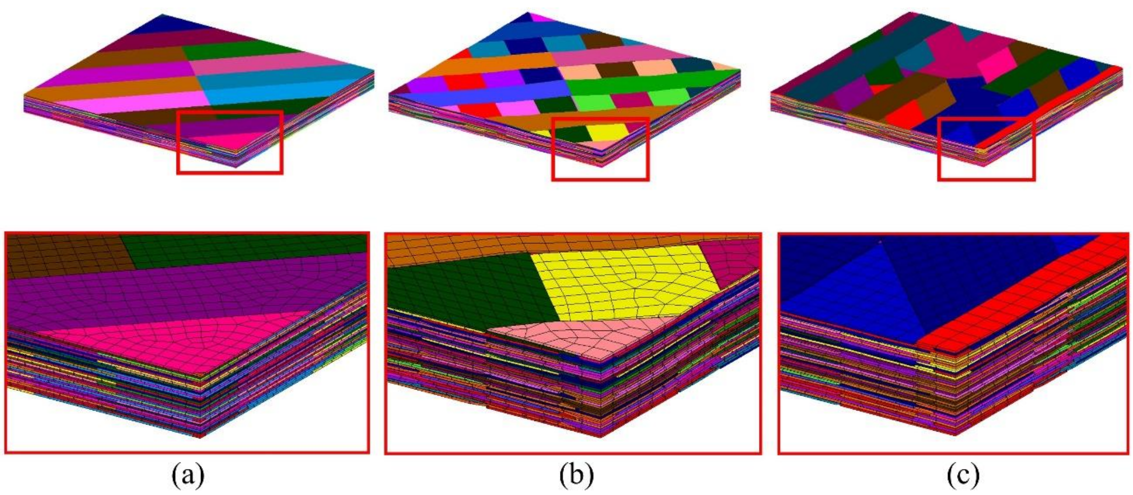

Figure 6.14. The FE representations of tow wise modelling in the region of interest.

(b) Failure modelling

The failure kinematics modelling of the LVI test was achieved by allocating the cohesive interactions along with the potential failure path, as shown in Figure 6.15. Specifically in this study, the cohesive interactions were allocated along with the tow-by-tow interfaces to capture both in-plane matrix cracking and out-of-plane delaminations. For fibre failures, the cohesive interactions were assigned within the tows, which were perpendicular to the fibre axis. This process was achieved via trimming the tows transversely, creating two independent segments for each tow as illustrated in Figure 6.16.

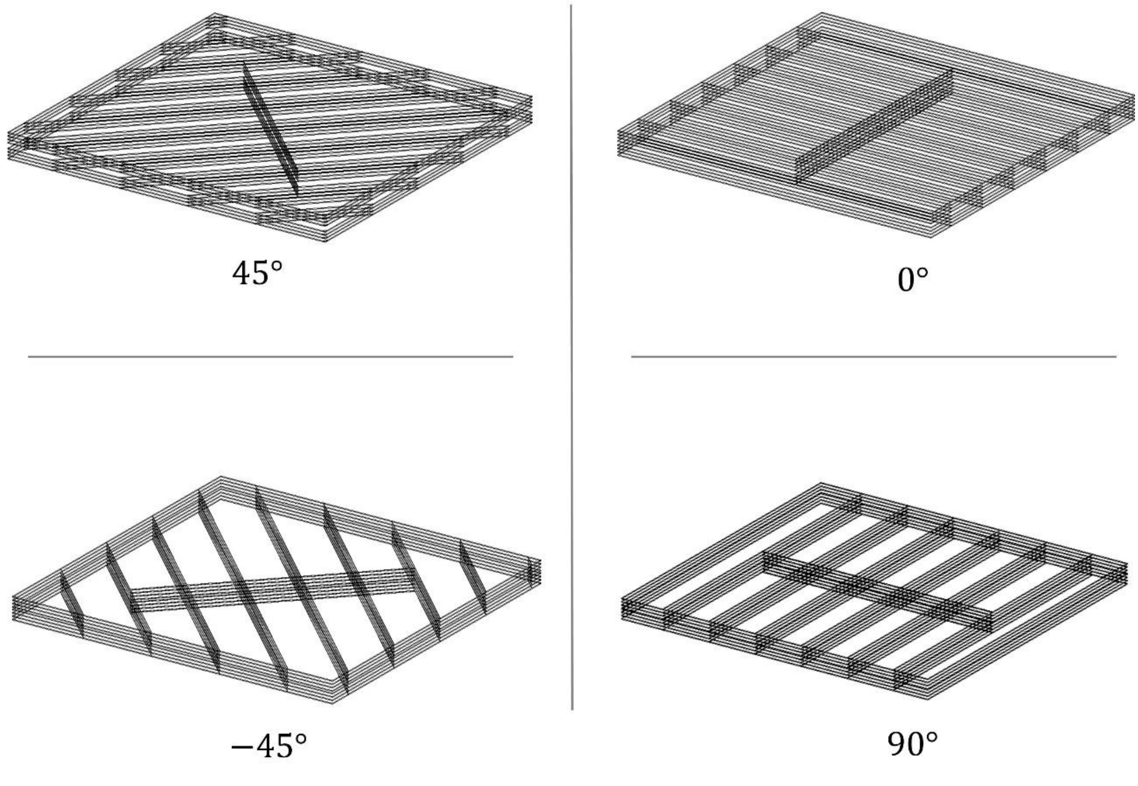

Figure 6.15. The schematic diagram of cohesive interfaces allocation.

It should be noted that for the trimming process, two cuttings were required to obtain two segments with gap. The main purpose of this gap is to allow the assignment of different cohesive interactions between these two segments in later procedures. The cohesive interactions between two different contact bodies were essentially built by the automatic contact detection with user-specified contact tolerances. For example, if no gap exists between these two segments, it would be challenging to distinguish the cohesive interaction used to model the in-plane matrix cracking and the cohesive interaction used to predict the fibre failures. The gaps allow users to explicitly build different cohesive interactions for describing various failure modes of the composite laminates by tailoring the contact tolerance. In general, the gap size can be around 0.01mm, hence will not affect the overall material behaviour.

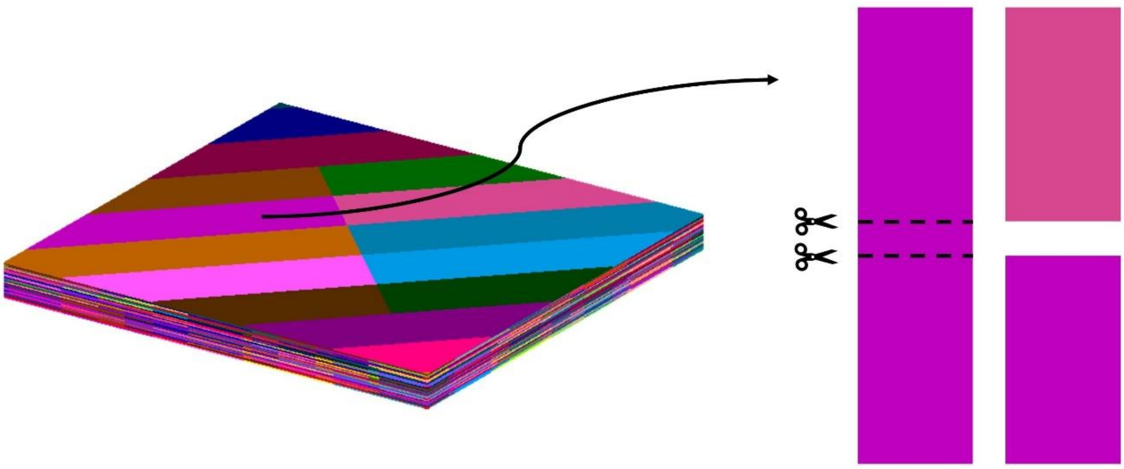

Figure 6.16. The illustration of tow cutting in order to allocate cohesive interfaces for fibre failure modelling.

The matrix cracking, fibre failure and delamination can be represented with different interaction IDs. In Marc-Mentat, a contact table is used to summarise the contact properties of the model, specifically including the contact pairs, as well as the interaction properties. This contact table can be exported as a 2D matrix, which stores the contact pair information and the associated interaction ID. Based on the interaction ID, the specific cohesive properties can be assigned accordingly to each contact pair.

6.4.2 Results

This section presents the numerical results of the LVI tests using the aforementioned high-fidelity FE technique. All the laminate configurations with an impact energy of 40J were simulated. The key results including the global load-displacement response and the internal damages are compared against the experimental results. With the aforementioned FE settings in Section 6.4.1, the LVI model in total have approximately 222k nodes and 100k elements. To further improve the computational efficiency, a high performance computing cluster in Katana UNSW which consists of 32 cores was adopted for this study. The total run time for this study is around in the range of 120-200 hrs.

(a) Global response

Figure 6.17 depicts the typical damage mechanisms of composite laminates under LVI. This figure comprehensively illustrates the damage onset and growth of the UD configuration. AP-Ply also showed similar failure response but with more complex through-thickness geometry, hence was not included for clarity. It can be noted that the 3-phases damage mechanisms were well predicted with the TWM including (i) no damage which refers to a linear elastic response, (ii) a load drop and stiffness variation which corresponds to matrix cracking and delamination initiation, (iii) a significant load drop which refers to fibre failure initiation and propagation. To further validate the numerical model, the global load-displacement response of each laminate configuration is presented in Figure 6.18. The key parameters involved in this 3-phases damage mechanisms were compared against the experiment results including the linear elastic stiffness, the first load drop (delamination threshold), and the significant load drop (peak load).

In general, a great correlation was achieved in terms of the trend of the global load-displacement response. For each laminate configuration, a good correlation regarding the initial stiffness before the first load drop was noticed between the numerical and experimental curves. The delamination thresholds were also in good agreement with the experiment. One critical feature was that AP2D indicated a higher delamination threshold than the other two laminate configurations and this difference was also observed in the experiments as discussed in Chapter 3, in which the results showed that AP2D had an approximate 10-20% higher delamination threshold than UD and AP3D. This can be induced by the difference in laminate stacking sequence as the delamination threshold was critically dependent on the interlaminar stress.

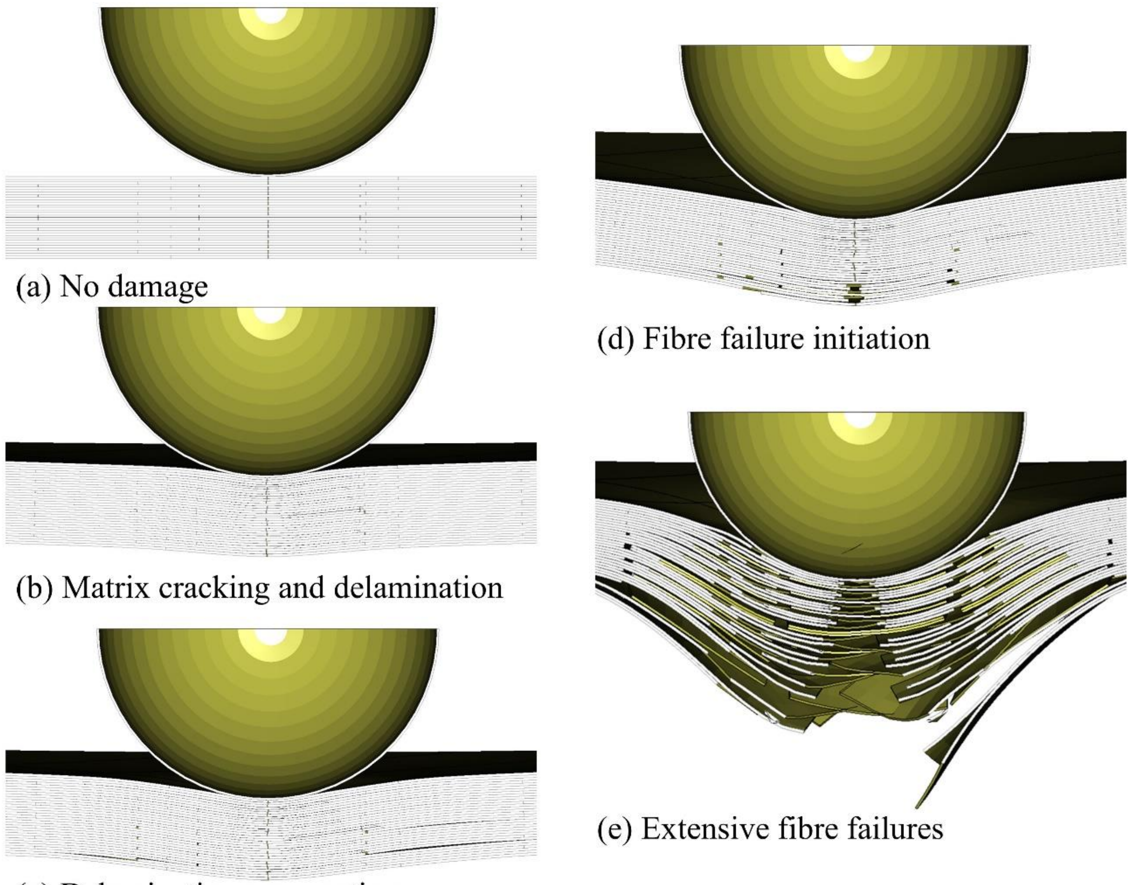

(a) No damage

(b) Matrix cracking and delamination

(c) Delamination propagation

(d) Fibre failure initiation

(e) Extensive fibre failures

Figure 6.17. The illustration of damage initiation and progression under LVI for UD.

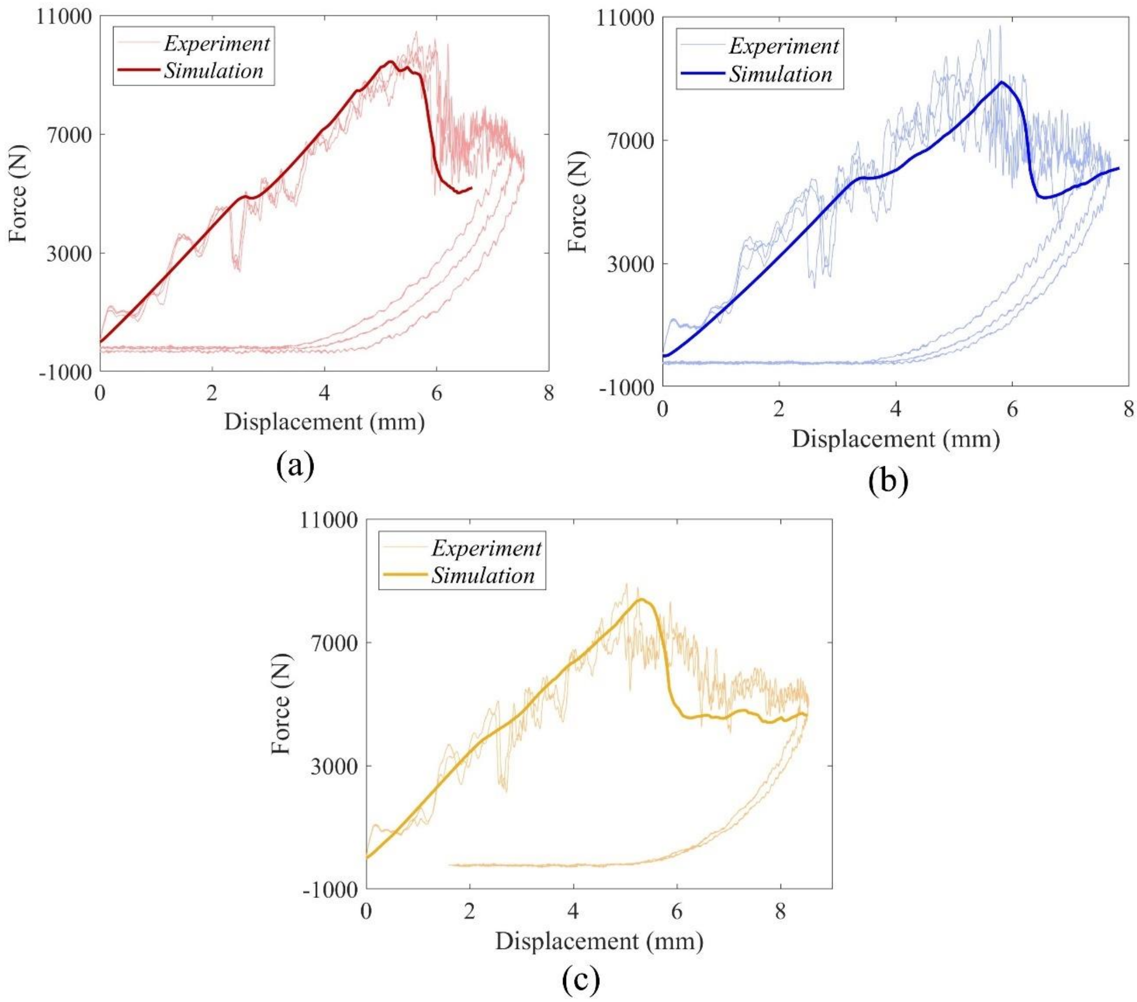

Figure 6.18. The comparison of global responses of different laminate configurations between simulation and experiment for the LVI test.

For each laminate configuration, the peak load of the simulation also exhibited a good agreement with the experiments. Slight differences can be attributed to the locations of assumed fibre failures. Adopting multiple potential fibre failure paths may alleviate this issue as in Sun et al.'s work [98] but also requires extra computational effort. This approach will be considered in the future applications as this study mainly aims to demonstrate the scaffold modelling framework for AFP laminates.

For the post-failure response, UD and AP-Ply laminates also exhibited a great correlation with the experimental results in terms of the percentage of load drop and ultimate retained load. However, instead of a few discrete load drops as shown in the experiments for AP-Ply laminates, the simulation indicated one primary load drop. It should be noted that it is very difficult to precisely capture the post-failure response of composite laminates especially for complex structures. Based on the experimental studies, the through-thickness view of impacted specimens indicated that more matrix cracking, delamination and fibre failures tended to occur in the AP-Ply laminates than UD. These fibre failures can be irregularly distributed and interact with other failure modes. In this study, the fibre failure was assumed to occur underneath the impact centre and well defined for model simplification. Again, allocating multiple potential fibre failure paths could potentially improve the model accuracy with extra computational effort.

(b) Damage prediction

In addition to the comparison of the global load-displacement response, the delamination threshold, the peak load and the post-failure response, it is also necessary to compare the internal damage patterns to facilitate understanding of the failure mechanisms of composite laminates. Figure 6.19 presents the damage status of UD, AP2D and AP3D under different impactor displacements. At a displacement of 1mm, no damage occurred, and the laminate behaved linear-elastically. Some trivial damages were observed in AP-Ply laminates underneath the impactor. This was attributed to the effect of the tow weaving area, which led to resin-rich zones and caused stress concentrations. At the displacement of 3mm, it can be clearly observed that a large delamination occurred in the UD configuration. AP2D and AP3D also exhibited some delaminations, but with a relatively smaller size compared to UD. This explains the first load drop and stiffness variation. The difference was primarily caused by the semi-woven fibre architecture and laminate stacking sequence, in which the former tended to impede the delamination propagation and the latter can result in different interlaminar stress states.

The delamination tended to propagate further, and fibre failure occurred, with increasing displacement loading. The ultimate damage size was compared to the experimental results obtained via an X-ray CT Scan, as presented in Figure 6.20. Both the experiment and simulation indicated a smaller damage size of AP-Ply compared to UD. For each laminate configuration, however, the simulation showed a slightly larger damage size than observed from the experiment. This can be attributed to three major factors. The first is due to the voxel resolution (~0.04mm), which was the same order of magnitude as the ply thickness due to the size of the sample. Hence, interface damage larger than this threshold can be captured, which resulted in a conservative damage size. The second critical factor is due to the material properties of composites. As aforementioned, the material properties used in this study were used as a means to demonstrate the TWM framework for AFP composites and have not been fully characterised. Although analytical calibrations and sensitivity studies were both conducted to mitigate the effect brought by the difference in material properties, variations still exist in composite laminates and cannot be removed completely. The last major reason is the assumption of localised fibre failure in the TWM, which can also affect the damage size as in reality, there is likely a lot more fibre breakage which absorb energy. In the absence of the capability of modelling this kind of energy absorption, the interlaminar damage will be larger to compensate. In general, the TWM exhibited a great capability in predicting the failure mechanisms of AFP laminates under LVI testing.

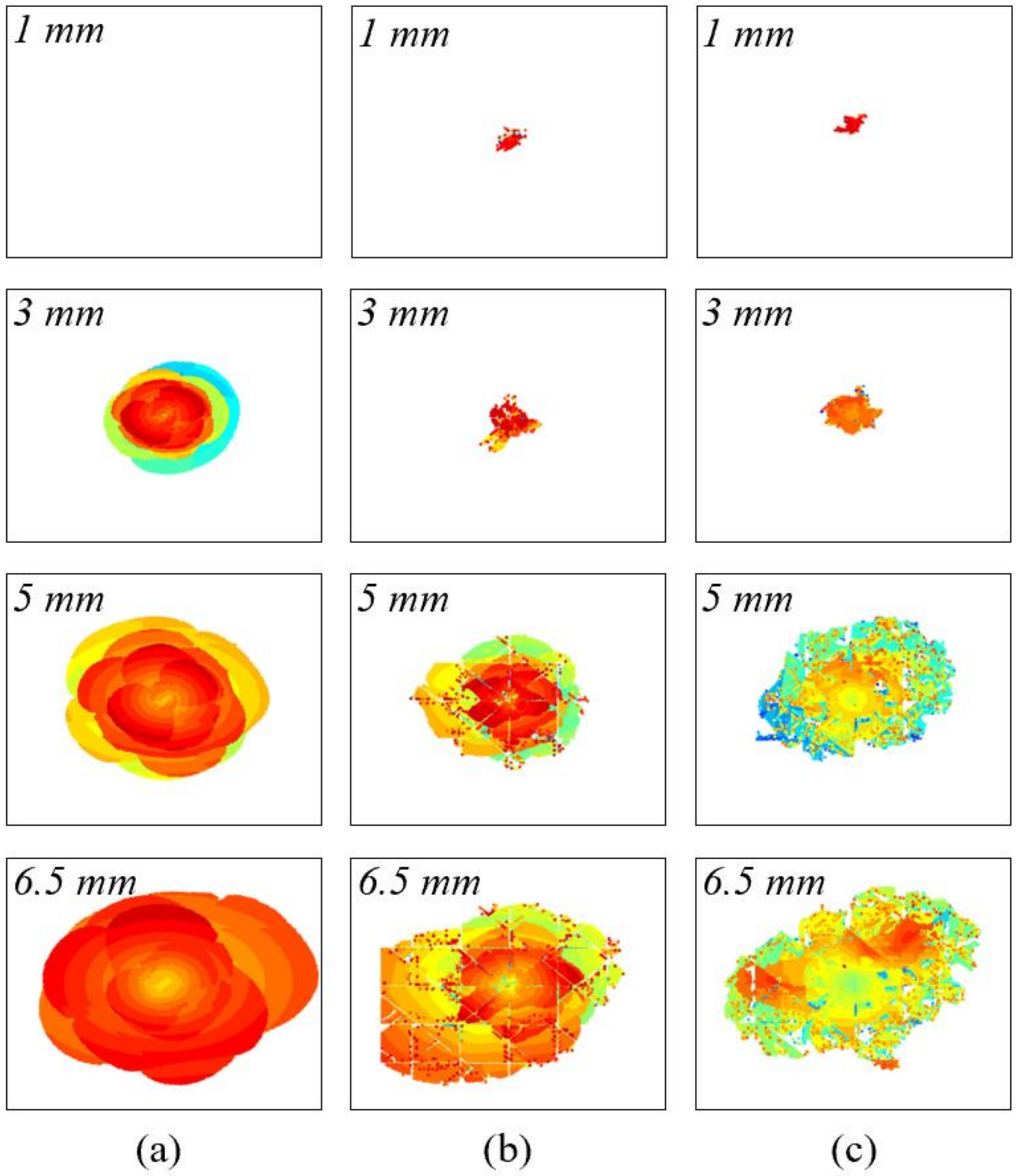

Figure 6.19. The top view of simulated internal damage progression for (a) UD, (b) AP2D and (c) AP3D. The colour refers to the depth of delamination in the thickness direction.

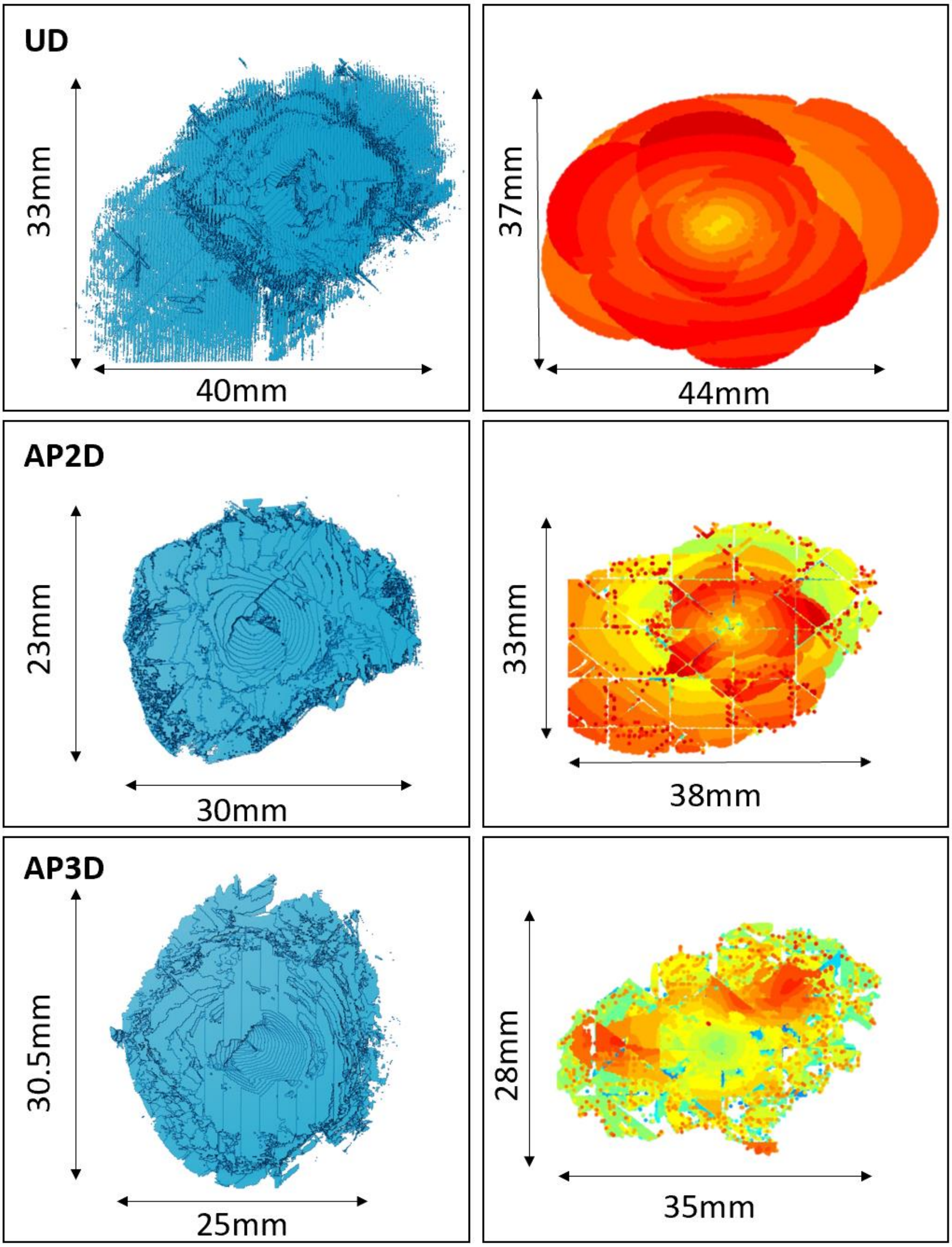

Figure 6.20. The comparison of ultimate damage size for different laminate configurations.

6.5 Summary

Due to the inclusion of defects in the AFP composites, the prediction of mechanical properties and failure mechanisms becomes more challenging than conventional laminates. A tow-wise modelling (TWM) framework was presented in this chapter with enhanced fidelity of mesoscale laminate features to model the AFP composites. The TWM approach is designed as an intermediate step between full micro-/meso- continuum models (very small scale but high fidelity) and homogenised laminate models (large scale but no resolution of internal features). The predictive capability is substantially improved with the refinement of model scale but also refers to a significant increase of computational cost. As an intermediate step, TWM offers great capabilities of predicting many unique failure events occurred at AFP composites with affordable computational resources.

AP-Ply, which is one of the typical AFP composites, was used in this study to demonstrate and validate the capabilities of the TWM framework. Due to their weave-like mesostructure, it has been proposed that AP-Ply laminates can reduce interlaminar damage propagation under certain loading conditions [3]. These laminates contain geometric features including gaps, overlaps, thickness variations, tow drops, etc, which have been demonstrated to significantly impact on failure initiation and progression [6, 61, 62]. Among the experimental studies of AP-Ply laminates in Chapter 3, the SBS and LVI tests were virtually simulated in this Chapter.

By modelling each tow individually, following the tow placement sequence of AFP, the TWM provides a native way for handling the semi-woven structures of AP-Ply laminates, retaining key features including gaps, overlaps, thickness variations, tow drops, etc.

Cohesive interactions along tow-by-tow contact interfaces allow the TWM to inherently capture discrete inter- and intra-ply damage, without the need for complex mesh splitting and re-meshing algorithms. Based on the present study, the following key conclusions can be drawn:

- The excellent correlation between numerical and experimental results has revealed that the TWM can predict interface failure, crack deflection, and the ultimate delamination fracture load of AP-Ply laminates with great accuracy.
- Based on the simulation of SBS testing, it was observed that the major crack initiated near a weaving corner and then propagated along both directions. This suggests that the SBS failure of AP-Ply laminates was induced by the stress concentrations due to tow crimping, and in turn demonstrated the significance of modelling these AFP manufactured mesoscale geometric features.

Fibre failure was considered in the LVI test. Slight differences were observed in terms of the peak load and post-failure response of AP-Ply laminates between experimental and numerical results. The main reason is that the fibre failure is an extremely complex phenomenon which is generally associated with explosive matrix splitting and large delaminations. This study greatly simplified the fibre failure modelling by assuming a well defined crack path, which was located near the indentation area and orthogonally to the material axis within the tow. Future applications could consider allocating multiple potential fibre and matrix failure paths within the tow to further improve the numerical accuracy.

Chapter 7 Conclusion

7.1 Overview

AFP is gaining increasing use in composites manufacturing, especially for complex structures in the aerospace sector. AFP also exhibits advances in making further lightweight composite structures due to the capability of fibre path customisation. One of the main issues of AFP applications are that the fibre path can be tailored in a very complex manner, such as a linearly varied curved path used in VSL, analysing the structural performance can be extremely challenging due to the anisotropic material properties. The challenge can be further increased with the introduction of manufacturing-induced geometric features, which were also described as AFP signature in some studies [7, 164]. Although a lot of research has attempted to characterise the effect of these defects, the understanding is still scarce due to the huge parameter space of the defects (morphology, location, distribution, etc.), particularly for advanced AFP laminates.

Numerical modelling is an important method to facilitate the understanding of the defects, and hence the structural performance of AFP composites without onerous and expensive experimental tests. The existing numerical methods, however, are limited to the length scale of laminate or ply, which cannot represent the individual tow morphology and innate geometric features effectively and precisely. Hence, as a step forward, this thesis developed a novel finite element approach based on a length scale of tow, called the tow wise modelling (TWM), to predict the mechanical properties of AFP composites. The TWM approach not only allows for modelling of general AFP laminates with complex fibre path, the advanced AFP laminates involving a great deal of mesoscale geometric features can also be directly modelled with less simplifications required than traditional methods.

AP-Ply is one of the representative AFP applications and involves numerous defects that are extremely challenging for available modelling methods in the literature. Thus, the AP-Ply has been experimentally investigated in this thesis to provide a database for model development and validation. Considering the pre-processing effort of the model generation at a length scale of tow, a python-based script has been developed to virtually build the FE model automatically following the robotic kinematics and user inputs. Through the development of a computationally efficient cohesive network approach, the critical failure kinematics of AFP composites at the length scale of tow can be represented. The key features of this method are having a large mesh size tolerance and being capable of dealing with non-conformal meshing interfaces easily. With the integration of the cohesive network approach into the TWM, the mechanical properties of AFP composites, as well as the failure mechanisms can be predicted.

7.2 Key findings and advancements

The key findings and advancements of each thesis chapter to the field are summarised in this section.

7.2.1 Experimental studies of AFP composites

The experimental studies of AP-Ply laminates are limited to a few studies, which demonstrates the potential of AP-Ply in improving the damage tolerance and reducing the thermal warpage [3, 34]. The understanding of AP-Ply is still scarce due to the huge design space. Hence, this thesis developed more experimental programs to facilitate the understanding of AP-Ply with emphasis being placed on the short beam shear (SBS), low-velocity impact (LVI), combined loading compression (CLC), and compression-after-impact (CAI) performance. Based on existing studies, the key findings include:

- It has been proven that a modest amount of inter-ply tow weaving has no effect on the short beam strength. Increasing the tow weaving depth, on the other hand, resulted in an 11.36% reduction in short beam strength. The variances can be attributed to the effect of weaving parameters. The results of the experiments also revealed that an optimal AP-Ply design may be established, which improves impact resistance while maintaining static laminate strength.
- The traditional AFP laminates and AP-Ply exhibited similar global load-displacement responses under LVI, which included 3-phase damage mechanisms that were commonly observed in the LVI tests of conventional laminates. One of the major differences of AP-Ply over traditional AFP laminates was a small degree of plasticity both observed in the AP-Ply configurations during the phase-3. In addition, the semi-woven structure has also been shown to have a great impact on the delamination threshold, peak load and energy absorption.
- A significant difference in the failure mechanisms was noted between traditional AFP laminates and AP-Ply under LVI, where the former only exhibited a few major delaminations and a minimum amount of fibre failures while the latter showed many more concentrated delaminations, matrix and fibre failures. The CT scanning results clearly indicated that

the damage size of AP-Ply was much smaller than the traditional AFP laminates.

- The CLC test showed similar global load-displacement results between AP-Ply and traditional AFP laminates, which indicated that a small degree of inter-ply tow weaving does not necessarily affect the laminate in-plane compressive strength.
- The CAI test showed a significant difference between AP-Ply and traditional AFP laminates. For the samples under lower impact energy 25J, AP-Ply outperformed traditional configurations by up to 17%. While for the case with 40J, the improvement is more advantageous and can be up to 29%. This result indicates that AP-Ply laminates have potential to achieve higher damage tolerances without sacrificing the in-plane properties as shown in CLC tests. The benefits of AP-Ply are more evident particularly at higher impact energy levels.

7.2.2 TWM method

Automation of composites manufacturing is an inescapable trend. It is not only capable of reducing production cost and waste but also enabling novel approaches to laminate design. Many design paradigms are being challenged by innovations, such as fibre steering, which can *only* be achieved through automation. This research is an important contribution to the suite of digital tools required to drive automated manufacturing into exciting new areas.

A significant advancement of this research is to model AFP composites at a length scale of tow rather than ply or laminate. The tow-wise modelling (TWM) aligns with the minimum structural unit in AFP manufacturing, which hence, creates the possibility for model generation with automation. The automation substantially reduces the pre-processing effort of modelling in finite element analysis, which is also a critical step to bring AFP into industry 4.0.

The major benefit of the TWM is the capability of explicitly modelling the manufacturing-induced defects, gaps, overlaps, tow crimping, tow drops etc., which are handled natively by modelling each discrete tow following the robotic kinematics. The TWM also allows for precise mapping of material orientations on the finite element model following the as-manufactured tow trajectories.

7.2.3 Cohesive network approach

Accurate prediction of material failures requires a model that is able to represent the failure kinematics. Available numerical methods in the literature are either computationally unaffordable or difficult to implement in the TWM. This thesis developed a novel cohesive network method which is a perfect fit into the TWM applications. Three key advancements of this approach are summarised below:

- The cohesive contact is developed based on an advanced segment-to-segment contact formulation in MSC Marc while previous comparable works are limited in the use of cohesive element or node-to-segment contact. These previously developed methods, although feasible, are extremely computational costly due to the strict requirement of the element size near the crack front. While our proposed approach can create multiple contact points within a single element area, which ensures a robust contact interaction and meanwhile allows much coarser meshing to be used in the cohesive zone.
- The use of cohesive contact in simulating different failure interactions including matrix cracking, delamination, and fibre fracture. Cohesive elements require conformal meshes between adjacent layers, which greatly limits their application to simple and flat structures where

partitioning processes are easy to be conducted. The cohesive contact, however, can be used for the interface with non-conformal meshes. The contact interaction is automatically detected and generated by the FE package without many users' inputs, and hence substantially reduces the pre-processing effort in generating the FE model, especially for large and complex composite structure designs.

- The implementation of a modified cohesive law to improve the numerical convergence in implicit FE analysis. Failure is a highly nonlinear problem, which can induce significant convergence issues. The modified cohesive law allows the contact behaviour to be regarded as locally linear within a single load increment, which greatly reduces the non-convergence issues resulting from the contact.

7.2.4 TWM demonstration in AFP composites

AP-Ply laminates are either modelled with plain strain elements in 2D applications or shell elements in 3D applications. These models, which greatly simplify the defects, cannot be used to accurately predict the structural responses and material failures of AP-Ply. This thesis utilises the TWM to facilitate understanding of the material behaviour, as well as the failure mechanisms of AP-Ply laminates. The semi-woven structure, tow crimping and tow gaps are explicitly modelled. The integration of the cohesive network method in the TWM, by allocating cohesive interactions along with the potential failure interfaces, allows for the simulation of different fracture modes of composites at mesoscale. The global response and the failure patterns are both compared against the experimental studies for validation of the feasibility of the TWM. Based on the numerical investigations, the following key conclusions can be drawn:

- The excellent correlation between numerical and experimental results has revealed that the TWM can predict the interface failure, crack deflection, and the ultimate delamination fracture load of AP-Ply laminates with great accuracy.
- Based on the simulation of SBS testing, it was noticed that the major crack initiated near the weaving corner and then propagated in both directions. This suggests that the short beam failure of the AP-Ply laminates was induced by the stress concentration due to tow crimping, and in turn, showed the significance of modelling these AFP manufactured mesoscale geometric features.

7.3 Recommendations for future work

A numerical method at a length scale of tow has been developed in this thesis. The following aspects can be considered for future work to further improve the predictive capabilities of the TWM.

- A consolidation model that can accurately predict the fibre/resin percolation during the curing process could be developed to further improve the fidelity of the TWM.
- The compressive failure modelling capability of the TWM would be needed if the part is subjected to compression-dominant loading. The compressive failure, although not validated in this thesis, can be modelled with a compression-penetration law as opposed to the traction-separation law. To the author's knowledge, a proper manipulation of the constitutive response in the cohesive interaction using the user developed subroutine would allow for a good predictive capability for compressive failures.

- The model scale is limited by the computational power. Future work could consider a full-scale TWM for the LVI tests. In addition, more cohesive interactions can be allocated within the tow to reduce the dependencies of crack locations.
- Further validation tests for the TWM could be performed with a well designed experiment, in which all the critical material parameters as well as their statistical variations can be obtained. A comparison between the TWM and traditional ply-based models can be conducted.
- Variable stiffness laminates would be another great application to further refine the predictive capability and improve the robustness of the TWM.

References

[1] Heinecke F, Willberg C. Manufacturing-induced imperfections in composite parts manufactured via automated fiber placement. Journal of Composites Science. 2019;3(2):56.
[2] Gurdal Z, Olmedo R. In-plane response of laminates with spatially varying fiber orientations-variable stiffness concept. AIAA journal. 1993;31(4):751-8.
[3] Nagelsmit MH. Fibre Placement Architectures for Improved Damage Tolerance. [PhD]: Delft University; 2013.
[4] Woigk W, Hallett SR, Jones MI, Kuhtz M, Hornig A, Gude M. Experimental investigation of the effect of defects in Automated Fibre Placement produced composite laminates. Composite Structures. 2018;201:1004-17.
[5] Croft K, Lessard L, Pasini D, Hojjati M, Chen J, Yousefpour A. Experimental study of the effect of automated fiber placement induced defects on performance of composite laminates. Composites Part A: Applied Science and Manufacturing. 2011;42(5):484-91.
[6] Li X, Hallett SR, Wisnom MR. Modelling the effect of gaps and overlaps in automated fibre placement (AFP)-manufactured laminates. Science and Engineering of Composite Materials. 2015;22(2):115-29.
[7] Nguyen MH, Davidson P, Waas AM. Influence of automated fiber placement (afp) manufacturing signature on the mechanical performance of a composite. AIAA Scitech 2020 Forum2020. p. 0473.
[8] Waldhart C, Gurdal Z, Ribbens C. Analysis of tow placed, parallel fiber, variable stiffness laminates. 37th Structure, Structural Dynamics and Materials Conference1996. p. 1569.
[9] Goldsworthy W. Geodesic path length compensator for composite-tape placement method. Patent US. 1974;3810(805):14.
[10] HENEY P. Trelleborg showcasing Automated Fiber Placement technology at SPE Offshore Europe. 2019.
[11] Dirk H-JL, Ward C, Potter KD. The engineering aspects of automated prepreg layup: History, present and future. Composites Part B: Engineering. 2012;43(3):997-1009.
[12] Oromiehie E. In-situ process monitoring in automated fibre placement-based manufacturing of advanced composites. Sydney, Australia: UNSW (University of New South Wales). 2017.

[13] TRIANGULAR ABO. An accurate path planning algorithm based on triangular meshes in robotic fibre placement. International Journal of Robotics and Automation. 2017;32(1).
[14] Jirka T, Skala V. Gradient vector estimation and vertex normal computation. Technical Report No. DCSE/TR-2002-08. University of West Bohemia in Pilsen; 2002.
[15] Li L, Wang X, Xu D, Tan M. A placement path planning algorithm based on meshed triangles for carbon fiber reinforce composite component with revolved shape. International Journal on Control Systems and Applications (IJCS). 2014;1(1):23-32.
[16] Land IB. Design and manufacture of advanced composite aircraft structures using automated tow placement: Massachusetts Institute of Technology; 1996.
[17] Schueler K, Miller J, Hale R. Approximate geometric methods in application to the modeling of fiber placed composite structures. J Comput Inf Sci Eng. 2004;4(3):251-6.
[18] Shirinzadeh B, Cassidy G, Oetomo D, Alici G, Ang Jr MH. Trajectory generation for open-contoured structures in robotic fibre placement. Robotics and Computer-Integrated Manufacturing. 2007;23(4):380-94.
[19] Rousseau G, Wehbe R, Halbritter J, Harik R. Automated Fiber Placement Path Planning: A state-of-the-art review. Computer-Aided Design and Applications. 2019;16(2):172-203.
[20] Olmedo R, Gurdal Z. Buckling response of laminates with spatially varying fiber orientations. 34th Structures, Structural Dynamics and Materials Conference1993. p. 1567.
[21] Tatting BF, Gurdal Z. Automated finite element analysis of elastically-tailored plates. 2003.
[22] Langley PT. Finite element modeling of tow-placed variable-stiffness composite laminates: Virginia Tech; 1999.
[23] Blom AW. Structural performance of fiber-placed, variable-stiffness composite conical and cylindrical shells. 2010.
[24] Mattheij P, Gliesche K, Feltin D. Tailored fiber placement-mechanical properties and applications. Journal of Reinforced Plastics and Composites. 1998;17(9):774-86.
[25] Brooks TR, Martins JR. On manufacturing constraints for tow-steered composite design optimization. Composite structures. 2018;204:548-59.
[26] Lee H, Hyer M. The Use of Curvilinear Fiber Format to Improve Buckling Resistance of Plates with Central Circular Holes1. Eighth DoD/NASA/FAA Conference on Fibrous in Structural Design1990. p. 167.
[27] Setoodeh S, Abdalla MM, IJsselmuiden ST, Gürdal Z. Design of variable-stiffness composite panels for maximum buckling load. Composite structures. 2009;87(1):109-17.

[28] Jegley DC, Tatting BF, Guerdal Z. Tow-steered panels with holes subjected to compression or shear loads. 2005.
[29] Lopes C, Gürdal Z, Camanho P. Variable-stiffness composite panels: Buckling and first-ply failure improvements over straight-fibre laminates. Computers & Structures. 2008;86(9):897-907.
[30] Ghiasi H, Fayazbakhsh K, Pasini D, Lessard L. Optimum stacking sequence design of composite materials Part II: Variable stiffness design. Composite structures. 2010;93(1):1-13.
[31] Lozano GG, Tiwari A, Turner C, Astwood S. A review on design for manufacture of variable stiffness composite laminates. Proceedings of the Institution of Mechanical Engineers, Part B: Journal of Engineering Manufacture. 2016;230(6):981-92.
[32] Prichard JC, Hogg P. The role of impact damage in post-impact compression testing. Composites. 1990;21(6):503-11.
[33] Richardson M, Wisheart M. Review of low-velocity impact properties of composite materials. Composites Part A: Applied Science and Manufacturing. 1996;27(12):1123-31.
[34] Rad CV, Thomas FD, Seay B, van Tooren MJ, Sockalingam S. Manufacturing and characterization of novel clutch non-conventional fiber-reinforced composite laminates. Composite Structures. 2019;215:454-70.
[35] Rad CV, Kodagali K, Roark J, Revilock D, Ruggeri C, Harik R, et al. High velocity impact response of hybridized pseudo-woven carbon fiber composite architectures. Composites Part B: Engineering. 2020;203:108478.
[36] Sun S, Han Z, Fu H, Jin H, Dhupia JS, Wang Y. Defect characteristics and online detection techniques during manufacturing of FRPs using automated fiber placement: A review. Polymers. 2020;12(6):1337.
[37] Harik R, Saidy C, Williams SJ, Gurdal Z, Grimsley B. Automated fiber placement defect identity cards: cause, anticipation, existence, significance, and progression. Submission to SAMPE 2018 Conference & Exhibition, Long Beach, California, US2018. p. 21-4.
[38] Oromiehie E, Prusty BG, Compston P, Rajan G. Automated fibre placement based composite structures: Review on the defects, impacts and inspections techniques. Composite Structures. 2019;224:110987.
[39] Blom AW, Tatting BF, Hol JM, Gürdal Z. Fiber path definitions for elastically tailored conical shells. Composites part B: engineering. 2009;40(1):77-84.
[40] Tatting BF, Gürdal Z, Jegley D. Design and manufacture of elastically tailored tow placed plates. 2002.
[41] Belnoue JP-H, Mesogitis T, Nixon-Pearson OJ, Kratz J, Ivanov DS, Partridge IK, et al. Understanding and predicting defect formation in automated fibre placement pre-preg laminates. Composites Part A: Applied Science and Manufacturing. 2017;102:196-206.

[42] Kermani NN, Gargitter V, Simacek P, Advani SG. Gap filling mechanisms during the thin ply Automated Tape Placement process. Composites Part A: Applied Science and Manufacturing. 2021;147:106454.
[43] Simacek P, Kermani NN, Gargitter V, Advani SG. Role of resin percolation in gap filling mechanisms during the thin ply thermosetting automated tape placement process. Composites Part A: Applied Science and Manufacturing. 2022;152:106677.
[44] Sawicki A, Minguett P. The effect of intraply overlaps and gaps upon the compression strength of composite laminates. 39th AIAA/ASME/ASCE/AHS/ASC Structures, Structural Dynamics, and Materials Conference and Exhibit 1998. p. 1786.
[45] Lan M, Cartié D, Davies P, Baley C. Influence of embedded gap and overlap fiber placement defects on the microstructure and shear and compression properties of carbon–epoxy laminates. Composites Part A: Applied Science and Manufacturing. 2016;82:198-207.
[46] Marouene A, Legay P, Boukhili R. Experimental and numerical investigation on the open-hole compressive strength of AFP composites containing gaps and overlaps. Journal of Composite Materials. 2017;51(26):3631-46.
[47] Guin WE, Jackson JR, Bosley CM. Effects of tow-to-tow gaps in composite laminates fabricated via automated fiber placement. Composites Part A: Applied Science and Manufacturing. 2018;115:66-75.
[48] Falcó O, Mayugo J, Lopes C, Gascons N, Costa J. Variable-stiffness composite panels: Defect tolerance under in-plane tensile loading. Composites Part A: Applied Science and Manufacturing. 2014;63:21-31.
[49] Falcó O, Lopes C, Mayugo J, Gascons N, Renart J. Effect of tow-drop gaps on the damage resistance and tolerance of Variable-Stiffness Panels. composite structures. 2014;116:94-103.
[50] Cruse TA. Boundary element analysis in computational fracture mechanics: Springer Science & Business Media; 2012.
[51] Swenson D, Ingraffea A. Modeling mixed-mode dynamic crack propagation nsing finite elements: theory and applications. Computational Mechanics. 1988;3(6):381-97.
[52] Perrone N, Kao R. A general finite difference method for arbitrary meshes. Computers & Structures. 1975;5(1):45-57.
[53] Dixit A, Mali HS. Modeling techniques for predicting the mechanical properties of woven-fabric textile composites: a review. Mechanics of composite Materials. 2013;49(1):1-20.
[54] Hyer M, Charette R. Innovative design of composite structures: use of curvilinear fiber format to improve structural efficiency. 1987.
[55] Wu KC, Stanford BK, Turpin JD, Martin RA. Structural performance of advanced composite tow-steered shells with cutouts. 55th

AIAA/ASMe/ASCE/AHS/SC Structures, Structural Dynamics, and Materials Conference2014. p. 1056.
[56] Wu KC, Turpin JD, Gardner NW, Stanford B, Martin RA. Structural Characterization of Advanced Composite Tow-Steered Shells with Large Cutouts. 56th AIAA/ASCE/AHS/ASC Structures, Structural Dynamics, and Materials Conference2015. p. 0966.
[57] Alhajahmad A, Abdalla MM, Gürdal Z. Optimal design of tow-placed fuselage panels for maximum strength with buckling considerations. Journal of Aircraft. 2010;47(3):775-82.
[58] Blom AW, Lopes CS, Kromwijk PJ, Gurdal Z, Camanho PP. A theoretical model to study the influence of tow-drop areas on the stiffness and strength of variable-stiffness laminates. Journal of composite materials. 2009;43(5):403-25.
[59] Falcó O, Lopes C, Naya F, Sket F, Maimí P, Mayugo J. Modelling and simulation of tow-drop effects arising from the manufacturing of steered-fibre composites. Composites Part A: Applied Science and Manufacturing. 2017;93:59-71.
[60] Abdi F, Gürdal Z, Huang D. Certification modeling of composites fuselage, considering effect of defects from fiber placement manufacturing processes. 55th AIAA Aerospace Sciences Meeting2017. p. 0691.
[61] Zheng W, Kassapoglou C. Prediction of delamination onset and growth for AP-PLY composite laminates using the finite element method. Composites Part A: Applied Science and Manufacturing. 2017;101:381-93.
[62] Zheng W, Kassapoglou C, Zheng L. Tailoring of AP-PLY composite laminates for improved performance in the presence of delaminations. Composite Structures. 2019;211:89-99.
[63] Lin H, Brown LP, Long AC. Modelling and simulating textile structures using TexGen. Advanced Materials Research: Trans Tech Publ; 2011. p. 44-7.
[64] Verpoest I, Lomov SV. Virtual textile composites software WiseTex: Integration with micro-mechanical, permeability and structural analysis. Composites Science and Technology. 2005;65(15-16):2563-74.
[65] Mollenhauera D, Iarveb E, Zhoub E, Breitzmana T, Hoosb K, Floresc M. Simulation of Damage Evolution in a Textile Composite Double–Cantilever Beam. ECCM16.
[66] Davies G, Olsson R. Impact on composite structures. The Aeronautical Journal. 2004;108(1089):541-63.
[67] Iarve E, Mollenhauer D, Kim R. Theoretical and experimental investigation of stress redistribution in open hole composite laminates due to damage accumulation. Composites Part A: Applied Science and Manufacturing. 2005;36(2):163-71.

[68] Jirásek M. Modeling of localized damage and fracture in quasibrittle materials. Continuous and discontinuous modelling of cohesive-frictional materials: Springer; 2001. p. 17-29.
[69] Song K, Li Y, Rose C. Continuum damage mechanics models for the analysis of progressive failure in open-hole tension laminates. 52nd AIAA/ASME/ASCE/AHS/ASC Structures, Structural Dynamics and Materials Conference 19th AIAA/ASME/AHS Adaptive Structures Conference 13t2011. p. 1861.
[70] Rybicki EF, Kanninen MF. A finite element calculation of stress intensity factors by a modified crack closure integral. Engineering fracture mechanics. 1977;9(4):931-8.
[71] Shivakumar K, Tan P, Newman Jr J. A virtual crack-closure technique for calculating stress intensity factors for cracked three dimensional bodies. 1988.
[72] Shokrieh M, Rajabpour-Shirazi H, Heidari-Rarani M, Haghpanahi M. Simulation of mode I delamination propagation in multidirectional composites with R-curve effects using VCCT method. Computational Materials Science. 2012;65:66-73.
[73] Orifici AC, Krueger R. Benchmark assessment of automated delamination propagation capabilities in finite element codes for static loading. Finite elements in analysis and design. 2012;54:28-36.
[74] Shokrieh M, Heidari-Rarani M, Rahimi S. Influence of curved delamination front on toughness of multidirectional DCB specimens. Composite Structures. 2012;94(4):1359-65.
[75] De Morais A, De Moura M, Gonçalves J, Camanho P. Analysis of crack propagation in double cantilever beam tests of multidirectional laminates. Mechanics of Materials. 2003;35(7):641-52.
[76] Xie D, Waas AM. Discrete cohesive zone model for mixed-mode fracture using finite element analysis. Engineering fracture mechanics. 2006;73(13):1783-96.
[77] Chau-Dinh T, Zi G, Lee P-S, Rabczuk T, Song J-H. Phantom-node method for shell models with arbitrary cracks. Computers & Structures. 2012;92:242-56.
[78] Rabczuk T, Zi G, Gerstenberger A, Wall WA. A new crack tip element for the phantom - node method with arbitrary cohesive cracks. International Journal for Numerical Methods in Engineering. 2008;75(5):577-99.
[79] Van der Meer F, Sluys L. A phantom node formulation with mixed mode cohesive law for splitting in laminates. International Journal of Fracture. 2009;158(2):107.
[80] Chen B, Pinho S, De Carvalho N, Baiz P, Tay T. A floating node method for the modelling of discontinuities in composites. Engineering Fracture Mechanics. 2014;127:104-34.

[81] Chen B, Tay T, Pinho S, Tan V. Modelling the tensile failure of composites with the floating node method. Computer Methods in Applied Mechanics and Engineering. 2016;308:414-42.
[82] Lu X, Chen B-Y, Tan VB, Tay T-E. Adaptive floating node method for modelling cohesive fracture of composite materials. Engineering Fracture Mechanics. 2018;194:240-61.
[83] Belytschko T, Gracie R, Ventura G. A review of extended/generalized finite element methods for material modeling. Modelling and Simulation in Materials Science and Engineering. 2009;17(4):043001.
[84] Iarve EV, Gurvich MR, Mollenhauer DH, Rose CA, Dávila CG. Mesh‐independent matrix cracking and delamination modeling in laminated composites. International journal for numerical methods in engineering. 2011;88(8):749-73.
[85] Van der Meer FP. Mesolevel modeling of failure in composite laminates: constitutive, kinematic and algorithmic aspects. Archives of Computational Methods in Engineering. 2012;19(3):381-425.
[86] Fries TP, Belytschko T. The extended/generalized finite element method: an overview of the method and its applications. International journal for numerical methods in engineering. 2010;84(3):253-304.
[87] Ling D, Yang Q, Cox B. An augmented finite element method for modeling arbitrary discontinuities in composite materials. International journal of fracture. 2009;156(1):53-73.
[88] Liu W, Yang Q, Mohammadizadeh S, Su X, Ling D. An accurate and efficient augmented finite element method for arbitrary crack interactions. Journal of Applied Mechanics. 2013;80(4).
[89] Harper PW, Hallett SR. Cohesive zone length in numerical simulations of composite delamination. Engineering Fracture Mechanics. 2008;75(16):4774-92.
[90] Chen MC, AJ Kinloch, EP Busso, FL Matthews, Y. Qiu, J. Predicting progressive delamination of composite material specimens via interface elements. Mechanics of composite materials and structures. 1999;6(4):301-17.
[91] Alfano G, Crisfield MA. Finite element interface models for the delamination analysis of laminated composites: mechanical and computational issues. International journal for numerical methods in engineering. 2001;50(7):1701-36.
[92] Garg N, Prusty BG, Ooi ET, Song C, Pearce G, Phillips AW. Application of scaled boundary finite element method for delamination analysis of composite laminates using cohesive zone modelling. Composite Structures. 2020;253:112773.
[93] Pearce G, Johnson A, Hellier A, Thomson R. A stacked-shell finite element approach for modelling a dynamically loaded composite bolted joint under in-plane bearing loads. Applied Composite Materials. 2013;20(6):1025-39.

[94] Pearce G, Johnson A, Hellier A, Thomson R. A study of dynamic pull-through failure of composite bolted joints using the stacked-shell finite element approach. Composite Structures. 2014;118:86-93.
[95] Johnson A, Holzapfel M. Influence of delamination on impact damage in composite structures. Composites science and technology. 2006;66(6):807-15.
[96] Joosten M, Yang Q, Blacklock M, Wang C. A cohesive network approach for modelling fibre and matrix damage in composite laminates. Composite Structures. 2018;206:658-67.
[97] Bouvet C, Rivallant S, Barrau J-J. Low velocity impact modeling in composite laminates capturing permanent indentation. Composites Science and Technology. 2012;72(16):1977-88.
[98] Sun X, Wisnom M, Hallett S. Interaction of inter-and intralaminar damage in scaled quasi-static indentation tests: Part 2–Numerical simulation. Composite Structures. 2016;136:727-42.
[99] Shi Y, Pinna C, Soutis C. Modelling impact damage in composite laminates: A simulation of intra- and inter-laminar cracking. Composite Structures. 2014;114:10-9.
[100] Turon A, Camanho PP, Costa J, Dávila C. A damage model for the simulation of delamination in advanced composites under variable-mode loading. Mechanics of materials. 2006;38(11):1072-89.
[101] Yang Q, Cox B. Cohesive models for damage evolution in laminated composites. International Journal of Fracture. 2005;133(2):107-37.
[102] Do B, Liu W, Yang Q, Su X. Improved cohesive stress integration schemes for cohesive zone elements. Engineering Fracture Mechanics. 2013;107:14-28.
[103] Mukhopadhyay S, Hallett SR. An augmented cohesive element for coarse meshes in delamination analysis of composites. Composite Structures. 2020;254:112890.
[104] Borg R, Nilsson L, Simonsson K. Simulation of low velocity impact on fiber laminates using a cohesive zone based delamination model. Composites Science and Technology. 2004;64(2):279-88.
[105] Borg R, Nilsson L, Simonsson K. Simulating DCB, ENF and MMB experiments using shell elements and a cohesive zone model. Composites Science and Technology. 2004;64(2):269-78.
[106] Puso MA, Laursen TA. A mortar segment-to-segment frictional contact method for large deformations. Computer methods in applied mechanics and engineering. 2004;193(45-47):4891-913.
[107] Chiu C, Lai M, Wu C. Compression failure mechanisms of 3-D angle interlock woven composites subjected to low-energy impact. Polymers and Polymer Composites. 2004;12(4):309-20.
[108] Fibre Placement Manager. 4.1.1.5 ed.

[109] ASTM D. 2344 Standard Test Method for Short-Beam Strength of Polymer Matrix Composite Materials and Their Laminates. ASTM: West Conshohocken, PA, USA. 2016.
[110] Xie M, Adams D. Contact finite element modeling of the short beam shear test for composite materials. Computers & structures. 1995;57(2):183-91.
[111] Cui W, Wisnom M, Jones M. Failure mechanisms in three and four point short beam bending tests of unidirectional glass/epoxy. The Journal of Strain Analysis for Engineering Design. 1992;27(4):235-43.
[112] Zhao C, Donough MJ, Prusty BG, Xiao J. Influences of ply waviness and discontinuity on automated fibre placement manufactured grid stiffeners. Composite Structures. 2021;256:113106.
[113] Corp PA. Park Advanced Composite Materials E-752-LT Epoxy Prepreg. 2015.2.13 ed2015.
[114] event. ADDM-stmfmtdroaf-rpmctad-wi.
[115] Abisset E, Daghia F, Sun X, Wisnom MR, Hallett SR. Interaction of inter- and intralaminar damage in scaled quasi-static indentation tests: Part 1–Experiments. Composite Structures. 2016;136:712-26.
[116] Lopes C, Sádaba S, González C, Llorca J, Camanho P. Physically-sound simulation of low-velocity impact on fiber reinforced laminates. International Journal of Impact Engineering. 2016;92:3-17.
[117] composite. ADDM-stmfcrspodpm.
[118] D6641 A. Standard test method for compressive properties of polymer matrix composite materials using a combined loading compression (CLC) test fixture. West Conshohocken, PA: American Society for the Testing of Materials. 2016.
[119] Haggerty D. Trimesh. 3.2.0 ed2020.
[120] Tabarraei A, Sukumar N. Adaptive computations on conforming quadtree meshes. Finite elements in Analysis and Design. 2005;41(7-8):686-702.
[121] Falcó O, Ávila R, Tijs B, Lopes C. Modelling and simulation methodology for unidirectional composite laminates in a Virtual Test Lab framework. Composite Structures. 2018;190:137-59.
[122] Lopes CS, Gómez DG, Falcó O, Tijs BH. Stochastic virtual testing laboratory for unidirectional composite coupons: from conventional to dispersed-ply laminates. Multi-Scale Continuum Mechanics Modelling of Fibre-Reinforced Polymer Composites: Elsevier; 2021. p. 579-607.
[123] Michael S. ABAQUS/Standard User's Manual, Version 6.9: Dassault Systèmes Simulia Corp; 2009.
[124] Johnson AF, Pickett AK, Rozycki P. Computational methods for predicting impact damage in composite structures. Composites Science and Technology. 2001;61(15):2183-92.

[125] Liu P, Liao B, Jia L, Peng X. Finite element analysis of dynamic progressive failure of carbon fiber composite laminates under low velocity impact. Composite Structures. 2016;149:408-22.
[126] Lampeas G, Fotopoulos K, Perogamvros N. Development and experimental validation of explicit dynamics simulation of composite structures using a stacked thick-shell methodology. Plastics, Rubber and Composites. 2016;45(2):58-67.
[127] Tabatabaei S, Lomov SV, Verpoest I. Assessment of embedded element technique in meso-FE modelling of fibre reinforced composites. Composite Structures. 2014;107:436-46.
[128] Chowdhury N, Joosten M, Pearce G. An embedded meshing technique (SET) for analysing local strain distributions in textile composites. Composite Structures. 2019;210:294-309.
[129] Zhang J, Zhang X. Simulating low-velocity impact induced delamination in composites by a quasi-static load model with surface-based cohesive contact. Composite Structures. 2015;125:51-7.
[130] Clark D. HIGHLIGHTS AND PITFALLS OF OPENING YOUR OWN BRICK AND MORTAR SHOP.
[131] Pinho S, Iannucci L, Robinson P. Physically-based failure models and criteria for laminated fibre-reinforced composites with emphasis on fibre kinking: Part I: Development. Composites Part A: Applied Science and Manufacturing. 2006;37(1):63-73.
[132] Hokkanen J. Introduction of a segment-to-segment penalty contact formulation. 2014.
[133] Hashin Z. Failure criteria for unidirectional fiber composites. 1980.
[134] Tsai SW, Wu EM. A general theory of strength for anisotropic materials. Journal of composite materials. 1971;5(1):58-80.
[135] Rots JG, Invernizzi S, Belletti B. Saw-tooth softening/stiffening-a stable computational procedure for RC structures. Computers and Concrete. 2006;3(4):213-33.
[136] Ridha M, Wang C, Chen B, Tay T. Modelling complex progressive failure in notched composite laminates with varying sizes and stacking sequences. Composites Part A: Applied Science and Manufacturing. 2014;58:16-23.
[137] Graça-e-Costa R, Alfaiate J, Dias-da-Costa D, Sluys L. A non-iterative approach for the modelling of quasi-brittle materials. International Journal of Fracture. 2012;178(1-2):281-98.
[138] Mindlin RD. Influence of rotatory inertia and shear on flexural motions of isotropic, elastic plates. J appl Mech. 1951;18:31-8.
[139] Reissner E. The effect of transverse shear deformation on the bending of elastic plates. J appl Mech. 1945:A69-A77.

[140] Kirchoff G. Uber das Gleichgewicht und die Bewegung einer elastischen Scheibe. Journal fur die reine und angewandte Mathematik (Crelle's Journal). 1850;40:51-88.
[141] Love A. H., 1944. A Treatise on the Mathematical Theory of Elasticity. Dover, New York; 1944.
[142] Lu X, Ridha M, Chen B, Tan V, Tay T. On cohesive element parameters and delamination modelling. Engineering Fracture Mechanics. 2019;206:278-96.
[143] Cao D, Duan Q, Hu H, Zhong Y, Li S. Computational investigation of both intra-laminar matrix cracking and inter-laminar delamination of curved composite components with cohesive elements. Composite Structures. 2018;192:300-9.
[144] Hallett SR, Jiang W-G, Khan B, Wisnom MR. Modelling the interaction between matrix cracks and delamination damage in scaled quasi-isotropic specimens. Composites Science and Technology. 2008;68(1):80-9.
[145] Hou JP, Petrinic N, Ruiz C, Hallett S. Prediction of impact damage in composite plates. Composites Science and Technology. 2000;60(2):273-81.
[146] Hou J, Petrinic N, Ruiz C. A delamination criterion for laminated composites under low-velocity impact. Composites science and technology. 2001;61(14):2069-74.
[147] Li X, Hallett SR, Wisnom MR. Predicting the effect of through-thickness compressive stress on delamination using interface elements. Composites Part A: Applied Science and Manufacturing. 2008;39(2):218-30.
[148] May M, Hallett SR. An assessment of through-thickness shear tests for initiation of fatigue failure. Composites Part A: Applied Science and Manufacturing. 2010;41(11):1570-8.
[149] Zhang X, Bianchi F, Liu H. Predicting low-velocity impact damage in composites by a quasi-static load model with cohesive interface elements. Aeronautical Journal. 2012;116(1186):1367.
[150] Gan KW, Hallett SR, Wisnom MR. Measurement and modelling of interlaminar shear strength enhancement under moderate through-thickness compression. Composites Part A: Applied Science and Manufacturing. 2013;49:18-25.
[151] D5528 A.
[152] D7905 A.
[153] Hwang J, Lee C, Hwang W. Effect of crack propagation directions on the interlaminar fracture toughness of carbon/epoxy composite materials. Applied Composite Materials. 2001;8(6):411-33.
[154] Pereira A, De Morais A, Marques A, De Castro P. Mode II interlaminar fracture of carbon/epoxy multidirectional laminates. Composites Science and Technology. 2004;64(10-11):1653-9.

[155] Polaha J, Davidson B, Hudson R, Pieracci A. Effects of mode ratio, ply orientation and precracking on the delamination toughness of a laminated composite. Journal of Reinforced Plastics and Composites. 1996;15(2):141-73.
[156] Rice J. The mechanics of earthquake rupture. International School of Physics "E. Fermi", Course 78, 1979: Italian Physical Society. North Holland Publ. Co; 1980.
[157] Gan KW, Allegri G, Hallett SR. A simplified layered beam approach for predicting ply drop delamination in thick composite laminates. Materials & Design. 2016;108:570-80.
[158] Allegri G, Wisnom M, Hallett S. A simplified approach to the damage tolerance design of asymmetric tapered laminates. Part I: Methodology development. Composites Part A: Applied Science and Manufacturing. 2010;41(10):1388-94.
[159] Abali F, Pora A, Shivakumar K. Modified short beam shear test for measurement of interlaminar shear strength of composites. Journal of composite materials. 2003;37(5):453-64.
[160] Aoki Y, Suemasu H, Ishikawa T. Damage propagation in CFRP laminates subjected to low velocity impact and static indentation. Advanced Composite Materials. 2007;16(1):45-61.
[161] Stout M, Koss D, Liu C, Idasetima J. Damage development in carbon/epoxy laminates under quasi-static and dynamic loading. Composites science and technology. 1999;59(16):2339-50.
[162] Olsson R. Mass criterion for wave controlled impact response of composite plates. Composites Part A: Applied Science and Manufacturing. 2000;31(8):879-87.
[163] Nettles AT, Douglas MJ. A comparison of quasi-static indentation to low-velocity impact. 2000.
[164] Nguyen MH, Vijayachandran AA, Davidson P, Call D, Lee D, Waas AM. Effect of automated fiber placement (AFP) manufacturing signature on mechanical performance of composite structures. Composite Structures. 2019;228:111335.